UNIVERSITÀ
degli STUDI
di CATANIA

Dipartimento
di Fisica
e Astronomia
"Ettore Majorana"

PhD programme in physics

Chiara Pinto

Light (anti)nuclei production with ALICE at the Large Hadron Collider

PhD thesis

Supervisors:
Prof. F. Riggi
Prof. P. La Rocca

---

academic year 2020/2021

Abstract

Ultra-relativistic Heavy Ion Collisions (HICs) allow to reproduce the extreme conditions of temperature and energy density where the Quark-Gluon Plasma (QGP) is formed. Based on the current cosmological picture, QGP was the state of our universe few μs after the Big Bang. Moreover, there is evidence that a degenerate state of matter with similar properties to the QGP exists in the inner core of neutron stars and other compact astrophysical objects.

Heavy ion collisions produce not only hadrons (among which pions, kaons and protons are the most abundantly produced) but also composite and even fragile objects such as light nuclei (d, t, ^{3}He, ^{4}He) and light Λ-hypernuclei, along with their antiparticles. Their measured yields decrease strongly with increasing (anti)baryon number – the penalty factor for each additional (anti)baryon is about 300 – hence (anti)^{4}He production is a very rare process. The production rate at the CERN Large Hadron Collider (LHC) for deuterons is approximately one every one thousand p–Pb collisions corresponding to a charged-particle density of about 20. The production rate of heavier nuclei, such as ^{3}He, is even lower (one every one million events). Hence, the study of light (anti)nuclei production is particularly challenging. At the same time, light nuclei and their antimatter counter parts are particularly interesting since the production mechanism of such loosely bound states is still under debate. (Anti)nuclei have a binding energy of the order of 1 MeV per nucleon. This value is extremely low if compared with the chemical freeze-out temperature of a nucleus-nucleus collision ($T_{\mathrm{chem}} \sim 150$ MeV). Hence, it is surprising

to see how these loosely-bound objects like light (anti)nuclei can be produced and survive in such extreme conditions. The production of light (anti)nuclei is usually described using two classes of phenomenological models: the Statistical Hadronisation Models (SHMs) and the Coalescence models. Both classes of models describe different aspects of the production of light (anti)nuclei. The comparison between the experimental results of (anti)nuclei production and the hadronization models currently available is crucial to shed light on the production mechanism.

A Large Ion Collider Experiment (ALICE) has been designed to deal with the harsh environment of the ultra-relativistic hadronic collisions and to study in details the characteristics of the QGP. ALICE has excellent tracking and Particle IDentification (PID) capabilities over a broad momentum range. This makes ALICE the most suited detector at the LHC to study light (anti)nuclei produced in such high-energy hadronic collisions.

(Anti)nuclei with mass numbers up to A = 4, such as (anti)deuterons, (anti)tritons, (anti)^{3}He and (anti)^{4}He have been successfully identified in ALICE in the pseudorapidity region $|\eta| < 0.9$ using different experimental techniques and different detectors, namely the Inner Tracking System (ITS), the Time Projection Chamber (TPC) and the Time Of Flight detector (TOF).

In this work, measurements of (anti)deuteron and (anti)^{3}He production as a function of the transverse momentum (p_{T}) and event multiplicity in p–Pb collisions at a centre-of-mass energy per nucleon–nucleon pair $\sqrt{s_{\mathrm{NN}}}$ = 8.16 TeV are presented. In order to compare the results from different collision systems and energies with the expectations of the models, it is useful to study the production yields of nuclei for different multiplicity classes. Consequently, it is possible to investigate whether the production mechanism of light (anti)nuclei is similar in small and medium-large collision systems. In this context, the p–Pb system is particularly interesting as it links existing results in pp and Pb–Pb collisions, corresponding to small and large system sizes, respectively. One of the most interesting results obtained from the large variety of experimental data analyzed from ALICE is that the dominant production mechanism of light (anti)nuclei seems to depend solely on the event charged-particle multiplicity. Evidence for this comes from the continuous evolution of the

nucleus-to-proton and nucleus-to-pion yield ratios with the event multiplicity across different collision systems and energies. The comparison with the predictions of the statistical hadronization and coalescence models favors the coalescence description for the deuteron-to-proton yield ratio with respect to the Canonical Statistical Model (CSM), which fails to simultaneously reproduce the deuteron-to-pion yield ratio.

Additionally, the coalescence parameters B_2 and B_3, which are related to the probability to form a deuteron or a ^{3}He via coalescence of their nucleon constituents, are measured as a function of the transverse momentum per nucleon and of the mean charged-particle multiplicity density. Such coalescence parameters confirm a smooth evolution from low to high multiplicity across different collision systems and energies. The results of B_2 as a function of the mean charged-particle multiplicity density show a good agreement with the coalescence model that uses the parameterization of the source radii based on femtoscopic techniques.

The light (anti)nuclei results are also relevant for background studies in the search for dark matter via the measurement of (anti)nuclei in space and as input for the understanding of the formation of QCD bound states in high energy hadron physics.

Contents

Chapter 1

High energy nuclear physics

In the current understanding, the energy density in the early universe was so high that the fundamental components of ordinary matter could not bind to form hadrons. The transition from this phase to the ordinary matter and the properties of the hot and dense nuclear matter is the main subject of study of High Energy Nuclear Physics.

1.1 Introduction

In ordinary matter quarks and gluons are confined inside hadrons by the strong interaction. Quantum Chromo Dynamics (QCD), the theory of strong interaction, predicts a phase transition from hadronic phase to a deconfined phase of quarks and gluons, called *quark-gluon plasma* (QGP), at temperatures and energy densities exceeding some critical thresholds. The interest in this particular phase of matter comes from the need to understand the structure of our universe in the early stages of its evolution. In fact, it has been established that few μs after the Big Bang the quark-gluon plasma was the state of our universe [1]. Moreover, the physical conditions in the inner core of neutron stars and other compact and massive astrophysical objects are believed to be suitable for the existence of the QGP as a stable phase of the matter. The study of the QGP properties is thus a common interest of Astrophysics, Cosmology, as well as Particle Physics. Since it is not possible to access the inner parts of a neutron star

or to look back in time when our universe was opaque, a promising way to study the quark-gluon plasma is to create it in the laboratory. Violent collisions of heavy ions, pushed to ultra-relativistic energies by powerful accelerators, create small drops of this matter, which have typical lifetimes of few tens of fm/c. They rapidly expand, undergoing several thermodynamic states before quarks and gluons recombine again to form hadrons (hadronization).

Several experiments performed in the last two decades at the Super Proton Synchrotron (SPS) at CERN and at the Relativistic Heavy Ion Collider (RHIC) at Brookhaven National Laboratory, have provided a significant evidence of the formation of this novel state of matter. The exploration of its physical properties now continues at higher energies with the Large Hadron Collider (LHC) at CERN, within its heavy ion experimental program.

The study of the transition to a deconfined phase of quarks and gluons is not only relevant to understand and characterize the beginning of our universe, but it has a deep impact on the theoretical aspects of the QCD. In physics, a phase transition is usually accompanied by a symmetry restoration. An analogy with the ferromagnetic phase transition can be made, where the isotropy symmetry is broken at low temperature when all dipole magnetic moments are aligned, giving a macroscopic magnetization. This symmetry is however restored at high temperatures, where the thermal motion of the particles prevents a preferred orientation of the magnetic dipole moments.

Chiral symmetry is an approximate symmetry of the QCD Lagrangian which is spontaneously broken at low temperatures and it is expected to be restored at high temperatures and energy densities. Lattice QCD calculations indicate that the transition which leads to restoration of chiral symmetry (chiral transition) and the deconfinement phase transition occur at the same critical temperature, providing strong evidence that these two different transitions might actually coincide. The understanding of the conditions for the restoration of chiral symmetry is crucial not only for theoretical reasons, but also for its impact on the structure of our universe: chiral symmetry breaking is, in fact, responsible for $\sim 99\%$ of the proton and neutron masses, hence most of the visible mass of our universe, i.e. excluding dark matter. Many open questions which need to

be addressed still remain, such as the order of the phase transition, the characterization of the QCD phase diagram, the equation of state of the QGP, its evolution and the exact mechanism of hadronization.

1.2 QCD and the strong interaction

In the '60s a large number of different hadronic states were already discovered (e.g. Δ resonance, the kaons) and yet there was no theoretical framework able to explain the experimental observations of such a large zoo of particles. The first theoretical success in explaining the hadron spectroscopy was the prediction of the existence of the Ω baryon starting from the three flavour families classification, SU(3), of the hadrons [2]. This classification evolved later into the static Quark Model that describes the hadron zoology in terms of constituent particles with fractional charge [3, 4].
The quark model was introduced by Murray Gell-Mann and George Zweig in 1964 [5] to provide a plausible explanation of the curious patterns of the *Eightfold Way*, i.e. the classification of hadrons according to their hypercharge and strangeness. According to this model, hadrons are bound states of quarks. More specifically, baryons are made of three quarks (antibaryons are made of three antiquarks) and mesons are made of a quark and an antiquark. Despite the success of the quark model in explaining the hadron multiplets and predicting new particles that had indeed been discovered (like the Ω), there was a diffuse skepticism by many physicists due to the lack of observation of free quarks. The notion of confinement was introduced in order to explain the failure of experiments to produce isolated quarks. A more comprehensive understanding of the mechanism responsible for quark confinement came a short time later when Greenberg introduced the colour quantum number to save the quark model from a deep inconsistency related to the Pauli exclusion principle: each quark has an additional degree of freedom, expressed by an additive quantum number called colour, which can assume three possible values (red, blue and green), as well as the corresponding anticolour for antiquarks. This can be expressed using the analogy between the colour states and 2-dimensional vectors: the three colour states correspond to

three vectors, all starting from the point (0, 0) and forming angles of 120° with the neighbor (Fig. 1.1). The colour quantum number of a composite object is given by the vector sum of the colours of its constituents. According to this geometrical analogy, a baryon is made of three quarks with different colour states, and a meson is made of a quark with a given colour and an antiquark with the corresponding anticolour.

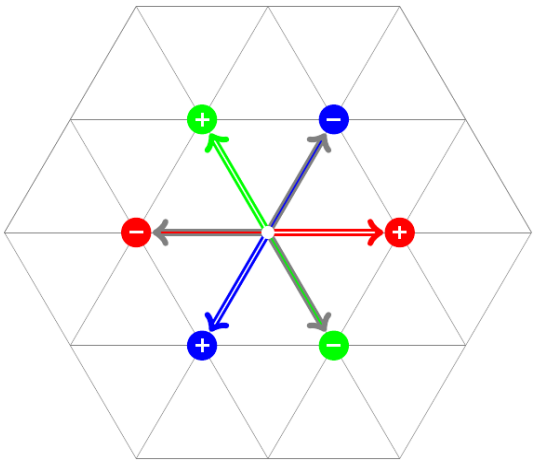

Figure 1.1: Geometrical analogy between colour states and 2-dimensional vectors. The colour of the bound state is given by the vector sum of the colours of its constituents.

Colour however cannot be observed directly, as composite (anti)hadrons are colour neutral and are either made up of three (anti)quarks (qqq) that carry all three (anti)colours, or consist of a pair of one quark and an antiquark ($q\bar{q}$). The mediators of the strong force that couple to the colour charges are called gluons. Unlike photons, the gluons are not neutrally charged but also carry colour. The colour charge of the gluons consists of a colour and a different anticolour (there is no colour neutral gluon). A gluon exchange between two quarks therefore results in a colour change. As gluons are coloured particles, they are bound to confinement, which results in the short range of the strong force. Confinement arises as the attractive force between quarks does not vanish with increasing distance, unlike Quantum Electro-Dynamics (QED), but remains constant. The energy in the field between the quarks rises until the threshold for quark-antiquark pair production is reached and a $q\bar{q}$ pair is created. Therefore

quarks can never be observed individually - they are confined in mesons and baryons.
The potential between a heavy quark-antiquark pair can phenomenologically be described by the Cornell potential [6].

$$V(r) = -\frac{4}{3}\frac{\alpha_s}{r} + \kappa r \tag{1.1}$$

For short distances (r), the potential resembles a Coulomb like potential while towards higher r the linear increasing term becomes dominant. The latter is often referred to as the *confinement* term and the constant κ is often associated with a string tension between the two quarks in analogy with the constant force of a spring. The shape of this potential is verified by model calculations of the QCD, such as lattice QCD [7]. The string tension is found to be in the order of κ = 1 GeV/ fm [8]. The Cornell potential in the vacuum is modified by the presence of the coloured medium of the deconfined phase that screens the interaction between quarks. Inside the medium the potential becomes:

$$V(r) = -\frac{\alpha_s}{r} e^{-r/r_D} \tag{1.2}$$

The potential is modulated by an exponential, driven by the attenuation length r_D that is called *Debye radius* such that hadrons with a radius larger than r_D cannot bind in the medium.
In QCD the coupling constant α_s decreases with increasing energy Q (Figure 1.2) [9].

This can be understood in a schematic picture. From the uncertainty relation of Heisenberg, it follows that high energy partons (quarks or gluons) will resolve a smaller volume around the colour charge, while low energy partons will resolve a larger volume. The colour charge however cannot be assumed to be static. A quark for example is constantly emitting and absorbing gluons. Thereby the gluons spread the effective charge over a larger volume - the colour charge is diffused. A high energy parton will resolve a smaller colour charge. The decreasing coupling in QCD is known as *asymptotic freedom*. For its discovery David J. Gross, H. David Politzer and Frank Wilczek were awarded with the Nobel Prize in 2004. The running coupling constant implies that calculations of QCD

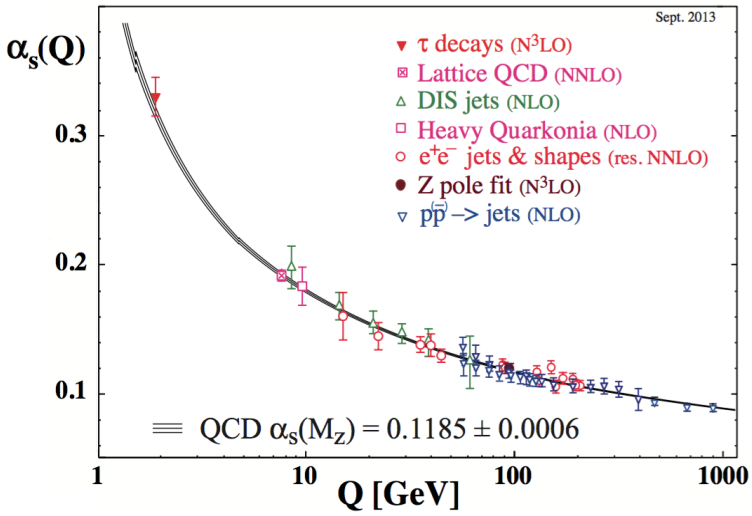

Figure 1.2: Strong coupling constant α_S as a function of the momentum transfer Q in the interaction [10].

can be performed using perturbation theory (pQCD) at high enough energies. Typically an energy larger than $\Lambda_{QCD} \sim 200$ MeV is required. The formation of particles, however, occurs at lower energy and therefore a process such as hadronization cannot be described perturbatively. The concept of asymptotic freedom is expressed in a mathematical way by the dependence of the strong coupling constant on the momentum transfer in the interaction between two (anti)quarks [9]:

$$\alpha_s(|Q^2|) = \frac{12\pi}{(11n_C - 2f)\ln(|Q^2|/\Lambda^2_{QCD})} \tag{1.3}$$

where n_C is the number of colours, f the number of quark flavors and $\Lambda_{QCD} \sim 200$ MeV is the scale parameter of the theory. In nature 11 $n_C > 2$ f, and as a consequence, the strength of the coupling constant decreases at high momentum transfer, i.e. at short distances. In Fig. 1.2, α_s is shown as a function of the energy including different calculations at different leading orders of the QCD perturbation theory [10]. The so-called anti-screening effect[1] causes the quarks inside hadrons to behave as quasi-free

[1]Anti-screening follows from the calculation of vacuum polarisation in QCD. The

particles, when probed at large enough energies. As already mentioned, this property of the strong interaction is called asymptotic freedom and it allows us to use perturbation theory achieving quantitative predictions for hard scattering cross sections in hadronic interactions [11].

Asymptotic freedom represents an important advantage for theoretical calculations. In the high-energy regime ($|Q^2| \geq 1\ \mathrm{GeV}^2$), when the strength of the interaction is weak, QCD can be treated perturbatively, thus enormously simplifying the calculations of cross sections and decay rates. The perturbative approach, however, cannot be applied in the domain where $\alpha \geq 1$ ($|Q^2| \leq 1\ \mathrm{GeV}^2$), since higher order Feynman diagrams give increasing contributions which cannot be neglected in the calculations.

On the other hand, at increasing distances (small Q) the coupling becomes so strong that is impossible to isolate quarks from hadrons. This mechanism is called confinement and it is verified in Lattice QCD calculations [12,13] but not mathematically proven from first principles due to its non-perturbative nature.

The previous considerations refer to what is called *running coupling constant*. In summary, according to Eq. 1.3, it is possible to conclude that:

- if $Q^2 \to \infty$, $\alpha_s(Q^2) \to 0$: asymptotic freedom;
- if $Q^2 \to 0$, $\alpha_s(Q^2) \to \infty$: confinement

The difficulty in solving QCD equations in the low-energy regime has led to the development of many effective models to obtain predictions, to explain phenomena and hadron properties at low energy, such as hadron masses, the hadronization mechanism and the coupling strength. Nowadays the application of QCD in the low-energy domain is based on lattice QCD, where the QCD equations are solved numerically in a finite space-time lattice, with the usage of computers.

QCD vacuum consists of virtual $q\bar{q}$ pairs, and if this would be all, the charge screening mechanism would be the same as in QED. However, due to the gluon self-coupling, the vacuum is also filled with virtual gluon pairs. Since the gluon cloud carries colour charge, it turns out that the effective charge becomes larger with larger distances. This effect is known as anti-screening.

1.3 States of the hadronic matter

One important consequence of the running of α_s is the possibility of creating different states of the hadronic matter. Considering a system with finite dimensions composed by quarks and gluons, the state of the hadronic matter of the system depends on the mean transferred momentum in the interactions inside the medium. It is convenient to describe these hadronic systems using variables typical of thermodynamics like temperature (T) and chemical potential (μ) associated with the baryonic number. Figure 1.3 shows the phase diagram of the QCD matters predicted by the theory and the values of T and μ that are accessible experimentally in high energy heavy ion collisions at colliders.

The origin of the phase diagram (T = μ = 0 GeV) corresponds to the QCD vacuum. At T = 0 GeV, μ is the energy required to create a baryonic state, thus ordinary QCD matter (proton, neutrons and nuclei) sits at almost zero temperature and $\mu \sim 1$ GeV. Moving further along the μ axis there is a phase transition to the deconfined state that has been hypothesised to be present in the core of neutron stars [15]. In a similar way, when moving towards T $\gg \Lambda_{\mathrm{QCD}}$ and $\mu \sim 0$, the system becomes similar to the primordial universe and undergoes a crossover transition to the deconfined state called QGP. As the temperature increases, the average momentum exchange between the constituents increases as well and the interaction becomes less and less strong. Quarks and gluons are no longer confined in colour singlets and they constitute a plasma of free coloured partons. The energy density ϵ and pressure p in this state of matter can be approximated using the equations of state of an ideal gas of massless particles confined in a bag of volume V [16]:

$$p = \frac{\pi^2}{90} n_{\mathrm{DOF}} T^4 \, , \, \epsilon = 3p \tag{1.4}$$

where n_{DOF} is the number of different particle states (degrees of freedom, DOF) populating the system.

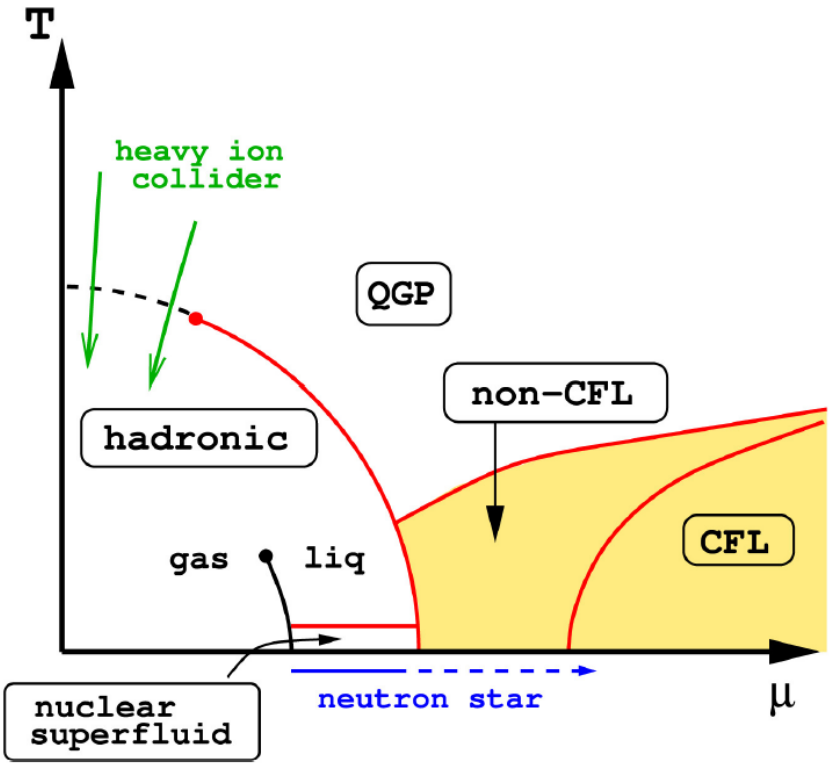

Figure 1.3: Schematic nuclear matter phase diagram from [14]. QGP refers to the Quark Gluon Plasma state, CFL (Colour-Flavour Locked) corresponds to the colour superconducting phase that is present in systems with high baryon chemical potential (e.g. core of neutron stars, from 5 to 10 times the baryon chemical potential of ordinary matter). The green arrows represent the phase space probed by collider experiments at the Relativistic Heavy Ion Collider (RHIC) and at the LHC.

1.4 Predictions of the QGP

Predictions of the QGP state can be achieved with different models and theories which are listed in the following.

- Perturbative QCD (pQCD) [11],
  - allows us to use a perturbative expansion in series of the strong coupling constant α_s with the requirement that $\alpha_s \ll 1$. The pro-

cesses that satisfy this condition are those with large transferred momentum Q^2 (see Sect. 1.2) such as the heavy flavor production in hadron collisions.

- Lattice QCD [12,13],
  - is a complex non-perturbative theory of the QCD based on a discrete lattice of the space-time coordinates which provides a quantitative understanding of the new phase of matter. For instance the calculations with this theory give a quite accurate estimate of the critical temperature [17] and of the hadron masses [18]. As a drawback, to reach a small pitch of the lattice, very high performance computers are needed.

- Effective models,
  - based on QCD, they provide a phenomenological description of the physical processes. For example, the MIT bag model [19] considers massless quarks confined into a bag of finite dimensions. The confinement derives from the balance between the pressure due to the kinetic energy of the quarks and the external pressure. If the internal pressure overcomes the external one, the bag breaks. The pressure in the bag can increase for two main reasons: the temperature becomes higher (kinetic energy associated to the quarks) or the baryon density grows (compression). Experimentally, it is possible to induce these conditions in the nuclear matter with heavy ion collisions.

1.5 Heavy Ion collisions

Currently, the only known way to cross the phase boundary between ordinary hadronic matter and QGP in the laboratory is by colliding ultra-relativistic heavy ions. The first experiments on Heavy Ion Collisions (HICs) were performed with a fixed target configuration, at the Alternate Gradient Synchrotron (AGS) at the Brookhaven National Laboratory, and at the Super Proton Synchrotron (SPS) at CERN, with centre-of-mass (CM) energies in the range between 2 GeV/nucleon and 18 GeV/nucleon. The next generation of experiments was based on ion-beam collisions.

The first experiments on HIC at energies $\geq$ 2 GeV/nucleon were performed at the Bevalac accelerator, at the Lawrence Berkeley National Laboratory. Starting from then, many HIC experiments at higher and higher energies took place. Nowadays two of the main hadron colliders with an active HIC program are: the Relativistic Heavy Ion Collider (RHIC) at the Brookhaven National Laboratory (BNL) and the Large Hadron Collider (LHC) at CERN. RHIC and LHC can provide heavy ion collisions with a CM energy up to 200 GeV/nucleon and 5.02 TeV/nucleon respectively.

To explore the existence of QGP in the laboratory, it is important to create a strongly interacting system which satisfies two main requirements:

- Large spatial extension: we want to use macroscopic variables and the system dimensions must be greater than the scale of the strong interaction ($\sim$ 1 fm). Large extension means also a large number of particles ($\gg$ 1).

- Long life: we want to use the language of thermodynamic, and the system must reach the thermal equilibrium ($\tau \gg$1 fm/c, where τ is the collision time).

Moreover we want to reach the correct energy density for the transition phase. The critical energy density ϵ_c can be calculated in statistical mechanics [20] as follows:

$$\epsilon_c = 37\frac{\pi^2}{30}T^4\frac{1}{(\hbar c)^3} \tag{1.5}$$

where 37 represents a factor containing the degrees of freedom of quarks and gluons. As a consequence ϵ_c/T^4 will be constant for the QGP. If one considers a critical temperature T_c = 170 MeV and $\hbar c$ = 197 MeV·fm, from Eq. 1.5 it is possible to calculate a critical energy ϵ_c = 1 GeV/fm^3. To obtain such an energy, it is not sufficient to make proton-proton (pp) or positron-electron (e^+e^-) collisions where a charged-particle multiplicity of few tens of particle is produced. The high energy heavy ion collisions carried out at the LHC can create a system with the correct requirements in terms of energy density and temperature. In fact, the system created in a Pb–Pb collision can reach a volume of the order of 1000 fm^3, consisting

of about 2000 charged particle in the pseudorapidity[2] interval $|\eta| < 0.5$ for central Pb–Pb collisions at 5.02 TeV/nucleon [21,22]. An energy density in the range 12–14 GeV/fm^3 has been measured for the initial stage of central Pb–Pb collisions at 2.76 TeV/nucleon [23,24] that is well above the critical energy density of about 1 GeV/fm^3.

1.5.1 The Bjorken model

The collision and the space-time evolution of the QGP is described in the *Bjorken model*. The two relativistic nuclei, which can be seen as discs due to Lorentz contraction, pass through each other and leave a group of highly excited particles behind in the interaction region, in a time scale of the order of 0.1 fm/c. The particles interact with each other and de-excite into new quarks and gluons. A mass of hot and dense matter is formed, which quickly thermalizes in a time of approximately 1 fm/c: at this time the quark-gluon plasma is formed. The temperature creates a thermal pressure, which causes the QGP to expand. This expansion cools the QGP until it reaches the phase transition temperature of $T_C \sim$ 170 MeV. At this point the QGP has lived for approximately 10 fm/c and will start to hadronize. When the mass reaches the chemical freeze out temperature T_{chem}, the QGP has completely hadronized into a hadron gas and the hadrons no longer undergo chemical transitions (i.e. they are fixed from changing to another type of hadron except through decay). The hadrons in the hadron gas continue to interact with each other while the gas expands. This keeps the hadrons in a kinetic equilibrium. When the gas reaches the kinetic freeze out temperature the particle interactions no longer maintain equilibrium. The particles move away from the collision point and will have a chance to decay depending on their lifetime. The detectors will then measure those particles or their decay products when they interact with the detectors.

[2]Pseudorapidity is a parameter (denoted by η) frequently used in colliding beam experiments to express angles with respect to the axis of the colliding beams. It has the value 0 for particle trajectories that are perpendicular to the beam, and positive or negative values for those at an angle to the beam. The pseudorapidity is often expressed in terms of the polar angle θ with respect to the beam axis. These two quantities are linked via the Eq. 1.12 that will be further discussed in Sect. 1.7

In the following the process which lead to the formation of hadrons out of quarks and gluons, shortly depicted above, is described in more detail, discussing the geometry and the space-time evolution of heavy ion collisions.

1.5.2 Collision geometry

Atomic nuclei are extended objects whose typical size is of the order of few fm. A collision between composite systems with finite dimensions, like the atomic nuclei colliding at the LHC, can be modelled starting from the constituents of the system. Indeed, it is natural to consider a heavy ion collision as the sum of the interactions between the constituent nucleons of the two colliding nuclei. The relevant parameters in such a description are the number of nucleons participating in the interaction between the nuclei N_{part} and the number of binary collisions between two nucleons N_{coll}. These two parameters are correlated with the impact parameter of the collision b. The impact parameter is defined as the distance between the directions of motion of the two approaching nuclei (Fig. 1.4). Nucleons involved in the collision are called *participants*, while the others are called *spectators*.

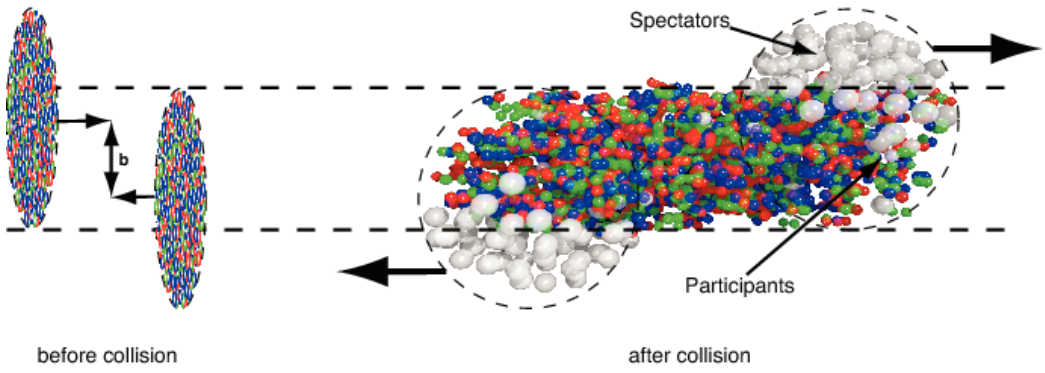

Figure 1.4: Representation of a heavy ion collision. Before the collision nuclei are similar to two disks with a small thickness due to the Lorentzian contraction of distances; after the collision there is a central zone where the participant nucleons are, while spectators continue their motion along the beam line.

In the most central collisions, which correspond to small impact parameter values, the nuclei collide almost head on. The overlap region is the largest and, thus, the largest number of N_{part} and N_{coll} can be obtained. The overlap region becomes smaller and less circular the more peripheral the two nuclei collide, i.e. for larger b. Thus, events can be characterized using the centrality according to the size and shape of the overlap region. Unfortunately, neither the impact parameter nor the number of participant nucleons or binary collisions can be measured directly. Nevertheless, these quantities can be inferred using a geometrical model of nucleus-nucleus collisions based on the Glauber model [25]. Roy Glauber in the 1950's used the quantum mechanical scattering theory to describe multiple scattering in composite systems. His work was found extremely useful in the calculation of total cross sections in p-A and A-A collisions and it is nowadays used to connect some microscopic geometrical quantities, like the impact parameter, to macroscopic experimental observables, thus representing the "theoretical magnifying glass" of heavy ion and proton-ion collisions.
The collision centrality in a typical HIC that occurs at the LHC will be further discussed in Sect. 4.8.

1.5.3 Space-time evolution of heavy ion collisions

As already mentioned, a long-lived and strongly interacting system is created when two ultra-relativistic atomic nuclei collide. The evolution of such a system, as well as the characterisation of its properties, is one of the subject of investigation of HI experiments.

Figure 1.5 summarises in a space-time plot the current view on the evolution of a HIC [26, 27]:

1. for t < 0 fm/c: the two atomic nuclei travel along the beam line. At the relativistic energies reached at the modern accelerators, the nuclei are strongly Lorentz contracted in the laboratory reference frame (by a factor 100 and 2700 at the RHIC and at the LHC respectively);

2. at t = 0 fm/c: collision time. The geometry of the collision can be described using the Glauber Model, as outlined in the previous

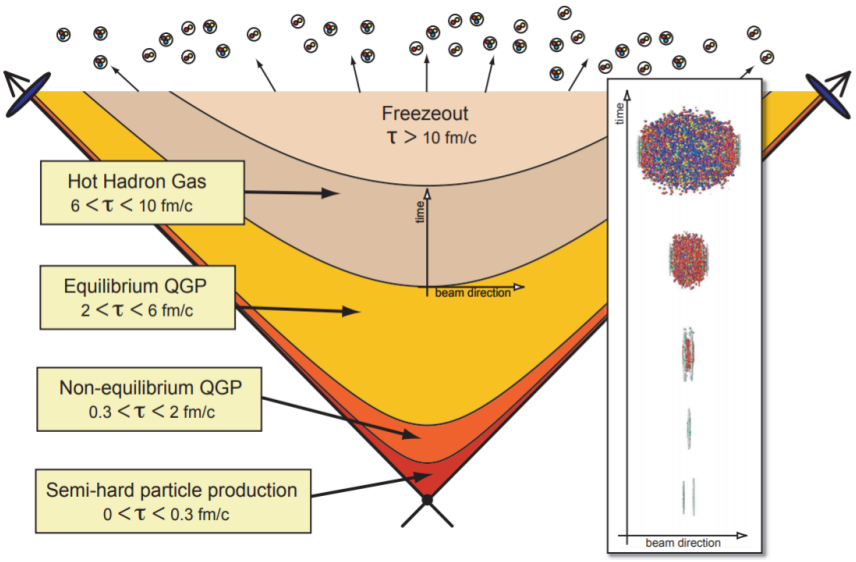

Figure 1.5: Schematic illustration of the space-time evolution of a collision between two high energy nuclei [26]. On the right, the two colliding nuclei are shown in the laboratory reference frame.

section;

3. for 0 fm/c < t < $\tau_0 \sim 1$ fm/c: due to their nature and the fundamental quantum mechanics uncertainty relation between time and energy ($\Delta E \Delta t \geq h/2$), hard processes (i.e. process with high transferred momentum) between the colliding partons occur at the very first instants of the collisions. In this phase, called pre-equilibrium, all the particles with high energy (either high momentum or/and high mass), are produced. The typical time scale for such processes is 0.1 fm/c. In high energy collisions, the momentum of the nuclei is such that, in the first instants of the collision, their constituent partons undergo several interactions, losing energy in the mid-rapidity region ($y \sim 0$), and then they escape at forward rapidities ($|y| \gg 0$). The resulting system has a hot, interacting medium at mid-rapidity with vanishing baryonic chemical potential. The baryonic potential carried by the colliding nuclei is brought at forward rapidity by the escaping valence quarks and by the nucleons that did not partici-

pate in the collision (the spectators). In HICs at RHIC and at LHC, the energy density is such that a transition to the QGP state is expected. After a short strong parton rescattering phase, the obtained droplet of QGP matter reaches the equilibrium at the proper time τ_0;

4. for 1 fm/c < t < 10 fm/c: the equilibrated QGP droplet rapidly expands under the push of the thermal pressure gradients generated at the system boundaries. This phase of rapid expansion of the QGP droplet is commonly modelled using relativistic hydrodynamics [28] which provides useful insights to interpret the experimental data, as shown in the following. With its expansion the system cools down, crossing eventually the phase boundary between QGP and ordinary hadronic matter;

5. for 10 fm/c < t < 15 fm/c: when the critical temperature between the two phases is reached, the hadronization starts and the system gradually evolves into an interacting hadron resonance gas. While expansion and contextual cooling of the system continue in this phase, elastic and inelastic interactions among the hadrons within the system continue to occur. The instant in which the momentum exchange between hadrons is not sufficient for inelastic interactions is called *chemical freeze-out*. Since no other inelastic processes will take place, the relative abundances of different particle species are fixed after the chemical freeze-out. The second landmark in the evolution of the hadron gas is the *kinetic freeze-out*, when the hadrons stop interacting with each other and the particle momenta are fixed;

6. for t > 15 fm/c: hadrons created in the collision escape the interaction region with no further interaction. This regime is also known as *free hadron stream*.

The last step, not mentioned in the list, is of course the detection by the experimental apparata of particles produced in the collisions: the technologies and methodologies implied in this last step will be presented in Chapters 3–5.

1.6 QGP probes

The short life-time of the QGP ($\tau \sim 10$ fm$/c \sim 3 \times 10^{-23}$ s [29]), together with the impossibility to detect free quarks, does not allow the direct measurement of the phase transition. For this reason, the observables that can probe the possible formation of the QGP are mainly indirect signals which should be able to test the properties of the medium at different stages of the collision evolution. The main types of observables are:

- Hard observables ($p_{\mathrm{T}} \geq 4$ GeV$/c$):
  - Processes with high transferred momentum; they are possible at the beginning of the collision when the energy has not degraded yet.
  - They are rare processes with a small cross section, their production rate is calculable with the pQCD (heavy flavors, jets).
  - They scale with the number of collisions that occur during a HIC (N_{coll}).
  - They are sensible to the successive phases of the collision.

- Direct photons:
  - They are irradiated from the plasma (both real and virtual photons that can be observed like lepton pairs of opposite sign).
  - They are early probes, but, since the photon background is high (successive phases of the collision), their detection is very difficult.

- Soft observables ($p_{\mathrm{T}} < 1$ GeV$/c$):
  - They represent the major part of the observables (the 99.5% of the hadrons produced is soft at RHIC).
  - They are produced in the last steps of the collision when the energy is highly degraded.
  - In this case the coupling constant is large, hence the non-perturbative QCD has to be considered.
  - They scale with the number of the participants in the collision (N_{part}).

In the following the hard and soft probes of the QGP described above will be further discussed.

1.6.1 Hard probes

High momentum particles and heavy flavours

High momentum quarks, as well as heavy flavour quarks (charm and beauty), can be created only at the very early stages of the collisions, when the processes at high transferred momentum occur. For this reason, the study of the hadrons with high momentum and/or containing heavy flavour quarks allows us to inquire into the mechanisms driving the parton propagation and energy loss in the QGP. The processes that create such hard partons can be modelled with the perturbative QCD approach, thus if the collision between two nuclei is the superposition of uncorrelated nucleon-nucleon collisions, the observed production cross section for hard particles when two heavy nuclei collide should be equal to the pp cross section scaled by the number of nucleon-nucleon collisions N_{coll}. Hence, it is expected that the p_{T}-spectra measured in nucleus-nucleus collisions can be evaluated from those in pp collisions with a simple scaling low (binary scaling):

$$\left(\frac{dN}{dp_{\mathrm{T}}}\right)_{AA} = N_{coll} \times \left(\frac{dN}{dp_{\mathrm{T}}}\right)_{pp} \tag{1.6}$$

Therefore, if a HIC is the incoherent sum of nucleon-nucleon collisions, then the nuclear modification factor, defined as:

$$R_{AA} = \frac{1}{\langle T_{AA} \rangle} \frac{d^2N_{AA}/dp_{\mathrm{T}}dy}{d^2\sigma_{pp}^{INEL}/dp_{\mathrm{T}}dy} \tag{1.7}$$

(where σ_{pp}^{INEL} is the cross-section in inelastic pp collisions and $\langle T_{AA} \rangle$ is the average value of the nuclear overlap function calculated from the Glauber model [25]) should be equal to unity for hard processes. The number of binary collisions between nucleons is included in the nuclear overlap function: $\langle T_{AA} \rangle = \sigma_{pp}^{INEL}/\langle N_{coll} \rangle$.
Studying the p_{T} dependence of the nuclear modification factor, other effects not related to the presence of QGP can cause deviations of the R_{AA} from unity, for instance the Cronin enhancement [30] and the modification of the parton distribution functions of neutrons and protons inside the nuclei (mainly the nuclear shadowing). Nevertheless, it is possible to

factorise these cold nuclear matter effects from the QGP induced effects by studying them separately in p–Pb collisions. Figure 1.6 shows the nuclear modification factors in p–Pb and Pb–Pb collisions measured by the CMS and the ALICE experiments [31,32].

It is possible to see that the R_{pA} measured by both experiments for hard particles ($p_{\mathrm{T}} > 3$ GeV/c) is close to one and it even overshoots one at very high transverse momenta. On the other hand, for $p_{\mathrm{T}} < 3$ GeV/c, the R_{AA} shows a clear suppression of the production of hard particles hinting for the presence of the energy loss of the partons in a hot and dense medium. At even higher transverse momentum the R_{AA} measured by the CMS experiment grows again to reach 1 ($p_{\mathrm{T}} > 100$ GeV/c): this trend is understood by the models reported in Ref. [31] and it can be naively interpreted as due to very fast partons that manage to escape the interaction region before the medium formation.

Jet quenching

Another interesting phenomenon related to hard processes in HICs is called *jet quenching*. In pp collisions, at the leading order (LO) in the vacuum (i.e. without any energy loss) dijets are physical objects consisting of two back-to-back jets of equal transverse momentum ($\Delta\phi_{dijet} \sim \pi$). If the two partons originating the dijet are created by a hard scattering in a HIC, they interact with the medium losing part of their energy and changing their direction. As a consequence, depending on the length of the path followed inside the medium by each parton, the dijet structure is modified leaving a leading jet (the most energetic) and a subleading jet with less energy. In addition, the direction of the two jets might also show large deviation from the $\Delta\phi_{dijet} \sim \pi$ observed in pp collision. The measurements by the CMS experiment [33] (Figure 1.7 shows an example of dijet event in Pb–Pb collisions), show that the jet energy imbalance is present and significant for $120 < p_{\mathrm{T}} < 210$ GeV/c and that it is possible to recover this energy imbalance by keeping into account, in a wider cone around the subleading jet, the charged particles with transverse momentum down to 2 GeV/c. This observation indicates that the fragmentation functions for jets in the QGP favour the production of soft hadrons at large angles with respect to the leading parton direction.

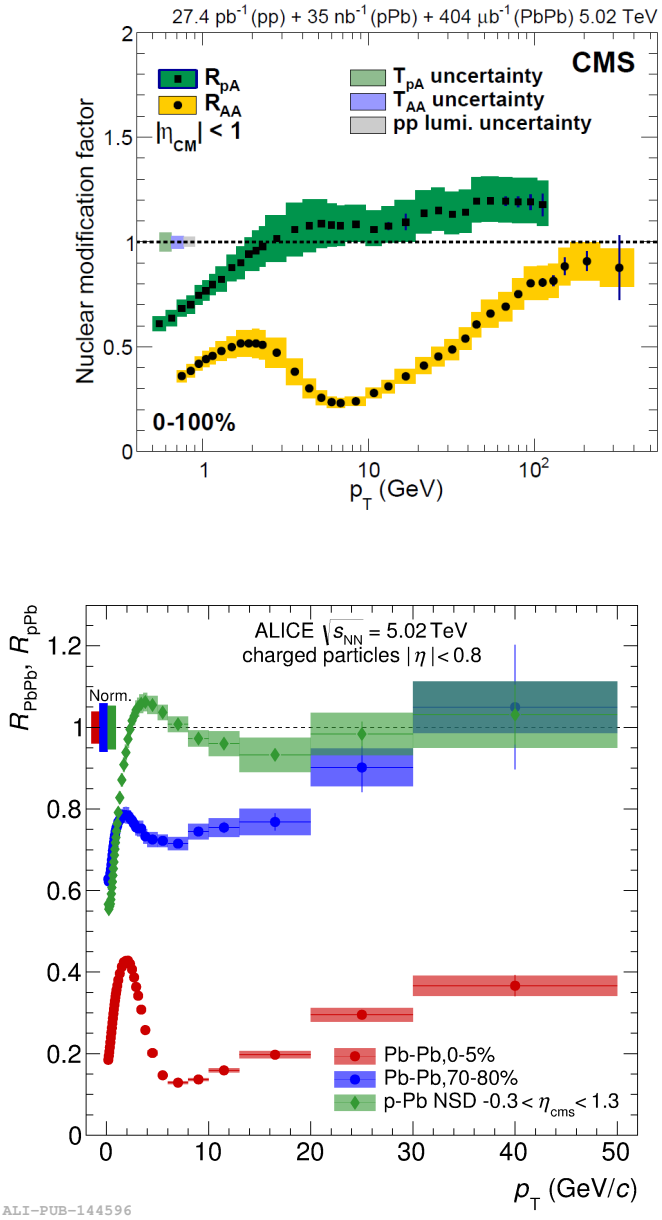

Figure 1.6: Nuclear modification factor of charged particles measured by the CMS experiment (top panel) [31] and by the ALICE experiment (bottom panel) [32] in p–Pb and Pb–Pb collisions at different energies.

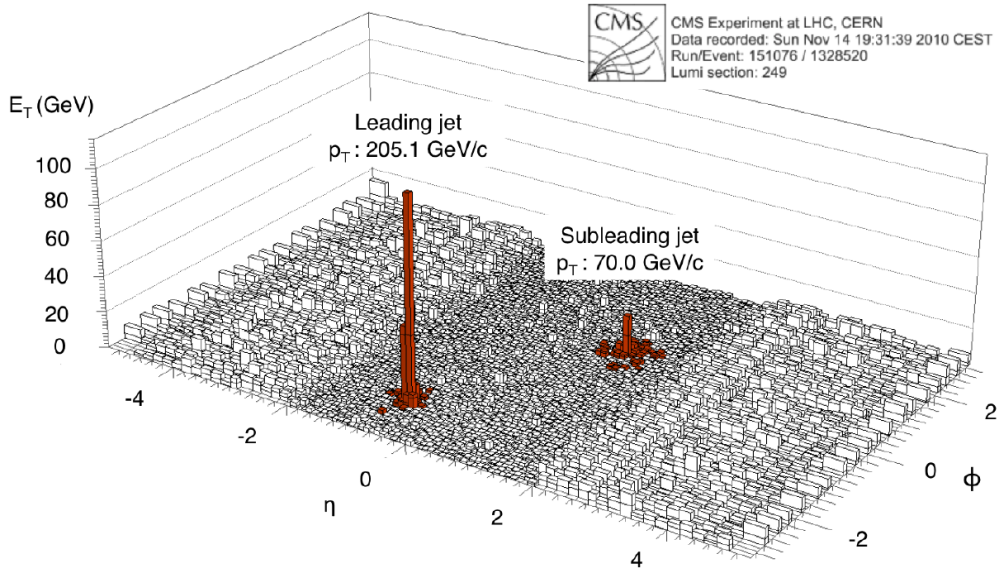

Figure 1.7: Event display of the sum of the energy deposit in the CMS electromagnetic and hadronic calorimeters as a function of the azimuthal angle ϕ and the pseudorapidity η for Pb–Pb collisions at $\sqrt{s_{\mathrm{NN}}}$ = 2.76 TeV [33]. The leading and sub-leading jet structures are highlighted in red and labelled with their transverse momentum.

1.6.2 Soft probes

Particle spectra and radial flow

Low momentum hadrons, often called soft hadrons, represent the large majority ($\sim$ 99%) of the particles produced in a HIC. The study of the momentum spectra of identified particle gives important insights about the condition of the medium at kinetic freeze-out. Assuming a Boltzmann-Gibbs distribution for the particle emission at kinetic freeze-out, the particle spectra for the species i can be modelled as:

$$\frac{1}{m_{\mathrm{T}}}\frac{d^2N_i}{dm_{\mathrm{T}}dy} \propto e^{-\beta m_{\mathrm{T}}} \tag{1.8}$$

These formulation keeps into account only the thermal component of the spectra and predicts a common emission temperature (β) for all the par-

ticle species. The measured spectra in HICs defy this prediction showing a different slope (i.e. temperature) for different particle species. This kind of behaviour can be interpreted adding a further component to the measured emission temperature for each particle species:

$$T_i = T_{kin} + \frac{1}{2} m_i \langle v_\perp \rangle^2 \tag{1.9}$$

where T_{kin} is the temperature at kinetic freeze-out while the additional term keeps into account the mean kinetic energy acquired by the particles of the species i due to the hydrodynamical collective expansion along the transverse plane[3]. This phenomenon, called *radial flow*, modifies the production spectra pushing the mean transverse momentum of the emission at higher values the higher is the particle species mass. This can be also seen qualitatively from the particle spectra in Figure 1.8, where it is possible to observe a steeper spectrum slope for pions (soft spectrum) while for protons the slope of the spectrum is reduced (hard spectrum) [34].
Another interesting feature related to the radial flow is the evolution of the particle spectra shape with the collision energy: the production spectra measured at lower collision energy [35, 36] show a profile softer than the ones measured at the LHC energies [34]. This trend suggests the presence of a stronger radial flow in more energetic collisions and thus stronger pressure gradients driving the hydrodynamical expansion at the LHC. The radial flow interpretation of the slope modification of the production spectra is well captured by the comparison with the hydrodynamical calculations shown in Figure 1.8, yet either a full description of the hadronic phase following the hydrodynamical expansion (as implemented in the HKM model[4] [38]) or some corrections due to the bulk viscosity at the freeze–out (as implemented in the Krakow model [39]) are required to obtain a proper description of the measured spectra over

[3] $\langle v_\perp \rangle$ is the average transverse velocity acquired by the particles due to the hydrodynamical expansion

[4] The hydrokinetic model (HKM) incorporates hydrodynamical expansion of the systems formed in A–A collisions and their dynamical continuous decoupling described by the escape probabilities. The HKM is the correct basis to switch over a hydrodynamic evolution of continuous medium to an evolution of particles within cascade model like UrQMD [37]. The model which matches the hydrokinetic model and UrQMD is called hybrid HKM (hHKM).

the full momentum range.
Finally, a simplified hydrodynamical model, corresponding to a Blast-Wave description, is usually fitted simultaneously to the measured spectra of pions, kaons and protons in order to extract the temperature T_{kin} and the mean radial velocity $\langle \beta_{\perp} \rangle$ of the particles at the kinetic freeze-out. From the results of these fits, the authors of [34] conclude that indeed both the radial flow velocity $\langle \beta_{\perp} \rangle$ and the kinetic freeze-out temperature T_{kin} at LHC energies are larger (of about 10%) than those extracted at the RHIC collision energies.

Anisotropic flow

Another signature of the collective motions of particles created in HICs is the presence of azimuthal anisotropies in the particle production spectra. In particular, when considering the geometry of a collision between two nuclei overlapping only partially (see Fig. 1.9), a correlation between the emission angles of the particles and the impact parameter can be found. This kind of azimuthal anisotropies can be measured by looking at the Fourier expansion in the azimuthal angle of the production spectra:

$$\frac{dN}{d\phi} \propto 1 + 2 \sum_{n=1}^{\infty} v_n \cos[n(\phi - \Psi_n)] \tag{1.10}$$

where the magnitude of the anisotropy with respect to the symmetry plane at Ψ_n is quantified by the coefficients v_n. The typical almond shape of the overlap region between the colliding nuclei, when the impact parameter is large, creates a pressure gradient parallel to the plane defined by the beam direction and the impact parameter vector (the reaction plane). The reaction plane direction cannot be measured directly, instead the n^{th} order event planes are used for the calculation of the Fourier expansion as shown in Equation 1.10.

From the properties of the Fourier expansion we can find:

$$v_n = \langle \cos[n(\phi - \Psi_n)] \rangle \tag{1.11}$$

According to the values that the v_n coefficients can assume, it is possible to distinguish the following cases:

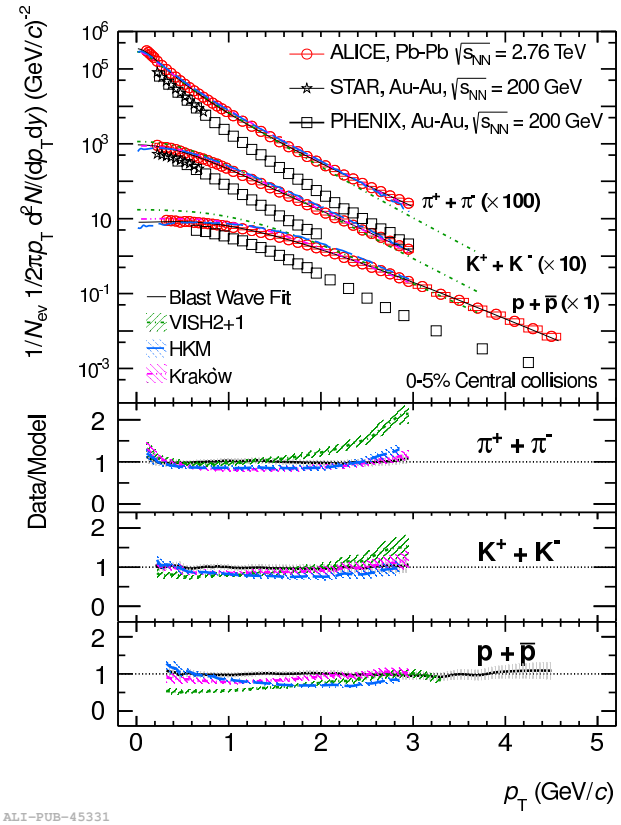

Figure 1.8: Pion, kaon and proton transverse momentum spectra in central (0-5%) Au–Au collisions at $\sqrt{s_{\mathrm{NN}}}$ = 200 GeV at the RHIC and in Pb–Pb collision at $\sqrt{s_{\mathrm{NN}}}$ = 2.76 TeV at the LHC (see [34] and references therein). The data are fitted with a Blast–Wave model (lines) and compared with three additional hydrodynamical models predictions (shaded areas).

- directed flow: if $v_1 \neq 0$ and $v_2 = 0$, there is an asymmetry in the number of particles emitted in parallel (0°) and anti-parallel (180°) to the impact parameter. Moreover, there is a preferential direction in the particle emission that is in the direction of the reaction plane (in plane emission);

- elliptic flow: if $v_2 \neq 0$ and $v_1 = 0$, there is a difference in the number of particles emitted in parallel (0° and 180°) and perpendicularly

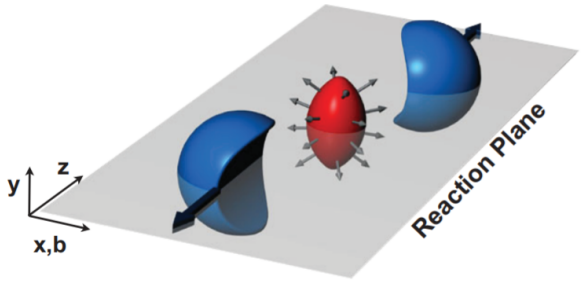

Figure 1.9: Non-central collision between two nuclei. The reaction plane is indicated in gray ($x - z$ plane). In the center, the almond-shaped interaction region after the collision is represented. The arrows indicates that the initial spatial anisotropy with respect to the reaction place is converted into a momentum anisotropy of the produced particles (anisotropic flow).

(90° and 270°) to the impact parameter. This is the expected effect of the difference between the pressure gradients being parallel and orthogonal to the impact parameter. It represents the elliptic deformation of the particle distribution in the transverse plane. If $v_2 < 0$, the emission is *out of plane*, otherwise is *in plane*.

The higher order Fourier coefficients are related to initial inhomogeneities of the colliding systems. The properties of the medium, such as the shear viscosity over entropy η/s, the bulk viscosity over entropy ζ/s and its lifetime, define how efficiently these initial geometric condition and inhomogeneities are translated in the v_n coefficients. For this reason, the detailed study and comparison of the experimentally measured v_n with the models allow us to uncover the characteristics of the medium and the dynamics of its thermalization. For instance, as discussed in [40], the v_n coefficients measured by the ALICE experiment in Pb–Pb collisions at different collision energies (Figure 1.10) are compared with hydrodynamical calculations that combines the initial spatial anisotropy and the hydrodynamical response. From this comparison it is possible to inquire into the value of η/s and it is possible to state that the current v_n measurements favour a medium with small shear viscosity values.

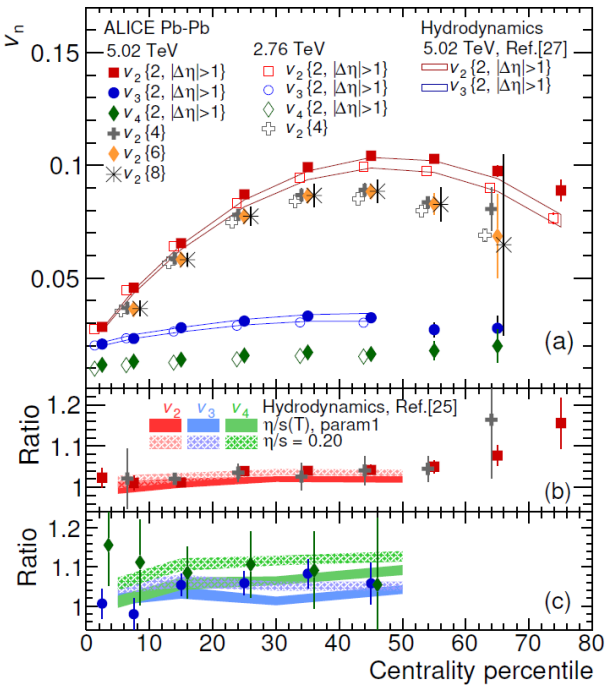

Figure 1.10: In panel (a) the Fourier coefficients up to the fourth order measured by the ALICE experiment at different collision energies [40] as a function of the centrality percentile are shown. The panels (b) and (c) show the ratio between the measurements at $\sqrt{s_{\mathrm{NN}}}$ = 5.02 TeV and those at $\sqrt{s_{\mathrm{NN}}}$ = 2.76 TeV. No striking difference between the two energies is seen, hinting that there is not a major change in the medium characteristics and thermalization dynamics. The results are then compared with hydrodynamical models (see the references in [40]) showing a good agreement with the model using a small η/s value. Data points are shifted for a better visibility.

1.7 Particle multiplicity

The main observables used to characterize the collision multiplicity are the rapidity and the pseudorapidity density distributions of primary charged particles. The pseudorapidity η is referred to the polar angle θ with respect to the beam axis with which a particle is emitted from the interac-

tion vertex. The pseudorapidity can be expressed as:

$$\eta = -\ln \tan(\theta/2) = \frac{1}{2} \ln \frac{|p| + p_z}{|p| - p_z} \tag{1.12}$$

where p and p_z are the total momentum and longitudinal momentum of the emitted particle, respectively. The rapidity y is defined instead as:

$$y = \frac{1}{2} \ln \frac{E + p_z}{E - p_z} \tag{1.13}$$

where E is the total energy of the emitted particle. Generally it is easier to measure η than y since the pseudorapidity does not require the particle identification. At high energy we have $\eta \sim y$ since $E \sim |p|$.

The particle multiplicity $\mathrm{d}N/\mathrm{d}y$ (from now on referred to as *multiplicity*), i.e. the number of particles produced per rapidity unity, is an extremely important observable. The multiplicity can be used to estimate the centrality of a p–A or a A–A collision, using the Glauber model, as it will be discussed in Sect. 4.8. Therefore, it is possible to measure indirectly the impact parameter from the measurement of multiplicity. Moreover, multiplicity is defined for each collision system and hence it allows the direct comparison of different observable across different collision systems.

In Fig. 1.11, the multiplicity of the different identified hadrons is shown as a function of the centre-of-mass energy for central collisions (Au–Au and Pb–Pb) at midrapidity ($|y| < 0.5$) [41, 42]. The multiplicity of each species depends on the energy of the collision. From the figure it is possible to see the chemical composition of the matter created in heavy ion collisions. At low energy ($\sqrt{s_{\mathrm{NN}}} \leq 5$ GeV), measured at the AGS, the matter created in the collision is dominated by the incoming nucleons while at higher energy ($\sqrt{s_{\mathrm{NN}}} > 5$ GeV) the pions represent the majority of the particles produced due to their lowest mass among the particles shown in the plot. The different isospin of π^+ and π^- is reflected in their different yields at low energy. The difference between K^+ and K^- meson yields and Λ and $\overline{\Lambda}$ hyperon production is determined by the quark content of the hadrons. In the collision, the presence of valence u and d quarks from colliding nucleons stopped in the matter

created in the HIC leads to a preferential production of hadrons carrying those quarks. These differences vanish gradually for higher energies, where the hadrons are mostly newly created (reflecting Einstein's equation m = E/c^2) and the production yields exhibit a clear mass ordering. The dependence of the hadron yields on the collision energy (and also on the collision system) disappears at LHC energies ($\gg$ 100 GeV).
Another interesting aspect that emerges from Fig. 1.11, is that while the yields of pions, kaons and lambdas (and of their corresponding antiparticles) increase with increasing energy, the yield of protons decreases. The production of antiprotons, instead, is largely suppressed at low energy due to its production treshold. The yields of protons and antiprotons become comparable starting from RHIC energies.

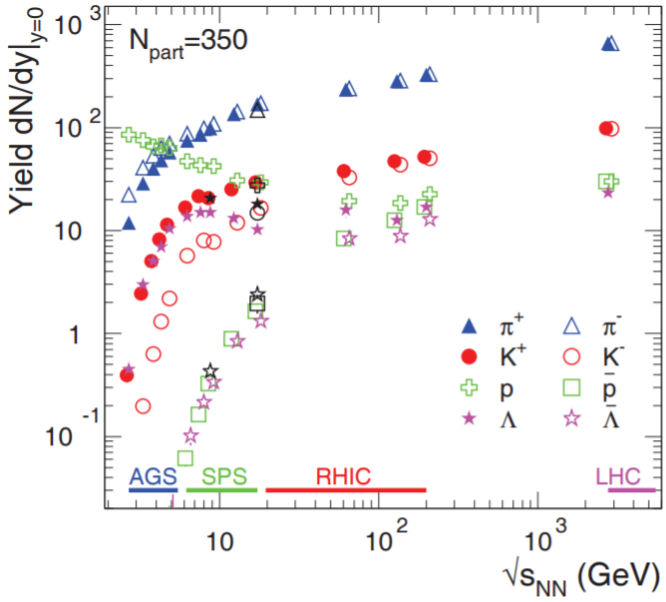

Figure 1.11: Energy dependence of different hadron yields at mid-rapidity ($|y| < 0.5$) as a function of the collision energy for central collisions (N_{part} = 350) [42].

From Fig. 1.12, where the yields of several particle species (pions, kaons, protons and their antiparticles) are summed up, it is possible to observe an increase of the yields with increasing collision energies. The

phenomenological $(\sqrt{s_{\rm NN}})^{0.3}$ behaviour seen at lower energies [42], is confirmed at LHC energies.

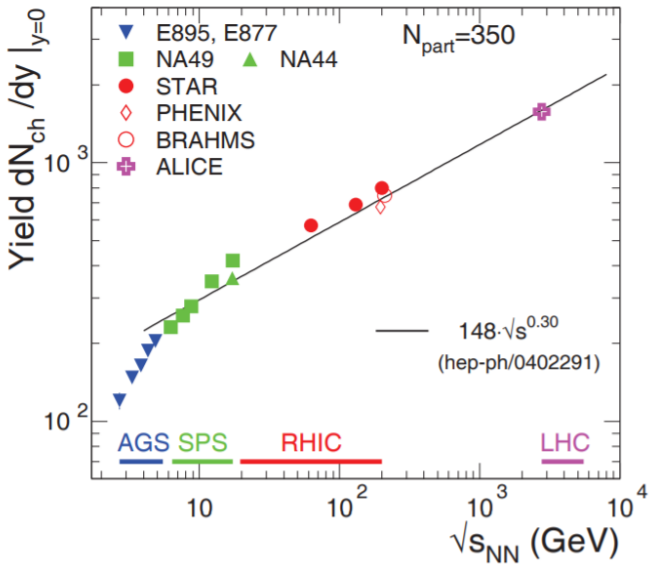

Figure 1.12: Collision energy dependence of charged-particle rapidity density $\mathrm{d}N_{ch}/\mathrm{d}y$ (sum of pions, kaons and protons and their antiparticles) at midrapidity, measured by various experiments in central collisions corresponding to N_{part} = 350. The figure is taken from Ref. [42].

1.7.1 Multiplicity and system size

Multiplicity can be related to the size of the colliding system. The radius of the collision system is usually estimated from the study of two-particle correlations using the Hanbury Brown-Twiss (HBT) method [43]. From femtoscopy measurements [44], it is known that the source radius (R) is related to the average charged particle multiplicity density ($\langle \mathrm{d}N_{\rm ch}/\mathrm{d}\eta_{\rm lab}\rangle$) through the following parametrization:

$$R = \mathrm{a}\langle \mathrm{d}N_{\rm ch}/\mathrm{d}\eta_{\rm lab}\rangle^{1/3} + \mathrm{b}, \tag{1.14}$$

where a = 0.473 fm and b = 0 [45]. Some examples of parameterisation of the HBT radius as a function of multiplicity are shown in Fig.

1.13. Therefore, the mean charged-particle multiplicity density allows the comparison of different collision systems at similar nuclear emission volumes.

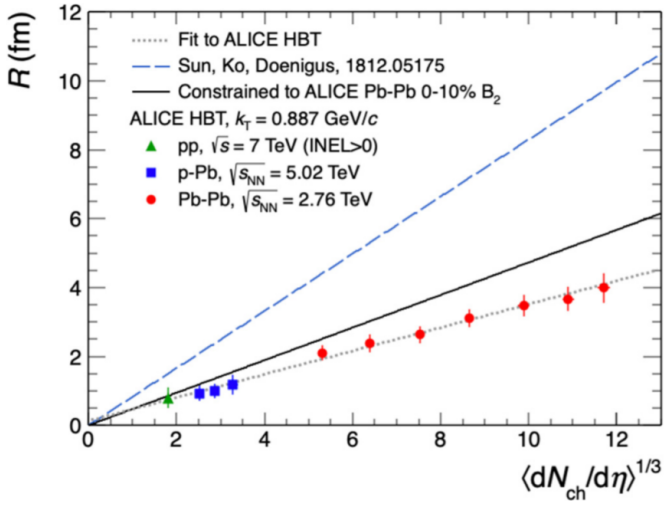

Figure 1.13: Comparison of different source volume parameterisations. The dotted gray line is the result of a linear fit to the ALICE HBT data [46–48], according to Eq. 1.14. The solid black line corresponds to a different parameterisation, obtained by fixing the parameters of Eq. 1.14 in order to reproduce the coalescence parameter B_2 (further detailed discussions about the coalescence parameters B_A will be given in Chapt. 2) in the most central Pb–Pb collisions at $\sqrt{s_{NN}}$ = 2.76 TeV. The dashed blue line shows the relation between the system radius and the charged particle multiplicity used in Ref. [49], which does not rely on the HBT data. (Figure taken from Ref. [45]).

Chapter 2

Light (anti)nuclei production in heavy ion collisions

2.1 Nuclei production in HIC

The production of nuclei and antinuclei in ultra-relativistic heavy ion collisions is interesting from many points of view. The study of matter and antimatter production is particularly useful to better understand the QCD phase transition from deconfined quarks and gluons to confined hadrons, a process which took place about 1 μs after the Big Bang in the early universe. In the first few microseconds after the Big Bang, matter consisted of fermions and bosons, the fundamental entities of the Standard Model.

The evolution of an ultra-relativistic heavy ion collision is usually connected to three characteristic temperatures, the (pseudo) critical temperature T_c, the chemical freeze-out temperature T_{chem} and the kinetic freeze-out temperature T_{kin}. When the temperature in the collision is higher than T_c, a quark-gluon plasma is formed. After a very short time, it cools down until again T_c is reached and the hadronisation starts. The particle yields are then fixed at T_{chem}, where the inelastic collisions cease. After further cooling down T_{kin} is reached, where also elastic processes stop and the spectra of the particles are frozen (see for instance Refs. [27,50–52] for a deeper discussion). Depending on the temperature T_{chem}, only partons with mass much less than T_{chem} are copious. For $T_{chem} < 1$ GeV,

or about 10^{13} K, these are the u, d and s quarks and the gluons of the strong interaction. In addition, there are of course photons, leptons and neutrinos.

The cosmic matter can be produced in the laboratory by collisions at relativistic energies between very heavy atomic nuclei, such as Pb at the Large Hadron Collider (LHC) and Au at Brookhaven's Relativistic Heavy Ion Collider (RHIC). Based on model comparison to data in a broad range of collision energies, one can extract the following ranges of the QGP characteristics, as described in the review done in Ref. [42] (values are in the system of units where $\hbar$ = c = 1):

- Temperature: T = 156 MeV [53], or up to a million times the temperature at the center of the Sun (1 MeV $\sim 10^{10}$ K);
- Pressure: P = 100–300 MeV/fm^3 (1 MeV/fm^3 $\sim 10^{33}$ Pa);
- Density: ρ = (1–10) $\cdot\rho_0$ (being ρ_0 the saturation density of nuclear matter, corresponding to 0.17 fm^{-3});
- Volume: several thousands of fm^3;
- Duration: 10–20 fm (or about 3–6 $\cdot$ 10^{-23} s).

The experimental "control parameters" are the size of the colliding nuclei, the collision energy (per nucleon pair, $\sqrt{s_{\rm NN}}$) and the centrality of the collision. Centrality is discussed in Sect. 1.5.2 and Sect. 4.8.

Heavy ion collisions produce not only hadrons in the classical sense but also composite and even fragile objects such as light nuclei (d, t, ^{3}He, ^{4}He) and light Λ-hypernuclei, along with their antiparticles. Their measured yields decrease strongly with increasing (anti)baryon number – the penalty factor for each additional (anti)baryon is about 300 – hence (anti)^{4}He production is a very rare process. Since light nuclei are produced in limited amounts with respect to lighter particles, their study is particularly challenging. At the same time, light (anti)nuclei measurements are very interesting because their study can lead to a better understanding of the hadronisation process.

Since the QGP created in the HI collision carries no net baryon number (at ultra-relativistic energies), the yields of the produced antiparticles closely coincide with the corresponding particle yields. Several

experiments have been carried out at the RHIC by the STAR [54] and PHENIX [55] collaborations and at the LHC by ALICE [56]. So far, the heaviest antinucleus which has been observed is ^{4}He (antiα); meanwhile, for lighter nuclei and antinuclei a detailed comparison of their properties is possible.

Detailed measurements of the production of light (anti)nuclei, up to ^{4}He, in the LHC energy regime have been carried out in recent years by the ALICE Collaboration [53, 57–66]. The production of light nuclei has been studied extensively also at lower collision energies, from the AGS at BNL [67–70], to the SPS at CERN [71] and RHIC at BNL [72–77]. At lower energies with respect to the LHC, light nuclei measurements have been carried out also at the CERN Intersecting Storage Rings (ISR) [78] and at Fermilab [79]. Additionally, also measurements carried out at the Large Electron-Positron Collider (LEP) have been reported in Ref. [80] and results obtained in fixed target experiments [81,82]. Finally, also from pp [78, 83], γp [84] and ep [85] collisions light nuclei have been studied extensively in the past years. Such published experimental results will be further discussed in the following sections, in comparison with the expectations of the hadronisation models.

2.2 Hadronisation models

The production mechanism of light (anti)nuclei is still under debate.
(Anti)nuclei have a binding energy of the order of 1 MeV per nucleon [86]. This value is extremely low if compared with the chemical freeze-out temperature of a Pb–Pb collision ($T_{\rm chem} \sim 150$ MeV). Hence, it is surprising to see how these loosely-bound objects like light (anti)nuclei can be produced and survive in such extreme conditions. The production of light (anti)nuclei has been described using two classes of phenomenological models: the Statistical Hadronisation Models (SHMs) and the coalescence models, which will be described in more detail in the following Sections.

2.3 Statistical Hadronisation Models (SHM)

The SHM was born with the aim of describing the abundances of different particle species produced in hadronic collisions. This model was first pioneered by Enrico Fermi and evolved until the Hagedorn formulation, which was able to describe successfully the production rate in proton-proton collisions. The general idea behind this model is that the final state of the interaction is composed by all the particle states compatible with the conservation laws imposed by the underlying theory of interaction (in this case the Standard Model of particle physics). The relative abundance of different particle states is set by the maximisation of the total phase space filled by the system, to which each particle species contributes according to its partition function. This model is of particular interest in HI collisions as the presence of an expanding medium that eventually reaches the thermal equilibrium seems appropriate for the statistical hadronisation approach. Depending on the system size, two different approaches are used:

- the grand canonical approach, which is typically used for systems characterised by a large reaction volume, such as Pb–Pb collisions;
- the canonical approach, necessary in small systems such as pp, p–Pb and e^+e^-, where the reaction volume is small, i.e. when the number of particles with particular conserved charge(s) is of the order of unity or smaller.

The two approaches will be described in the following sections.

2.3.1 Grand Canonical SHM

As described in [14], the system created in a relativistic HIC is large enough to be modelled using the Grand Canonical ensemble. This formalism can be used as the experiments measure only the characteristics of a small portion of the system, like the central rapidity region in the case of the ALICE central detectors. This part of the phase space is in equilibrium with a thermal reservoir (the rest of the medium created in a HIC) and quantities like energy, baryon number, charge and isospin are

conserved on average. Within the Grand Canonical formalism the parameters describing the equilibrium condition of a HIC include the temperature T and the baryon chemical potential μ_B. The statistical properties of the system at thermodynamic equilibrium are described by the grand partition function Z:

$$Z(T, V, \mu) = Tr\left[\exp\left(-\frac{H + \sum_i \mu_i Q_i}{T}\right)\right] \tag{2.1}$$

being $\sum_i \mu_i Q_i = \mu$, H the Hamiltonian of the system, T the system temperature, V the system volume, Q_i the conserved charges and μ_i their respective chemical potentials. The Hamiltonian of a Hadron Resonance Gas (HRG) is used because it can describe the interaction of a strongly interacting medium and it can reproduce the equation of state obtained with lattice-QCD over a wide range of temperature values before the transition to a deconfined state. For a strongly interacting medium created in relativistic HIC, the main conserved quantum numbers are the electric charge Q, the strangeness content of the system S and the baryon number B. The partition function Z of the system is given by the product of all partition functions Z_i of the particles included in the HRG:

$$Z(T, V, \mu) = \Pi_i Z_i(T, V, \mu_i) \rightarrow \log Z(T, V, \mu) = \sum_i \log Z_i(T, V, \mu_i) \tag{2.2}$$

The partition functions Z_i are defined as:

$$\log\ Z_i(T, V, \mu_i) = \frac{V g_i}{2\pi} \int_0^\infty \pm p^2 dp\ \log\left(1 \pm \lambda_i(T, \mu_i) e^{-\epsilon_i/T}\right) \tag{2.3}$$

where the sign $\pm$ is determined by the nature of the state, – for bosons and + for fermions. The factor g_i takes into account the degeneracy due to spin and isospin and $\epsilon_i = \sqrt{m_i^2 + p^2}$ is the energy of a particle of the species i with momentum p and mass m_i. The dependence on the chemical potential is included in the fugacity λ_i, defined as:

$$\lambda_i(T, \mu_i) = e^{(B_i\mu_B + S_i\mu_S + Q_i\mu_Q)/T} = e^{\mu/T} \tag{2.4}$$

where the subscript refers to the particle species i, and the μ_B, μ_S, μ_Q are the chemical potentials related to the baryon number, the strangeness content and the electric charge, respectively. As illustrated in [87], through a Taylor expansion of the logarithm and integrating over the momentum, the partition function for the species i becomes:

$$\log Z_i(T, V, \mu_i) = \frac{VTg_i}{2\pi^2} \sum_i \frac{(\pm 1)^{k+1}}{k^2} \lambda_i^k m_i^2 K_2(\beta k m_i) \tag{2.5}$$

where K_2 is the second modified Bessel function and β is the inverse temperature ($\beta = 1/\mathrm{T}$). For a system described by the Grand Canonical ensemble, the average number of particles for the species i, $\langle N_i \rangle^{th}$, is defined as:

$$\langle N_i \rangle^{th}(T, V, \mu_i) = \frac{1}{\beta} \frac{\partial}{\partial \mu_i} \log Z_i(T, V, \mu_i) = \frac{VTg_i}{2\pi^2} \sum_i \frac{(\pm 1)^{k+1}}{k^2} \lambda_i^k m_i^2 K_2(\beta k m_i) \tag{2.6}$$

although it does not describe fully the particle production measured in a HIC. For the measured yields one should consider the feed–down contributions from all the other particle species (resonances) j in the thermal system that can decay strongly in a final state containing particles of the species i:

$$\langle N_i \rangle(T, V, \mu_i) = \langle N_i \rangle^{th}(T, V, \mu_i) + \Gamma_{j \to i} \langle N_j \rangle^{th}(T, V, \mu_j) \tag{2.7}$$

where $\Gamma_{j \to i}$ is the branching ratio of the species j decaying into the species i.

This definition of particle yields holds in the limit of a low density system, where the repulsive interaction between the hadrons constituting the systems is negligible. Equation 2.7 outlines the crucial dependencies of the observed particle yields on the temperature, volume and the three chemical potentials (μ_B, μ_Q and μ_S). Out of these five parameters, two are constrained from the HI collision conditions as no net strangeness is present in the colliding nuclei, thus $\mu_S \sim 0$, and μ_Q is fixed by the isospin asymmetry in the collision. One might think that also the baryon chemical potential is constrained in HI collisions, but this is not true as the amount of baryonic number transported in the equilibrium region varies

with the energy of the collision. The dependence on the volume of the system can be removed looking at the ratio between the yields of different particle species, which therefore depends only on the temperature of the system and on the baryon chemical potential. For this reason, one of the most powerful tool to test the hadronisation models is the ratio of integrated yields of different particle species, as it will be further discussed in Chapter 6, where the resulting ratios of the yields measured in this thesis work will be compared with the expectations of the models.

The statistical thermal model is used to predict hadron yields in a collision, going from pions to light nuclei. In principle, as we previously outlined, one would not expect to see any light nuclei in HI collisions, since the chemical freeze-out temperature is much higher than their binding energy. However, the thermal model is blind to the internal structure of hadrons and the hadron yields are the result of their distribution in the phase space. In the framework of the thermal models, light nuclei yields arise naturally when the chemical freeze–out temperature and the baryon chemical potential are set. A possible explanation on how the light nuclei can survive to the high temperature of the chemical freeze–out was pointed out in Ref. [88]: as the system expansion after the chemical freeze–out is supposed to conserve the entropy density, such conservation could be the steering mechanism for the nuclei production.

Figure 2.1 shows the thermal model fit to all the light-flavoured hadrons measured in central (0–10%) Pb–Pb collisions at $\sqrt{s_{\rm NN}}$ = 2.76 TeV by ALICE up to hypertriton. For ^{3}He and ^{4}He the predictions of the yields, computed with the parameters obtained from the fit, are reported. Three different implementations of the thermal model are used to fit the data: THERMUS [89], GSI-Heidelberg [90] and SHARE [91]. These models differ in the list of resonances included in the Hamiltonian. Moreover, while hadrons are assumed to be point-like in SHARE, the hadron volume is taken into account in THERMUS and in GSI-Heidelberg. All the model fits to the hadron yields provide a chemical freeze-out temperature T_{chem} = 156 MeV [53]. It is interesting to notice that light nuclei, from (anti)deuterons to (anti)^{4}He, are produced at statistical equilibrium at the same temperature as the other (lighter) hadrons.

Finally, from the fit of the particle abundances at lower energies, the authors of Ref. [88] predicted, using the thermal model, the energy de-

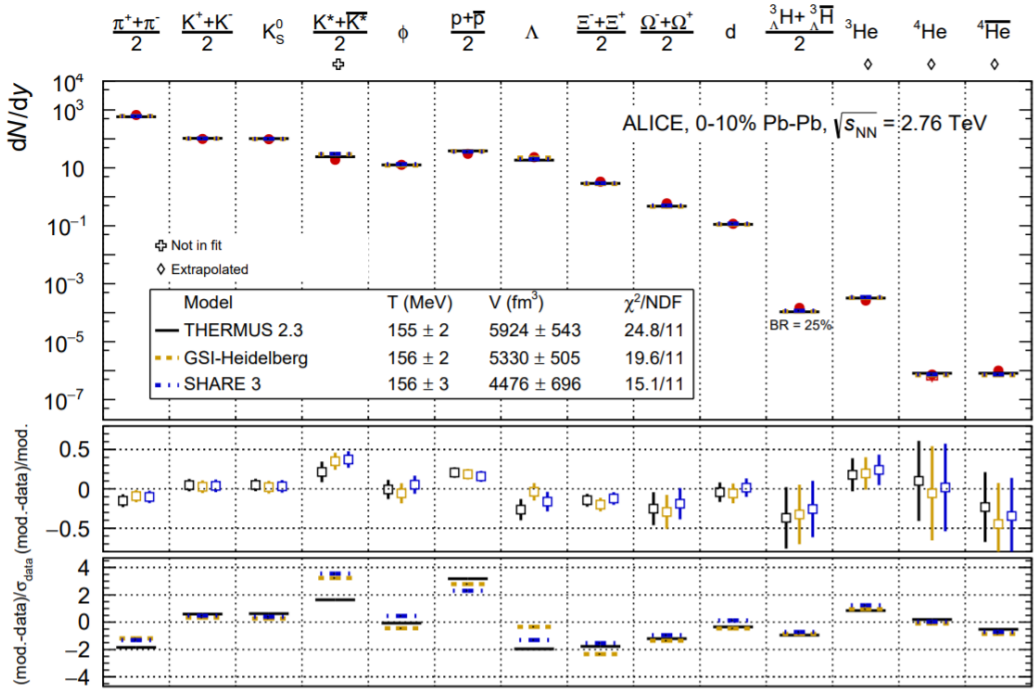

Figure 2.1: Thermal model fit to the light-flavoured hadron yields in central Pb–Pb collisions at $\sqrt{s_{\rm NN}}$ = 2.76 TeV [53], with three different SHM implementations: THERMUS (black line), GSI-Heidelberg (yellow line) and SHARE (blue line).

pendence of the yields of (anti)nuclei and also of multi-strange light (anti)hypernuclei, i.e. nuclei where a neutron is replaced with a hyperon (Fig. 2.2). Such a figure is complementary to Fig. 1.11 shown in Sect. 1.7, where the energy dependence of the particle yields is depicted. From Fig. 2.2, it is possible to notice that the production of nuclei (solid line) is favoured against that of antinuclei (dashed line) at low energy. This is due to the dependence of the baryon chemical potential μ_B on the collision energy (see the bottom panel of Fig. 2.3) [41]. As it is clear from the figure, at low collision energies the baryon chemical potential is larger than zero and therefore the production of matter is favoured with respect to antimatter production. With increasing collision energy (such as at LHC energies), the baryon chemical potential decreases, approaching zero, and the same amount of matter and antimatter is predicted.

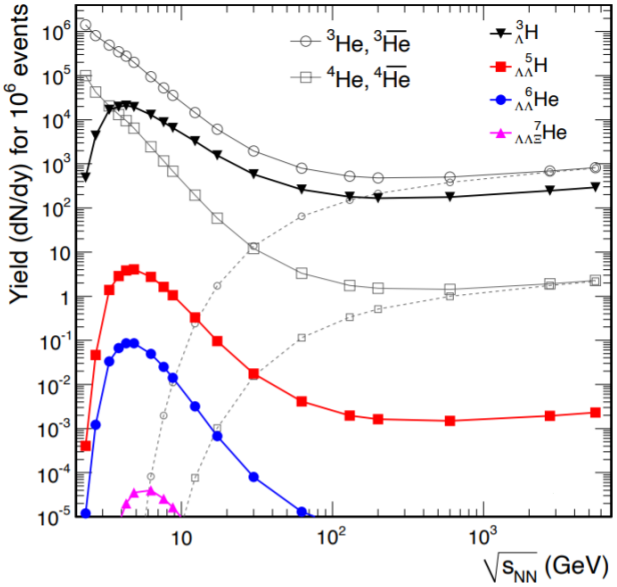

Figure 2.2: Particle yields as a function of the collision energy. The data are compared with the predictions of the Statistical Hadronisation model (shown as solid and dotted lines for particles and antiparticles, respectively).

The thermal model describes a snapshot of the collision, namely the chemical freeze-out, which is assumed to be quasi-instantaneous. The phenomenological phase diagram is shown in Fig. 2.4. Each point corresponds to a fit of hadron yields in central Au–Au or Pb–Pb collisions at a given collision energy. The agreement between the results from several independent analyses [92–96] is remarkable.

2.3.2 Canonical model

In small systems such as pp and p–Pb collisions, the exact conservation of the quantum numbers across the correlation volume V_c has to be taken into account since the abundance of hadrons with a given quantum number is small. Thus, the canonical ensemble version of the SHM has to be used. The main difference between the two approaches is that while in the grand-canonical ensemble all charges are conserved on average, in the

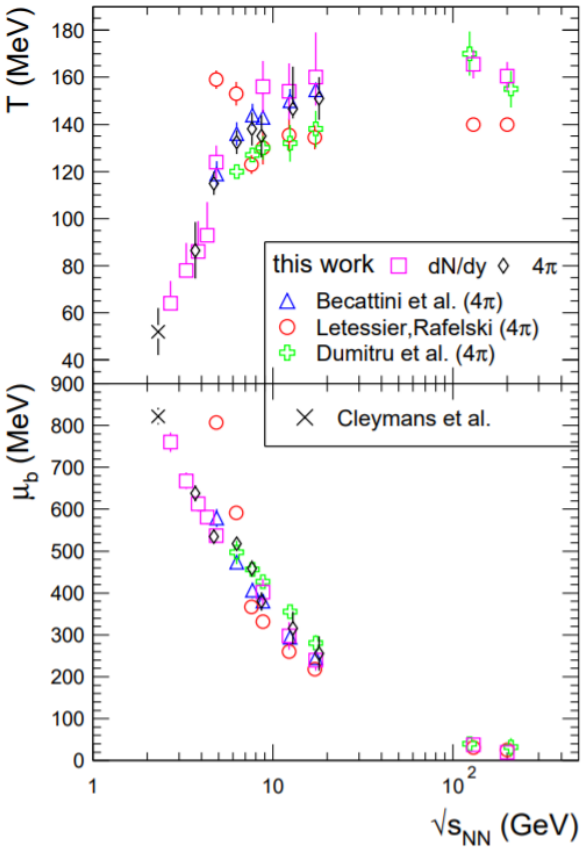

Figure 2.3: The energy dependence of temperature and baryon chemical potential. The figure is taken from Ref. [41], where the results of the authors are compared to the values obtained in earlier studies [87, 93, 97–100], that show similar trends.

canonical one the charges are conserved exactly and they do not fluctuate from one microscopic state to another. Therefore, the yields of particles carrying the conserved charges are suppressed with respect to a grand canonical description. This effect is the so-called *canonical suppression*, and it is stronger for multi-charged particles, such as multi-strange hyperons or light nuclei. In particular, nuclei are a very interesting test for canonical suppression because they are characterised by a baryon number B > 1, and therefore they are affected in larger measure by canonical

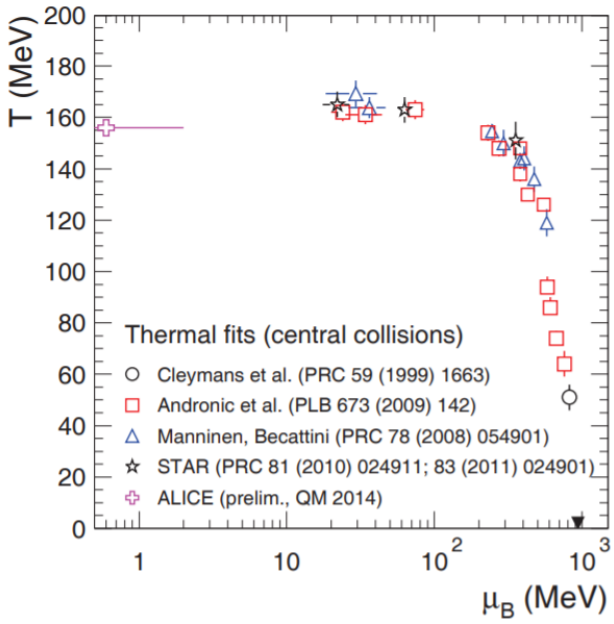

Figure 2.4: The phase diagram of strongly interacting matter with the points representing the thermal fits of hadron yields at various collision energies [92–96]. For the LHC, $\mu_B = 0$ is the outcome of the fit, 0.6 MeV is used here for the sake of proper representation with the logarithmic scale. The down-pointing triangle indicates ground state nuclear matter (atomic nuclei).

suppression. In the following, the approach described in Ref. [101], which considers the full canonical treatment of baryon number, electric charge and strangeness, and includes also light (anti)nuclei, is discussed. In such an approach, the ideal hadron resonance gas (HRG) in the Boltzmann approximation is considered, as done in the previous Section for the grand-canonical approach, and it is considered in full chemical equilibrium. In the canonical ensemble the three abelian charges considered (B, Q, S) are fixed exactly to the values that are conserved exactly across the V_c. The partition function of the HRG model, in the canonical ensemble at a given

temperature T and correlation volume V_c, is given by:

$$Z(B,Q,S) = \int_{-\pi}^{+\pi} \frac{d\phi_B}{2\pi} \int_{-\pi}^{+\pi} \frac{d\phi_Q}{2\pi} \int_{-\pi}^{+\pi} \frac{d\phi_S}{2\pi} e^{-i(B\phi_B + Q\phi_Q + S\phi_S)} \times \exp\left[\sum_j z_j^1 e^{-i(B_j\phi_B + Q_j\phi_Q + S_j\phi_S)}\right] \tag{2.8}$$

where, as before, the subscript j refers to the particle species (including both hadrons and light nuclei). The single-particle partition function z_j^1 is defined as follows:

$$z_j^1 = V_c \int dm \rho_j(m) d_j \frac{m^2 T}{2\pi^2} K_2(\beta m) \tag{2.9}$$

where d_j is the degeneracy factor for particle species j, $\rho_j(m)$ is the mass distribution and K_2 is the second modified Bessel function. Thus, the mean multiplicities of the various particle species, calculated in the canonical ensemble $\langle N_j^{th} \rangle^{ce}$ are:

$$\langle N_j^{th} \rangle^{ce} = \frac{Z(B - B_j, Q - Q_j, S - S_j)}{Z(B,Q,S)} \langle N_j^{th} \rangle^{gce} \tag{2.10}$$

where $\langle N_j^{th} \rangle^{gce}$ are the mean multiplicities calculated in the grand canonical ensemble at the same temperature T and volume V_c. The factor in between the mean multiplicities is the chemical factor, which reflects the exact conservation of the conserved charges. As for Eq. 2.7, the final particle yield $\langle N_j^{th} \rangle^{ce}$ is obtained by adding the feed–down contributions from resonances:

$$\langle N_j \rangle^{ce} = \langle N_j^{th} \rangle^{ce} + \sum_j \Gamma_{i \to j} \langle N_j^{th} \rangle^{ce} \tag{2.11}$$

being $\Gamma_{i \to j}$ the branching ratio of the species i decaying into the species j. In Ref. [101], the CSM calculations are implemented within the Thermal-FIST package [102]. One of the main features of this package is that the conserved charges are fixed to the initial values Q = S = B = 0. The baryon number at mid-rapidity at the LHC is actually consistent with zero, as proved by the antibaryon-to-baryon ratios, which are compatible

with unity [103]. Additionally, in this implementation of CSM, all the particles in the HRG are considered point-like. A finite exclusion volume for all the particles would affect the yields and for this reason further implementations of the model that consider also exclusion volumes are currently under study. The temperature of chemical freeze-out is fixed to T_{chem} = 155 MeV, in agreement with the fits to the production yields of hadrons in central Pb–Pb collisions performed by the ALICE experiment [104]. Different values of $V_{\rm c}$ are tested, extending from one to three units of rapidity.

In Fig. 2.5, the charged multiplicity dependence of the yield ratios of different particle species in the CSM at T_{chem} = 155 MeV are depicted, namely d/p, ^{3}He/p, $^3_\Lambda$H/p and ^{4}He/p integrated yield ratios. The solid line refers to a $V_{\rm c}$ corresponding to a single unity of rapidity, the dashed line refers to $V_{\rm c} = 3{\rm d}V/{\rm d}y$, while the shaded area in between corresponds to the intermediate $V_{\rm c}$ between the uppermost and lowermost limits. Additionally, the calculations for T_{chem} = 170 MeV and $V_{\rm c} = {\rm d}V/{\rm d}y$ are shown as dash-dotted blue lines. The CSM calculations are compared with the experimental data of the ALICE Collaboration, measured in Pb–Pb collisions at $\sqrt{s_{\rm NN}}$ = 2.76 TeV [53, 105, 106] and in pp collisions at several energies [60]. In order to make the comparison possible, the yield ratios are shown as a function of the pion multiplicity ${\rm d}N_\pi/{\rm d}y$, which is measured in the experiments and can also be calculated in the CSM.

The theoretical predictions grow monotonically with increasing ${\rm d}N_\pi/{\rm d}y$ and eventually saturate at the corresponding grand-canonical values at high multiplicity. The few experimental points available at low multiplicity seem to confirm canonical suppression. Such a behaviour is further confirmed by the most recent results of the ALICE Collaboration, including the results from this work, as it will be shown in Chapt. 6. It is also interesting to notice that a better agreement is shown for $V_c \sim 3\ {\rm d}V/{\rm d}y$.

In Fig. 2.6, the p/π, K/π, ϕ/π, Λ/π, Ξ/π, and Ω/π ratios as a function of the charged pion multiplicity ${\rm d}N_\pi/{\rm d}y$ are reported. Such experimental results are compared to the so-called Vanilla-CSM (such a name relates to the simplest version of the model) with $V_c = {\rm d}V/{\rm d}y$, 3 ${\rm d}V/{\rm d}y$ or 6 ${\rm d}V/{\rm d}y$ [107]. The figure reflects the limited level of agreement of the statistical model with the data. Indeed, the model struggles in the description of such ratios, showing severe difficulties when describing the

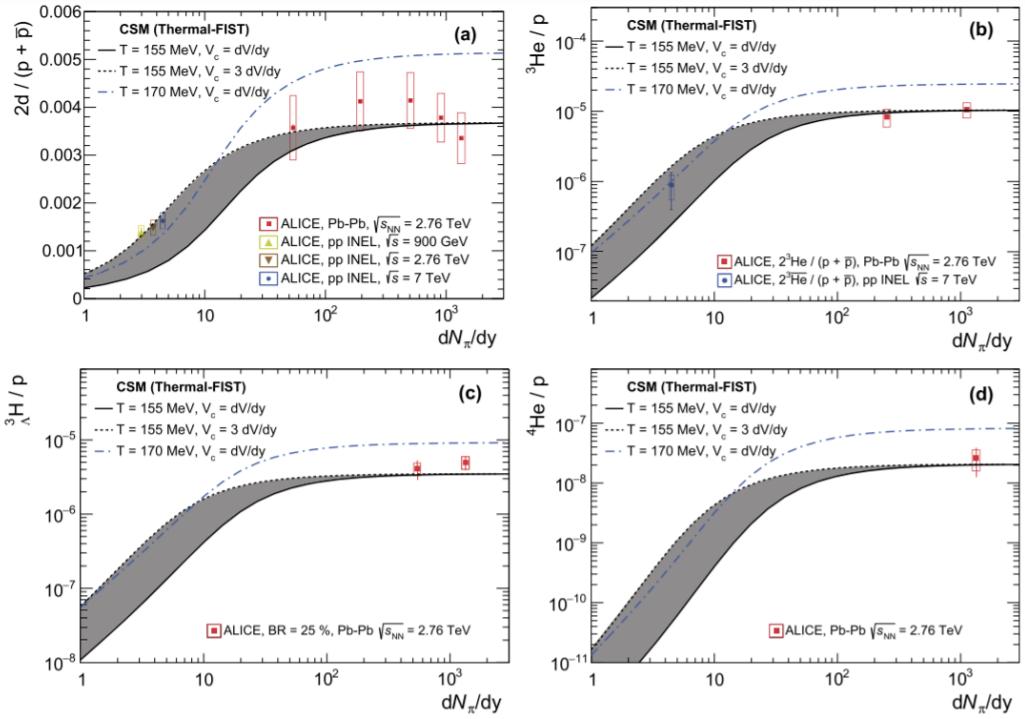

Figure 2.5: Charged pion multiplicity dependence of (a) d/p, (b) ^{3}He/p, (c) $^3_\Lambda$H/p, and (d) ^{4}He/p ratios calculated in the canonical ensemble HRG model at T_{chem} = 155 MeV for $V_c = \mathrm{d}V/\mathrm{d}y$ (solid black lines) and $V_c = 3\mathrm{d}V/\mathrm{d}y$ (dashed black lines), and at T_{chem} = 170 MeV for $V_c = \mathrm{d}V/\mathrm{d}y$ (dash-dotted blue lines). Experimental data of the ALICE collaboration [53, 60, 105, 106] are shown where available. The figure is taken from Ref. [101].

data of the ϕ/π ratio. This is due to the fact that the ϕ meson yield is unaffected by canonical suppression, as ϕ is a neutral meson. Therefore, this leads to a predicted strong increase of the ϕ/π ratio towards smaller multiplicities. However, the data show just the opposite: the ϕ/π ratios are smaller at smaller multiplicities. Unless the production mechanism for ϕ is completely different from all other hadrons, this invalidates the vanilla CSM picture in pp and p–Pb collisions.

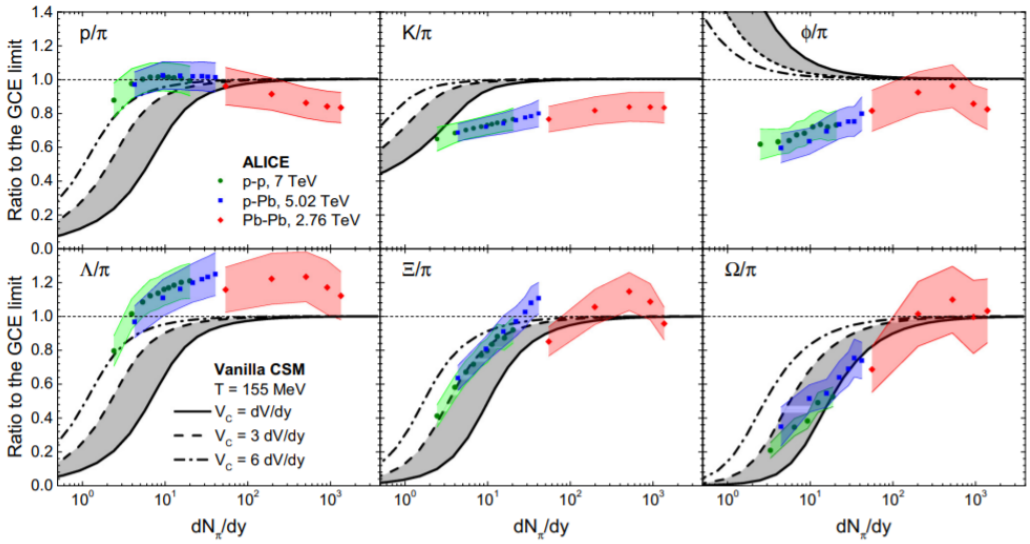

Figure 2.6: The dependence of yield ratios (a) p/π, (b) K/π, (c) ϕ/π, (d) Λ/π, (e) Ξ/π, and (f) Ω/π on the charged particle multiplicity $\mathrm{d}N_{ch}/\mathrm{d}\eta|_{|\eta|<0.5}$, evaluated in the Vanilla-CSM with $V_c = \mathrm{d}V/\mathrm{d}y$, $3\,\mathrm{d}V/\mathrm{d}y$ and $6\,\mathrm{d}V/\mathrm{d}y$ and $T_{chem} = 155$ MeV. The green circles, blue squares, and red diamonds depict the corresponding ratios measured by the ALICE Collaboration in pp 7 TeV, p–Pb 5.02 TeV, and Pb–Pb 2.76 TeV collisions, respectively; the bands show the corresponding experimental uncertainties.

2.3.3 Alternative implementation of CSM

Recent developments of the CSM, called γ_SCSM, include an incomplete equilibration of strangeness, described by the strangeness saturation parameter γ_S, a multiplicity-dependent chemical freezeout temperature and a correlation volume extending over three units of rapidity [107].

In Fig. 2.7, the p/π, K/π, ϕ/π, Λ/π, Ξ/π, and Ω/π ratios as a function of the charged particle multiplicity $\mathrm{d}N_{ch}/\mathrm{d}\eta|_{|\eta|<0.5}$ are reported. Such experimental results are compared to the state-of-the-art γ_SCSM with $V_c = 3\,\mathrm{d}V/\mathrm{d}y$. The γ_SCSM reproduces quite well the trends observed in the data, including also the rather abrupt jump in the Ξ/π ratio when going from peripheral Pb–Pb collisions to most central p–Pb

collisions. With respect to the predictions of the Vanilla-CSM shown in Fig. 2.6, there is a quite remarkable improvement in reproducing the trend of data, especially for what concerns the ϕ/π ratio. However, as it is clear from the figure, the model overpredicts systematically the p/π ratio, roughly on a 2σ level. Separately, the proton yields are overpredicted on a 1σ level, while the yields of pions are underpredicted on a 1σ level. In the implementation of the model used for this comparison [107], energy-dependent Breit-Wigner widths are used, which reduce the p/π ratios by about 15% relative to the common zero-width approximation [108]. If the zero-width approximation would be used instead, then the disagreement with the p/π data would be even larger. The application of energy-dependent Breit-Wigner widths leads to a systematic improvement of the data description at all multiplicities, although the description of the p/π ratio is still not fully satisfactory.

No prediction is currently available for the nuclei-to-proton and nuclei-to-pion ratios from the γ_SCSM model. Therefore, the comparison between the Vanilla-CSM predictions and the most recently published experimental results from ALICE – including the results of this work – will be shown in Chapt. 6.

2.4 Coalescence models

Another theoretical approach that aims to explain the measured light nuclei production in HIC is represented by the hadron coalescence model. In this static model the nuclei are created at the kinetic freeze-out and there is no attempt to give a detailed description of the interactions that lead to their formation. The coalescence models provide a clear prediction about the momentum distribution of the produced light nuclei given the momentum spectra of the constituent nucleons. The fundamental idea that enables this prediction is that if a certain number of constituent nucleons are close enough in phase space at the kinematic freeze-out and match the spin, they can bind to form a nucleus.
The first coalescence model was developed in the 1960s by Butler and Pearson for proton-nucleus collisions [109]. In their study, the authors suggested that the deuteron production mechanism was the binding of

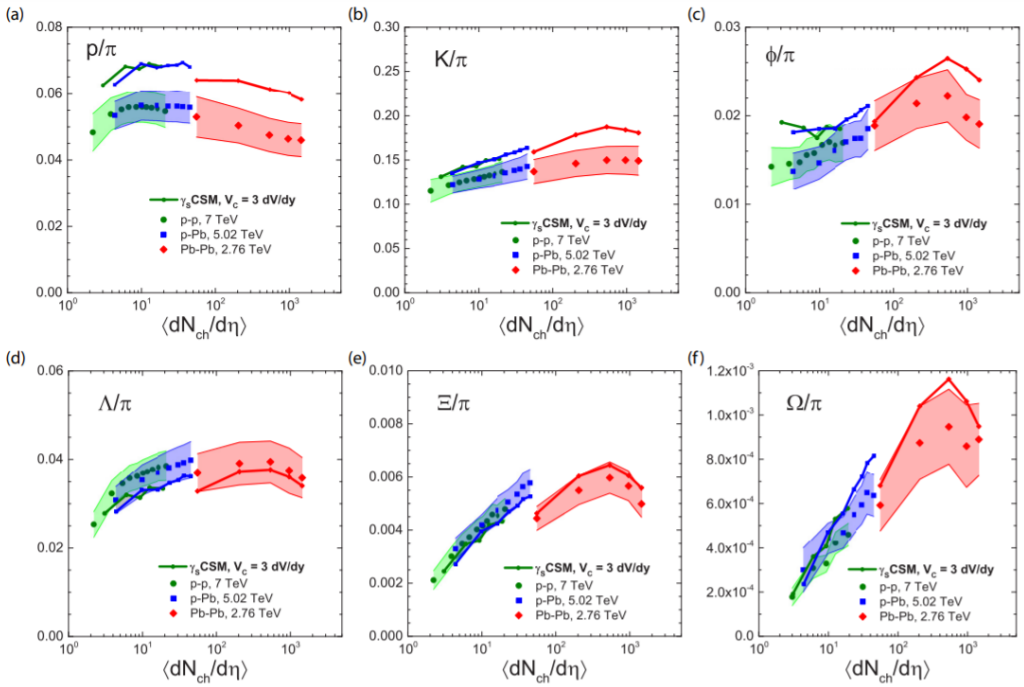

Figure 2.7: The dependence of yield ratios (a) p/π, (b) K/π, (c) ϕ/π, (d) Λ/π, (e) Ξ/π, and (f) Ω/π on the charged particle multiplicity $\mathrm{d}N_{ch}/\mathrm{d}\eta|_{|\eta|<0.5}$, evaluated in the γ_{S}CSM with $V_c = 3\ \mathrm{d}V/\mathrm{d}y$ for the thermal parameters extracted for each multiplicity bin through the χ^2 minimization. The green circles, blue squares, and red diamonds depict the corresponding ratios measured by the ALICE Collaboration in pp 7 TeV, p–Pb 5.02 TeV, and Pb–Pb 2.76 TeV collisions, respectively; the bands depict the corresponding experimental uncertainties.

cascade nucleons in the presence of the target nuclear optical potential.

The coalescence parameter B_A is used to quantify the coalescence probability to produce a nucleus of mass number A and is defined via

$$B_A = \left(E_A \frac{\mathrm{d}^3 N_A}{\mathrm{d}p_A^3}\right) \Big/ \left(E_{\mathrm{p}} \frac{\mathrm{d}^3 N_{\mathrm{p}}}{\mathrm{d}p_{\mathrm{p}}^3}\right)^A = \\ = \left(\frac{1}{2\pi p_{\mathrm{T}}^A} \frac{\mathrm{d}^2 N_A}{\mathrm{d}y \mathrm{d}p_{\mathrm{T}}^A}\right) \Big/ \left(\frac{1}{2\pi p_{\mathrm{T}}^{\mathrm{p}}} \frac{\mathrm{d}^2 N_{\mathrm{p}}}{\mathrm{d}y \mathrm{d}p_{\mathrm{T}}^{\mathrm{p}}}\right)^A, \tag{2.12}$$

being the numerators the invariant momentum spectra of nuclei and the denominators the invariant spectra of primary protons. These nucleon spectra are not those measured in the experiments, but the ones produced in the collision and not yet modified by the coalescence mechanism. Nevertheless, the amount of observed nuclei is so small with respect to the amount of protons and neutrons created that this difference is often neglected in the practice. Moreover, in principle one should consider separately the neutron and proton invariant spectra. However, neutrons and protons belong to the same isospin multiplet and since at LHC energies the isospin chemical potential is expected to be vanishing [103], protons and neutrons are assumed to have the same production spectra. Protons are used in the formula instead of neutrons because they are easier to measure in an experiment. Moreover, in Eq. 2.12, the invariant spectrum of protons is evaluated at $p_{\mathrm{T}}^{\mathrm{p}} = p_{\mathrm{T}}^{A}/A$, because the momentum of the nucleus is the sum of the momenta of A nucleons.

In the following, the coalescence models will be treated in more detail, distinguishing among the simple version of the model which takes into account only momentum-space correlations and the most advanced versions of the model that also consider the geometry of the system and the source size.

2.4.1 Simple Coalescence

One of the first implementations of the coalescence model is that from Kapusta [110], usually referred to as *simple coalescence*. This model considers an emitting source of nucleons randomly distributed like a gas of nucleons in thermal and chemical equilibrium. In such a picture, only momentum-space correlations are considered and not space-time: for two nucleons to have coalescence it is sufficient that they have similar momenta, i.e. they are close in momentum space ($\Delta p < p_0$, being p_0 the so-called coalescence momentum), regardless of their space distance. In small systems, such as pp collisions, this assumption is plausible because the system size is comparable with the size of the nucleus, thus nucleons are produced close to each other. On the contrary, in large systems, such as central Pb–Pb collisions, the system size is larger than the nucleus size and two nucleons can be produced very far from each other and hence

they cannot coalesce and form a nucleus even though their momenta are similar. The system size can be determined from the charged-particle multiplicity (see Sect. 1.7.1). Neglecting nucleon isospin, the coalescence parameter can be expressed as:

$$B_A = \left(\frac{4\pi}{3}p_0^3\right)^{A-1}\frac{m_A}{m_p^A} \tag{2.13}$$

being A the nucleus mass number, m_A and m_p the nucleus and proton masses respectively, and p_0 the coalescence momentum, defined as the maximum distance in momentum-space at which coalescence can happen.

According to such a simple coalescence picture, B_A should not depend neither on transverse momentum nor on the system volume, nor on the charged particle multiplicity.

Indeed, the B_A parameter has been found to be constant at low transverse momentum in light-particle collisions [84, 85]. At the LHC, the coalescence parameter B_A has been measured as a function of p_{T}/A in different collision systems. In Fig. 2.8 the B_2 parameter measured before LHC, in pp collisions [78, 83], from the deep inelastic scattering of electrons at the Hadron-Electron Ring Accelerator (HERA) at DESY [84, 85], and from p–Cu and p–Pb collisions at the LBNL Bevalac [58], are shown in addition to the results from ALICE measured in pp collisions at $\sqrt{s} =$ 7 TeV [111]. The measurements at the LHC reveal a p_{T} dependence in B_2 not seen in the previous experiments. Such a p_{T} dependence can be reproduced with QCD-inspired event generators, such as PYTHIA 8.2 (Monash tune) [112] and EPOS (LHC), when adding a coalescence-based afterburner [113] that takes into account the momentum correlations between nucleons (Fig. 2.9). The afterburner looks for clusters of nucleons among the final particles produced by the event generators and boosts them to their center-of-mass frame. If the momentum of each individual nucleon is less than a certain value, a nucleus is generated. With the afterburner, a constant B_2 is recovered when selecting protons from one event and neutrons from the next event (event mixing), in agreement with the expectation of an uncorrelated distribution of nucleons (Fig. 2.9). The p_{T} dependence in B_2 is still present in the results from an alternate PYTHIA 8.2 (Monash tune) simulation with color reconnection turned off (Fig.

2.9). Thus, this p_{T} dependence can be explained as a purely hard scattering effect, in contrast to A–A collisions, where it is usually attributed to collective flow.

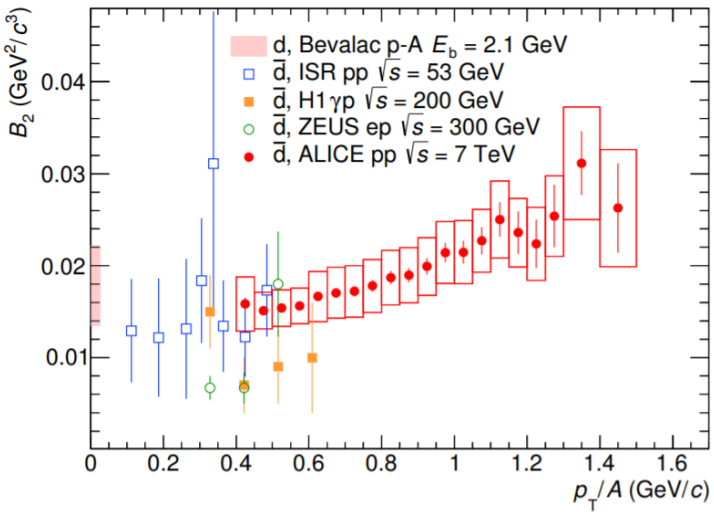

Figure 2.8: B_2 of antideuterons in inelastic pp collisions at $\sqrt{s}$ = 7 TeV (circles) compared with the values measured at lower energies in pp [78, 83], γp [84], ep [85] (squares and hollow circles), and in p–Cu and p–Pb collisions [58] (band at p_{T}/A = 0 GeV/c). The figure is taken from Ref. [111].

In Fig. 2.10, the B_2 parameters in pp collisions at $\sqrt{s}$ = 13 TeV are shown for several multiplicity classes and in the minimum bias[1] (MB) case. The B_2 measured in pp collision is found to be flat with p_{T}/A in all multiplicity classes [61, 65], in agreement with the predictions of the simple coalescence model discussed above. In the minimum bias case, instead, an increase of the coalescence parameter with increasing transverse momentum is observed, in both pp at several collision energies [111] and p–Pb collisions [64], as shown in Fig. 2.11. Nevertheless, the rising trend of B_A observed in the MB case can be explained within a simple coalescence picture as a consequence of the hardening of the proton spectra

[1] In this context, *minimum bias* is referred to the integrated multiplicity class, corresponding to the centrality interval 0–100%.

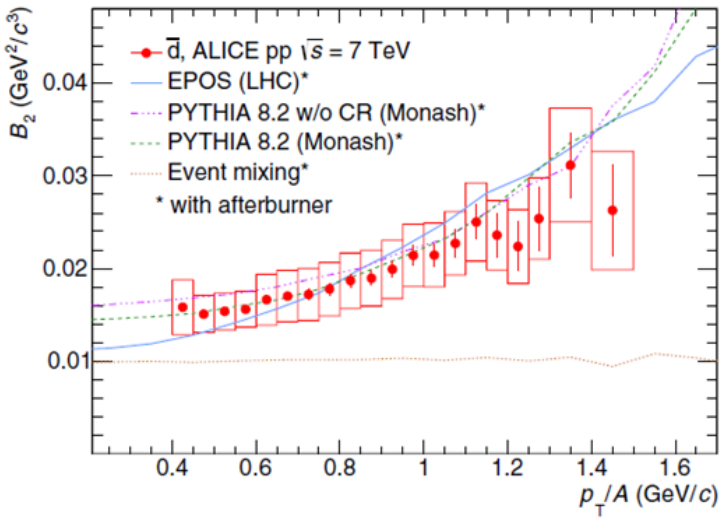

Figure 2.9: B_2 parameter of antideuterons in inelastic pp collisions at $\sqrt{s}$ = 7 TeV (circles) compared with EPOS (LHC), PYTHIA 8.2 (Monash tune) with and without color reconnection (CR), and an event mixing procedure with the afterburner (lines). The figure is taken from [111].

with increasing multiplicity in addition to hard scattering effects at high p_{T} [111].

As one can see from the right panel of Fig. 2.11, the coalescence parameter B_3 in p–Pb collisions is slightly increasing with p_{T}. Furthermore, it is known from previous measurements that the B_A parameters in A–A collisions also increase as a function of transverse momentum for each centrality class and decrease with increasing centrality of the collision [58, 114–116]. The behaviour of B_3 with p_{T}/A in p–A and A–A collisions cannot be explained by simple coalescence hypotheses, as investigated in Ref. [64].

Therefore, the observed results, in addition to what is known from earlier measurements, suggest that more sophisticated coalescence models have to take into account the volume dependence in order to explain the data.

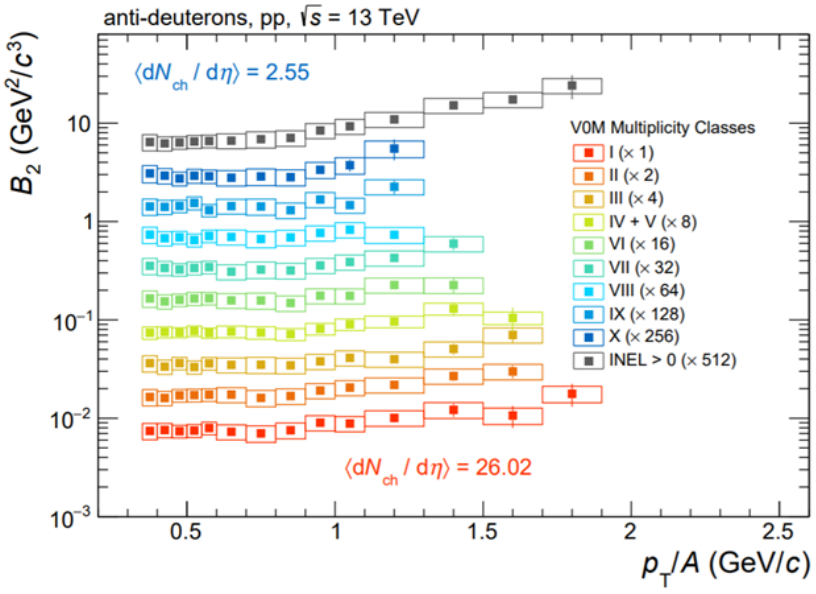

Figure 2.10: B_2 as a function of p_{T}/A in pp collisions at $\sqrt{s}$ = 13 TeV [65], in several multiplicity classes (coloured points) and in the minimum bias case (black points).

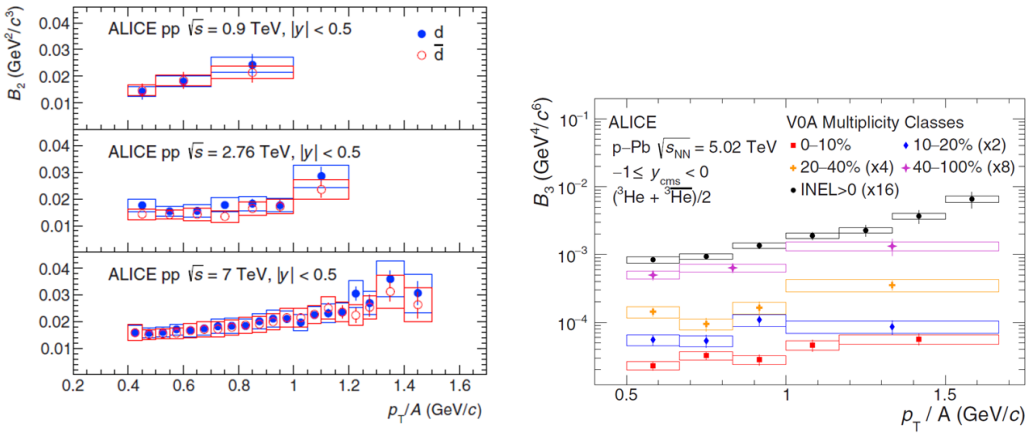

Figure 2.11: B_2 as a function of p_{T}/A in pp collisions at several collision energies ($\sqrt{s}$ = 0.9, 2.76, 7 TeV), in the MB case (left panel) [111] and B_3 in p–Pb collisions at $\sqrt{s_{\mathrm{NN}}}$ = 5.02 TeV (right panel) in several multiplicity classes and in the MB case [64].

2.4.2 State-of-the-art coalescence models

Other extensions of the model predict a dependence on the geometry of the system. For instance, if one assumes that neutrons and protons are emitted in thermal and chemical equilibrium [117], in the limit of high temperature their momentum spectra can be described by the Boltzmann-Gibbs distribution. This formulation of the model predicts a smaller coalescence parameter for central collisions (bigger volume) than in peripheral collisions (smaller volume).

In a more sophisticated approach, as the one described in Ref. [118], the volume of the emitting system can be computed starting from femtoscopic measurements of the profile radii (as discussed in Sect. 1.7.1). Such coalescence models take into account the source size, as the coalescence probability naturally decreases for nucleons with similar momenta that are produced far apart in configuration space. As coalescence is a quantum-mechanical process, the classical definition of phase space is replaced by the Wigner formalism. Indeed, in such an approach, the phase-space aspects of the coalescence process are more explicitly stressed out, starting from a quantum mechanical approach based on the density matrix of the source or the equivalent Wigner function formalism [119–123] and its classical phase-space analogues [124, 125]. In this approach the size of the cluster itself enters as an additional dimensionful quantity into the calculation of B_A, and it allows to address the problem of energy-momentum conservation in the coalescence process. The production probability of a nucleon cluster is given by the overlap of the Wigner function with the phase-space distributions of the constituents. If we focus on deuterons, for instance, we can follow the treatment of Ref. [45], based on Ref. [118] formalism. The deuteron wave function is approximated by the ground-state of an isotropic harmonic oscillator with one single characteristic size parameter, r_d:

$$\phi_d(r) = (2\pi r_d^2)^{-3/4} \exp\left(-\frac{r^2}{2r_d^2}\right) \tag{2.14}$$

where $r_d = \sqrt{8/3}\lambda_d$, being λ_d the RMS of the charge wave-function of deuterons. The harmonic-oscillator approximation has the advantage that the resulting Wigner function is Gaussian and allows for fully analytical

solutions, although it is not the most realistic wave function for a nucleus. The quantum-mechanical nature of the coalescence products is explicitly accounted for by means of the average correction factor, $\langle C_d \rangle$, which is approximated as:

$$\langle C_d \rangle \sim \frac{1}{\left[1 + \left(\frac{r_d}{2R_\perp(m_T)}\right)^2\right] \sqrt{1 + \left(\frac{r_d}{2R_\parallel(m_T)}\right)^2}} \tag{2.15}$$

where $R_\perp$ and $R_\parallel$ are the lengths of homogeneity of the coalescence volume, and m_T is the transverse mass of the coalescing nucleons. The nucleus size enters the calculation of B_2 via $\langle C_d \rangle$, as well as the homogeneity volume $R_\perp^2 R_\parallel$. $\langle C_d \rangle$ introduces a length scale defined by the deuteron size relative to the source size. In Fig. 2.12 the source radius (R) dependence of $\langle C_d \rangle$ and B_2, calculated assuming (a) r_d = 0, (b) r_d = 0.3 fm, (c) the actual value r_d = 3.2 fm [126], and (d) a larger, unrealistic r_d = 10 fm are shown. $\langle C_d \rangle$ suppresses significantly the production of objects with a radius larger than the source. Assuming $R_\perp = R_\parallel = R$ (source radius) and following the discussion described in Ref. [118], one obtains:

$$B_A = \frac{2J_A + 1}{2^A} \frac{1}{\sqrt{A}} \frac{1}{m_T^{A-1}} \left(\frac{2\pi}{R^2 + (r_A/2)^2}\right)^{\frac{3}{2}(A-1)} \tag{2.16}$$

being J_A the spin of the nucleus.

This general formula can be used to directly compare the predicted B_A with data. For small sources, as $R \to 0$, the coalescence probability is antiproportional to the harmonic oscillator size parameter and, thus, proportional to the depth of the attractive potential in the harmonic oscillator picture (and, thus, to the nucleus binding energy). Quite naturally, the allowed momentum difference between the coalescing nucleons is larger for more attractive, i.e. deeper, potentials. For a large source where $R \gg r_A$, the coalescence probability is dominated by the classical phase-space separation and, thus, decreases for large distances in configuration space.

Finally, following the discussion in Ref. [49], one can use the coalescence model to study the system size or charged particle multiplicity

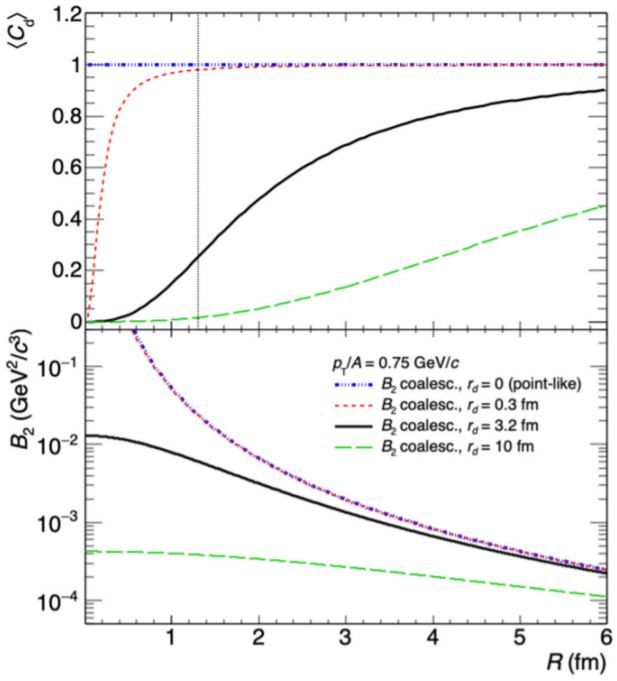

Figure 2.12: Quantum-mechanical correction factor $\langle C_d \rangle$ (top panel) and coalescence parameter B_2 for the deuteron (bottom panel) as a function of the radius of the source R, calculated assuming a size parameter for the deuteron r_d = 0, 0.3, 3.2, and 10 fm. The inflection point of $\langle C_d \rangle$ corresponds to $R = r_d/\sqrt{6}$ and is indicated in the top panel by the dotted vertical line for r_d = 3.2 fm. The Fig. is taken from [45].

dependence of the d/p and ^{3}He/p ratios by taking into account the finite size of deuteron and ^{3}He through their internal wave functions. In such a way, one can compare the results of this work and the previous experimental results from ALICE with the expectations of the coalescence model (see Chapt. 6), which are found in good agreement with the available experimental data.

Jumping to the conclusions drawn in Ref. [49], the yield ratio d/p can be expressed as:

$$\frac{N_d}{N_p} \sim \frac{3N_n}{4(mT_kR^2)^{3/2}} \left[1 + \left(\frac{1.6\,\text{fm}}{R}\right)^2\right]^{-3/2} \tag{2.17}$$

where m is the mass of the nucleon, $N_{p,n}$ the number of protons or neutrons, R the aforementioned source radius, T_k is the kinetic freeze-out temperature for nucleons, which is of the order of 100 MeV. The last factor of the above equation expresses the suppression of deuteron production, due to its finite size with respect to the nucleon emission source. Its value is significantly lower than unity for a radius $R < 1.6$ fm and approaches unity when the radius R is larger than the deuteron size. The first factor on the right-hand side of Eq. 2.17, instead, corresponds to the d/p limit for a source with radius R much larger than the deuteron size.

Similarly, it is possible to calculate the charged-particle multiplicity dependence of the ^{3}He/p ratio by extending the formalism for deuteron production from proton and neutron coalescence to the production of ^{3}He from the coalescence of two protons and one neutron. Thus, the yield ratio ^{3}He/p can be expressed as:

$$\frac{N_{^3He}}{N_p} \sim \frac{N_n N_p}{4(mT_k R^2)^3} \frac{1}{\left(1 + \frac{r^2_{^3He}}{2R^2}\right)^3} \tag{2.18}$$

where $r_{^3He}$ = 1.76 fm is the matter radius of ^{3}He [127]. In obtaining the above equation, the statistical factor of 1/4 to form a spin 1/2 ^{3}He from three spin 1/2 nucleons is also included.

Finally, it is possible to consider the ^{3}He production from the coalescence of a deuteron and a proton. In this case, the root-mean-square radius of ^{3}He can be estimated as $r_{^3He} \sim (3/8)^{1/2} \sqrt{\langle r_p d \rangle^2}$ = 1.15 fm with $\sqrt{\langle r_p d \rangle^2} \sim 2.6$ fm being the distance between proton and the center of mass of the deuteron inside the ^{3}He. Using the statistical factor of 1/3 for the coalescence of a spin 1 deuteron and a spin 1/2 proton to ^{3}He, the ^{3}He/p ratio is then given by:

$$\frac{N_{^3He}}{N_p} \sim \frac{7.1 \times 10^{-6}}{\left[1 + (\frac{1.15fm}{R})^2\right]^{3/2} \left[1 + (\frac{1.16fm}{R})^2\right]^{3/2}} \tag{2.19}$$

where the suppression factor for deuteron production has been included as well.

The evolution of d/p as a function of multiplicity, hence of the system size, is reported in panel (a) of Fig. 2.13. It is possible to see that at low multiplicities, where the system size is smaller or comparable with the size of the deuteron, the second factor in Eq. 2.17 is dominant. For the comparison with data, the neutron number N_n can be replaced with the proton number N_p, due to the vanishing chemical potential at the LHC. In panel (b) of Fig. 2.13, the contribution from the coalescence of deuteron and proton is larger than that from the coalescence of two protons and one neutron in collisions of small charged particle multiplicities, although the two processes give similar contributions to ^{3}He production in collisions of large charged particle multiplicities. Possibilities to discriminate between the two-body and three-body coalescence would come from the measurement of the ^{3}H/^{3}He yield ratio. As shown in panel (c) of Fig. 2.13, at low multiplicities the expectations of the model are quite different and therefore it would be possible to test the model with such a measurement. Nevertheless, such a ratio in that range of multiplicity (roughly corresponding to high-multiplicity pp collisions) is quite challenging from an experimental point of view, since both the triton and the ^{3}He nuclei are rare probes.

2.5 Do the models describe the data?

State-of-the-art SHM and coalescence model provide similar predictions for the yields of (anti)nuclei [45, 50, 130], and both are very much successful. In Fig. 2.14, the particle yields measured in ALICE are compared with the expectations of the SHM. The particle yields of light flavor hadrons are described over 9 orders of magnitude with a common chemical freeze–out temperature of $T_{chem} \sim 156$ MeV. This certainly is a non-trivial accomplishment of the SHM. However, not even the state-of-the-art γ_SCSM model is able to properly reproduce the measured p/π ratio as a function of multiplicity, which is systematically overestimated by the model approximately by 2σ. Nevertheless, it works fairly well in reproducing the hadron-to-pion ratios.

Possibilities to discriminate between the two hadronisation models could come from the study of the production yields of different nuclei

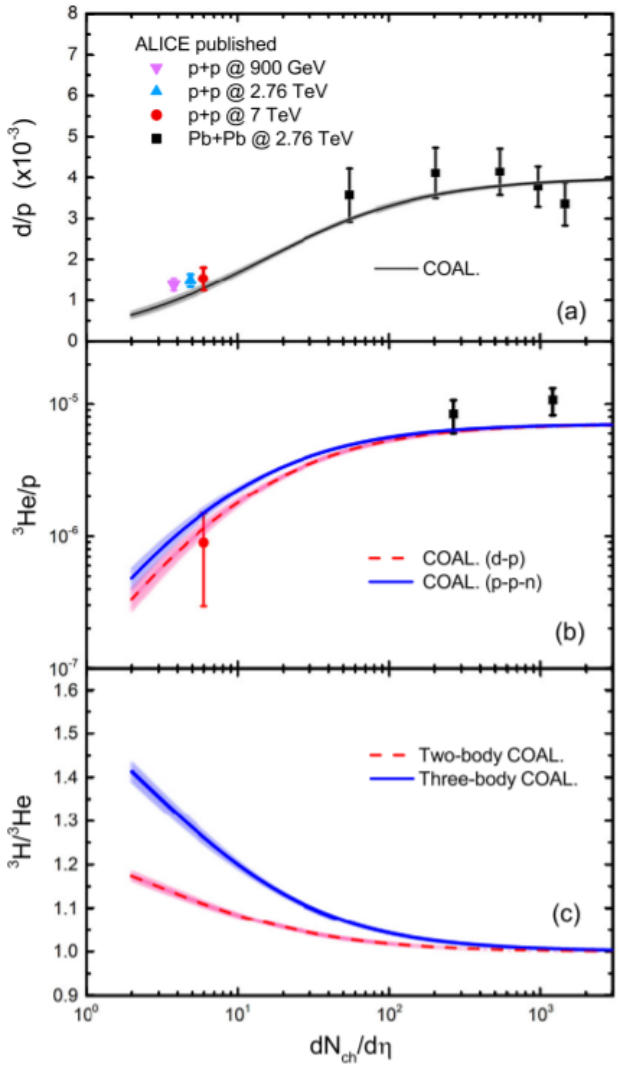

Figure 2.13: Charged particle multiplicity dependence of the yield ratios d/p (a), ^{3}He/p (b) and ^{3}H/^{3}He (c). The lines denote the predictions of coalescence model with theoretical uncertainties on the emission source radius given by the shaded band. Experimental data from the ALICE Collaboration are shown as symbols with error bars [58, 111, 128, 129].

that differ in size. The coalescence model, indeed, is sensitive to the size of the nucleus relative to that of the emission source [118, 119], while

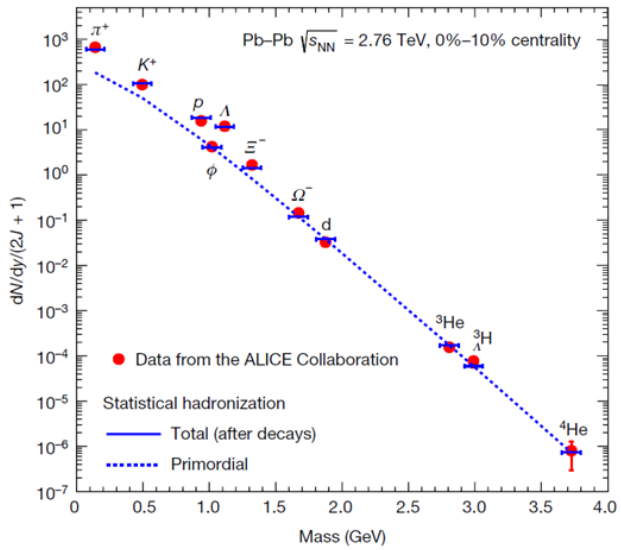

Figure 2.14: Particle yields as a function of the mass, measured in Pb–Pb collisions at $\sqrt{s_{\rm NN}}$ = 2.76 TeV. The data are compared with the predictions of the Statistical Hadronisation model.

the size of the nucleus does not enter in the SHM calculations. In a simple coalescence model, in which the size of the emitting source is not taken into account, the B_A parameter is expected to be independent of transverse momentum, multiplicity and source size. However, previous experimental results have shown that B_A at a given $p_{\rm T}/A$ weakly depends on multiplicity in pp collisions [61,65], while in Pb–Pb collisions it shows a strong decrease with multiplicity [58,64,82] (as it will be shown in Fig. 6.17, in Chapt. 6). From femtoscopy measurements [44], it is known that the source radius is related to the average charged particle multiplicity density [45], as discussed in Sect. 1.7.1. Therefore, the mean charged-particle multiplicity density allows the comparison of different collision systems at similar nuclear emission volumes. The p–Pb collision system, subject of this thesis work, covers multiplicities that are between pp and Pb–Pb collisions and thus offers the possibility to explore intermediate source sizes.

The production mechanism of light (anti)nuclei can be further investigated by comparing the ratio of their yields to those of protons for differ-

ent multiplicities with the SHM and coalescence models predictions. In addition, the ratio of the yields of light (anti)nuclei and those of charged pions should test for the first time the consistency of the models against the simultaneous description of the nuclei-to-proton and proton-to-pion ratios for different multiplicities.

As already anticipated, further comparisons between the model predictions and the experimental results from ALICE, including the results from this work, will be discussed in Chapt. 6.

2.6 Astrophysical implications and dark matter background

We understand only $\sim 5\%$ of the energy-matter content of our Universe, which is made of ordinary baryonic matter. The nature of the remaining 95% is still mysterious. The missing part of our Universe is made of an invisible form of matter, called *dark matter* ($\sim 27\%$) and a mysterious form of energy which is responsible for the accelerating expansion of the visible Universe, called *dark energy* ($\sim 68\%$). Also the matter-antimatter asymmetry is still a subject of study.

The observation of antinuclei heavier than antiprotons in cosmic rays could indicate the existence of antimatter that has survived since the Big Bang or could be a signature of dark matter annihilation in the galactic halo [131]. Thus, the search for these particles addresses two of the most fundamental questions in modern physics: the baryon to antibaryon asymmetry in the universe as well as the existence and nature of dark matter. The understanding of the (anti)nuclei production mechanism is therefore important to provide inputs for the background determination in dark matter searches in space [132, 133] and to better understand the formation of QCD bound states in high energy hadron physics. For this reason, it has been subject to a great effort of the scientific community over the past years.

Among the experiments dedicated to the dark matter and antimatter measurements, the Alpha Magnetic Spectrometer (AMS-02) [134], installed in the International Space Station (ISS), is the most sensitive particle detector ever deployed in space. The main goal of this experiment

is to measure antimatter in cosmic rays outside the Earth atmosphere. The role of antihelium is particularly important due to its relatively large mass and its rare production in spallation of cosmic rays: if antihelium is produced in dark matter annihilation, a larger signal-to-background ratio is expected with respect to the measurements of antiproton and antideuteron.

A crucial ingredient for this experiment is the precise estimation of the production yield of light antinuclei (namely antideuteron and anti^{3}He) in high energy collisions between cosmic rays and the interstellar medium, which represents the dominant physical background [135]. This is currently done with extrapolation from low energy experiments and theoretical models. Indeed, considering that $> 90\%$ of cosmic rays are protons and the interstellar gas is mostly made of hydrogen, the measurement of antideuteron and anti^{3}He is a fundamental baseline for the theoretical models used to estimate the flux of secondary nuclei produced by cosmic ray spallation.

The indirect search of dark matter in space experiments is based on the observation of antimatter which exceeds the estimates of the ordinary matter produced in cosmic ray spallation. The contributions from cosmic rays interactions at low energy (1-2 GeV/c per nucleon) should be small [138–141] and the sensitivity to dark matter annihilation should be enhanced. The estimate of the cosmic ray spallation is obtained from theoretical model calculations constrained by measurements of the coalescence parameter B_A. In Fig. 2.15, the predictions for the observation probability of $A \geq 1, 2, 3, 4$ secondary anti^{3}He in the latest years of operation of the AMS-02 experiment as a function of the coalescence parameter B_3 [132] are shown. The green band represents the estimate for the B_3 coalescence parameter in pp collisions, obtained using 20 anti^{3}He and 20 ^{3}H events measured in pp collisions at $\sqrt{s}$ = 7 TeV from ALICE [137] as a constraint. The detection of even a single anti^{3}He nucleus in the energy range predicted for dark matter could constitute a very compelling hint in favor of the existence of dark matter, or at least of a very exotic process different from spallation of cosmic rays.

Even if in the last years the search of such a signal has been intensified with the experiments AMS-02 and GAPS [142], no clear evidence of antinuclei production was found [143, 144]. However, in May 2018, professor

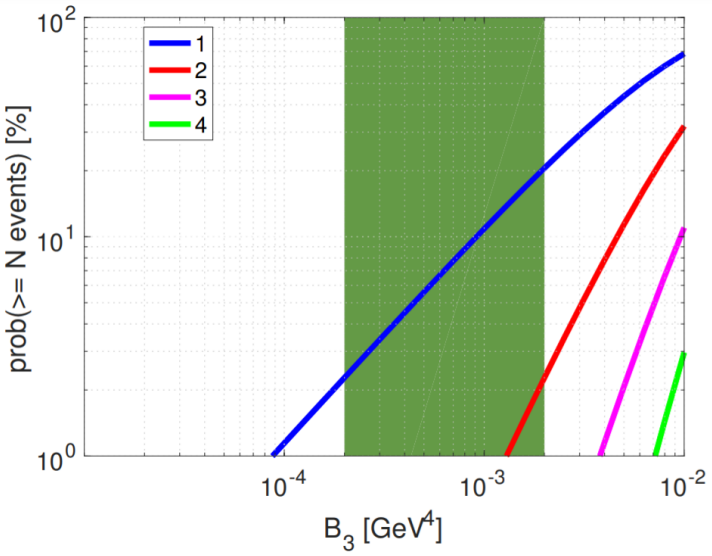

Figure 2.15: Poisson probability for detecting $N \geq 1$, 2, 3, 4 ^{3}He events in a 5-years analysis of AMS-02, assuming the same exposure as in the $\overline{\text{p}}$ analysis [136]. The green band represents the estimate for the B_3 parameter in pp collisions, obtained using 20 anti^{3}He and 20 ^{3}H events measured from ALICE [137] as a constraint.

Samuel Ting announced at a CERN seminar [145] that the AMS collaboration reported the possible observation of two potential candidates of anti^{4}He and six potential candidates of anti^{3}He (see Ref. [146] and the references therein for further discussions). Such an observation would be a striking result for the search of indirect dark matter. Further dedicated experiment for the search of antideuteron and antihelium from dark matter annihilation are ongoing [133,147]. A realistic model for the production of antideuterons and anti^{3}He would provide an input for the determination of background in the search for dark matter. Hence their measurement are crucial for further development in the indirect dark matter searches.

Chapter 3

The experimental setup

The largest and most powerful particle collider in the world, the Large Hadron Collider (LHC), is able to produce the high energy density required to melt hadronic matter. Indeed, while most of the LHC uptime is dedicated to the proton−proton physics that led to the discovery of the Higgs Boson and of two charmed pentaquark states, a significant part of the physics programme at the LHC is dedicated to heavy ion physics and the characterisation of the Quark Gluon Plasma. Among the four major collaborations running experiments at the LHC, ALICE is focused on the investigation of the properties of the QGP.
In this Chapter the ALICE layout and its different subsystems are presented, in the conditions as they were during the p–Pb at 8.16 TeV campaign in 2016. Particular emphasis will be given to the detectors of the central barrel, in the mid-rapidity region, which are employed for the measurement of the hadronic observables object of this thesis. In 2021 ALICE is completing a significant upgrade of its detectors to further enhance its capabilities. Sect. 3.4 will be dedicated to the ALICE upgrade, with specific interest to the upgrade of the central barrel detectors.

3.1 The Large Hadron Collider

The Large Hadron Collider is the last component of the complex acceleration setup installed at CERN (Fig. 3.1). Each machine in the chain accel-

erates particles to increasingly higher energies. The LHC was designed to provide proton-proton (pp) collisions with a centre-of-mass energy ($\sqrt{s}$) up to 14 TeV with a maximum luminosity[1] of 10^{34} cm^{-2} s^{-1}. For ions, the centre-of-mass energy, given per nucleon-nucleon pair ($\sqrt{s_{\mathrm{NN}}}$), is reduced compared to protons due to the different ratio of the charge to the mass. It can be calculated as:

$$\sqrt{s_{\mathrm{NN}}} = \sqrt{Z_i / A_i}\sqrt{Z_k / A_k}\sqrt{s} \tag{3.3}$$

where $\sqrt{s}$ is the centre-of-mass energy in the case of pp collisions and $\sqrt{Z_{i,k} / A_{i,k}}$ is the correction for the ions of type i and k contained in each of the beams. Thus, the top centre-of-mass energy for lead-lead (Pb–Pb) collisions is $\sqrt{s_{\mathrm{NN}}}$ = 5.52 TeV, while it is $\sqrt{s_{\mathrm{NN}}}$ = 8.79 TeV for proton-lead (p–Pb) collisions[2]. The maximum energy reached until now is $\sqrt{s}$ = 13 TeV for pp collisions, $\sqrt{s_{\mathrm{NN}}}$ = 8.16 TeV and $\sqrt{s_{\mathrm{NN}}}$ = 5.02 TeV for p–Pb and Pb–Pb, respectively. To reach these high energies, the protons and ions have to be accelerated to increasingly higher energies by a chain of pre-accelerators before being injected into the LHC.

[1] In scattering theory luminosity is defined as the ratio of the number of events detected (N) in a certain time (t) to the interaction cross section (σ):

$$L = \frac{1}{\sigma}\frac{dN}{dt} \tag{3.1}$$

Dealing with two colliding beams, both beams serve as target and incoming beam at the same time. Thus, the luminosity of two colliding beams is

$$L \propto K \int\int\int\int_{-\infty}^{+\infty} \rho_1(x, y, s, -s_0)\rho_2(x, y, s, s_0) dx dy ds ds_0 \tag{3.2}$$

being $\rho_1(x, y, s, -s_0)$ and $\rho_2(x, y, s, s_0)$ the time dependent beam density distribution functions, while K is a kinematic factor. Assuming that the beams are two Gaussian colliding head-on, luminosity depends on the number of particles per bunch (N_1 and N_2) and on the beam sizes, according to: $L = \frac{N_1 N_2 f N_b}{4\pi\sigma_x\sigma_y}$, being f a revolution frequency and N_b the number of bunches. In other words, luminosity is a measure of how many particles are sent through a given transverse area in a given time. It is thus linked to the interaction rate R via the cross section (σ) which quantifies the probability that a given process, here a collision, is taking place. More details about luminosity can be found in [148].

[2] For lead, the charge number is Z = 82 and mass number is A = 208.

Protons and lead ions go through different acceleration chains. Protons are extracted from a source producing ionised hydrogen and then are accelerated up to 50 MeV by LINAC 2. The resulting beam is injected in the Proton Synchrotron Booster (PSB), which accelerates the protons to 1.4 GeV and provides the beam, now structured in bunches, to the Proton Synchrotron (PS). The Proton Synchrotron pushes protons at 25 GeV into the Super Proton Synchrotron (SPS) where they are accelerated to 450 GeV before their injection to the LHC. Lead ions, instead, are produced ionising the gas obtained heating up a small isotopically pure ^{208}Pb sample. The obtained ions travel through the LINAC 3 that provides the ion beam at the energy of 4.5 MeV per nucleon to the Low Energy Ion Ring (LEIR) where the beam is split into 4 short bunches and it is further accelerated from 4.2 MeV to 72 MeV. From the LEIR, the ion beam is then transferred to the Proton Synchrotron and it follows the same path previously described for the proton beams.

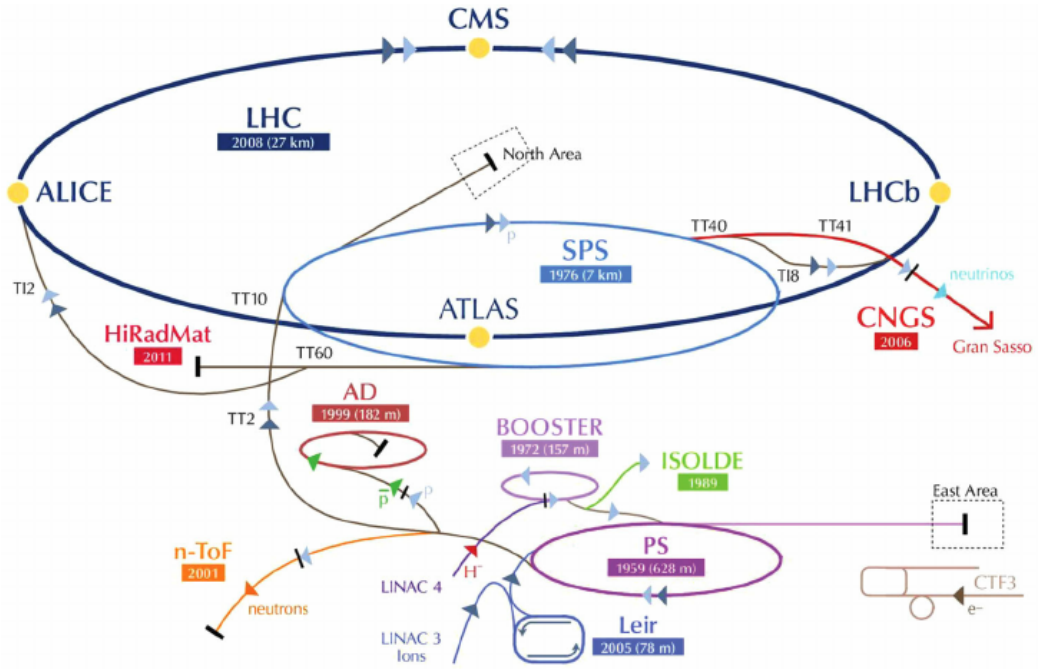

Figure 3.1: The accelerator complex at CERN [149].

Along with the top energy, one of the most important parameters for

the experiments at the LHC is the luminosity delivered by the collider. The reaction rate R for a process can be easily evaluated using the process cross section and the luminosity:

$$R = L\sigma_{\text{process}} \tag{3.4}$$

The luminosity delivered by a hadron collider can be measured experimentally through a special procedure called van der Meer scan. Such procedure foresees that the beams are swept transversely across each other. Once circulating beams have been established at the LHC, the first step towards collisions is to remove the physical separation used to avoid collisions during injection and ramp. A residual separation can remain after the collapsing of the separation bumps. The so-called Van Der Meer method allows for a minimization of this unwanted separation by transversely scanning one beam through the other. The scans are performed by moving the beams step-wise across each other in the two transverse planes. The beam sizes at the interaction point can also be determined by this method and used to give an absolute measurement of the luminosity. The Van Der Meer scan method for luminosity determination was pioneered by S. Van Der Meer at the ISR [150], in 1968. Despite the honourable age, it remains the preferable tool at hadron colliders, since it delivers the lowest calibration systematic uncertainties, which still often dominates the overall luminosity uncertainty at LHC experiments.

3.2 The LHC experiments

Seven experiments at the Large Hadron Collider (LHC) use detectors to analyse the myriad of particles produced by collisions in the accelerator. These experiments are run by collaborations of scientists from institutes all over the world. Each experiment is distinct, and characterized by its detectors.
The biggest of these experiments, ATLAS (A Toroidal LHC ApparatuS) [151] and CMS (Compact Muon Solenoid) [152], use general-purpose detectors to investigate the largest range of physics possible. ATLAS and CMS have a broad physics programme ranging from studying the Standard Model (including the Higgs boson) to searching for extra dimen-

sions and particles that could make up dark matter. Although ATLAS has the same scientific goals as the CMS experiment, they use different technical solutions and a different magnet-system design. Having two independently designed detectors is vital for cross-confirmation of any new discovery made. As for the case of the Higgs boson, which was announced at CERN on July the 4^{th}, 2012, by the ATLAS and CMS collaborations, when both experiments found evidences in the LHC data for a particle consistent with a Higgs boson, the particle linked to the mechanism proposed in the 1960s to give mass to the W, Z and other particles. The other two big experiments at the LHC, ALICE (A Large Ion Collider Experiment) [153] and LHCb (Large Hadron Collider beauty) [154], have detectors specialized for focussing on specific phenomena. The LHCb experiment is specialized in investigating the slight differences between matter and antimatter by studying the beauty quark, or *b quark*. Instead of surrounding the entire collision point with an enclosed detector as ATLAS, CMS and ALICE do, the LHCb experiment uses a series of subdetectors to detect mainly forward particles - those thrown forwards by the collision in one direction. The ALICE detector, used to collect the data analyzed in this thesis, is instead extensively described in the following Sections.

These four detectors sit underground in huge caverns along the LHC ring, as shown in Fig. 3.2.
The smallest experiments at the LHC are TOTEM and LHCf, which focus on "forward particles" − protons or heavy ions that brush past each other rather than smashing head on when the beams collide. TOTEM uses detectors positioned on either side of the CMS interaction point, while LHCf is made up of two detectors which sit along the LHC beamline, at 140 metres either side of the ATLAS collision point. Finally, MoEDAL uses detectors deployed near LHCb to search for a hypothetical particle called the magnetic monopole.

3.2.1 The ALICE detector

The aim of ALICE is to study the physics of strongly interacting matter at the highest energy densities reached so far in the laboratory. For this purpose, the ALICE Collaboration is carrying out a comprehensive study of

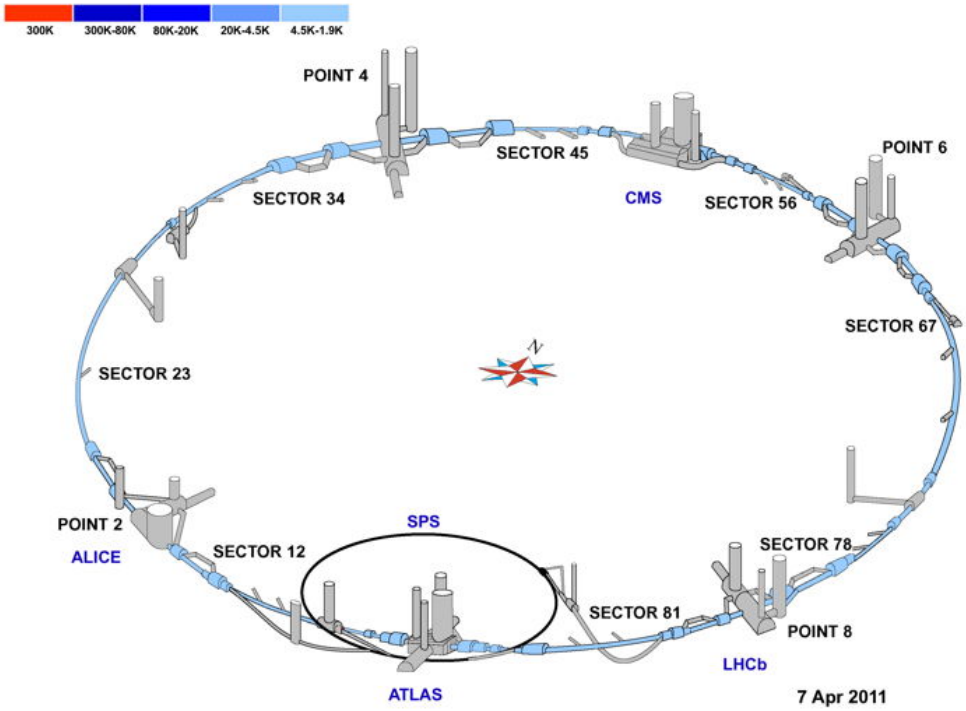

Figure 3.2: Layout of the LHC ring shown along with main experiments positions.

the hadrons, electrons, muons, and photons produced in the collisions of heavy nuclei (^{208}Pb). ALICE is also studying proton-proton and proton-nucleus collisions both as a comparison with nucleus-nucleus collisions and in their own right.

Collisions in the LHC generate temperatures more than 10^5 times higher than the centre of the Sun. For part of each year the LHC provides collisions between lead ions, recreating in the laboratory conditions similar to those just after the Big Bang. Under these extreme conditions, protons and neutrons melt, freeing the quarks from their bonds with the gluons. This is quark-gluon plasma. The existence of such a phase and its properties are key issues in the theory of quantum chromodynamics (QCD), for understanding the phenomenon of confinement, and for a

physics problem called chiral-symmetry restoration. The ALICE collaboration studies the quark-gluon plasma as it expands and cools, observing how it progressively gives rise to the particles that constitute the matter of our universe today.
The ALICE collaboration uses the 10000-tonne ALICE detector – 26 m long, 16 m high, and 16 m wide – to study quark-gluon plasma. The detector sits in a vast cavern 56 m below ground close to the village of St Genis-Pouilly in France, receiving beams from the LHC.
The collaboration counts more than 1800 scientists from over 170 physics institutes in 41 countries.

3.3 Design of ALICE

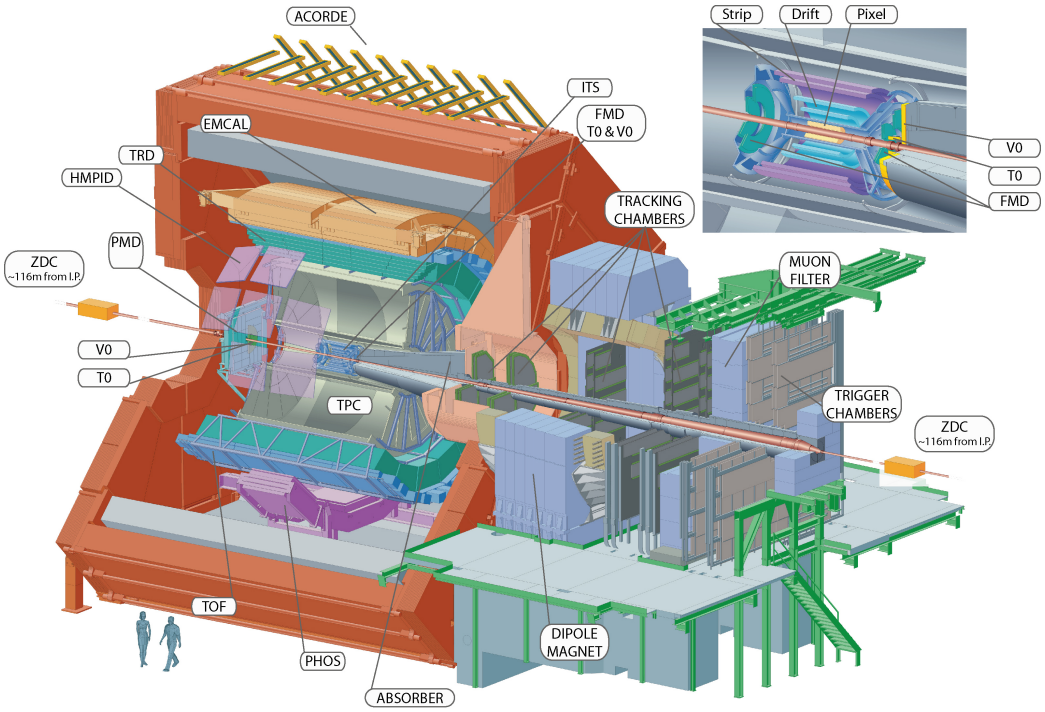

Figure 3.3: The setup of ALICE detectors.

ALICE has been specifically designed and optimised to be a general purpose heavy ion experiment. The main goal is studying the properties

of the QGP and for that purpose it is necessary to track and to identify all the particles produced in heavy ion collisions. The ALICE subdetectors were designed when the foreseen number of charged particles per pseudorapidity unit was ranging between 2000 and 8000, for this reason detectors with high granularity and low material budget, such as the Time Projection Chamber (TPC) and the Inner Tracking System (ITS), have been adopted. When using these two detectors in the data acquisition, the maximum readout rate for minimum bias events of the ALICE experiment is 1 kHz, regardless of the colliding system. The setup of the ALICE experiment, as it was during the 2016 p–Pb campaign at 8.16 TeV, is shown in Fig. 3.3 while Table 3.1 lists the position and some geometrical details of the ALICE detectors. In the apparatus two main parts can be distinguished: the central barrel, consisting of all the detectors located inside and outside the L3 magnet in the pseudorapidity region $|\eta| < 0.9$, and the muon arm, sitting in the $-4 < |\eta| < -2.5$ region and consisting of an absorber with small atomic number Z, a spectrometer with a dipole magnet, five tracking stations and finally an iron absorber. The ALICE coordinate system, used also in Table 3.1, is a right-handed Cartesian system with the origin sitting at the nominal Interaction Point (IP). The x-axis of the reference frame is aligned with the accelerator plane and it points to the centre of the LHC while the y-axis is perpendicular to the accelerator plan and it points upward. Finally the z-axis is parallel to the beam line and its pointing is defined by the chirality of the coordinate system. The central barrel tracking detectors cover the full azimuthal acceptance and they include, going from the beam line outward: a silicon tracker (ITS) made with three different technologies (Silicon Pixel Detector, Silicon Drift Detector and Silicon Strip Detector), a Time Projection Chamber (TPC), a Transition Radiation Detector (TRD) and a Time Of Flight (TOF) detector. In order to extend the transverse momentum[3] reach of the experiment down to 80 MeV/c, a mild solenoidal magnetic field − with respect to the other LHC experiments − of 0.5 T has been adopted. ALICE is the only experiment at the LHC using a warm-resistive magnet to

[3]The component of momentum transverse (i.e. perpendicular) to the beam line. Its importance arises because momentum along the beamline may be left over from the beam particles, while the transverse momentum is associated with the physics that happened at the vertex.

measure the momentum of the charged particles, the same magnet used for the L3 experiment at LEP. As it will be shown in the following, the track reconstruction efficiency at low p_{T} strongly profited from the usage of tracking detectors with a very low material budget. The resolution on the momentum does not depend only on the magnetic field B used, but also on the lever arm length of the tracking detectors L and on the resolution on the track sagitta measurement σ_S:

$$\frac{\sigma_p}{p} \propto p\frac{\sigma_S}{BL^2} \tag{3.5}$$

Thanks to the large radial coverage (0.039 m $\leq$ r $\leq$ 3.680 m), despite the mild solenoidal magnetic field, the ALICE apparatus is able to reconstruct tracks up to $p > 100$ GeV/c. The above mentioned tracking detectors are also among the detectors of ALICE providing PID.

In the following, the relevant detectors for the analysis of this thesis are further described, with particular emphasis on the detectors located in the central barrel inside the solenoidal magnetic field B = 0.5 T: the ITS, the TPC and the TOF detector, as extensively described in [155, 156].

3.3.1 Inner Tracking System (ITS)

The Inner Tracking System (ITS) [157] is the first detector encountered by particles produced in the collision events that travel through the experimental apparatus. It consists of 6 cylindric layers of silicon detectors, concentric and coaxial to the beam pipe, with a total pseudorapidity coverage $|\eta| \leq 0.9$. Three different technologies have been used for this detector: the two innermost layers are made of Silicon Pixel Detectors (SPD), the two central layers of Silicon Drift Detectors (SDD) and the two outermost layers of double sided Silicon Strip Detectors (SSD) (Fig. 3.4). The main parameters for each of the three detector types are summarized in Table 3.2. The main tasks of the ITS are to localise the primary vertex of the collision, with a resolution of 10 μm in central Pb–Pb collisions, to find the displaced secondary vertices, with a resolution better than 100 μm, to perform tracking and identification of particles down to low momenta (< 200 MeV/c) as well as to enhance the momentum resolution of the particles reconstructed with the TPC.

Detector	Acceptance (η, ϕ)	Position (m)	Surface (m^2)	Channels
ITS layer 1,2 (SPD)	$\pm 2, \pm 1.4$	0.039 , 0.076	0.21	9.8 M
ITS layer 3,4 (SDD)	$\pm 0.9, \pm 0.9$	0.150 , 0.239	1.31	133 K
ITS layer 5,6 (SSD)	$\pm 0.97, \pm 0.97$	0.380 , 0.430	5.00	2.6 M
TPC	± 0.9 at r=2.8 m ± 1.5 at r=1.4 m	0.848 , 2.466	Readout 32.5 m^2 Volume 90 m^3	557568
TRD	± 0.84	2.90 , 3.68	716	1.2 M
TOF	± 0.9	3.78	141	157248
HMPID	$\pm 0.6, 1.2^\circ \leq \phi \leq 58.8^\circ$	5	11	161280
PHOS	$\pm 0.12, 220^\circ \leq \phi \leq 320^\circ$	4.6	8.6	17920
EMCAL	$\pm 0.7, 80^\circ \leq \phi \leq 187^\circ$	4.36	44	12672
ACORDE	$\pm 1.3, -60^\circ \leq \phi \leq 60^\circ$	8.5	43	120
Muon tracking	$-2.5 \leq \eta \leq -4.0$	-14.22, -5.36	95	1.08 M
Muon trigger	$-2.5 \leq \eta \leq -4.0$	-17.12, -16.12	138	21000
PMD	$2.3 \leq \eta \leq 3.7$	3.64	2.59	221184
V0A	$2.8 \leq \eta \leq 5.1$	3.4	0.548	32
V0C	$-3.7 \leq \eta \leq -1.7$	-0.897	0.315	32
T0A	$4.61 \leq \eta \leq 4.92$	3.75	0.0038	12
T0C	$-3.28 \leq \eta \leq -2.97$	-0.727	0.0038	12

Table 3.1: Geometrical details of the configuration of ALICE detectors. This table has been adapted from the extensive description of the ALICE apparatus in [155]. When it is not specified, the azimuthal coverage for the detector is 2π. The position of the detector corresponds to the radial distance from the beam axis for the barrel detectors and to the distance along z for the others. When more than one position values are specified the detector is subdivided in two or more parts and those values are the minimum and maximum distances from the interaction point.

The choice of different technologies is mainly related to the radial distance of the detector layers. The SPDs are the innermost layers and therefore have to deal with a very high-density of tracks ($\sim$ 100 tracks/cm^2)

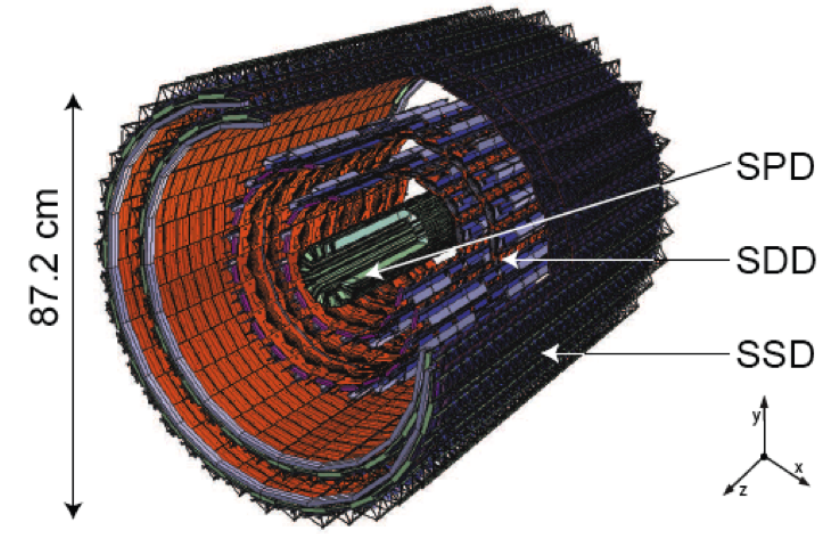

Figure 3.4: Layout of the Inner Tracking System.

and a larger radiation environment (200 krad in 10 years). The SPD is fundamental for the quality of vertexing, both for the primary vertex reconstruction and the measurement of secondary tracks impact parameter. The two-dimensional segmentation combines the advantages of unambigous 2D readout with geometrical precision, double-hit resolution and speed. Thus, its high segmentation leads to a low individual diode capacitance, resulting in an excellent signal-to-noise ratio at high speed. The SDDs are selected to equip the two intermediate layers of the ITS, since they couple a very good multi-track capability with $\mathrm{d}E/\mathrm{d}x$ information. The drift detectors are used as trigger, requiring at least three measured samples per track and therefore at least four layers carrying $\mathrm{d}E/\mathrm{d}x$ information. Finally, the two outer layers use strip detectors and are crucial for the connection of tracks from the ITS to the TPC. SSDs provide $\mathrm{d}E/\mathrm{d}x$ information to assist particle identification for low-momentum particles. Double-sided SSDs are also commonly used in several high-energy physics experiments where they function reliably.

Parameter	Silicon Pixel	Silicon Drift	Silicon Strip
Spacial precision rϕ (μm)	12	35	20
Spacial precision z (μm)	100	25	830
Two track resolution rϕ (μm)	100	200	300
Two track resolution z (μm)	850	600	2400
Cell size (μm^2)	50×425	202×294	95×40000
Active area per module (mm^2)	12.8×69.6	72.5×75.3	73×40
Readout channels per module	40960	2×256	2×768
Total number of modules	240	260	1698
Total number of readout channels (k)	9835	133	2608
Total number of cells (M)	9.84	23	2.6
Max. occupancy for central Pb–Pb (inner layer) (%)	2.1	2.5	4
Max. occupancy for central Pb–Pb (outer layer) (%)	0.6	1.0	3.3
Power dissipation in barrel (W)	1350	1060	850
Power dissipation end-cap (W)	30	1750	1150

Table 3.2: Parameters of the various detector types of the ITS detector. A module represents a single sensor element.

Vertex reconstruction in ALICE

The reconstruction of the primary vertex is based on the SPD of the ITS. In order to determine the z coordinate (position) of the vertex, pairs of reconstructed points in the two SPD layers are selected (tracklets). Given that the two layers are very close in azimuthal angle in the transverse plane, a linear extrapolation is used to estimate the z position of the primary vertex. Finally, a similar procedure is also performed in the transverse plane. This procedure does not take into account the track bending due to the magnetic field. However, since the distances from the interaction point are short, the x and y coordinates of the primary vertex are determined with a good precision so that they can be used to constrain the first tracking step. This estimate of the primary vertex position is used to correct the z coordinate of the primary vertex. If the beam position

is stable in time, it is also possible to determine the transverse position of the vertex by averaging the measurements performed on many events. The resolution on the vertex position depends on the track multiplicity (particle per units of rapidity).
In Pb–Pb collisions, a resolution of about 10 μm is reached while, in average, a $\sim$ 100 μm resolution is obtained for pp collisions. The measurement of the vertex position is finally used as an input for the tracking. After the track reconstruction, the vertex position is corrected using the parameters of the track. To improve the vertex position in the transverse plane, the nominal beam position is added in the fit as an independent measurement [155]. The vertex resolution of tracks as a function of the half event tracklet multiplicity is shown in Figure 3.5.

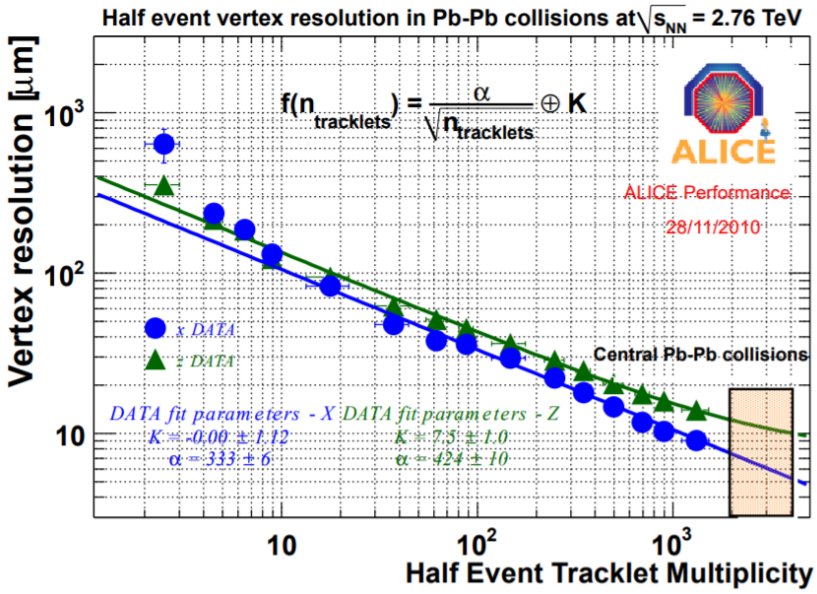

Figure 3.5: Vertex resolution in Pb–Pb collisions at $\sqrt{s_{NN}}$ = 2.76 TeV as a function of half of the tracklets multiplicity of the event.

3.3.2 Time Projection Chamber (TPC)

The Time Projection Chamber (TPC) serves as a major tracking detector in ALICE [158]. It is used to identify the charged particles and measure their

momentum, and to help in the reconstruction of the primary vertex of the collision. The pseudorapidity range covered by the TPC is $|\eta| < 0.9$. The detector covers the transverse momentum from $\sim$ 0.1 GeV/c to $\sim$ 100 GeV/c. The TPC has also the full coverage of the azimuthal angle (excluding the dead zones of the detector).

The scheme of the TPC is shown in Fig. 3.6, and a summary of its main parameters is presented in Table 3.3.

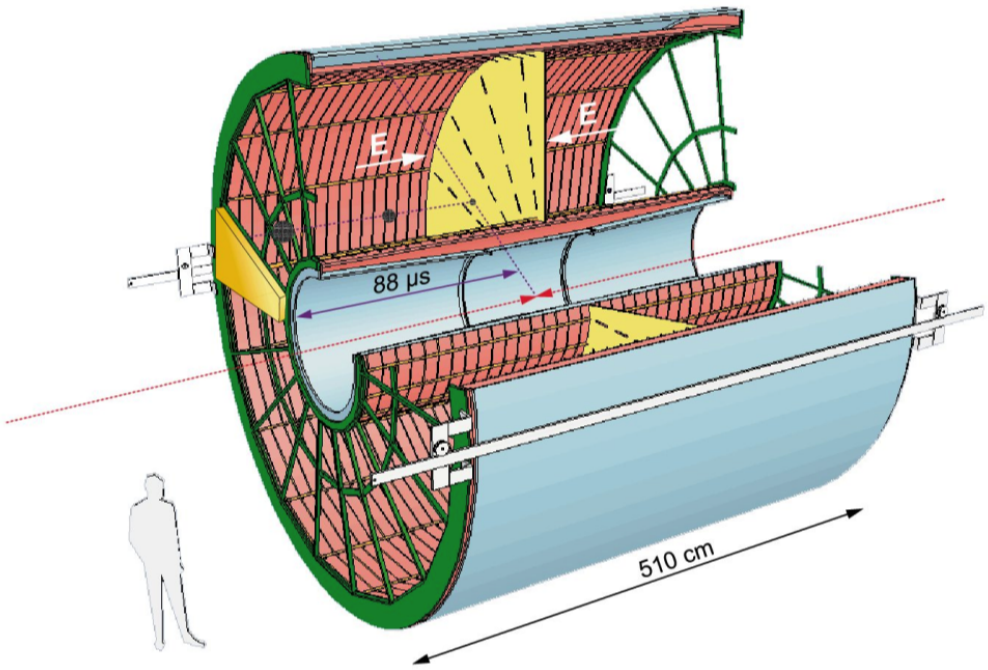

Figure 3.6: Layout of the Time Projection Chamber.

The skeleton of the TPC is built of a cylindrical field cage which is filled with 90 m^3 of the mixture $Ne/CO_2/N_2$. Both end plates are segmented into 18 trapezoidal sectors where multi-wire proportional chambers (MWPC) and cathode pad readout are installed. In the centre of the field cage (see Fig. 3.7), there is a high voltage electrode and two potential degraders creating a uniform electrostatic field along the beam axis. The drift gas was optimised with the aim of reaching the eligible drift speed, and to ensure low multiple scattering. The field cage of the TPC is sur-

Lenght (active volume)	2×2500 mm
Segmentation in ϕ	18 sectors
Segmentation in r	2 chambers per sectors
Total number of readout chambers	$2 \times 2 \times 18 = 72$
Detector gas	$Ne/CO_2/N_2$ 90/10/5
Gas volume	90 m^3
Drift lenght	2×2500 mm
Drift field	400 V/cm
Drift velocity	2.7 cm/μs
Maximum drift time	92/μs
Total HV	100 kV
Diffusion	$D_L = D_T$ = 220 $\mu m/\sqrt{cm}$
Material budget	$X/X_0 = 3.5\%$ near $\eta = 0$
Event size (for dN/dy = 8000)	$\sim$ 90 MB
Event size (for pp)	$\sim$ 1–4 MB
Total bandwidth	$\sim$30 GB/s
Trigger rate limits	300 Hz Pb–Pb central events
Position resolution (σ) in rϕ	1100 to 800 μm inner/outer radii
Position resolution (σ) in z	1250 to 1100 μm
dE/dx resolution, isolated tracks	5.0%
dE/dx resolution, dN/dy = 8000	6.8%

Table 3.3: Synopsis of TPC parameters.

rounded by double-shelled containment vessels with CO_2 as an insulator. Composite materials based on carbon fiber were chosen for high mechanical stability and low material budget (only 3.5 % of a radiation length for tracks with normal incidence). The working principle of the TPC is based on the ionisation effect induced by charged particles traversing the barrel. Free electrons drift towards the end plates. Since they cannot induce sufficiently large signal in the readout pads, it needs to be amplified by the creation of an avalanche near the anode wires. Cathode planes are seg-

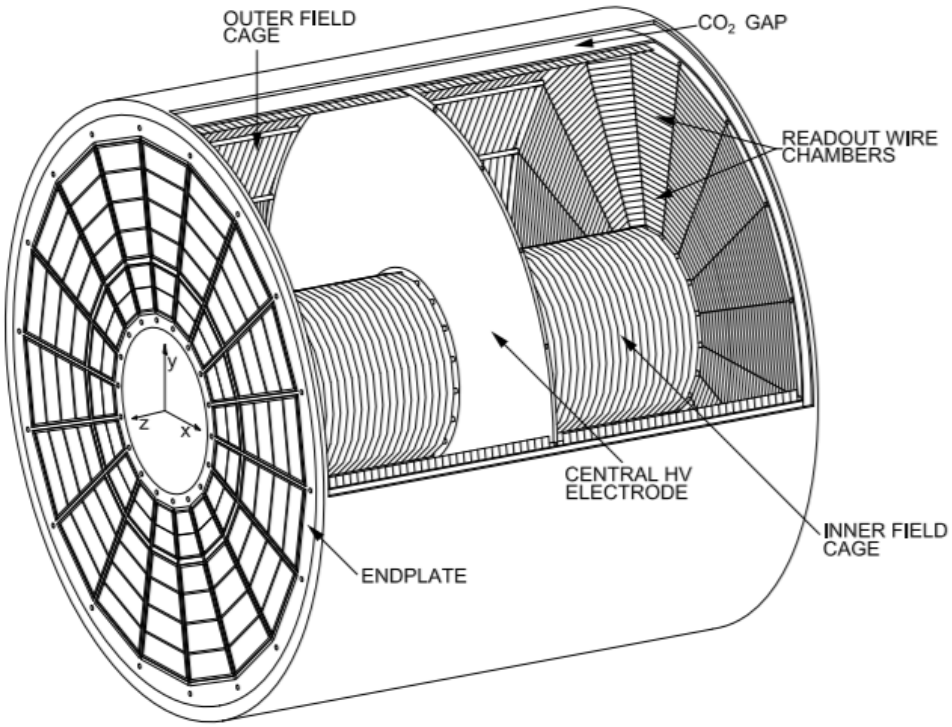

Figure 3.7: 3D view of the TPC field cage. The high voltage electrode is located at the center of the drift volume. The endplates with 18 sectors and 36 readout chambers on each end are shown [158]

mented in two dimensions, therefore one can measure many space points per track in the transverse plane. In addition, the three-dimensional reconstruction of the track is possible by the measurement of the arrival time of the ionisation electrons to the pad with respect to the certain reference time, e.g. the collision time from the LHC. Identification of charged particles traversing the TPC volume is based on the calculation of their momentum and charge in combination with the measurement of the specific ionisation energy loss per unit path length $\mathrm{d}E/\mathrm{d}x$. The former is done using the radius and the direction of curvature of the particle trajectory bent in the ALICE magnetic field. The trajectory of a charged-particle is estimated measuring the gas ionization in up to 159 samples

along a path of about 160 cm. By combining the reconstructed clusters in the TPC and the hits in the ITS, the tracks of charged-particles are reconstructed and finally back-propagated to the nominal collision point, which is inside the beam pipe, in order to find the primary vertex position, as already discussed in Sect. 3.3.1. The tracking procedure will be further discussed in Sect. 4.7.3. Thanks to its design requirements, the TPC provides a measurement of the charged-particle transverse momentum (p_{T}) with a resolution ranging from about 1% at 1 GeV/c to about 3% at 10 GeV/c, and a measurement of the specific energy loss with a resolution ranging from about 5.2% in pp collisions to about 6.5% in central Pb–Pb collisions [155], for minimum ionizing particles crossing the full detector.

3.3.3 Time of Flight (TOF)

The Time Of Flight detector (TOF) [159] measures the time spent by particles to travel from the collision point to the TOF radius. It covers the full azimuth and the pseudorapidity interval $|\eta| < 0.9$, except for the region $|\eta| < 0.12$, to avoid covering the photon spectrometer with more material. The TOF detector has a cylindrical shape, covering polar angles between 45 degrees and 135 degrees over the full azimuth. The detector is composed of 18 sectors in azimuthal angle (see Fig. 3.8) and 5 segments in the direction of the beam axis. Multigap Resistive-Plate Chamber (MRPC) technology is used to build the TOF [156]. This is a stack of resistive glass plates. A high voltage is applied to the external surfaces of the stack. Further out there are pickup electrodes. A charged particle ionizes the gas and the high electric field amplifies this ionization by an electron avalanche. The resistive plates stop the avalanche development in each gap. They are however transparent to the fast signal induced on the pickup electrodes by the movement of the electrons. The total signal is the sum of the signals from all gaps (the reason for many gaps is to achieve high efficiency), whereas the time jitter of the signal depends on the individual gap width (the reason for narrow gaps is to achieve good time resolution). The detector element is a long strip with an active area of 7.4 $\times$ 120 cm^2. It has 96 readout pads of 2.5 $\times$ 3.5 cm^2 arranged in two rows. It consists of 2 stacks of glass, each with 5 gas gaps of 250 μm.

Spacers made of nylon fishing line keep the distance between the glass plates fixed. The time resolution of the TOF MRPC is about 50 ps and its efficiency reaches 99.9 %.

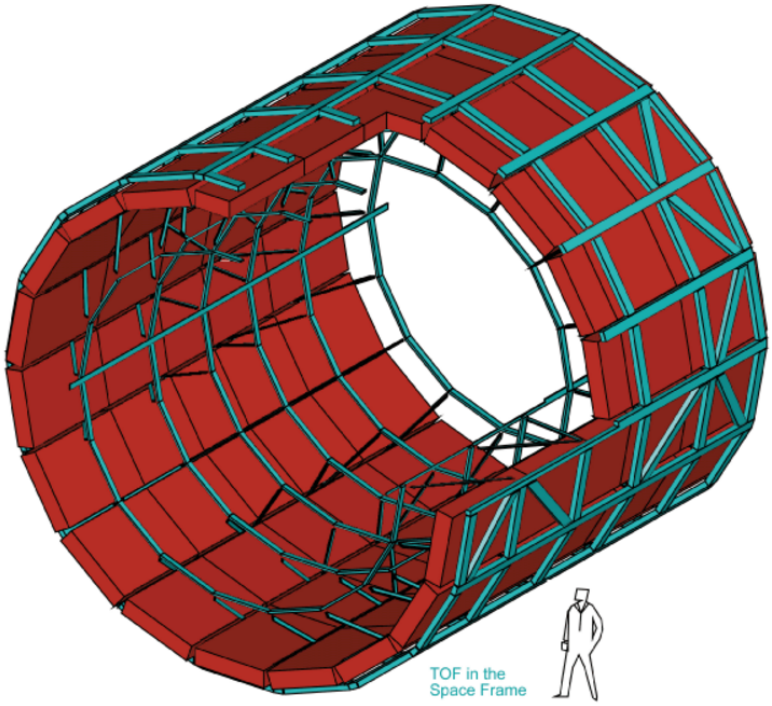

Figure 3.8: Schematic view of the ALICE TOF.

The starting time is provided by the T0 detector [160], a fast scintillator placed at forward rapidity. The T0 consists of two arrays of Cherenkov counters, T0A and T0C, placed on opposite sides of the nominal interaction point. A weighted average is performed when both detectors have measured the start time [161]. If a measurement from only one part of the T0 is available, the time has to be corrected for the primary vertex z position obtained using the SPD. Another option to estimate the collision time is to use a χ^2-minimization procedure based on the arrival time of all the particles at the TOF detector. Using one of three possible mass hypothesis (pion, kaon or proton mass) for each track, different collision times can be calculated as the weighted average of the differences between the measured arrival times of all the particles and the expected times of flight

for the chosen mass hypothesis. The final collision time is obtained as the value which minimizes the weighted sum of the squared differences between the expected time of flight for a chosen mass hypothesis and the arrival time in TOF corrected by the collision time corresponding to the set of mass hypothesis chosen. In both cases, the weights are given by the inverse of the sum of the time resolution of the TOF detector and the uncertainty on the expected time of flight for the chosen mass hypothesis. The last option is to use the bunch crossing time from the LHC. A detailed description of the determination of the event collision time can be found in [161]. TOF measures the time of flight of particles with an overall resolution ranging from about 80 ps (in Pb–Pb collisions) to about 120 ps (in pp collisions) [159].

3.3.4 Other detectors

Besides the central barrel detectors, in the forward region of the ALICE experiment there are the forward detectors and many other detectors which give complementary information or have been specifically dedicated to some particular analyses. The forward detectors are installed at small angles to the beam and are used for timing information, trigger and centrality estimation. These include fast scintillators, calorimeters, Cherenkov and silicon detectors. The forward detectors (FWD) serve as centrality estimators, and thus are particularly useful for the analysis of this thesis.

- T0 Detector: It consists of 2 arrays of PMTs equipped with Cherenkov radiators [160]. The arrays are installed on the opposite sides of the interaction point, covering the pseudorapidity ranges: $-3.3 < \eta < -2.9$ and $4.5 < \eta < 5$. The main task of $T0$ is to supply fast timing signals which will be used in the L_0 trigger for ALICE, to send a signal to activate the TRD and to deliver collision time reference for the TOF detector. The time resolution of T0 is better than 50 ps (σ). The triggering efficiency varies from about 50% for pp collisions up to 100% for A–A collisions. $T0$ is also used to give a fast evaluation of the multiplicity using a pre-programmed 3-grade scale (minimum bias, central and semi-central).

- FMD: It consists of 51200 silicon strip channels distributed over 5 ring counters of two types which have 20 and 40 sectors each in azimuthal angle, respectively [160]. The main function of the Forward Multiplicity Detector (FMD) system is to provide (offline) precise charged particle multiplicity information in the pseudorapidity range $-3.4 < \eta < -1.7$ and $1.7 < \eta < 5.0$. The FMD also allows the study of multiplicity fluctuations on an event by event basis.

- V0 Detector: The V0 detector consists of two arrays of scintillator counters (named V0A and V0C), installed on both sides of the ALICE collision vertex at small angles [160]. The V0A device is installed on the positive z-direction at a distance of about 340 cm from the IP, while the V0C is installed on the negative z-direction along the absorber nose at a distance of 900 mm from the IP. The counters cover the pseudorapidity ranges $2.8 < \eta < 5.1$ (V0A) and $-3.7 < \eta < -1.7$ (V0C). Each array consists of 32 counters distributed in 4 rings. Each of these rings covers $0.5 - 0.6$ unit of pseudorapidity and is divided into 8 sectors (45 degrees) in azimuth. This detector system has several functions. It provides minimum-bias (MB) triggers for the central barrel detectors in pp and Pb-Pb collisions, it serves as centrality estimator via the measurement of charged particle multiplicity and is used to reduce the background of beam gas interactions.

- ZDC: The Zero Degree Calorimeters (ZDCs) are hadronic calorimeters, made by a stack of heavy metal plates grooved to allocate a matrix of quartz fibers (called "spaghetti calorimeters"), which detect the energy of the spectator nucleons [162]. This is used to determine the overlap region of the two colliding nuclei, i.e. the centrality. It is composed of four calorimeters, two to detect protons (ZP) and two to detect neutrons (ZN). These are located 115 meters away from the interaction point on both sides, exactly along the beam line.

3.4 ALICE Upgrade

The ALICE experiment has planned upgrades of several subsystems and the online/offline system for data acquisition and processing during the Long Shutdown 2 (LS2) 2019-20 of the LHC, presently in progress at the time of writing. This will enable the experiment to do high precision measurements of rare probes from high to very low transverse momentum. Excellent tracking efficiency and track resolution down to low p_{T}, gaining a factor 100 in the available data with minimum bias trigger compared to the present program while preserving particle identification capabilities are the key elements of the upgrade. The large increase in the available data will be achieved by reading out Pb–Pb interactions at maximum rate of 50 kHz, corresponding to an instantaneous luminosity of $6 \cdot 10^{27}$ cm^{-2}s^{-1}. This will enable ALICE to accumulate ten times more integrated luminosity (more than 10 nb^{-1}) and hundred times larger data sample (about 10^{11} collisions) than what has been obtained so far. This necessitates the upgrade of the subdetector readout electronics and the entire online/offline system. A detailed description of the ALICE upgrade plans is presented in the Letter of Intent [163]. The upgraded detector is the outcome of a well-coordinated global collaboration effort that brought together more than 35 institutes and research centres from 15 countries. Following an intense 5-years R&D programme, the successful prototyping and production of the different parts of the detector took place in 2017-2019. The assembly and tests of the upgraded detectors took place in 2019-2020 and starting from mid 2020 the final phase of installation and commissioning started. The TPC and the ITS have undergone major modifications to meet the requirements for the period after LS2. In the following, the upgrade of these two subdetectors will be further described.

3.4.1 Physics objectives of the Upgrade

The scientific goals of the upgraded ALICE detector are described in a comprehensive Letter of Intent [163]. They are aimed at improving measurements for understanding heavy-quark production at low transverse momentum, mechanisms of quarkonium production and interaction in

the QGP, initial temperature and partonic equation of state, possible effects of chiral symmetry restoration, parton energy loss, medium modification and its dependence on properties of the parton and the QGP, and exotic hadronic states. To accomplish these, the following measurements will be undertaken in the central barrel of the ALICE detector:

- Yields and azimuthal distributions of hadrons containing heavy quarks (c, b) to study the mechanism of heavy-quark thermalization in the QGP.
- Production of quarkonia at low p_{T}, in particular the study of their possible dissociation and regeneration mechanisms in the QGP.
- Low-mass dielectron production to extract information on early temperature and the partonic equation of state, and to characterize the chiral phase transition.
- Jets and jet correlations, in particular their structure and particle composition, to study the mechanism of partonic energy loss in medium and its dependence on parton color-charge, mass and energy.
- The production of nuclei, antinuclei and hypernuclei as well as exotic hadronic states such as the H-dibaryon.

These measurements require excellent charged-particle tracking capabilities as well as a variety of PID techniques in the central barrel, down to the lowest possible p_{T}. Measurements at low transverse momenta typically imply small signal-to-background ratios, which limits the applicability of standard low level triggering schemes. As a consequence, the detectors and readout systems must allow to operate at very high readout and data acquisition rates in order to collect sufficient data.

3.4.2 Upgrade of the ITS

During the long shutdown of the LHC in 2019-20 the present Inner Tracking System of the ALICE experiment based on silicon pixel, silicon drift and silicon strip detectors, has been entirely replaced by a new tracker

using novel monolithic silicon pixel chips. This new tracker will significantly enhance heavy flavour measurements, reaching precisions which are out of reach for the present system, e.g. charmed baryons measurements, such as the Λ_C, and will allow studying hadrons containing a beauty quark.
The present ITS has six layers and covers a radius from 3.9 cm up to 43 cm. At radii larger than 43 cm the tracking information is provided by the TPC. The two innermost layers of the ITS are equipped with hybrid silicon pixel detectors with an average material budget of 1.14% X_0 per layer. While the present detector is fully meeting the requirements for the present run, the precision measurements of rare probes over a large momentum range foreseen after LS2 require significant improvement in tracking and readout speed. Therefore, the present ITS has been removed during LS2 and replaced with a new, 7-layer pixel detector using monolithic silicon pixel chips with a total surface of about 10 m^2. The new tracker will provide an improved pointing resolution in rϕ and z, decreasing the present values by a factor 3 and 5, respectively, to about 40 μm for a p_T of 500 MeV/c. Each of the seven layers will be constructed using 50 μm and 100 μm thin silicon chips on a very light weight carbon fibre based support structure for the innermost and the outer layers respectively. The material budget for the first three layers corresponds to 0.3% X_0/layer while the four outer layers will have an average material budget of 1% X_0/layer. The innermost layer will be placed at 23 mm radius, compared to presently 39 mm. The new ITS will also enhance the readout capabilities, allowing data readout and recording at interaction rates in excess of 50 kHz, the expected Pb–Pb interaction rate at the LHC after Run 2. Indeed, the readout rate of the new ITS will increase from presently 1 kHz to 50 kHz for Pb–Pb collisions and 400 kHz for pp collisions. This increase in readout speed, together with the deployment of a new data acquisition system that will allow recording all collisions, translates to an increase by about two orders of magnitude in the collectible minimum-bias data compared to the present ALICE setup, thus matching the expected event rate for Pb–Pb collisions after LS2.

A schematic view of the new ITS is shown in Fig. 3.9. The new

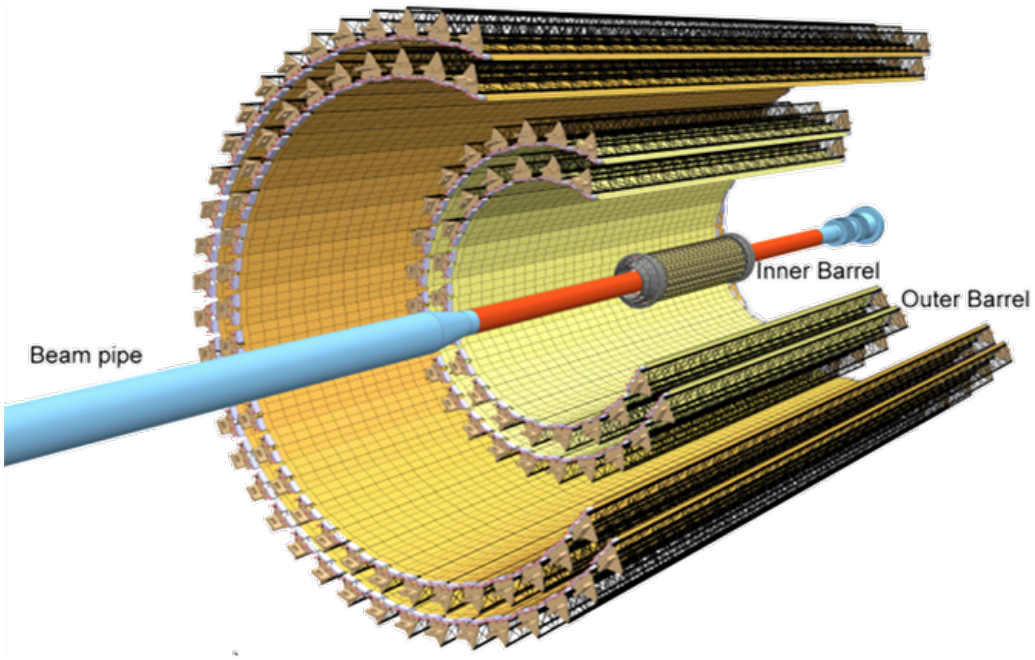

Figure 3.9: A schematic layout of the ITS after the Upgrade carried out during LS2.

ITS is an all-pixel silicon detector based on CMOS[4] monolithic active pixel sensor (MAPS) covering the mid-rapidity ($|\eta| < 1.3$) region. In the MAPS technology both the sensor for charge collection and the readout circuit for digitization are hosted in the same piece of silicon instead of being bump-bonded together. The chip developed by ALICE is called ALPIDE [164], and uses a 180 nm CMOS process provided by Tower Semiconductor. With this chip, the silicon material budget per layer is reduced by a factor of 7 compared to the previous ITS. The ALPIDE chip is 15×30 mm^2 in size containing more than half a million pixels organized in 1024 columns and 512 rows. Its low power consumption ($<$ 40 mW/cm^2) and excellent spatial resolution ($\sim$5 μm) are perfect for the inner tracker of ALICE.

Thus, the new ITS consists of seven cylindrical layers of ALPIDE chips summing up a total area of 10 m^2 and 12.5 billion pixels. The pixel chips

[4]Complementary Metal-Oxide Semiconductor.

are installed on staves with radial distances ranging from 22 mm to 405 mm from the interaction point. The beam pipe is also newly designed with a smaller radius of 18.6 mm, allowing the first detection layer to be placed closer to the IP at a radius of 22.4 mm compared to the presently 39 mm.

The improved performance of ITS, in momentum and pointing resolutions as a function of p_{T}, as well as the efficiency as a function of transverse momentum are shown in Fig. 3.10 in comparison with the performance of the present ITS.

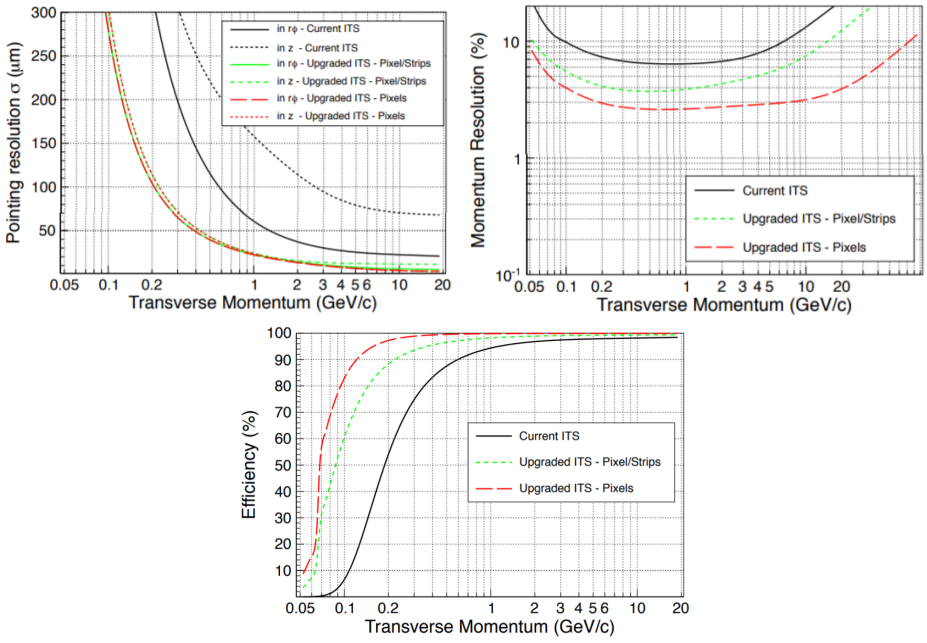

Figure 3.10: *Top*: Pointing resolution to the vertex (left) and momentum resolution (right) of charged pions as a function of the transverse momentum for the current ITS and the upgraded ITS (stand-alone ITS). *Bottom*: Tracking efficiency of charged pions for the current and upgraded ITS for the ITS stand-alone.

3.4.3 Upgrade of the TPC

The main objective of the TPC upgrade is to provide sensitivity to a minimum-bias interaction rate of 50 kHz in Pb–Pb collisions, as foreseen for LHC operation in Run 3 and beyond. This goal requires elimination of the intrinsic trigger rate limitation of the original MWPC-based TPC [158]. The limitation to about 3 kHz was imposed by the operation of an active ion gating grid, which is used to collect ions from the amplification region and prevent them from drifting back into the drift volume, where they would lead to substantial space-charge distortions of the drift field. Further limitations in MWPC-based readout chambers arise from space-charge effects at the amplification wires and ion tail accumulation, both resulting in substantial rate-dependent non-linearities of the signal response. Despite the tightened operational demands, the ambitious ALICE physics program for Run 3 and Run 4 does not allow a degradation with respect to the excellent momentum and $\mathrm{d}E/\mathrm{d}x$ resolution of the original TPC. The design considerations emerging from these challenging requirements and their technical solutions were worked out in an extensive R&D program [165,166] and will be briefly outlined below.

The present TPC MWPCs, 72 in total, have now been replaced by detectors based on Gas Electron Multipliers (GEM) [167], a micro-pattern structure developed at CERN. These new devices, together with new readout electronics that features a continuous readout mode, will allow ALICE to record the information of all tracks produced in lead–lead collisions at rates of 50 kHz, producing data at a staggering rate of 3.5 TB/s.

Operation of the TPC at a collision rate of 50 kHz implies that on average five collision events pile up within the TPC readout time window of about 100 μs, as given by the typical electron drift time over the maximal drift length of 2.5 m. This excludes triggered operation and defines the need for continuous readout, demanding novel gas amplification techniques which provide sufficient ion blocking without an active gate. The requirement to keep the ion-induced space-charge distortions at a tolerable level leads to an upper limit of 2% for the fractional ion backflow, i.e. the ion escape probability per effective electron-ion pair produced in the gas amplification stage, at the operational gas gain of 2000 in a Ne-CO_2-N_2 gas mixture. At the same time, the readout system must ensure

that the $\mathrm{d}E/\mathrm{d}x$ resolution of the TPC is preserved, which translates into a required local energy resolution better than 14% at the ^{55}Fe-peak [166]. GEMs provide a viable solution to this challenge. They can be easily stacked in layers, allowing separation of several amplification stages. After a careful optimization of the gain share among the GEMs and the electric transfer fields between them, the drift path of back-drifting ions that emerge from subsequent layers can be efficiently blocked.

3.5 Particle identification

Particle IDentification (PID) is vital in numerous analyses performed in heavy ion collisions [168]. In particular, light (anti)nuclei studies with nuclei which are not as abundantly produced in collisions as pions are extremely sensitive to the track selection. On one hand, a high-purity sample is essential to obtain reliable results. On the other hand, there is a need to collect as big amount of particles of interest as possible since the abundance of light (anti)nuclei is suppressed by roughly three orders of magnitude for each additional unit of mass number A.
In this analysis the approach used to perform the particle identification is the nσ method. It can be applied for the detectors with a Gaussian response function. The nσ observable is defined as:

$$n\sigma = \frac{S - S(H_i)}{\sigma} \tag{3.6}$$

where S is the measured signal, $S(H_i)$ is the expected signal for a hypothesis of the i-type particle (which in our case is estimated using the Bethe-Bloch equation), and σ is the resolution of the detector. A particle is identified to be of an i-type once the nσ value computed using eq. 3.6 is smaller than the assumed n value which defines how rigorous the PID selection is. For instance, the notation "3σ cut" denotes that $|\mathrm{n}\sigma| < 3\sigma$ for a given detector and a specific particle. The specific value of n depends on the desired precision and amount of data required for a given analysis. The larger the n value is, the more particles are selected, but simultaneously the probability of false identification increases. For the analysis of this thesis, (anti)deuterons are identified up to a transverse

momentum of 1.2 GeV/c using only the specific energy loss in the TPC, since the (anti)deuteron signal is well separated from that of other particles only in the low momentum range. For higher transverse momentum values, due to the contamination of other particle species in the TPC signal, the velocity information from the TOF detector is in addition used for the (anti)deuteron identification. On the contrary, (anti)^{3}He nuclei are very well identified using only the specific energy loss inside the active volume of the TPC. In the following, the particle identification methods used in the relevant detectors for the analysis of this thesis, TPC and TOF, are further discussed.

3.5.1 PID in TPC

For the analysis of this thesis, both (anti)d and (anti)^{3}He are identified measuring the ionisation energy loss per unit distance (dE/dx) in the TPC region. When a charged particle passes through the medium (in the TPC case, a mixed gas), it ionizes the molecules and atoms of the medium along its path. Ionization causes continuous energy loss of the charged particle. The average energy loss dE/dx, is different for different particles, and is described by the Bethe-Bloch formula:

$$\frac{dE}{dx} = -\frac{4\pi}{m_e c^2}\frac{nZ^2}{\beta^2}\left(\frac{e^2}{4\pi\epsilon_0}\right)^2\left[ln\left(\frac{2m_e c^2\beta^2}{I(1-\beta^2)}\right) - \beta^2\right] \tag{3.7}$$

in which $\beta = v/c$ (v is the velocity of the particle, and c is the speed of light in the vacuum), E is the energy of the particle, x is the distance traveled, Z is the charge of the particle, e and m_e are the charge and mass of the electron, n is the electron density of the target, and I is the mean excitation potential of the target. Since the energy loss depends on the charge and momentum of the incident particle, the energy loss information can be used to distinguish or identify different particles. In the ALICE experiment, the momentum (p) of the particle is calculated using the applied magnetic field (B) information and the curvature of path travelled by the charge particle in the TPC region. This calculation assumes that the particle is of unitary charge ($|Z| = 1$). Thus, the expected energy loss (dE/dx) of a certain kind of particle is given by a function named *Bichsel function*, which is a modified Bethe-Bloch function with

$|Z|$= 1 in Eq. 3.7. This is helpful in identifying particles like π, k, p and also d having unitary charge. However, for (anti)nuclei with charge $|Z| > 1$, as for ^{3}He, some modification is needed. Therefore, particles with charge $|Z| > 1$ are converted into the unit charge before using the Bichsel function to make their $\mathrm{d}E/\mathrm{d}x$ predictions. Figure 3.11 shows the specific energy loss ($\mathrm{d}E/\mathrm{d}x$) as a function of rigidity (momentum/charge) for the TPC tracks in p−Pb collisions at $\sqrt{s_{\mathrm{NN}}}$ = 5.02 TeV. Thanks to its performance, the TPC can identify light nuclei and antinuclei like d ($\bar{\mathrm{d}}$), t ($\bar{\mathrm{t}}$) and ^{3}He ($^3\overline{\mathrm{He}}$) over a wide momentum range as shown in the figure. The solid curves represent the expected values of Bethe-Bloch function for different particles.

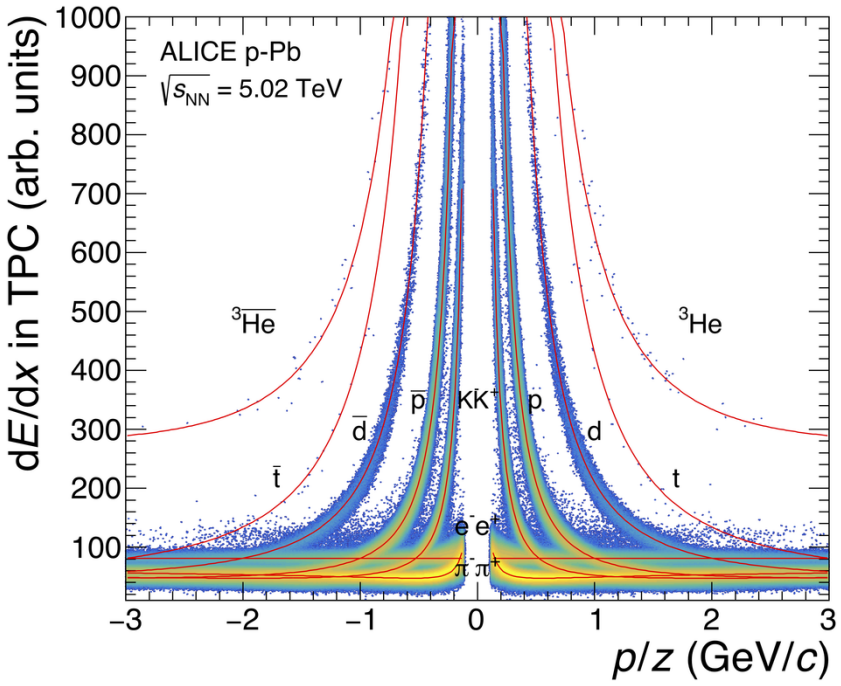

Figure 3.11: Specific energy loss of particles traversing the TPC volume as a function of their rigidity p/Z in p−Pb collisions at $\sqrt{s_{\mathrm{NN}}}$ = 5.02 TeV. The solid red lines represent the expected detector response for different particle species [169].

3.5.2 PID in TOF

The time of flight (t_{TOF}) measured by the TOF system, complemented with the measurement of the track length L and momentum p, provided by the tracking detectors, is used to calculate the particle mass:

$$m = p \cdot \frac{t_{TOF}}{L} \sqrt{1 - \frac{L^2}{c^2 t_{TOF}^2}} \tag{3.8}$$

The procedure which is actually used in ALICE is to compare the time-of-flight measured by the TOF for a given track with the expected values obtained using different mass hypotheses for the particle, as discussed in Sect. 3.3.3. The difference between the measured and the expected time of flight for a given mass hypothesis is expressed, as usual, in units of σ. Using the time of flight and the total length of the track, the velocity of the particle can be calculated and compared to the expected one for a given particle species. The distribution of the particle velocities compared to the speed of light (β) as a function of the particle momentum obtained in p–Pb collisions at $\sqrt{s_{\rm NN}}$ = 8.16 TeV is reported in Figure 3.12. Despite the background coming from incorrect assignment of TOF clusters to a track, this method allows us to distinguish different particle species. The mismatch background is strongly dependent on the track density in the event. The particle identification information provided by the TOF detector complements the particle identification capability of the TPC, and therefore it is crucial to identify light (anti)nuclei. In this analysis, the $n\sigma_{\rm TOF}$ procedure is defined as follows:

$$n\sigma_{\rm TOF} = \frac{(time_{\rm hit} - startTime) - time_{\rm exp}(p, m, L)}{\sigma_{\rm PID(TOF)}} \tag{3.9}$$

being $\rm time_{hit}$ the time of each hit recorded by the detector, startTime the start time of the collision, given by the T0 detector (see Sect. 3.3.3 for more details on the start time estimate) and $\rm time_{exp}$ the experimental measurement of time, using the momentum, mass and track length information.

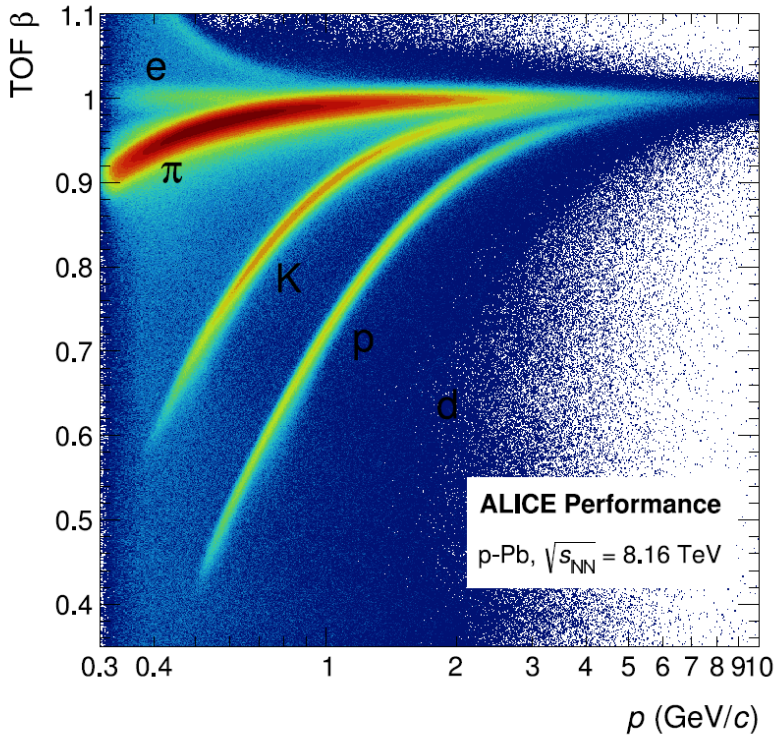

Figure 3.12: The distribution of the velocity, expressed as a fraction β of the speed of light, measured by the TOF detector is shown as a function of the particle momentum measured in p–Pb collisions at $\sqrt{s_{\mathrm{NN}}}$ = 8.16 TeV. The bands belonging to the different particle species are labeled with the particle names. The background is coming from mismatched hits in the TOF detector.

3.5.3 Bayesian approach

The particle identification methods in ALICE make use of the Bayesian approach. The Bayesian approach is based on the probability P of a particle to belong to a certain species i (i = e,π,μ, k, p) which can be easily calculated [168]. If $\left(\frac{dE}{dx}\right)_{\mathrm{meas}}$ and p are the measured TPC $\mathrm{d}E/\mathrm{d}x$ signal

and momentum, the probability for the species i is:

$$P(i) = \frac{1}{\sqrt{2\pi\sigma_{dE/dx}}} \cdot exp\left(-\frac{\left(\left(\frac{dE}{dx}\right)_{meas} - \left(\frac{dE}{dx}\right)_{fit} \right)^2}{2\sigma^2_{dE/dx}} \right) \tag{3.10}$$

The obtained probabilities P(i) can contribute to a combined Bayesian approach of PID. In this context, the P(i)s are referred to as *detector response probabilities*. In the Bayesian context, these probabilities are weighted with the so-called priors C(i) which describe the relative concentrations of particle species. They have to be determined for each analysis individually as they are dependent on the applied selection criteria. Then the probability *w(i)* of a particle to be of type i is given by:

$$w(i) = \frac{C(i) \cdot P(i)}{\sum_{k=e,\pi,\mu,K,p} P(k) \cdot w(k)} \tag{3.11}$$

This ansatz also allows combinations of the PID information from several detectors. The overall detector response probability $P_{tot}(i)$ is – under the assumption of independent measurements – the product of several single detector response probabilities:

$$P_{tot}(i) = P_{TPC}(i) \cdot P_{ITS}(i) \cdot ... \cdot P_{TOF}(i) \tag{3.12}$$

Nevertheless, the Bayesian PID has the drawback that the efficiency of the PID selection often cannot be easily determined and that the determined probabilities are very sensitive to eventual imperfections of the calibration.

Chapter 4

Data acquisition and event reconstruction

Collisions between oppositely circulating particles at the LHC occur at higher energies and rates than ever before. The amount of charged particles produced in high-energy collisions increases as a function of the centre-of-mass energy of colliding particles, hence a large number of particles is created at LHC energies. These particles travel through the detectors and produce several signals which are then used in the reconstruction of their trajectories and in the particle identification. Due to a large geometrical coverage, complex and sophisticated composition and fine granularities of modern particle detectors are needed. Large numbers of signals are produced for each particle, thus the LHC experiments at CERN generate colossal amounts of data, corresponding to roughly 30 petabytes every year. In order to efficiently cope with such a huge wealth of information, the LHC experiments have developed highly advanced data handling technologies, which include high efficiency trigger, data acquisition (DAQ) systems and data archive, which are further described in this Chapter. Moreover, in this Chapter the offline event selection, the Analysis Framework and the track reconstruction are discussed.

4.1 Trigger and data acquisition

At every bunch crossing, the Central Trigger Processor (CTP) receives the signal from the triggering detectors and decides, within less than 1 μs from the collision, whether to collect the data from the collision event and sends its decision to each detector Front End Electronics (FEE) via the Detector Data Links (DDL) [156]. In the case of a positive decision, the data collected by each subdetector are sent to a cluster of 300 computers, called Local Data Collectors (LDC). After a check of their integrity, data are processed and assembled into sub-events and sent over the second layer of computers, the Global Data Collectors (GDC). This is a cluster of 40 computers which are responsible for the event construction, i.e. each of these computers receives the event fragments by the LDC and builds a full event, which is sent to a temporary storage site in the experimental pit called Local Data Storage (LDS). Afterwards, data are moved to the Permanent Data Storage (PDS) at the CERN computing center, and eventually published via the GRID infrastructure for the offline physics analysis.

4.1.1 The ALICE Trigger System

Virtually, all collision events contain physics information that can be extracted by the offline analysis. In reality, not all events that are registered by the data acquisition system fulfill the quality requirements for the offline analysis. The trigger is a system which decides whether to collect data from a given collision event according to some specific criteria. The role of the trigger is to reduce the amount of data to be handled by the DAQ system by applying online filters which reject non interesting events before they are stored in the system. This is needed not only for a more efficient data recording but also to fit the available storage bandwidth, defined as the amount of data that can be transmitted in a given amount of time.

The *Central Trigger Processor* (CTP) receives the trigger input from the triggering detectors and sends the trigger signal (accept or reject) to the readout system of the detectors via the *Local Trigger Unit* (LTU), which is the interface between the CTP and the readout system.

The ALICE trigger system is a three-level system: the CTP can receive up to three consecutive trigger inputs (called L0, L1 and L2) and to each of them it can respond by sending trigger signals to the readout system. The first decision is made at 1.2 μs after the event (L0), L1 decision comes after 6.5 μs and L2 trigger is issued after 88 μs.

4.1.2 The High Level Trigger

The data flow that passes the L2 trigger can easily reach up to 25 GB/s. This can be further reduced by the *High Level Trigger* (HLT) [170] to about 1.25 GB/s. The HLT receives a copy of the data that are sent to the DAQ by the CTP (after passing the L2 trigger) and does a full online event reconstruction using a large farm of computers made up of 1000 multiprocessor nodes. The data are sent to several processing layers and analyzed online using automatic algorithms for specific pattern recognition (track finding, jet reconstruction, etc.). The results are eventually forwarded to the final stage for the trigger decision. The size of selected events is reduced by using advanced data compression techniques, based on Huffman encoding [171], without losing the physics information contained in the event.

4.2 Offline Event Selection

The role of the offline event selection is to select the hadronic component of nucleus-nucleus interactions, excluding diffraction, by rejecting the machine-induced and physical background. The main components of the machine-induced background are represented by beam-gas inelastic interactions, where ions in the beam collide with residual molecules of gas inside the beam pipe, and interactions between the beam halo[1] with mechanical structures in the machine. This background component represents almost 25% of all selected events. The physical background is essentially represented by electromagnetic processes, where the electromagnetic field of one nucleus interacts with charged particles inside the other nucleus.

[1]Peripheral low-density region of the bunch of particles in the beam.

4.2.1 Machine Induced Background (MIB)

Beam-gas collisions can be rejected using the timing information from the V0 detectors [160]. These are two arrays of scintillators placed at different distances on either side of the interaction point along the beam axis (see Section 3.3.4). The bunch spacing (25 ns) is tuned such that two ion bunches cross at the geometric center of the ALICE experiment. During the crossing of two bunches, the following bunches are approaching the collision point from either side of the beam. Inelastic collisions can occur between these bunches and residual molecules of gas inside the beam pipe away from the nominal position of the interaction point. Such a collision produces a signal on the same side of V0, that is too early in time with respect to the signal coming from a beam-beam collision happening at $z = 0$. The timing information from V0 is used to set its time gate to trigger on beam-beam collisions.

Another source of machine-induced background are *parasitic collisions* involving debunched ions. The frequency of the radio-frequency (RF) accelerating cavities has to be an integer multiple of the revolution frequency for the particle to always see an accelerating electric field:

$$\nu_{\mathrm{RF}} = N \cdot \nu_{\mathrm{rev}} \tag{4.1}$$

The number N defines the number of RF buckets which can contain clumps of particles. Not all RF buckets are filled with ions: usually several buckets are not loaded with particles to form a gap in the circumference. The purpose of this gap is that in the dump process it takes a short but significant time to switch on the magnets which divert the beam from the LHC into the beam dump. During the circulation of the beams inside the LHC, ions can jump from a full bucket to a supposedly empty bucket. In the bunch crossing region collisions can happen between ions in the full bucket and ions in an empty bucket, that is displaced by one or more RF cycles. These collisions are displaced along the z-axis and only part of the event would be visible to the detector. These parasitic collisions can be rejected exploiting the correlation between the sum and the difference between the times measured in the neutron ZDCs (see Section 3.3.4).

These satellite collisions can also be rejected applying a cut on the reconstructed vertex z-coordinate since they happen outside the fiducial

region $|z_{vtx}| < 10$ cm. This cut is normally used in most of the analyses in order to guarantee uniformity in the detector response and avoid edge effects.

4.2.2 Physical Background

The cross section for electromagnetic (EM) processes at the LHC is very large (of the order of kbarn [155]), since it scales as the atomic number squared (Z^2). EM processes consist of photon-photon interactions, relevant only in ultra-peripheral collisions (see below Section 4.8 for the definition of collision centrality) and photon-nucleus interactions, which produce low multiplicity events of soft particles. This second class of processes is also relevant only in peripheral collisions.

4.3 Pile up

In high-luminosity colliders, such as at the LHC, there is a non-negligible probability that one single bunch crossing may produce several separate events, so-called *pile-up* events.
The first selection criterion applied to remove the pile-up is on the number of primary vertices reconstructed with SPD with more than n contributors, where n is a parameter of the selection [155]. From previous analyses, looking at the multiplicity dependence of the false positive pile-up tagging, the n parameter was set to 5 for events with more than 50 tracklets, to 3 for events with less than 20 tracklets and it was set to 4 for the remaining events. This method removes only the pile-up of collisions occurring either during the same bunch crossing or out of bunch pile-up within the SPD readout time (300 ns). The pile-up tagging method based on the SPD vertex finding is not able to resolve collisions spaced along the beam axis coordinate by less than 8 mm. In this case the pile-up is not detected and the two collisions are merged. Other selections that help reducing the effect of the pile-up background are based on the correlation of different centrality estimators. For instance, the outliers in the correlation between the centrality estimator V0M, based on the V0 detector (whose readout window is 25 ns), and CL0, based on the SPD clusters,

are interpreted as events with residual pile-up. Some outliers can be spotted also in the correlation between the V0M centrality estimator and the SPD tracklets. In order to suppress such outliers, a 5σ selection has been applied on the aforementioned correlations. Another visible effect due to the very high multiplicity events, for instance those containing two piled up central collisions, is in the distribution of the z-coordinate of the primary vertices. In such conditions the vertex finding algorithm using the reconstructed tracks fails to find the correct primary vertex. As a consequence, the distribution of the primary vertex position along the z-axis shows some spikes before the event selection and a large difference is seen between the reconstructed vertex position obtained with the SPD based method and the track based vertex finding algorithm ΔV_z. These discrepancies are filtered at the level of the event selection, picking only events where ΔV_z is less than $20\sigma_{\text{track}}$ and $10\sigma_{\text{SPD}}$, where σ_{track} and σ_{SPD} are the resolutions of the primary vertex computed with the track based and the SPD only vertex finding algorithms respectively.

In 2016 p–Pb collisions at $\sqrt{s_{\text{NN}}}$ = 8.16 TeV, analysed in this work, the interaction rate of the data taking was of the order of 100 kHz. Therefore, the fraction of pile-up events amounts to 2% of the total number of triggered events.

4.4 Data reconstruction

The data collected by the experiment contain all the necessary information for the reconstruction of the collision events in the format of digits (ADC counts) structured in ROOT trees [172]. Such a data format, called *raw data*, cannot be directly used in the analysis and needs to be processed in a first reconstruction pass. As a preliminary step, a local reconstruction takes place in each subdetector independently, i.e. without exchanging information with other subdetectors. During this stage, called *clusterization*, the digits are converted into clusters, which are sets of adjacent digits coming from the same active element of a detector presumably produced by the same particle. Clusters are then used for the track and vertex reconstructions. The output of the reconstruction framework is the Event Summary Data (ESD) which contains all information for the physics anal-

ysis. This is also structured in ROOT trees. ESDs contain all reconstructed tracks including their kinematic variables, secondary vertices, calibrated particle identification signals and global event properties. ESDs usually contain a lot more information than really needed, and running on these files makes the analysis more time consuming and more demanding in terms of computing resources. To make the data analysis faster and more efficient the information contained in the ESDs is filtered, retaining only the necessary variables and rejecting the redundant information. The files resulting from refiltering of the ESDs are called Analysis Object Data (AOD) and are approximately five times smaller in size than the original ESDs. Most of the analyses, including the work for this thesis, use AODs as input files, which is the recommended data format for any official analysis within the ALICE Collaboration. The detector responses, and particularly the signals used for particle identification, usually need to be recalibrated after the first reconstruction pass. This is due to non-uniformity of the experimental apparatus, space charge effects in the TPC, distortions, etc. Parametrized corrections of detector response are obtained, run by run, by a careful and detailed offline analysis. The reconstruction of raw data is repeated by implementing these corrections to get a new version of ESDs (and AODs by refiltering), which will contain correctly recalibrated detector responses. This second reconstruction of raw data is called reconstruction pass 2. Sometimes additional recalibration or correction of detector responses are needed after the reconstruction pass 2, which lead to pass 3, pass 4, etc.
The results of this thesis are based on reconstruction pass 2 of the p–Pb datasets of periods LHC16r and LHC16s.

4.5 Analysis framework

The software used for data reconstruction, simulation and off-line analysis is an Object-Oriented ROOT-based framework, written in the C++ programming language. The software is divided into two main substructures:

- AliROOT: This is the core of the software which contains the ROOT fundamental libraries and the ALICE specific libraries and tools

used for data reconstruction, simulation and analysis [173].

- AliPhysics: This is the analysis-oriented part of the framework, which contains specific user analysis tasks and more complex and structured packages used by the analysis groups.

ALICE data and the output of simulations are published and made available for the analyzers by ALIEN (ALICE ENvironment) via the GRID infrastructure. This is a network of thousands of computers and computer clusters, connected via the internet, holding a limited amount of data and used to run the analysis tasks producing small output files, which are eventually merged together by the virtual analysis manager. This infrastructure has been created in order to efficiently handle huge amounts of data which would be impossible to store and analyze using one single computer. The data analysis proceeds in parallel on the computers connected to the GRID. These are placed at different locations in research institutes and universities, making the process much faster and less demanding in terms of computer resources and memory consumption since each computer handles only a fraction of the total amount of data.

4.6 Monte Carlo Simulations

In high energy physics experiments, Monte-Carlo (MC) simulations are extremely useful in order to predict the behaviour of the systems which cannot be calculated analytically. To each experimental data set corresponds a MC-simulated data set, which allows to correct the data taking into account as many variables as possible.
Simulations are produced using event generators, which generate particles by simulating elementary processes or by using phenomenological hadronization models according to parametrized input distributions and particle ratios. Event generators simulate also particle decays based on real measurements of their branching ratios. The event generator widely used to simulate nucleus-nucleus collisions is HIJING (Heavy Ion Jet INteraction Generator) [174]. This combines a QCD-based model of jet production with the Lund string fragmentation model. A nucleus-nucleus collision is regarded as a superposition of multiple nucleon-nucleon col-

lisions, with no collective effects, in which parton shadowing effects are also taken into account. Stable particles or long-lived decay products of the generated particles are "transported" through the detector, simulating all processes which characterize the interaction between particles and the detector material, including ionization, excitation, bremsstrahlung or other physical processes such as photon conversion in the material or absorption. The propagation of particles through the detector, in the ALICE magnetic field, is simulated by GEANT3 or GEANT4 [175], depending on the MC production. The energy deposited by the simulated particles in the active elements of the detector is converted into digits, which are ADC counts, produced considering the real energy thresholds measured in the calibration and testing phase of the detectors during their construction and assembling. The signals produced by simulated particles traversing the experimental apparatus are treated on the same footing as real raw data, which are then reconstructed by the offline framework. Dead or noisy channels and blind areas of the detectors are also taken into account during the reconstruction phase, in order to reproduce the detector status in the simulation on a run-by-run basis. The output of the simulation contains reconstructed tracks and their measured properties, such as momentum and PID signals, together with the information on the real kinematics of the particles that have produced them.
In the MC production used for the analysis of this thesis, (anti)nuclei generated by HIJING are injected on top of the underlying event. For particle propagation and simulation of the detector response, the GEANT4 package is used.

4.7 Track reconstruction

The track finding in a very high track density environment is one of the most challenging tasks of the ALICE experiment [176]. Tracking in the ALICE central barrel is based on an inward-outward-inward propagation scheme which starts with the preliminary determination of the collision vertex using the ITS (see Sect. 3.3.1). Tracks are first reconstructed in the outer regions of the TPC, which is the main tracking detector, and are propagated inward to the ITS. Then tracks are propagated back from the

ITS to the outer layers of the TPC and extended further to match the outer detectors. Eventually, tracks are refitted inward down to the point of closest approach to the interaction vertex. Once tracks are reconstructed, the position of the primary vertex is determined with higher precision using fully reconstructed tracks. The determination of secondary tracks (originating from displaced vertices) and cascades concludes the tracking procedure in the central barrel. The steps of track reconstruction are described in further details in this Section.

4.7.1 Preliminary Vertex Determination

The primary vertex is the point where the collision occurs and from which the particles produced in the collision emerge. A preliminary determination of the primary vertex position can be done, already with quite high precision, using the SPD tracklets. These are defined as straight lines connecting pairs of clusters in the SPD layers, one cluster in each layer. The primary vertex is the space point where the maximum number of tracklets converge. This measurement is based on the straight line approximation of the particles trajectories. It is justified by the proximity of the two innermost layers of the ITS which makes the deviation between a curved and a straight trajectory negligible also for low momentum particles. Particles produced in the collision, together with their decay products due to strong and electromagnetic interactions, are referred to as "primary particles", while those produced by weak decays of primary particles or created in the interaction between particles and the detector material are called "secondary particles". These definitions strictly depend on the tracking capabilities of the ALICE detector, including the resolution in the measurement of the primary vertex. The vertex resolutions are reported in Chapt. 3.

4.7.2 TPC seed finding

Track reconstruction begins in the outer regions of the TPC where the track density is the lowest. The first step in the tracking procedure and the most time-consuming is the seed finding. Track seeds are sets of a few neighbor clusters, located in the outer layers of the TPC, roughly compat-

ible with a track, i.e. lying on a helix pointing roughly to the primary vertex. One of the most common algorithms used for seed finding is the combinatorial seeding [177]. This method searches for all pairs of clusters in the outer regions of the TPC, separated by few pad rows (usually no more than 20), compatible with a helix which can be projected down to the primary vertex. The main steps of the algorithm are the following:

- Loop over all clusters in the i^{th} pad row of the TPC.

- Loop over all clusters in the j^{th} pad row, with a number of rows $n \leq 20$ closer to the inner wall of the TPC, within a given window defined by the curvature of a track with minimum momentum above a certain threshold pointing down to the main vertex. Track parameters and their corresponding covariance matrix terms are calculated using the errors on the points and the uncertainty on the position of the primary vertex. This is the only step where a vertex constraint (not too strong) is applied. In the following tracking procedure, tracks are allowed to have any impact parameter at the primary vertex, both along the z direction and in the transverse plane.

- Using the calculated helix parameters and their covariance matrix the Kalman filter is applied starting from the outer cluster in the TPC to the inner one to find the clusters to be associated with the track. The Kalman filter is a simultaneous track recognition and reconstruction algorithm, which offers a natural way to take into account multiple scattering, the magnetic field non-homogeneities and energy loss. It allows the reconstruction of complicated decay topologies (such as cascades) and it provides an efficient way to match tracks between different detectors.

- If at least 50% of the potential clusters are correctly associated with a track candidate, the track is saved as *seed*.

The procedure is schematically sketched in Figure 4.1.

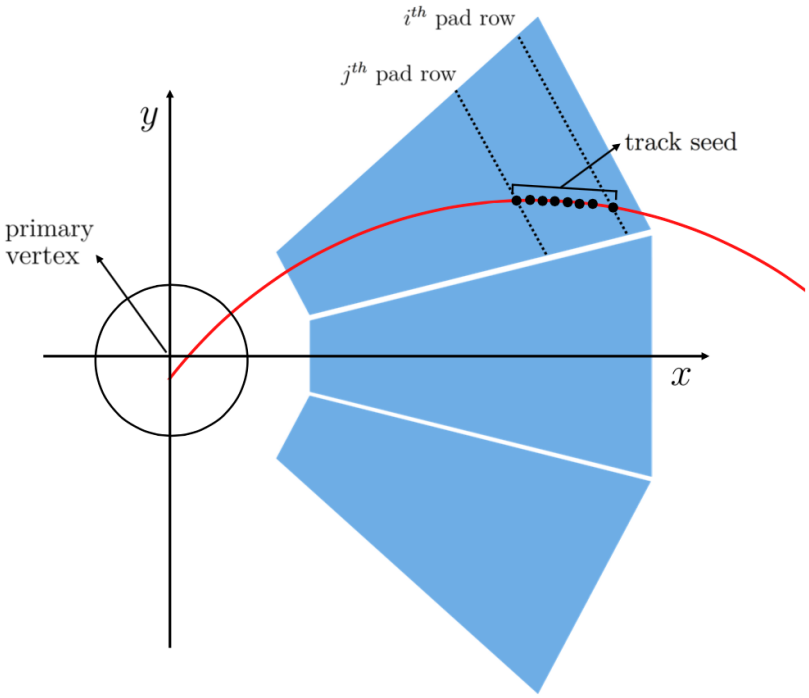

Figure 4.1: Schematic view of the combinatorial seeding algorithm.

4.7.3 Track Reconstruction in the TPC

Track seeds are propagated inward following the helical trajectory defined by the initial track parameters. Whenever a cluster, which satisfies a proximity cut, is associated with the existing track, the track parameters and their corresponding covariance matrix terms are updated. The cluster association criterion takes into account the energy loss and the Coulomb multiple scattering suffered by the particle for every track segment. These effects produce small variations in the track curvature. The particle mass, needed to calculate these corrections, is assigned based on the specific energy loss measured by the TPC and the track momentum. In case the information is not conclusive (especially at high momentum) the pion mass is assigned. Once the tracking in the TPC is complete, the algorithm does a preselection of the tracks checking some quality criteria. Tracks with less than 20 clusters and those missing more than 50% of the clusters expected for that track are rejected. If two tracks share a signif-

icant amount of clusters in the TPC (between 25% and 50%, depending on their momentum) the worse track, in terms of some quality parameters, is discarded. Tracks fulfilling these criteria are propagated further down for matching with the ITS. Track extrapolation to the ITS is a delicate task because the distance between the inner wall of the TPC and the outer layer of the ITS is rather large ($\sim$ 0.5 m) and the track density in the ITS is usually so high that there are always several clusters within the prolongation window defined by the multiple scattering. This is also the case between two ITS layers. This leads to a non-negligible probability of wrong cluster-track matching if just the criterion of minimal χ^2 is applied. For this reason, several prolongation hypotheses are built starting from clusters lying on the outermost layer of the ITS which give a χ^2 below a given threshold, and not just the one with minimal χ^2. Tracking in the ITS is performed in two passes, with and without the vertex constraint. Each track candidate is propagated down and, at each ITS layer, several further prolongation hypotheses are built considering all clusters within the window defined by multiple scattering. In summary, for each track entering the ITS from the TPC there is a *tree* of possible extensions, and the most probable candidate is eventually selected based on the quality of the whole track. When the ITS tracking is completed, all tracks are extrapolated to their point of closest approach to the primary vertex, and the back-propagation starts. Tracks are refitted by the Kalman filter in the outward direction using the points already associated at the previous stage. During the outward propagation, the track length integral and the time-of-flight for 5 particle hypotheses (electrons, muons, pions, kaons and protons) are updated at each step. When the back propagation in the TPC is complete, the track is extended outward to match a tracklet in the TRD and a cluster in the TOF. At this stage, the track length integration and the computation of the time-of-flight stops. The track is then propagated further out to match (possible) clusters in the EMCAL, HMPID and PHOS. The detectors located at radii larger than the TPC are not used to update the track parameters but only for particle identification purposes. The final stage of track reconstruction is the inward propagation and refit of the data points already found, starting from the outer layers of the TPC to the point of closest approach to the primary vertex. At this stage the track parameters, their covariance matrix terms and the curvature are

determined.

4.7.4 Final Vertex Determination

Global tracks, reconstructed in ITS and TPC, are used to find the position of the interaction vertex with higher precision compared to the procedure based on the SPD tracklets. Tracks are extrapolated to the point of closest approach to the nominal position of the beam line and the far outliers are removed. The distributions of the coordinates of the points of closest approach are then fitted using proper weights for the tracks to further reduce the contribution from tracks with large DCA. In low multiplicity events, to improve the precision in the determination of the transverse vertex position, the nominal beam position is also added as an independent fit parameter with errors corresponding to the transverse spread of the beam.

4.7.5 Tracking Performances

The tracking efficiency as a function of transverse momentum is defined as the ratio between the reconstructed tracks and the generated primary particles in the simulation. The track reconstruction efficiency at low momenta is limited by absorption in the material (the energy loss in the detector material causes the particles to spiral down because of their small curvature radius in the magnetic field), track bending in the magnetic field and particle decays. It rises from about 45% at 0.15 GeV/c to about 75% around p_{T} = 1 GeV/c [172]. These low momentum particles do not leave enough clusters in the TPC for the reconstruction. At higher momenta, the efficiency saturates at about 90% which is determined by the cluster loss in the dead zones between active sectors in the TPC. The tracking efficiency is almost independent on the occupancy, showing no substantial difference between different colliding systems and centralities. Indeed, Fig. 4.2 shows that the TPC tracking efficiency as a function of p_{T} has the same shape both for Pb–Pb collisions and for pp ones; thus the same behaviour can be taken into account for p–Pb collisions.

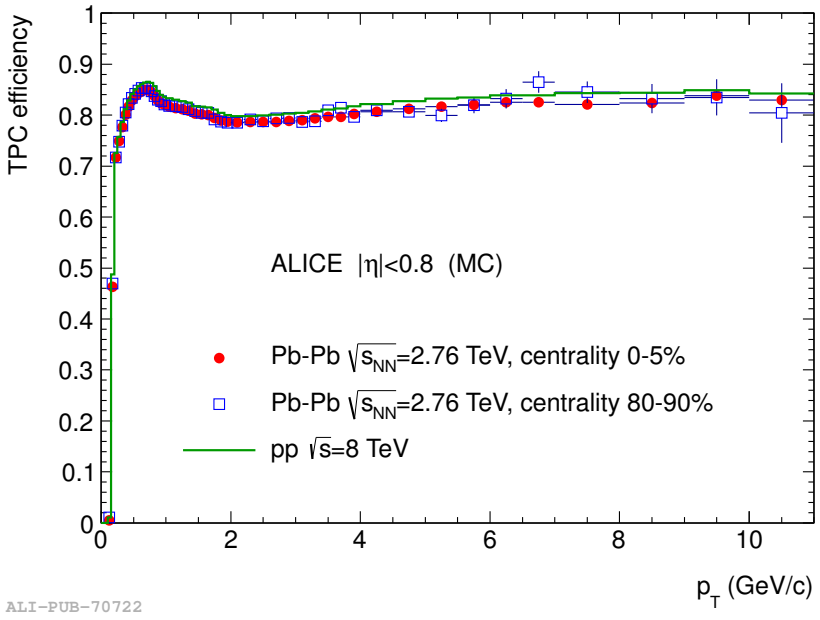

Figure 4.2: Tracking efficiency as a function of p_{T} for pp and Pb–Pb collisions (simulation). The tracking efficiency does not depend on the detector occupancy.

4.7.6 Secondary Tracks

The search for secondary tracks, i.e. those originating from particle weak decays or photon conversion in the material, is done among those tracks with a distance of closest approach to the primary vertex exceeding a given limit. Pairs of unlike-sign secondary tracks are then combined to search for V0 topologies. The position of the secondary vertex is determined by the point of closest approach (PCA) of the two unlike-sign tracks. The criteria used by the V0 finder algorithm to select the V0 candidates are:

- The distance of closest approach (DCA) between two tracks is requested to be less than 1.5 cm;

- The PCA is requested to be closer to the interaction vertex than the innermost hit in the ITS of both tracks;

- The cosine of the pointing angle, defined as the angle between the total V0 momentum and the vector connecting the primary to the secondary vertex, is requested to be larger than 0.9 (this cut is relaxed for V0 candidates with p_{T} below 1.5 GeV/c).

Two main algorithms for V0 finding are used by the ALICE reconstruction framework: the "offline" and the "on-the-fly" V0 finders. In the offline algorithm, secondary tracks are searched among global ITS-TPC tracks, propagated down to the primary vertex, and the track momentum is estimated at the PCA to the vertex. The energy loss corrections are therefore overestimated for these tracks since they are applied also for layers of the detector which were actually never crossed. Moreover, the track momentum is not estimated at the secondary vertex, which is the true production point. This causes a small bias in the measurement of the particle direction (Fig. 4.3). The *on-the-fly* algorithm works as part of the ITS tracker, having access to the track parameters at each tracking step in the ITS. In this algorithm, the pairing between unlike-sign particles to search for V0 topologies is done on-the-fly during the inward propagation. For each of these pairs, the track momenta are estimated at the point of closest approach between the two tracks, which is the closest point to the true secondary vertex.

4.8 Collision centrality

As already discussed in Sect. 1.5.2, it is natural to consider a heavy ion collision as the sum of the interactions between the constituent nucleons of the two colliding nuclei in a HIC. The relevant parameters in such a description are the number of nucleons participating in the interaction between the nuclei N_{part} and the number of binary collisions between two nucleons N_{coll}. These two parameters are correlated with the impact parameter of the collision b, defined as the distance between the directions of motion of the two approaching nuclei.

Two observables directly related to the centrality are the average charged-particle multiplicity and the energy deposited in the forward calorimeters by the spectators, called zero degree energy (EZDC). While the charged-particle multiplicity decreases monotonously with increasing impact pa-

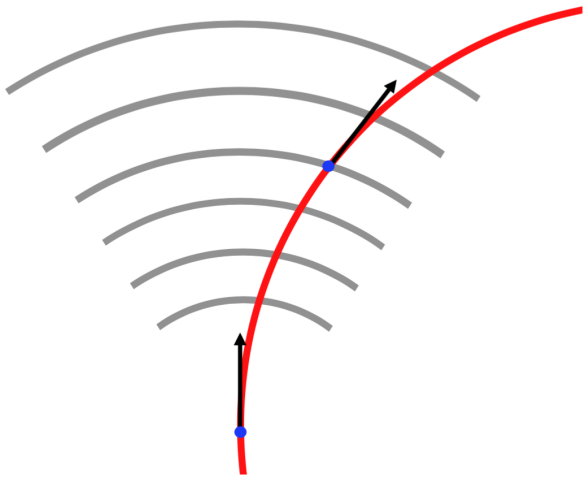

Figure 4.3: Sketch of the working principle of the offline V0 finder. If momentum is estimated at the point of closest approach to the primary vertex its direction is different from the one estimated at the true production point (in the 4^{th} ITS layer in this picture).

rameter, the zero degree energy does not always show a monotonous behaviour with the impact parameter: nuclear fragments with the same magnetic rigidity as the beam particles could be formed in the collision. These particles move inside the beam pipe curved by the magnetic field together with the beam particles and therefore are not detected by the forward calorimeters. The monotonic relationship between b and EZDC holds only for the most central collisions. For this reason, the zero degree energy is used as a reliable centrality estimator only when combined with another observable that is monotonically correlated with the impact parameter.

Based on this, the centrality is commonly expressed in centrality classes by fitting the distribution of the charged-particle multiplicity with a theoretical description obtained from a Glauber Monte Carlo simulation convoluted with a particle-production model which is based on a negative binomial distribution (NBD) [178]. The production model uses a two-component approach. One component for particles produced in hard initial scattering processes, which scale with N_{coll}. The rest of the particles are assumed to be produced in soft interactions and, thus, the num-

ber is proportional to N_{part}. The NBD-based model was chosen because it succeeds in describing the charged-particle multiplicity measured in high-energy proton-proton collisions over a wide range of rapidity [179]. This allows to define centrality classes as percentiles of the total integral of the charged-particle multiplicity distribution in Monte Carlo and data. Hereby, the most central collisions are identified with values close to 0% while the most peripheral ones belong to the percentile range close to 100%. This is indicated in Figure 4.4 where the amplitude measured in the ALICE V0 detector is used as a proxy for the charged-particle multiplicity. A more detailed discussion of the determination of the event centrality can be found in [180].

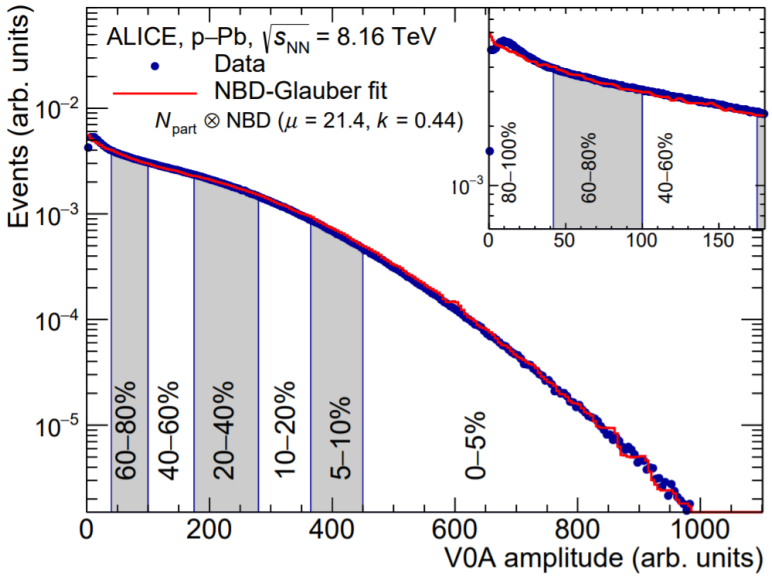

Figure 4.4: Distribution of amplitudes measured by the V0 scintillators fitted by NBD-Glauber. The centrality classes are indicated in the figure. The inset shows a zoom of the most peripheral region.

For the analysis subject of this thesis work, several centrality classes have been investigated for the measurement of (anti)deuterons, while the (anti)^{3}He analysis was performed in the multiplicity-integrated class, due to the limited amount of available data, as it will be further discussed in Chapt. 5.

Chapter 5

Analysis procedure

5.1 Event and track selection

The p–Pb data sample used for the analysis presented in this thesis consists in about 40 million events collected during the LHC running campaign at $\sqrt{s_{\rm NN}}$ = 8.16 TeV in 2016.
Two configurations of colliding beams were exploited, one corresponding to the proton beam travelling in the direction from V0A to V0C while ^{208}Pb ions circulated in the opposite direction (denoted by p–Pb), the other corresponding to a reversed direction of both beams (denoted by Pb–p).
To obtain a symmetric acceptance, all the events characterised by a primary vertex outside a fiducial region of $\pm$ 10 cm along the beam direction from the nominal collision point are rejected ($|V_z| < 10$ cm). Collisions with multiple primary vertices are tagged as pile-up events and rejected as well.
For the study of d and $\overline{\rm d}$, the sample is divided into four multiplicity classes, defined as percentiles of the V0A signal: 0-10%, 10-20%, 20-40% and finally 40-100%. For the ^{3}He analysis, instead, the integrated multiplicity class is used, due to the limited available data.
In order to select primary tracks of suitable quality, several track selection criteria are applied. (Anti)d and (anti)^{3}He candidates are selected in the pseudorapidity range $|\eta| < 0.8$. Tracks are required to have a minimum

number of clusters in the TPC, $N_{\rm cls}^{\rm TPC}$, of at least 70 out of a maximum of 159, and in the ITS, $N_{\rm cls}^{\rm ITS}$, of at least 2 with one cluster located in any of the two innermost ITS layers. The number of TPC clusters used in the $\mathrm{d}E/\mathrm{d}x$ calculation, $N_{\rm cls}^{\rm TPC}\,(\mathrm{d}E/\mathrm{d}x)$ is required to be larger than 50. Good quality of the track fit is also required, expressed by $\chi^2/N_{\rm cls}^{\rm TPC} < 4$ and a ratio of the number of TPC clusters attached to the track over the number of findable TPC clusters (accounting for track length, location, and momentum) larger than 80%. The contribution from secondary tracks is reduced by requiring an upper limit on the Distance of Closest Approach (DCA) to the primary vertex in the transverse plane ($\mathrm{DCA_{xy}} < 0.1$ cm) and in the longitudinal direction ($\mathrm{DCA_z} < 0.1$ cm). In this analysis, the production of primary (anti)deuterons and (anti)^{3}He nuclei are measured in the rapidity window $-1 < y_{\rm cms} < 0$ in the centre-of-mass system (cms). For asymmetric systems, such as p–Pb collisions, the cms and the lab system do not coincide. Indeed, since the energy per nucleon of the proton beam is higher than that of the Pb beam, the nucleon-nucleon system moves in the laboratory frame with a rapidity of –0.465. Therefore, a rapidity shift Δy=0.465 of cms with respect to the lab system is expected, so that the rapidity of each track in the lab system needs to be transformed into the cms system by the following relation:

$$y_{\rm cms} = y_{\rm lab} - 0.465 \tag{5.1}$$

For this analysis only tracks within $-1 < y_{\rm cms} < 0$ were selected.
The selection criteria are summarized in Table 5.1.

5.2 Raw spectra construction

5.2.1 Particle identification

(Anti)^{3}He nuclei are well identified using the specific energy loss inside the active volume of the TPC, over the entire momentum range 1.5 GeV/c $< p_{\rm T} <$ 6.0 GeV/c. In order to perform the identification, the expected average $\mathrm{d}E/\mathrm{d}x$ for (anti)nuclei, $\langle \mathrm{d}E/\mathrm{d}x \rangle$, is given by the Bethe-Bloch formula and the standard deviation of the distribution of $\mathrm{d}E/\mathrm{d}x - \langle \mathrm{d}E/\mathrm{d}x \rangle$, denoted $\sigma_{\mathrm{d}E/\mathrm{d}x}$, is the TPC $\mathrm{d}E/\mathrm{d}x$ resolution measured for (anti)nuclei.

Variable	Selection cut
$\|\eta\|$	< 0.8
y_{cms}	(-1, 0)
$n_{ITSclusters}$	>1
$n_{TPCclusters}$	>70
$n_{TPCdE/dxClusters}$	> 50
$n_{TPCCrossedRows}$	> 70
$n_{TPCCrossedRows}/n_{TPCFindableCls}$	> 0.8
$\chi^2/N_{\mathrm{cls}}^{\mathrm{TPC}}$	< 4
$\|DCA_{xy}\|$	< 0.1
$\|DCA_z\|$	< 0.1
$\|n\sigma_{TPC}\|$	< 3.0

Table 5.1: Track selection criteria applied for the present analysis.

In the following, this procedure will be addressed as nσ_{TPC} signal extraction, defined as follows:

$$n\sigma_{\mathrm{TPC}} = \frac{\frac{dE}{dx} - < \frac{dE}{dx} >_{nucleus}}{\sigma_{\frac{dE}{dx}}} \tag{5.2}$$

For the (anti)^{3}He identification, the d$E/$dx measured in the TPC is required to be within $3\sigma^{^3\mathrm{He}}_{\mathrm{d}E/\mathrm{d}x}$from the expected average for ^{3}He.
For the (anti)deuteron identification, two methods are used depending on the transverse momentum region, as discussed in Section 3.5. In the low p_{T} region the identification is performed using only the specific energy loss in the TPC, as for (anti)^{3}He, whereas for higher values of momentum, the combined information of TPC and TOF is used. For transverse momenta up to 1.2 GeV$/c$ the specific energy loss in the TPC gives a clean sample of (anti)deuterons by requiring a maximum deviation of $3\sigma^{\mathrm{d}}_{\mathrm{d}E/\mathrm{d}x}$ with respect to the expected signal of (anti)d. In order to reduce the number of tracks with a wrongly assigned TOF cluster, in the kinematic region of $p_{\mathrm{T}} > 1.2$ GeV$/c$ only the candidates with a d$E/$dx measured in the TPC compatible within $3\sigma^{\mathrm{d}}_{\mathrm{d}E/\mathrm{d}x}$ with the expected value of (anti)d are selected. Hence, the (anti)d signal is extracted by integrating the signal function in an asymmetric range centered at μ_0 (mean of the Gaussian signal), which is slightly different from zero because of small miscalibration effects of the TOF detector: $[-3\sigma_{\mathrm{TOF}} + \mu_0, +3.5\sigma_{\mathrm{TOF}} + \mu_0]$, being σ_{TOF}

the resolution of the time-of-flight measurement. A similar shift in the peak position of the TOF signal was also observed in [57]. In this case, such procedure will be addressed as nσ_{TOF} signal extraction, defined as follows:

$$n\sigma_{\mathrm{TOF}} = \frac{(\Delta t - \Delta t_{\mathrm{d}})}{\sigma_{\mathrm{TOF}}} \tag{5.3}$$

being Δt is the measured time-of-flight, Δt_{d} its expected value for deuterons and σ_{TOF} the TOF resolution.

5.2.2 Recentering procedure

Because of a miscalibration of the TPC detector, the nσ signal of both (anti)d and (anti)^{3}He is not peaked around zero as expected, instead it is shifted to negative values at low transverse momenta, as usually observed in similar analyses. The limited number of ^{3}He candidate tracks makes the task of recentering the signal using only primary nuclei not trivial. We assume that the miscalibration of the detector affects both ^{3}He and $^3\overline{He}$ nuclei, regardless of the fact they are produced in the primary vertex or not. Therefore, in order to recenter the nσ_{TPC}, we released the DCA selection criteria ($|\mathrm{DCA}_{xy}| < 1$ cm and $|\mathrm{DCA}_{z}| < 1$ cm), allowing secondary nuclei to affect the data and extracted the nσ distributions as a function of momentum p, summing the counts of nuclei and antinuclei (see Fig. 5.1). For the recentering procedure the momentum intervals for (anti)^{3}He have been slightly changed, according to the amount of available tracks.
Similarly to (anti)^{3}He, also (anti)d nσ_{TPC} distributions are not well centered around zero and therefore a recentering procedure is applied. The assumption that the miscalibration of the detector affects both nuclei and antinuclei remains valid and therefore the two distributions of d and $\overline{\mathrm{d}}$ are summed (see Fig. 5.2). Moreover, an additional cut on $|n\sigma_{\mathrm{TOF}}| < 3$ is applied, in order to obtain a clean sample of (anti)deuterons.
In each momentum interval, the nσ_{TPC} distributions are fitted with a Gaussian function and the centroids of the fit functions are reported as a function of the weighted average value of momentum inside each bin, as shown in Fig. 5.3 for both particle species. These points are fitted with

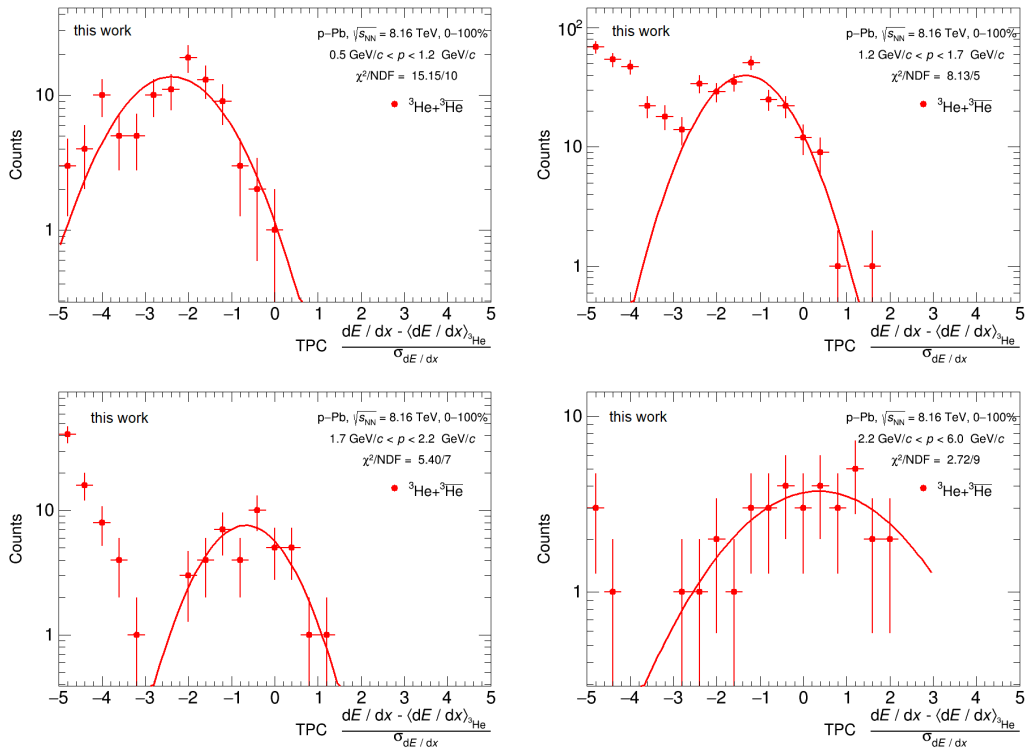

Figure 5.1: Distributions of nσ_{TPC} of ^{3}He + $^3\overline{\text{He}}$ nuclei as a function of momentum, in 4 momentum ranges, after releasing the DCA selection criteria for the purpose of the recentering procedure. The nσ distributions are fitted with a Gaussian function.

the function reported below, where a, b and c are fit parameters:

$$\langle n\sigma_{TPC} \rangle = a + b(1 - exp(-c \cdot p)) \tag{5.4}$$

The resulting fit parameters of d and ^{3}He are reported in Table 5.2. Using the results of the fit, the nσ_{TPC} signal is recentered, as shown in Fig. 5.4, where the centroids of the nσ_{TPC} distributions of d + $\overline{\text{d}}$ are shown as a function of the transverse momentum.
The signal extraction after the recentering procedure is discussed and illustrated in the next Section.

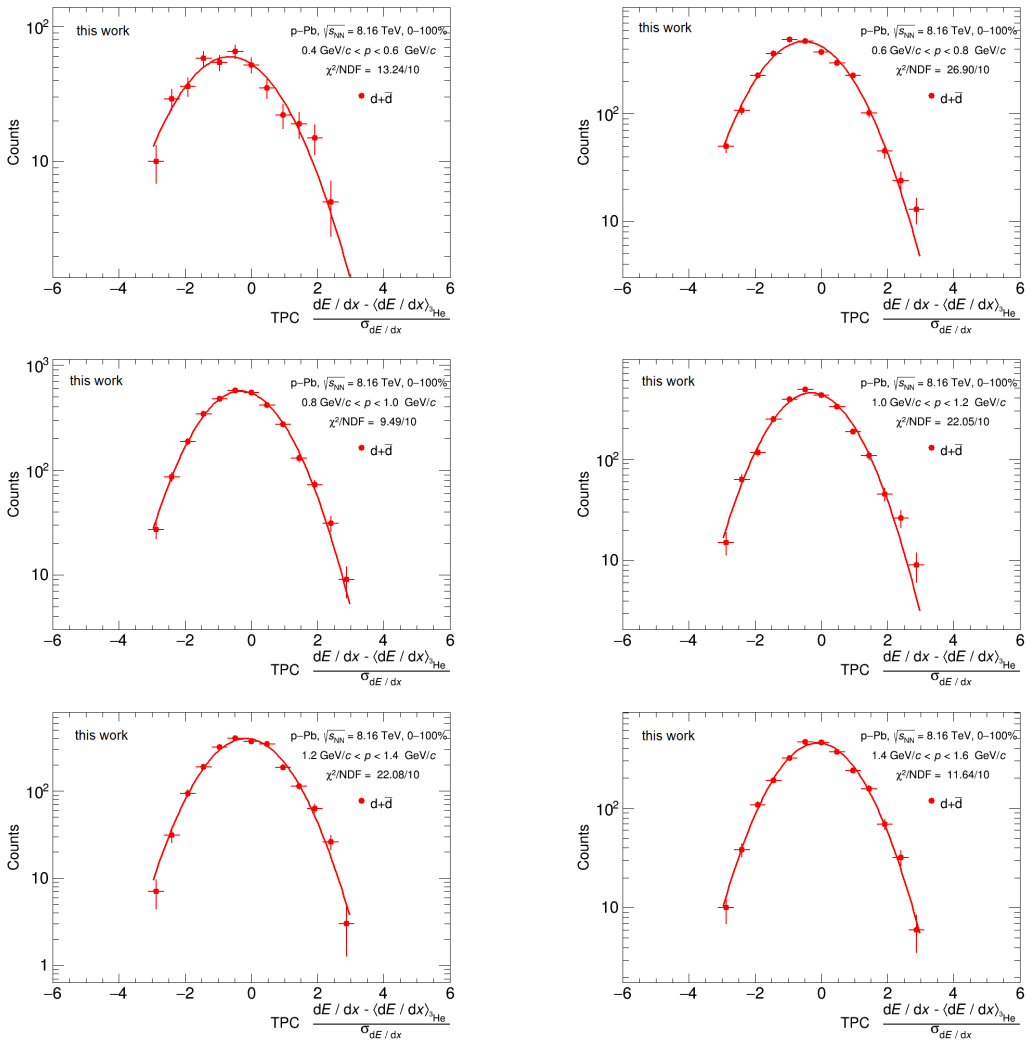

Figure 5.2: Distributions of $n\sigma_{TPC}$ of d+$\bar{d}$ nuclei as a function of momentum, in 8 momentum ranges. The $n\sigma_{TPC}$ distributions are fitted with a Gaussian function.

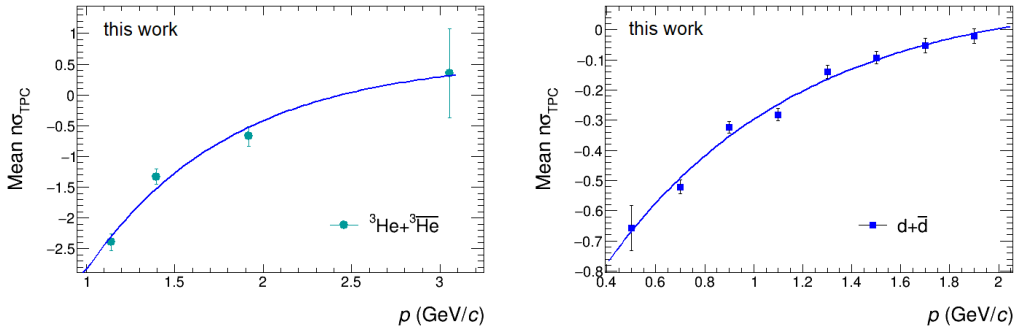

Figure 5.3: Distributions of the centroids of the Gaussian fit of ^{3}He + $^3\overline{\text{He}}$ (left) and d+$\overline{\text{d}}$ (right) nσ_{TPC}, as a function of the mean value of track momentum inside each bin. The solid line represents the fit by equation 5.4.

particle species	a	b	c
^{3}He + $^3\overline{\text{He}}$	–11.09 ± 7.28	11.68 ± 6.82	1.22 ± 0.61
d+$\overline{\text{d}}$	–1.37 ± 0.16	1.49 ± 0.11	1.27 ± 0.25

Table 5.2: Results of the fit with the recentering function, both for deuterons and ^{3}He.

5.2.3 Signal extraction

The distribution of $(\mathrm{d}E/\mathrm{d}x - \langle \mathrm{d}E/\mathrm{d}x \rangle_{^3\mathrm{He}})/\ \sigma^{^3\mathrm{He}}_{\mathrm{d}E/\mathrm{d}x}$in the transverse region 1.5 GeV/c < p_{T} < 2.0 GeV/c is shown in the left panel of Fig. 5.5. On the left side of the ^{3}He signal a contamination due to other particle species is visible. As one can see by looking at the specific energy loss in the TPC detector (see Fig. 3.11), the curve of ^{3}He is affected by the contamination of triton nuclei at low p_{T}. The contamination from ^{3}H is estimated by means of a fit using a Gaussian function. Hence, it is subtracted from the ^{3}He signal. Moreover, in order to address any systematic uncertainty in the estimate of such contamination, also the exponential function is used to fit the triton contamination, as it will be discussed in Sect. 5.4.
For the (anti)deuteron signal extraction, as described above, two methods

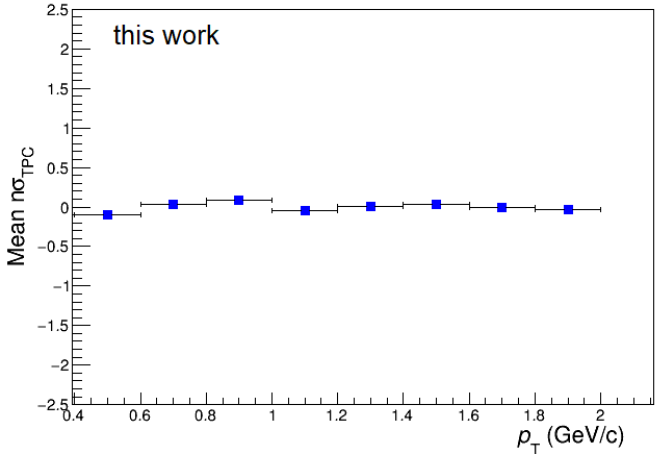

Figure 5.4: Centroids of the Gaussian fit of d+$\overline{\text{d}}$ nσ_{TPC} spectra as a function of the transverse momentum, after the recentering procedure.

are used depending on the p_{T} region. For low transverse momenta, only the specific energy loss in the TPC is used. As an example, in the right panel of Fig. 5.5 the signal extraction of (anti)d in the transverse momentum region (0.8, 1.0) GeV/c is shown. In the kinematic region $p_{\text{T}} > 1.2$ GeV/c, the (anti)d signal is extracted using the measured time of flight, and specifically looking at the nσ_{TOF} distribution. The signal extracted using TOF is fitted with a Gaussian function with an exponential tail. A significant background, originating from mismatched tracks, is present for $p_{\text{T}} \geq 1.6$ GeV/c and modelled with two exponential functions. The functional form of the signal function is given below:

$$f_{\text{signal}}(n\sigma_{\text{TOF}}) = \begin{cases} \text{A} \exp\left(-\frac{1}{2}\left(\frac{n\sigma_{\text{TOF}} - \mu}{\sigma}\right)^2\right) & n\sigma_{\text{TOF}} < \mu + \tau\sigma \\ \text{B} \exp\left(-\left(\frac{n\sigma_{\text{TOF}} - \mu}{\sigma} + \frac{\tau}{2}\right)\tau\right) & n\sigma_{\text{TOF}} \geq \mu + \tau\sigma \end{cases} \tag{5.5}$$

where A and B are normalization factors, μ and σ are respectively the centroid and the width of the Gaussian and τ is the number of σs from μ at which the function becomes an exponential.

The functional form of the background is given by:

$$f_{\mathrm{bkg}}(n\sigma_{\mathrm{TOF}}) = f_{\mathrm{signal}}(n\sigma_{\mathrm{TOF}}) + \mathrm{C}\ \exp(\mathrm{D}\cdot n\sigma_{\mathrm{TOF}}) + \mathrm{E}\ \exp(\mathrm{F}\cdot n\sigma_{\mathrm{TOF}}) \quad (5.6)$$

where C, D E and F are the fit parameters of the exponential functions which represent the background on the left and on the right side of the signal. In the range where the background is negligible, the raw yield is extracted by directly counting the candidates. Otherwise, the background function is subtracted by the signal. The raw yield is obtained counting the candidates in the asymmetric region $[-3\sigma_{\mathrm{TOF}} + \mu_0, +3.5\sigma_{\mathrm{TOF}} + \mu_0]$, centered at μ_0 (mean of the Gaussian signal), which is slightly different from zero because of small miscalibration effects of the TOF detector, as discussed above. Such an asymmetric window of integration allows us to take into account the exponential tail on the right-hand side of the signal. In Fig. 5.6, an example of the signal extraction of deuterons (left panel) and antideuterons (right panel), in the kinematic region 2.4 GeV/c < p_{T} < 2.8 GeV/c is shown.
Finally, the raw p_{T} spectra are extracted and the resulting distributions for the integrated multiplicity class for both particle species are shown in Fig. 5.7.
The same procedure is carried out to extract the signal in all the multiplicity classes as well. As an example, the signal extraction in the kinematic region (2.8, 3.4) GeV/c in several multiplicity classes are shown in Fig. 5.8 and Fig. 5.9 for d and $\overline{\mathrm{d}}$, respectively.

5.3 Corrections to raw spectra

5.3.1 Transverse momentum correction

Low-momentum particles lose a considerable amount of energy while traversing the detector material. The track reconstruction algorithm takes into account the Coulomb scattering and energy loss, assuming the pion mass for each particle [58]. Therefore, a track-by-track correction for the energy loss of heavier particles (i.e. (anti)^{3}He) can be needed. This correction is obtained from MC simulations, in which the difference of the

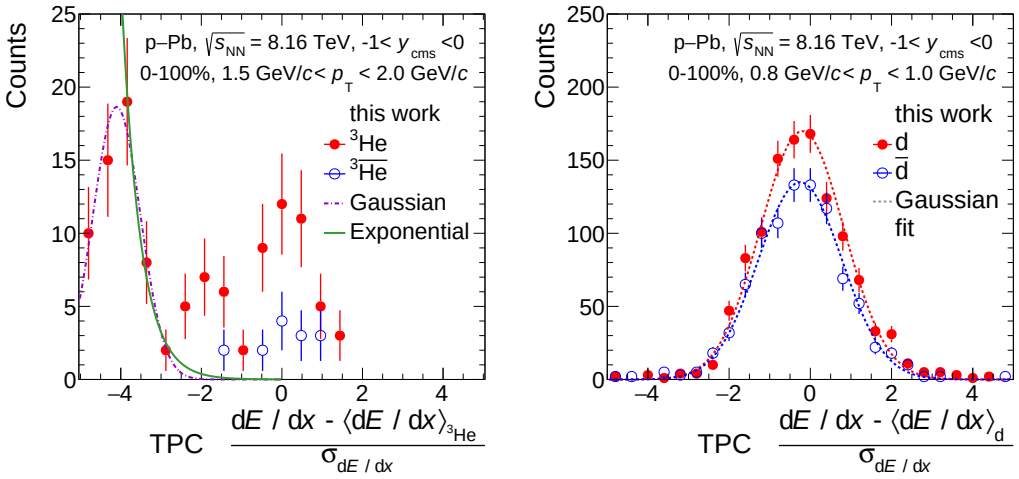

Figure 5.5: (anti)^{3}He (left panel) and (anti)deuteron (right panel) signal extraction using the TPC specific energy loss.

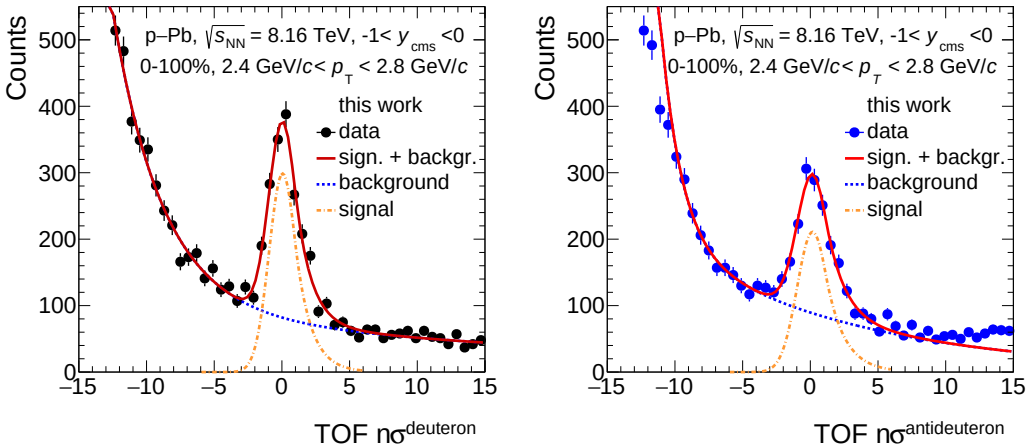

Figure 5.6: Deuteron (left panel) and antideuteron (right panel) signal extraction using the velocity information given by the TOF detector.

reconstructed and the generated transverse momentum is studied on a track-by-track basis. Figure 5.10 shows the average p_T difference as a function of the reconstructed track momentum ($p_{T,rec}$) for $^3\overline{\text{He}}$ and ^{3}He.

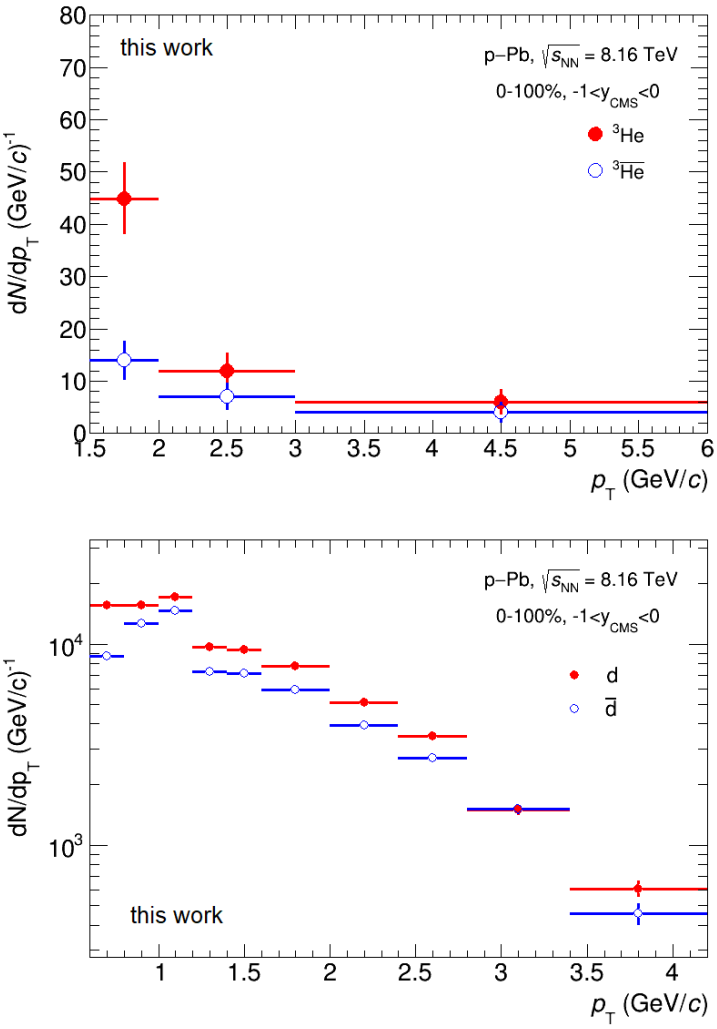

Figure 5.7: Raw spectra of (anti)^{3}He (top plot) and (anti)d (bottom plot), in the integrated multiplicity class.

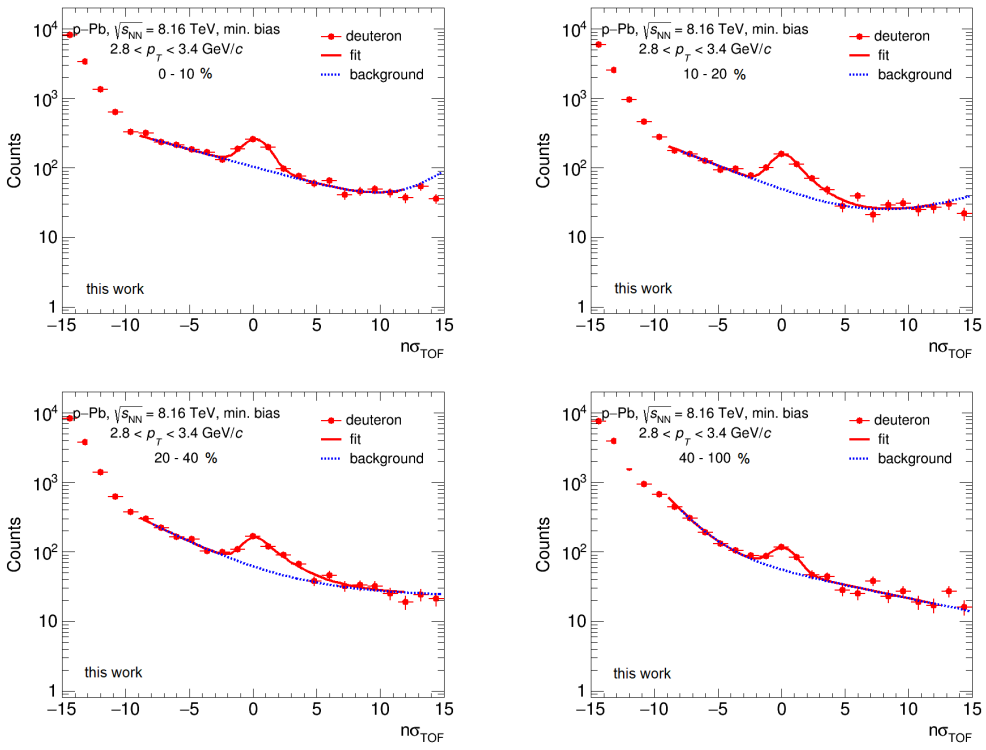

Figure 5.8: Deuteron signal extraction using the velocity information given by the TOF detector in the p_{T} interval (2.8, 3.4) GeV/c in several multiplicity classes.

The distribution can be fitted using the following empirical function:

$$f(p_{\mathrm{T}}^{rec}) = A + B \cdot exp(C \cdot (p_{\mathrm{T}}^{rec})^3) \tag{5.7}$$

where the free parameters A, B and C are extracted from the fit. The results are reported in Table 5.3. It can be seen that the correction is larger at low momenta. This reflects the typical $1/\beta^2$ behaviour of the energy loss.

5.3.2 Acceptance and efficiency correction

The reconstruction efficiencies of (anti)d and (anti)^{3}He are obtained from Monte Carlo simulations, in which the propagation of particles through

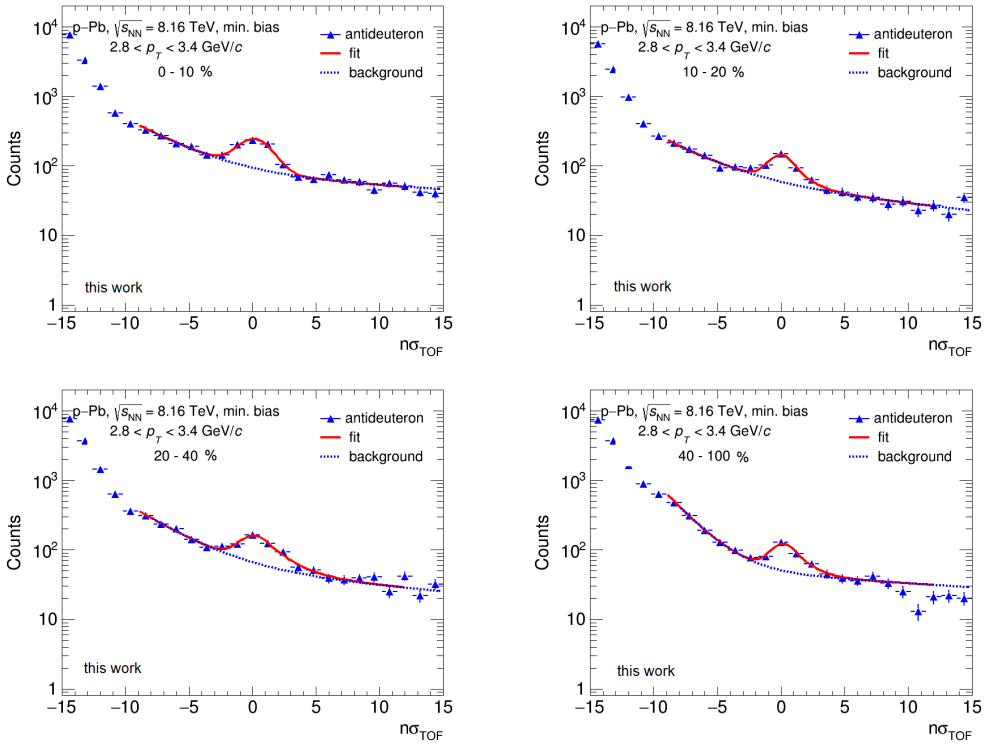

Figure 5.9: Antideuteron signal extraction using the velocity information given by the TOF detector in the p_{T} interval (2.8, 3.4) GeV/c in several multiplicity classes.

A	**B**	**C**
$(1.71 \pm 0.09) \cdot 10^{-3}$	$(-3.80 \pm 0.03) \cdot 10^{-1}$	$(-2.53 \pm 0.01) \cdot 10^{-1}$

Table 5.3: Fit parameters of the p_{T} difference distribution in Fig. 5.10 by means of Eq. 5.7.

the detector is simulated using the GEANT4 package. The reconstructed Acceptance $\times$ Efficiency ($A \times \epsilon$) is defined as the ratio of reconstructed over generated primary tracks, in the rapidity and pseudorapidity regions of interest for our analysis, as given below:

$$A \times \epsilon = \frac{\mathrm{N}_{\mathrm{rec},|y|<0.5,|\eta|<0.8}}{\mathrm{N}_{\mathrm{gen},|y|<0.5}} \tag{5.8}$$

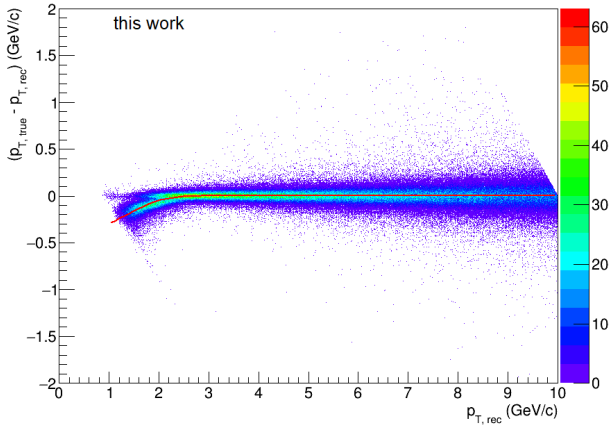

Figure 5.10: The difference between the reconstructed and the generated transverse momentum as a function of the reconstructed one, as extracted from MC simulations. The red line represents the fit by Eq. 5.7.

The same track selection criteria as those used for the data are applied to the reconstructed tracks in MC. The Acceptance $\times$ Efficiency distributions used to correct the raw (anti)d and (anti)^{3}He spectra are shown in Fig. 5.11 as a function of transverse momentum, using squares and circles respectively. The efficiency for antinuclei is reduced compared to that of nuclei due to annihilation processes with the beam pipe and the detector material. The efficiency for (anti)d is lower compared to that of (anti)^{3}He due to the additional requirement of a hit in the TOF detector for (anti)d tracks with a $p_{\mathrm{T}} > 1.2$ GeV/c. The latter implies the crossing of additional material between the TPC and the TOF detector, leading to a lower efficiency for (anti)d. The abrupt change in the (anti)deuteron efficiency occurring at $p_{\mathrm{T}} = 1.2$ GeV/c is due to the different strategy used for the signal extraction: at low p_{T} only the TPC information is used, resulting in an increasing efficiency as a function of transverse momentum, while for $p_{\mathrm{T}} > 1.2$ GeV/c the TOF information is used for the PID in addition to the TPC requirement, resulting in a lower efficiency due to the additional material traversed by nuclei. Despite the efficiency reduction, the use of the TOF detector in addition to the TPC information for $p_{\mathrm{T}} > 1.2$ GeV/c is fundamental in order to properly identify (anti)deuterons. Indeed, as

shown in Fig. 3.11, the PID of deuterons using the TPC is well performed at low p_{T} only, while for $p_{\mathrm{T}} > 1.2$ GeV/c, the TOF information has to be used as well.
In the case of (anti)deuterons, the procedure to estimate the $A \times \epsilon$ is carried out differentially for each multiplicity class as well. In Fig. 5.12 the efficiencies of d (left panel) and $\overline{\mathrm{d}}$ (right panel) in each multiplicity class are shown and compared to the efficiency of the integrated multiplicity class (black markers). As it is clear from the Figure, the efficiencies calculated in each multiplicity class are consistent with those calculated for the integrated distributions. Hence, in order to avoid differences due to statistical fluctuations, the efficiencies estimated in the integrated multiplicity class (as shown in Fig. 5.11) are used to correct each (anti)d multiplicity class spectrum.

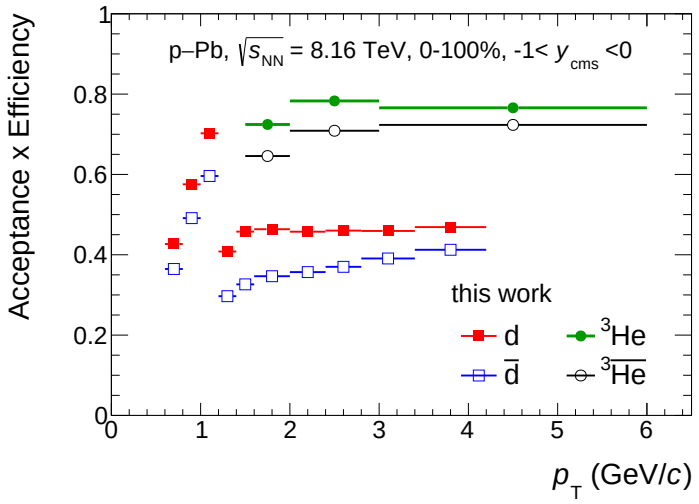

Figure 5.11: Acceptance $\times$ Efficiency as a function of p_{T} for (anti)deuterons (squares) as well as for (anti)^{3}He (dots), for the integrated multiplicity class.

5.3.3 Secondary nuclei contamination

The interaction of primary particles and nuclei in the detector material and in the beam pipe produces nuclear fragments, called spallation prod-

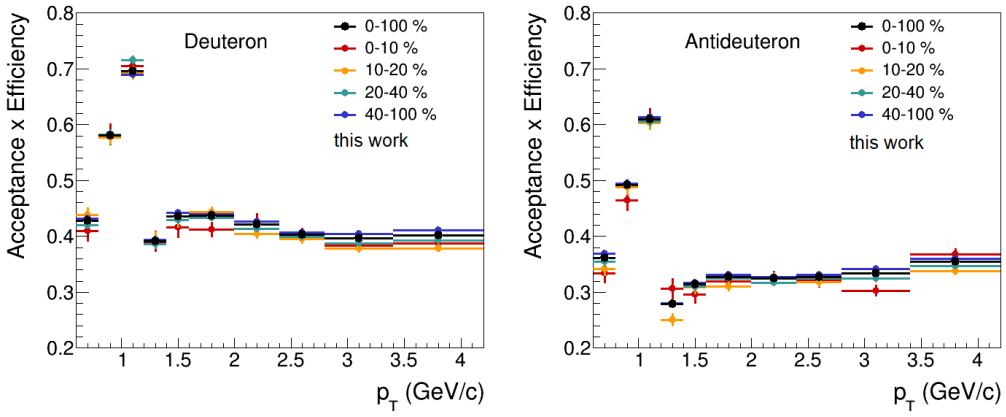

Figure 5.12: Efficiency x Acceptance based on G4 for each multiplicity class used to correct the transverse momentum spectra.

ucts. The DCA distributions of primary and secondary nuclei are different. The tracks of primary nuclei point to the primary vertex and therefore have a narrow distribution peaked at zero, similar to that of antinuclei, which can only be primary. Spallation fragments, instead, show a broader and flatter distribution. Therefore, secondary nuclei produced by spallation can be discriminated using the DCA of their reconstructed tracks to the primary vertex [58]. The preselection on the DCA_z reduces the background, without affecting primary nuclei. As an example, in the left panel of Fig. 5.13, the DCA_{xy} distributions of deuterons (red circles) and antideuterons (blue circles) are shown: the former is rather flat for $|\mathrm{DCA}_{xy}| > 0.2$ cm with a peak well centered around zero, whereas the latter shows only the peak around zero, with a negligible background for $|\mathrm{DCA}_{xy}|$ larger than 0.2 cm. This implies that the secondary contamination affects only the nuclei and not the antinuclei. Therefore, to remove the residual contribution of secondary nuclei, a data-driven approach as in similar previous analyses [64, 169] is used. The distribution of the DCA_{xy} is fitted with two distributions (called *templates* in the following) obtained from Monte Carlo (MC) simulations describing primary and secondary from material deuterons, respectively, as shown in the right panel of Fig. 5.13. The fit is performed in the range $|\mathrm{DCA}_{xy}| < 0.9$ cm which allows the contribution from material to be constrained by the plateau of

the distribution at larger distances ($|\mathrm{DCA}_{xy}| > 0.2$ cm). The contamination of secondary deuterons amounts to about 15% in the lowest p_{T} interval and decreases exponentially towards higher p_{T} until it becomes negligible above 1.6 GeV/c. In Fig. 5.14 the primary fraction of deuterons, given by the difference between the secondary fraction and the unity, is shown. The limited number of ^{3}He candidate tracks, instead, does not allow a background subtraction based on templates. Therefore, such contamination is inherited from a similar analysis in p–Pb at $\sqrt{s_{\mathrm{NN}}} = 5.02$ TeV [64], where the template method was used thanks to the larger amount of ^{3}He candidates available in such dataset. Such contribution is estimated as a 9% secondary nuclei contribution in the kinematic region $1.0 < p_{\mathrm{T}} < 1.5$ GeV/c due to spallation processes.

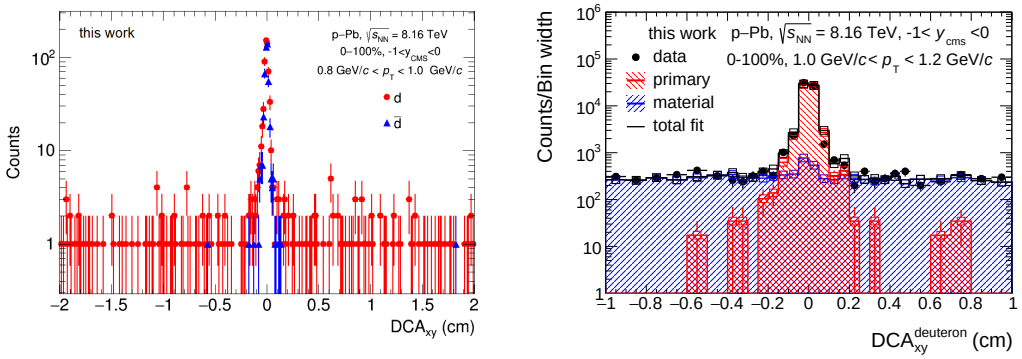

Figure 5.13: *Left.* $\mathrm{DCA_{xy}}$ distribution of deuterons (red dots) and antideuterons (blue triangles) in the p_{T} interval (0.8, 1.0) GeV/c. *Right.* Secondary contamination estimate for deuterons using the MC template method.

Another contribution to the secondary nuclei contamination is related to the feed-down from hypertriton decay. The dominant feed-down contribution for (anti)^{3}He is the π^- mesonic decay of (anti)hypertritons [181]:

$$^3_{\Lambda}\mathrm{H} \rightarrow ^3\mathrm{He} + \pi^- \tag{5.9}$$

The contribution of secondary (anti)^{3}He produced by the decay of (anti)$^3_{\Lambda}$H is estimated using MC simulations and then subtracted from the inclusive p_{T} distribution, as described in Ref. [64]. The fraction of

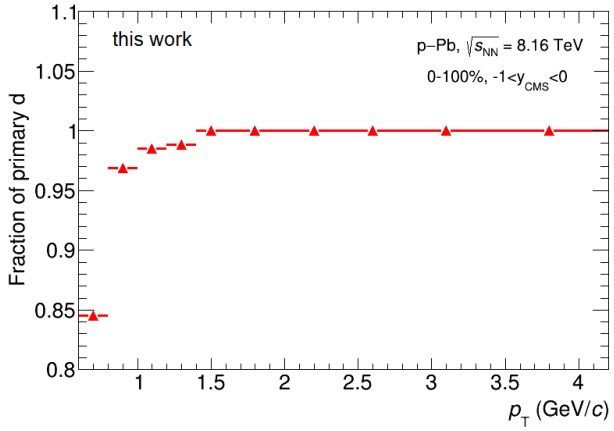

Figure 5.14: Primary fraction of deuterons estimated using the MC template method.

secondary (anti)^{3}He from (anti)hypertriton decays is given by:

$$f_{\text{feed-down}}(p_{\text{T}}) = \frac{\epsilon_{\text{feed-down}}(p_{\text{T}})}{\epsilon_{^3\text{He}}(p_{\text{T}})} \cdot \text{BR} \cdot \frac{^3_\Lambda\text{H}}{^3\text{He}} \tag{5.10}$$

The (anti)$^3_\Lambda$H-to-(anti)^{3}He ratio is extrapolated for the integrated multiplicity class of p–Pb collisions at 8.16 TeV, using the measured ratio as a function of $\mathrm{d}N_{\text{ch}}/\mathrm{d}\eta_{\text{lab}}$ in Pb–Pb collisions at $\sqrt{s_{\text{NN}}}$=2.76 TeV [106], assuming a linear trend. Such ratio resulted to be also consistent with the expectations of the Vanilla Canonical Statistical Model [101]. The BR represents the Branching Ratio of the mesonic decay of $^3_\Lambda$H, which amounts to about 25%, as reported in [106]. The fraction of hypertritons which passes the track selection in the ^{3}He (anti)nucleus channel is estimated with the Monte Carlo simulation, as the ratio between the efficiency of the reconstruction of (anti)^{3}He from weak decay and the efficiency of the reconstruction of primary (anti)^{3}He. The former is estimated as a function of the transverse momentum and shown in Fig. 5.15 using the three p_{T} intervals of the analysis. The latter is the efficiency described in Sect. 5.3.2. The ratio between the $\epsilon_{feed-down}$ and the efficiency of primary (anti)nuclei $\epsilon_{primary}$ is shown in Fig. 5.16.
Finally, the fraction of secondary nuclei from (anti)$^3_\Lambda$H weak decay is estimated, resulting to be about 4 % with a weak dependence on transverse

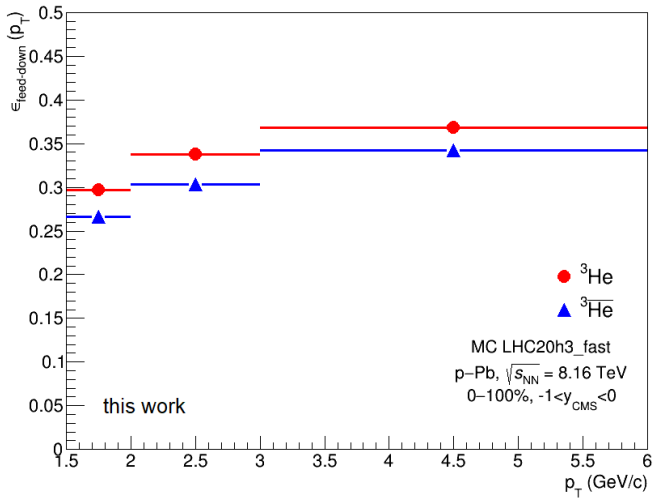

Figure 5.15: Efficiency $\times$ Acceptance of (anti)^{3}He from weak decay, estimated using the Monte Carlo simulations, as a function of the transverse momentum.

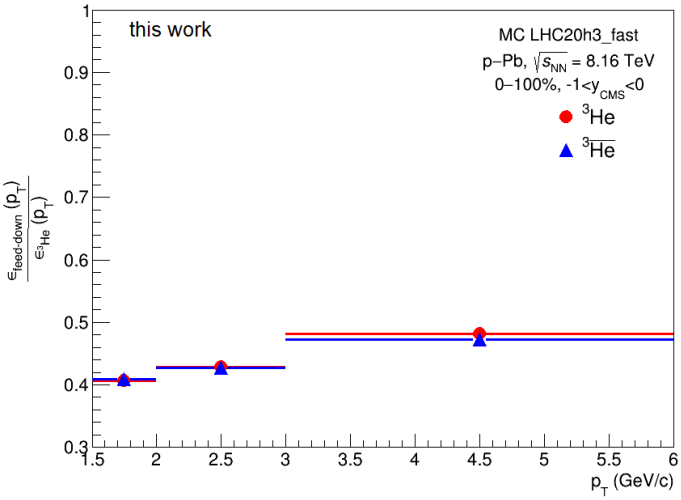

Figure 5.16: Ratio between the reconstruction efficiency of nuclei from weak decay and the reconstruction efficiency of primary nuclei, estimated as a function of p_{T}.

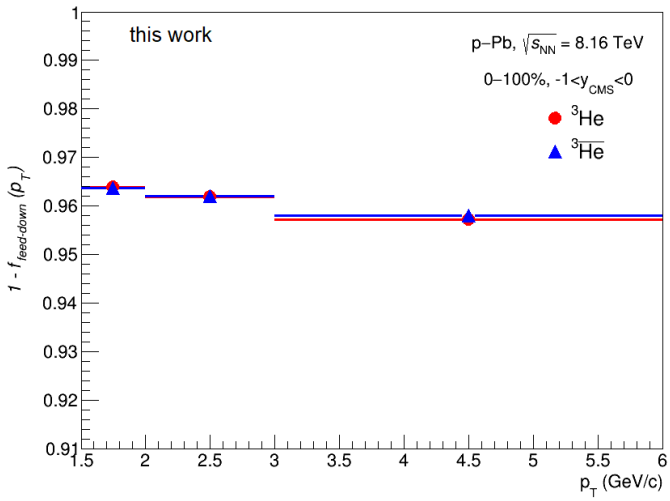

Figure 5.17: Fraction of primary nuclei after the subtraction of feed-down nuclei, estimated using Eq. 5.10, as a function of transverse momentum.

momentum. This amount is subtracted from the overall number of observed (anti)^{3}He, correcting the raw spectra by the fraction reported in Fig. 5.17.
The relative contribution of secondary (anti)deuterons from the three-body channel decay of (anti)$^3_\Lambda$H is estimated with the same method and is found to be negligible, due to the much larger abundance of primary deuterons with respect to $^3_\Lambda$H. Hence no correction is applied to account for secondary deuterons due to feed-down from the weak decay of (anti)hypertriton.

5.3.4 Signal and event loss

An additional correction is related to the trigger efficiency. The selected events are those in which the colliding ions interact via inelastic collisions and at least one charged-particle could be measured in the pseudorapidity region $|\eta| < 1$ (INEL > 0). In order to account for the INEL > 0 events that are wrongly rejected (event loss) and for all the (anti)deuterons lost because produced in the wrongly rejected events (signal loss), MC simu-

lations are used to correct the raw spectra.

Specifically, in order to obtain the total integrated yield, the raw spectra are corrected as follows:

$$\frac{d^2N}{dp_{\mathrm{T}}dy} = \frac{1}{N_{ev}} \frac{N_{\mathrm{obs}}}{\Delta y \Delta p_{\mathrm{T}}} \frac{\epsilon_{event}}{\epsilon_{signal}} \epsilon_{mult} \tag{5.11}$$

being N_{obs} the raw counts observed corrected by the $A \times \epsilon$ and the primary fraction, as discussed above, N_{ev} the number of total selected events available in the data set (~ 40 M), Δy and Δp_{T} the intervals of rapidity and transverse momentum respectively to normalize the raw spectra, $\epsilon_{\mathrm{event}}$ the event selection efficiency, $\epsilon_{\mathrm{signal}}$ the signal loss efficiency and finally ϵ_{mult} the efficiency related to the multiplicity dependence of the event efficiency. In the following the latter efficiencies are further discussed.

In MC both the number of rejected events and the number of (anti)d produced in those same events are known. The event loss is calculated by dividing the number of events selected with the minimum-bias trigger by those found in all INEL > 0 events. In Fig. 5.18, such efficiency ($\epsilon_{\mathrm{event}}$) is shown in very narrow multiplicity bins (black squares) and in the multiplicity bins of the analysis (red stars). A linear fit is also executed in order to evaluate the average event selection efficiency.

The event efficiency in MC is rather flat with multiplicity, whereas the event distribution in data has a multiplicity dependence, as shown in Fig. 5.19. Therefore, a correction for the multiplicity event efficiency (ϵ_{mult}) is calculated and applied to the raw spectra. For this purpose, the constant fit value of the event efficiency from MC (p_0=0.92) is assigned to the efficiency of the highest multiplicity class 0-10% of data. For other multiplicity classes, the efficiency ϵ_{mult} is calculated by dividing the bin content in each multiplicity interval by that in the highest multiplicity interval. The dotted line is the average centrality for the integrated multiplicity class. The resulting ϵ_{mult} are summarized in Table 5.4.

Moreover, the MC productions used for this purpose are heavily injected with light (anti)nuclei, thus it is not possible to count the number of lost (anti)deuterons directly. Instead, the primary protons in the pseudorapidity region $|\eta| < 0.8$ are used to estimate the signal loss of (anti)deuterons, assuming a particle-independence of such behaviour. The resulting signal efficiencies ($\epsilon_{\mathrm{signal}}$) as a function of transverse momentum in the four

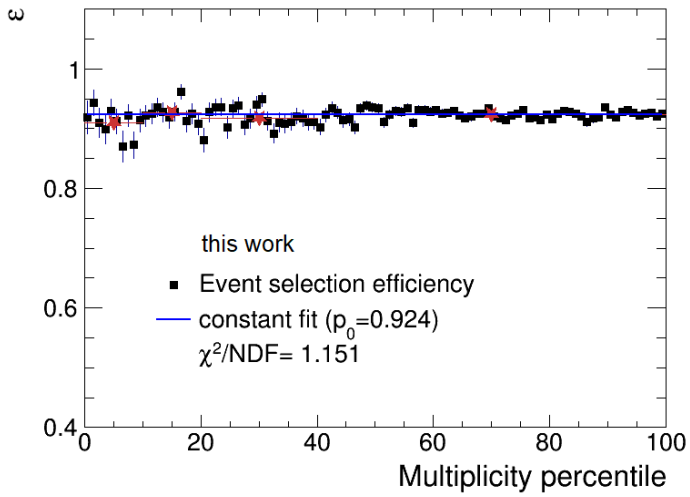

Figure 5.18: Event selection efficiency as a function of the multiplicity percentile.

multiplicity classes of the analysis are summarized in Figure 5.20.

	0-10 %	**10-20** %	**20-40** %	**40-100** %	**0-100** %
ϵ_{mult}	1.	0.995	0.993	0.977	0.983

Table 5.4: Summary of the ϵ_{mult} calculated for each multiplicity class.

Finally, the raw p_{T} spectra are corrected by means of the event-to-signal loss efficiency ratio, depending on the multiplicity class, as it is shown in Fig. 5.21: it is a 2% correction for the most central collisions and < 1% for the most peripheral ones.

5.4 Systematic uncertainties

In this Section the effect of systematic uncertainties on the results of this work is discussed. The evaluated contributions to systematic uncertainties can be divided into the following groups:

- Tracking (reconstruction)

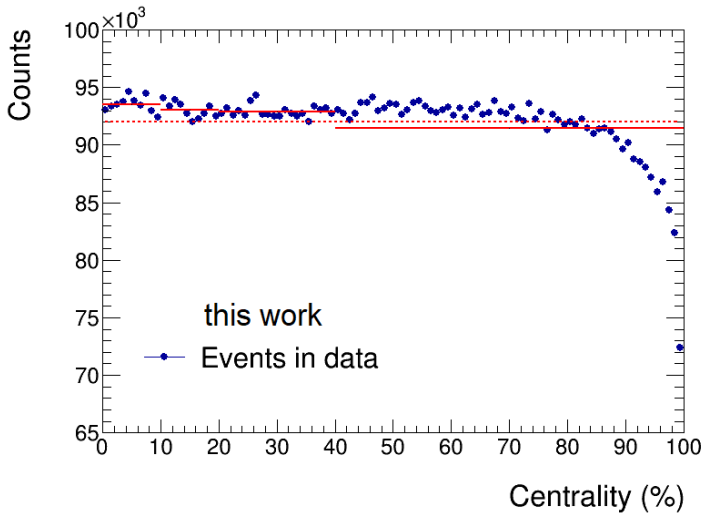

Figure 5.19: Centrality distribution of events in data. The solid red lines are the average values of centrality in the analysis bins, whereas the dotted red line is the value for the multiplicity integrated distribution.

- ITS-TPC matching efficiency
- TPC-TOF matching efficiency
- Signal extraction
- ^{3}H contamination
- Secondary from material
- Secondary from feed-down
- Hadronic interaction
- Material Budget
- Signal loss efficiency

Each contribution to the systematic uncertainty is described in more detail in the following Subsections. In Tables 5.5-5.6 and in Figures 5.22-5.23 the various contributions to the systematic uncertainties of (anti)d and

(anti)^{3}He, respectively, are summarized. The total systematic uncertainty is calculated as the sum in quadrature of each contribution.

Tracking (reconstruction)

For the tracking-related systematic uncertainty, each track selection cut discussed in Sect. 5.1 has been varied using a random uniform distribution around the nominal value (see Table 5.7). Specifically, the selection on nTPC Clusters, nTPC Crossed Rows and nTPC dE/dx Clusters have been applied simultaneously since they are highly correlated. Such procedure has been repeated 50 times in the case of (anti)^{3}He and 100 times in the case of (anti)d. The same set of selection criteria used for data is also applied to reconstructed MC in order to obtain the corresponding efficiency. After correcting the raw spectra of data obtained with the different selec-

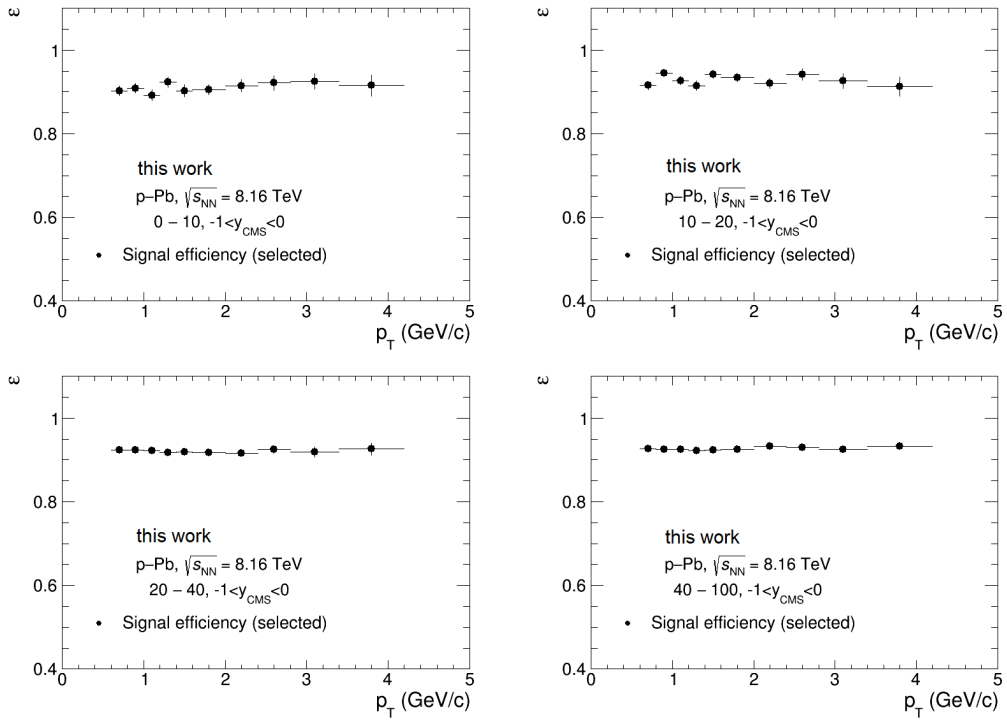

Figure 5.20: Signal loss efficiency calculated using the primary protons in the pseudorapidity interval $|\eta| < 0.8$.

particle	**d ($\overline{\mathrm{d}}$)**	
p_{T} **range**	**0.6 -0.8 GeV/c**	**3.4 - 4.2 GeV/c**
Source of uncertainty		
Tracking	1.6 % (2.3 %)	1.1 % (2.5 %)
ITS-TPC matching	1.0 % (1.0 %)	1.0 % (1.0 %)
TPC-TOF matching	negl.	4.2 % (5.2 %)
Signal extraction	1.4 % (1.3 %)	3.3 % (3.0 %)
Secondary material	0.2 %	negl.
Hadronic interaction	0.6 % (1.0 %)	1.5 % (6.0 %)
Material Budget	1.0 % (1.0 %)	1.0 % (1.0 %)
Signal loss efficiency	1.0 % (1.0 %)	1.0 % (1.0 %)
Total	3.6 % (3.4 %)	5.9 % (6.8 %)

Table 5.5: Summary of the systematic uncertainties, in the uppermost and the lowermost investigated p_{T} intervals for (anti)d.

particle	**^{3}He ($^3\overline{\mathrm{He}}$)**	
p_{T} **range**	**1.5 - 2.0 GeV/c**	**3.0 - 6.0 GeV/c**
Source of uncertainty		
Tracking	2.8 % (4.5 %)	2.8 % (4.5 %)
ITS-TPC matching	1.0 % (1.0 %)	1.0 % (1.0 %)
^{3}H Contamination	2.7 %	negl.
Secondary material	9.0 %	negl.
Secondary feed-down	3.4 % (3.5 %)	2.6 % (2.8 %)
Hadronic interaction	1.0 % (3.0 %)	1.0 % (3.0 %)
Material Budget	0.2 % (0.3 %)	0.2 % (0.3 %)
Total	10.3 % (6.4 %)	3.8 % (6.0 %)

Table 5.6: Summary of the systematic uncertainties, in the uppermost and the lowermost investigated p_{T} intervals for (anti)^{3}He.

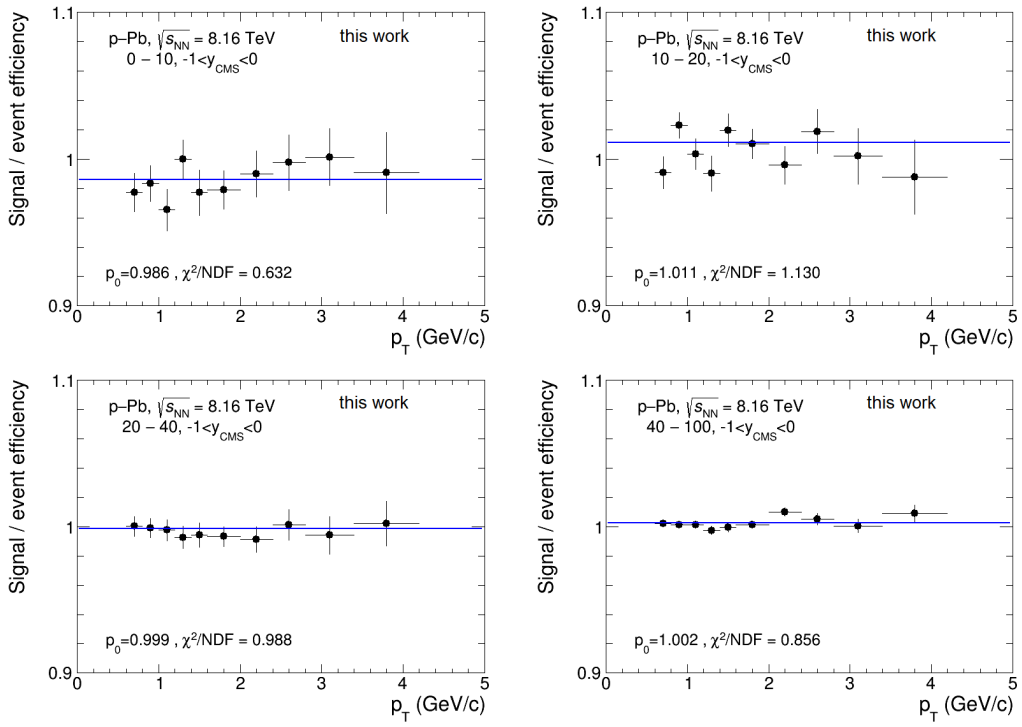

Figure 5.21: Signal-to-event efficiency ratio calculated in each multiplicity class. The blue line shows the linear fit performed in each multiplicity class. The result of the fit is reported as text in the Figure.

tion criteria by the primary fraction and the corresponding efficiency, an histogram for each p_{T} bin is filled with the corresponding yield. The systematic uncertainty is estimated using the root mean square (RMS) of the number of (anti)nuclei candidates evaluated as the integral of the nσ distribution used to extract the signal, within 3σ, divided by the mean value of such distribution, as shown in the left panel of Fig. 5.24 for the case of ^{3}He. Due to the limited amount of available ^{3}He tracks, and also considering the current knowledge based on other analyses in different collision systems, such uncertainty is considered p_{T} independent. Such assumption overestimates the systematic uncertainty but it allows us to safely take into account the uncertainty in the whole p_{T} range explored (1.5, 6.0) GeV/c. For deuterons, instead, the calculation is p_{T}–differential and the resulting systematic uncertainty is shown in the right panel of

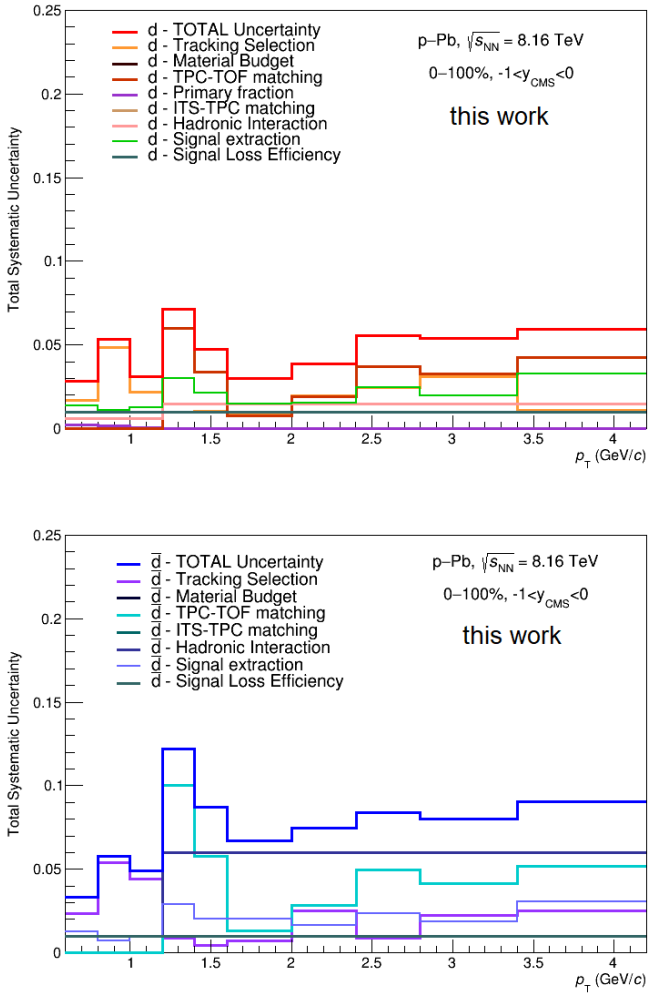

Figure 5.22: Different contributions to the sytematic uncertainty, for deuterons on the top panel and antideuterons on the bottom panel.

Fig. 5.24. Finally, the same procedure is repeated for each multiplicity class separately as well and the resulting systematic uncertainty is shown in Fig. 5.25.
In order to verify that this systematic uncertainty was not affected by statistical issues, the Barlow test is applied, as discussed in the following Section.

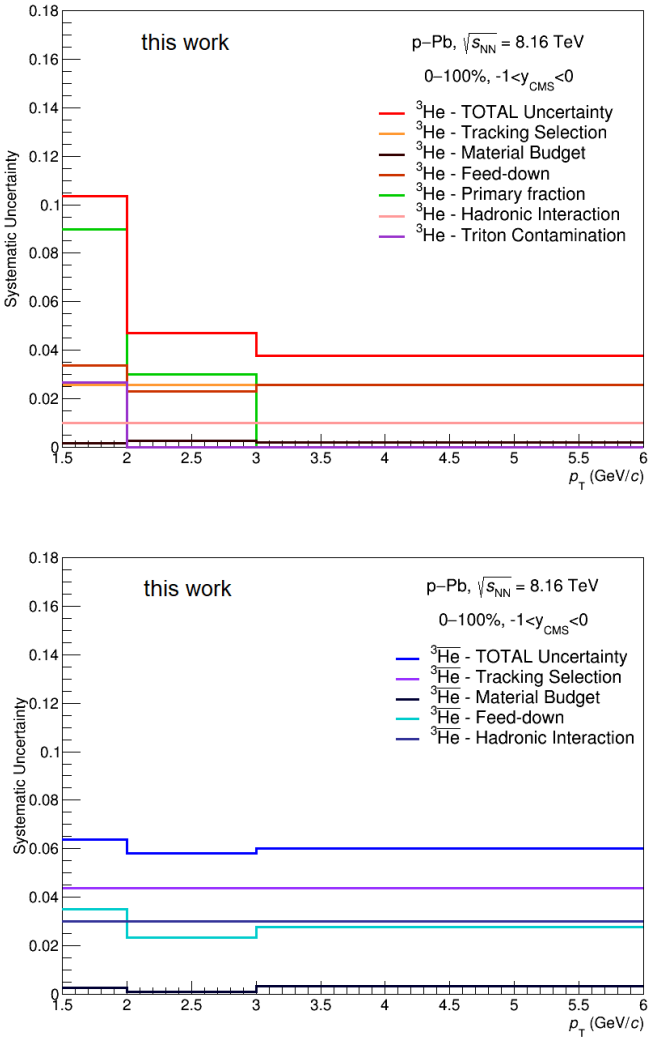

Figure 5.23: Different contributions to the systematic uncertainty, for ^{3}He on the top panel and $^3\overline{He}$ on the bottom panel.

Barlow Test

In order to verify whether the systematic uncertainties are dominated by statistical effects or not, the Barlow test is performed [182]. The Barlow test allows us to understand if the variation is consistent with a statistical

Selection	Default value	Range for random variation
$n_{ITSclusters}$	1	(1 - 3)
$n_{TPCclusters}$	70	(50, 60, 70, 80, 90, 100)
$n_{TPCdE/dxClusters}$	50	(30, 40, 50, 60, 70, 80)
$n_{TPCCrossedRows}$	70	(50, 60, 70, 80, 90, 100)
$\frac{n_{TPCCrossedRows}}{n_{TPCFindableCls}}$	0.8	(0.6 - 1.0)
χ^2/NDF	4	(3.0, 3.5, 4.0, 4.5)
$\lvert DCA_{xy}\rvert$	0.1	(0.08 - 0.15)
$\lvert DCA_{z}\rvert$	0.1	(0.08 - 0.15)

Table 5.7: Summary of the track selection variations applied for the evaluation of the systematic uncertainties related to the Track selection criteria. Within the range reported in the Table, each quantity is varied using a random uniform distribution.

fluctuation, and consequently if that variation should not be considered as a systematic effect.
For each set of selection criteria the difference between the number of selected candidates with varied criteria (x_{Var}) and the number of those extracted applying the default criteria ($x_{Default}$) is compared to the statistical error of this difference. If this quantity is less than one, it is rejected:

$$\frac{x_{Default} - x_{Var}}{\sqrt{\sigma^2_{Default} - \sigma^2_{Var}}} < 1 \rightarrow \text{rejected} \tag{5.12}$$

Therefore, the small variations are rejected since dominated by statistical effects, whereas the systematic uncertainty is dominated by variations greater than the statistical ones. The result of this test for the 100 cut variations is reported in Fig.5.26 as a function of the number of variations over the statistical error. For ^{3}He, it is reported as a p_{T}–integrated study, while for deuteron it is shown for the lowermost and uppermost p_{T} intervals. As it is clear from the figure, the Barlow test is verified for most of the variations.

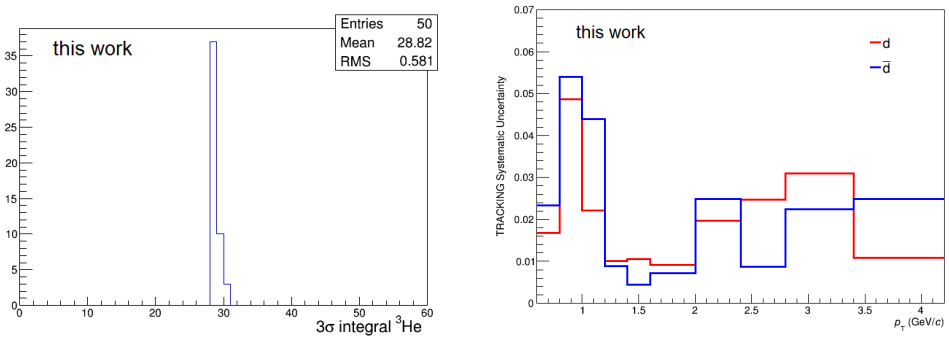

Figure 5.24: *Left.* Distribution of the number of ^{3}He candidates evaluated as the integral of the TPC nσ distribution, within 3σ. The systematic uncertainty due to the track selection contamination is taken from the RMS/Mean of the shown distributions for ^{3}He. *Right.* Contribution to the p_{T}–differential systematic uncertainty due to tracking selection variation for (anti)d.

ITS-TPC matching efficiency

The contribution to the Tracking systematic uncertainty is also related to ITS-TPC matching efficiency. Such contribution is taken from the report of the ALICE Data Preparation Group [183] and it amounts to about 1% for all the particle species studied in this work.

Signal extraction

For (anti)deuterons, the signal extraction procedure introduces an uncertainty that increases at high p_{T} and is estimated based on the variation of the nσ-selection in the TPC d$E/$dx and in the TOF and also on a variation in the $n\sigma$ TPC and TOF signal extraction using the fit function or the bin counting integral. The first contribution to the systematic uncertainty is estimated using the root mean square (RMS) of the distributions of the corrected yields for each p_{T} bin, divided by the mean value of such distributions. This contribution is added in quadrature to the systematic uncertainty estimated as half the difference between the integral of the fit function which describes the signal and the integral of the histogram after the subtraction of the background, both within the interval (-3σ, 3σ).

The resulting uncertainty is shown in Fig. 5.27. The same procedure is repeated to calculate the systematic uncertainties in each multiplicity class as well and the corresponding results are shown in Fig. 5.28.

^{3}H contamination

In the case of ^{3}He, the contribution to the systematic uncertainty on the estimate of the triton contamination at low p_{T} (1.5 - 2.0 GeV/c) is calculated. This contribution is given by the semidifference between the integrals after the contamination subtraction using an exponential or a Gaussian fit function. The fit executed on the triton contamination are shown in the left panel of Fig. 5.5. The systematic uncertainty is estimated as the full difference between the integrals within a 3σ window after the subtraction with the two fit functions.

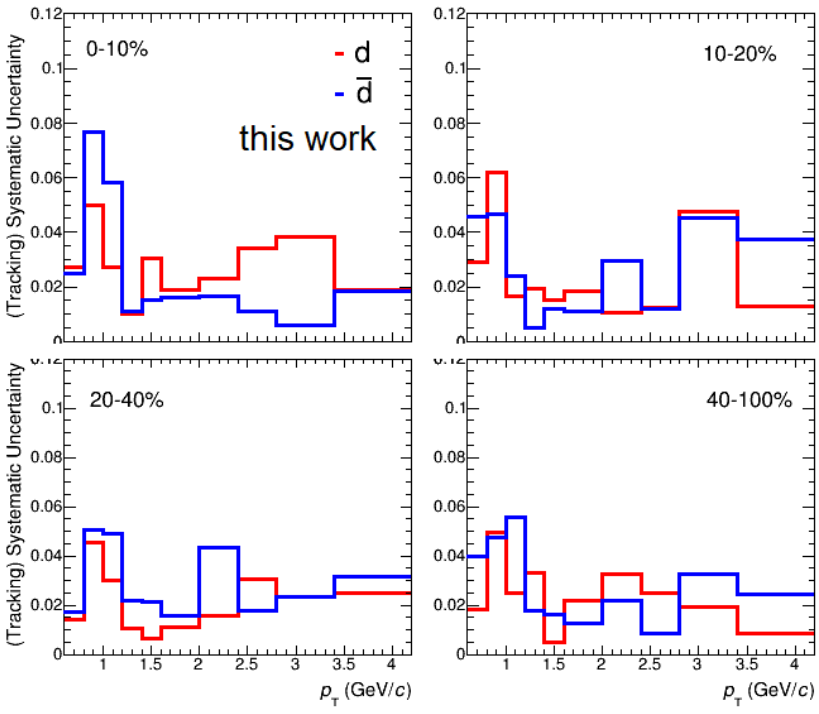

Figure 5.25: Contribution to systematic uncertainty due to tracking cuts variation for several multiplicity classes.

Secondary nuclei from material

The contribution to the systematic uncertainty due to the estimate of secondary nuclei from spallation processes is already partially taken into account in the tracking-related systematic uncertainties, since the DCA_{xy} and DCA_{z} windows are randomly varied in the interval (0.08, 0.15) cm. For deuterons, an additional contribution to this systematic uncertainty is calculated varying the binning and the fit range used for the template method. After applying the variations, the primary fraction is recalculated and shown in Fig. 5.29, along with the comparison to the default primary fraction used to correct the raw spectra. As it is clear from the figure, the fit in the fourth p_{T} bin is unstable because of the limited amount

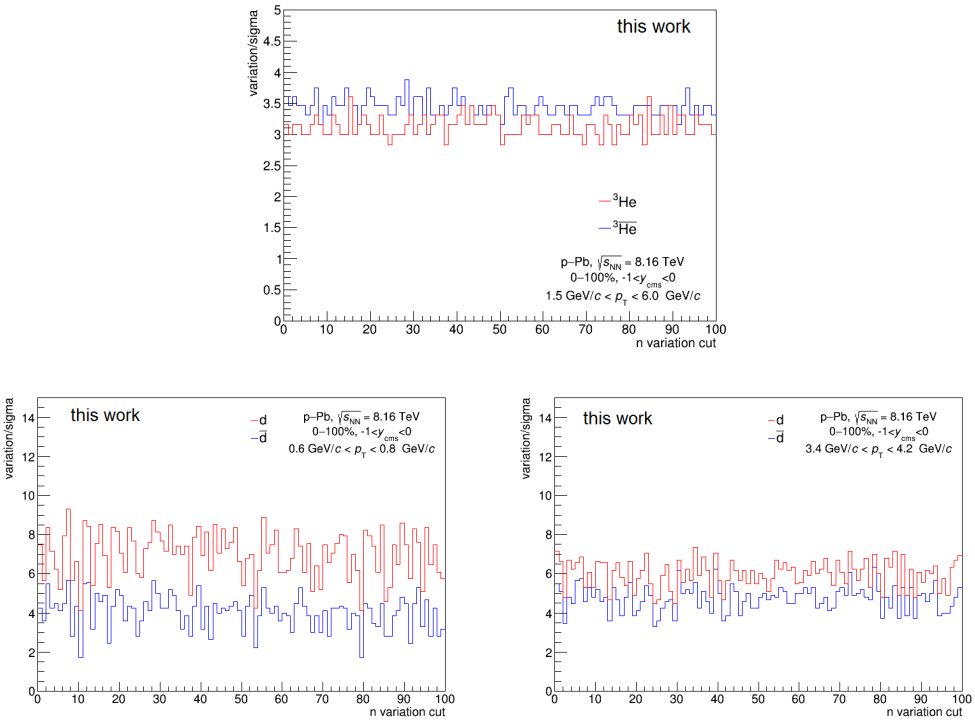

Figure 5.26: Barlow test applied to systematic uncertainties due to the track selection variation criteria for (anti)^{3}He (top panel) and for the lowermost and uppermost p_{T} intervals of (anti)d (bottom panels).

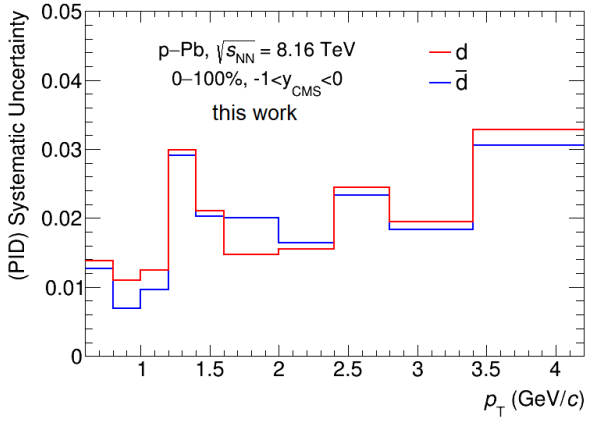

Figure 5.27: Contribution to systematic uncertainty due to the signal extraction procedure.

of available tracks in the MC secondary template. The systematic uncertainty is calculated as half the difference between the maximum spread of all primary fractions. In the critical p_T bin 1.2-1.4 GeV/c, the systematic uncertainty is calculated as the difference between the systematic uncertainty in the previous (1.0-1.2 GeV/c) and in the following (1.4-1.6 GeV/c) p_T bin, divided by $\sqrt{12}$. This contribution to the final systematic decreases exponentially becoming negligible for $p_T > 1.4$ GeV/c.
For ^{3}He, the contribution is inherited from [64] for the first p_T bin and an additional 3% contribution is added to the second p_T interval to take into account the presence of a contamination hidden by the lack of available data, taking into account the current knowledge of similar analyses.

Secondary nuclei from feed-down

For ^{3}He, the systematic uncertainty due to the estimate of secondary nuclei from weak decay of hypertriton is also estimated. The corresponding contribution is estimated as half the difference between the maximum and the minimum values obtained by repeating the linear extrapolation of the $^3_\Lambda$H-to-^{3}He ratio moving upwards and downwards the average values by their uncertainties.

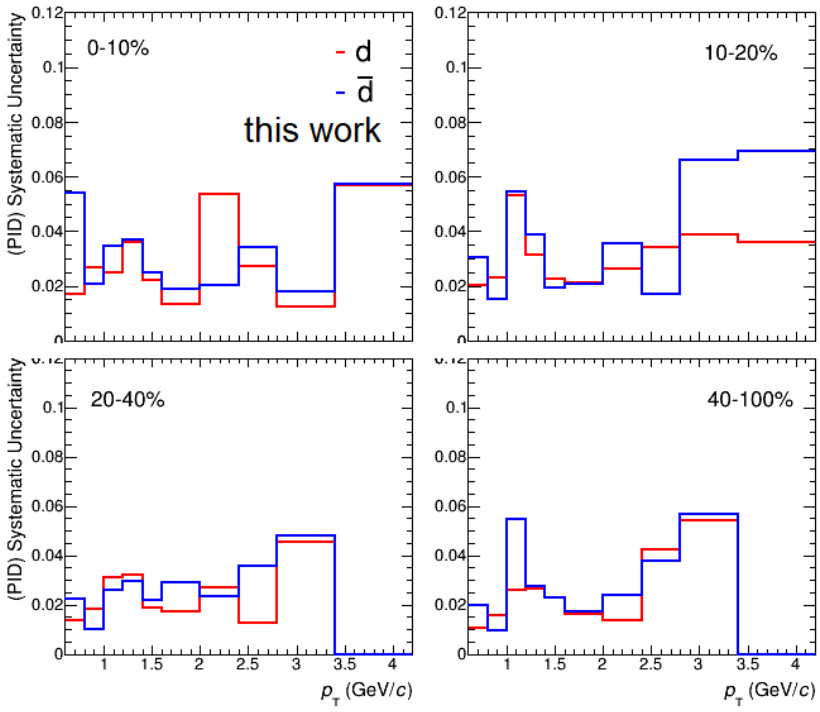

Figure 5.28: Contribution to systematic uncertainty due to the signal extraction procedure calculated in several multiplicity classes.

Material budget

Another source of systematic uncertainty is related to the incomplete knowledge of the material budget of the detector in the Monte Carlo simulations. The relative uncertainty on the determination of the material budget is given by photon conversion measurements and it is 4.5 %. The effect is evaluated by comparing different MC simulations with a material budget varied by $\pm$ 4.5%. Anchored to our dataset of p–Pb collisions at 8.16 TeV there are no MC productions with a different material budget, thus the MC productions for peripheral Pb–Pb collisions are used to estimate the systematic uncertainty. The efficiencies for (anti)^{3}He are shown in Fig. 5.30. The systematic uncertainty is then evaluated as half the difference between the maximum and the minimum values of the efficiency

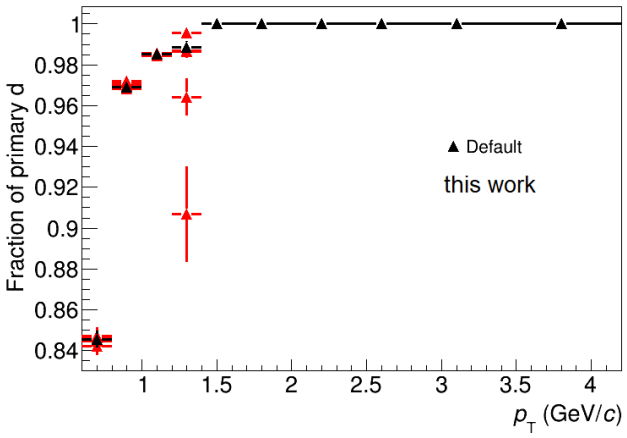

Figure 5.29: Primary fraction of deuterons recalculated applying several variations of the binning and the fit range used for the template method, compared to the default one.

obtained in a given p_T interval, using the following equation:

$$\sigma_{\text{material budget}}(p_T) = \frac{|\epsilon_{+4.5\%}(p_T) - \epsilon_{-4.5\%}(p_T)|}{2} \tag{5.13}$$

This particular systematic uncertainty is below 1% for (anti)^{3}He. For (anti)d, this systematic uncertainty is taken from [169], and it amounts to 1 %.

Hadronic interaction

The imperfect knowledge of the hadronic interaction cross section of (anti)d and (anti)^{3}He with the material contributes to the systematic uncertainty as well. Such uncertainty reflects the constraints on the antideuteron and $^3\overline{\text{He}}$ inelastic cross sections and on previous experimental measurements of (anti)deuteron and (anti)^{3}He absorption on different targets [184, 185].
Concerning the systematic uncertainty of $^3\overline{\text{He}}$, using full MC simulations anchored to p–Pb at 5.02 TeV dataset, the ALICE data of $\sigma_{\text{inel}}(^3\overline{\text{He}})$ are fitted using the momentum dependence from GEANT4. The best-fit to

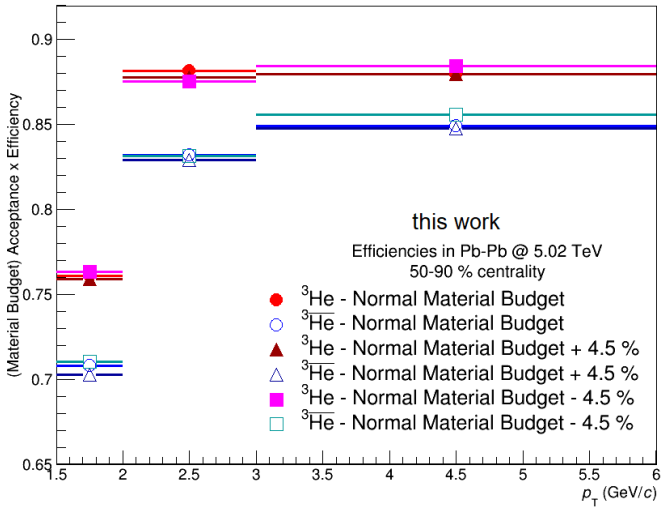

Figure 5.30: Reconstruction efficiency for the peripheral Pb − Pb samples at 5.02 TeV with normal material budget, normal material budget plus 4.5 % and normal material budget minus 4.5 % for (anti)^{3}He.

ALICE data results to be 0.77 $\pm$ 0.21, as shown in Fig 5.31. Hence, the cross section is scaled by 0.77 and varied by $\pm$ 0.21 in full MC simulations and therefore a rescaling factor using the best-agreement method between data and the fit is calculated. The subsequent variation on the transverse momentum spectra is estimated, resulting in a change of about 7% in the reconstructed $^3\overline{\text{He}}$ spectrum (see Fig. 5.32). The resulting uncertainty on the spectrum is finally calculated as the semidifference of the variations upwards and downwards with respect to the default value: it amounts to 3% uncertainty for $^3\overline{\text{He}}$, flat in p_{T}. Similar calculations for the ^{3}He uncertainty lead to a 1% contribution, also in this case flat in transverse momentum.
For what concerns the (anti)d calculations, the techniques to obtain the systematic uncertainty are discussed separately for d and $\overline{\text{d}}$ in the following, depending on the different measurements available for each particle species.
Several measurements of the inelastic cross section of deuterons are available [185], especially in the low p_{T} range. The overview of such measure-

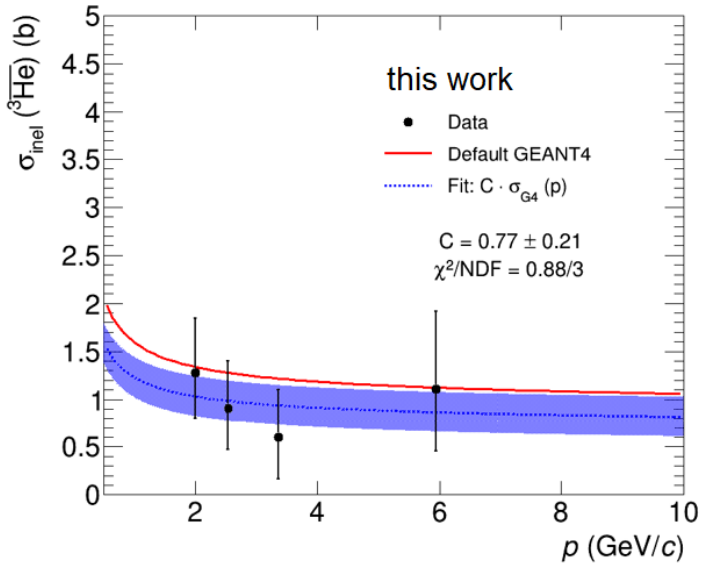

Figure 5.31: Inelastic cross section of $^3\overline{He}$ as a function of momentum. The best-fit to the data points using the σ_{inel}(p) taken from GEANT4 is reported as a text in the figure.

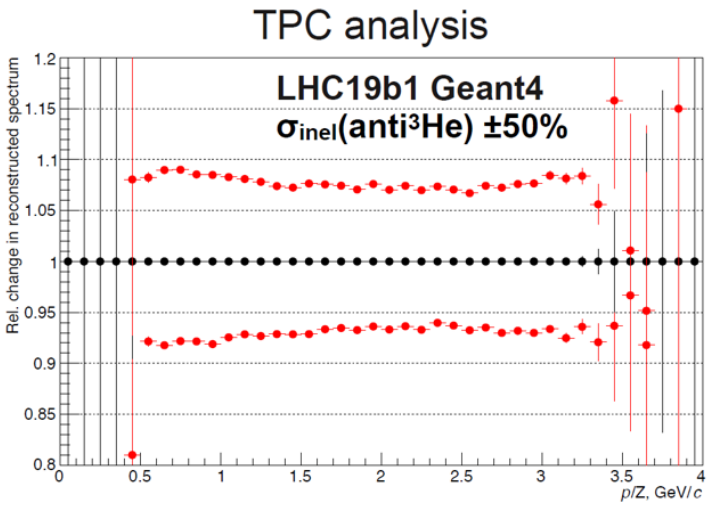

Figure 5.32: Resulting change in the $^3\overline{He}$ spectrum after a variation of $\pm$ 50 % in the default GEANT4 inelastic cross section.

ments is shown in Fig. 5.33, together with the GEANT4 parametrizations. However, considering the scarceness of experimental data in the relevant momentum range (between 0.5 and 5.0 GeV/c), a conservative variation of $\pm$ 10% has been used to check the impact on the deuteron spectrum. The corresponding uncertainty is estimated by fitting the change in the reconstructed p_{T} spectrum with a constant function.
Recent antideuteron inelastic cross section measurements by ALICE are the only available information on $\sigma_{\mathrm{inel}}(\bar{\mathrm{d}})$ in the relevant momentum range. These results have been parametrized by fitting the data with a function inspired by the Glauber model which is implemented in GEANT4: data and parametrizations are shown in Fig. 5.34. The upper and lower edges of the uncertainty band are parametrized by shifting the measured data points up and down by their uncertainties and fitting the data using the same functions. In this conservative approach, the statistical uncertainties are considered to be negligible and the systematic uncertainties are assumed to be fully correlated from one momentum interval to another. Therefore, the corresponding correction factor for the GEANT4 parametrizations amounts to 0.86 $\pm$ 0.14 for the TOF analysis (p_{T} > 1.0 GeV/c) and is momentum–dependent for the ITS+TPC analysis below p_{T} < 1.0 GeV/c. In order to see the corresponding impact on the reconstructed antideuteron spectrum, full ALICE Monte Carlo simulations have been used: a GEANT4-based MC production with default inelastic cross sections and another one with $\sigma_{\mathrm{inel}}(\bar{\mathrm{d}})$ set to 0.2 and to 2.0. In each momentum interval the agreement between GEANT4 and experimental data has been converted into a correction factor and an uncertainty for antideuteron spectrum.
Finally, the resulting contribution to the systematic uncertainty is 0.6 (1.0) % for the ITS+TPC analysis and 1.5 (6.0) % for the ITS+TPC+TOF analysis of deuterons (antideuterons).

TPC-TOF matching efficiency

The uncertainty related to the TPC-TOF matching efficiency should reflect several contributions: the multiple scattering effects, which are negligible because of a large ($\sim$ 10 cm) search window in TOF; the absorption of antideuterons, which is accounted for in the hadronic interaction related

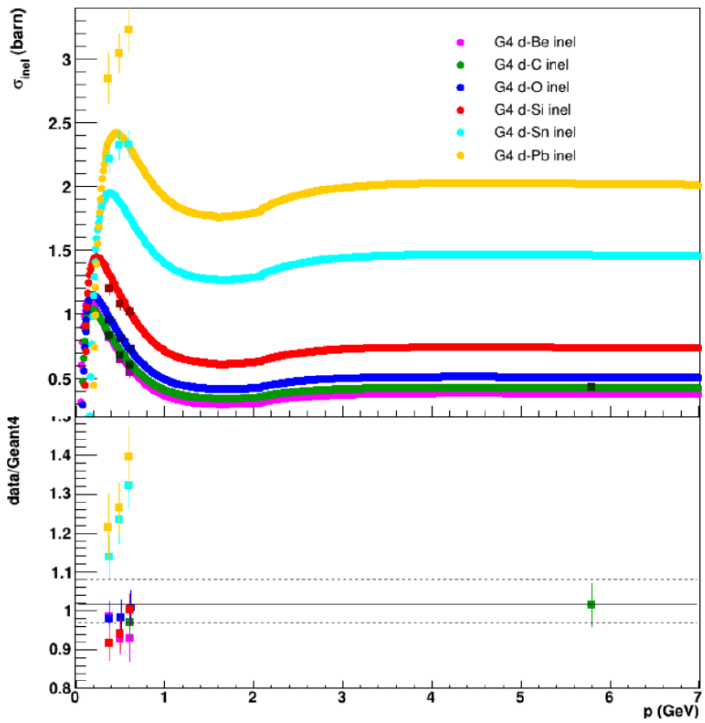

Figure 5.33: Inelastic cross section of deuterons as a function of momentum. The parametrization of the data points using GEANT4 is shown as well.

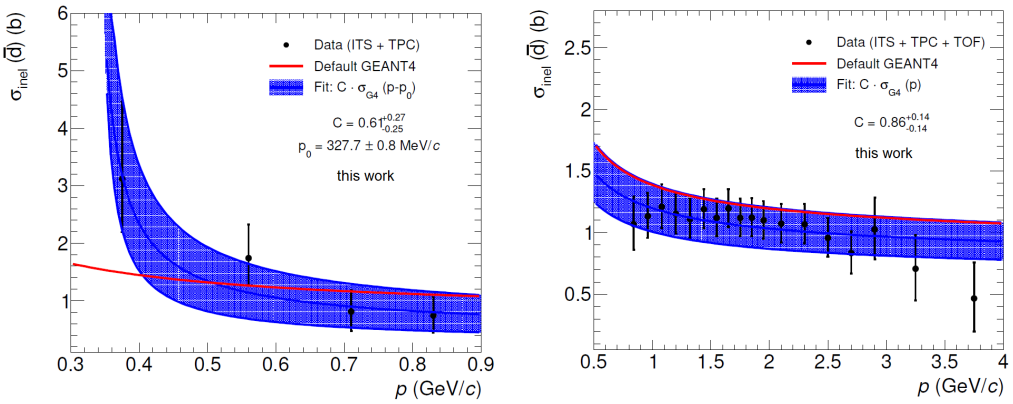

Figure 5.34: Inelastic cross section of antideuterons as a function of momentum. The best-fit to the data points using the $\sigma_{\text{inel}}(\overline{\text{d}})$ taken from GEANT4 is reported as a text in the figure.

systematic uncertainty; the TRD material budget. The latter is estimated for $p_{\text{T}} > 1.2$ GeV/c, where the TOF information is used to extract the signal of (anti)deuterons. A sketch of deuterons crossing through the TRD material is shown in Fig. 5.35. The efficiency when nuclei pass through a width Δx of TRD is given by $\epsilon = e^{-\Delta x/\lambda_I}$, where λ_I is the hadronic interaction length of the nucleus. The uncertainty on the efficiency, considering only the losses due to inelastic interactions is given, using the error propagation, by:

$$\Delta\epsilon = |-\frac{1}{\lambda_{\text{I}}}| \cdot \Delta\text{x} \cdot e^{-\Delta\text{x}/\lambda_{\text{I}}} \rightarrow \frac{\Delta\epsilon}{\epsilon} = \frac{\Delta\text{x}}{\lambda_{\text{I}}} \tag{5.14}$$

The ratio between Δx and the interaction length, as a function of momentum, is measured for protons and shown in the left panel of Fig. 5.36. The interaction length of protons is proportional to $1/\sigma_{\text{proton}}$, as well as the interaction length of deuterons is proportional to $1/\sigma_{\text{deuteron}}$, being σ the inelastic cross section of nuclei, thus leading to a ratio given by:

$$\frac{\Delta\text{x}}{\lambda_{\text{d}}} = \frac{\Delta\text{x}}{\lambda_{\text{p}}}\frac{\sigma_{\text{d}}}{\sigma_{\text{p}}} \tag{5.15}$$

Since the ratio $\sigma_{\text{d}}/\sigma_{\text{p}}$ is measured (see right panel of Fig. 5.36), such uncertainty can be estimated, resulting to be 4.2 (5.2) % at high p_{T} for

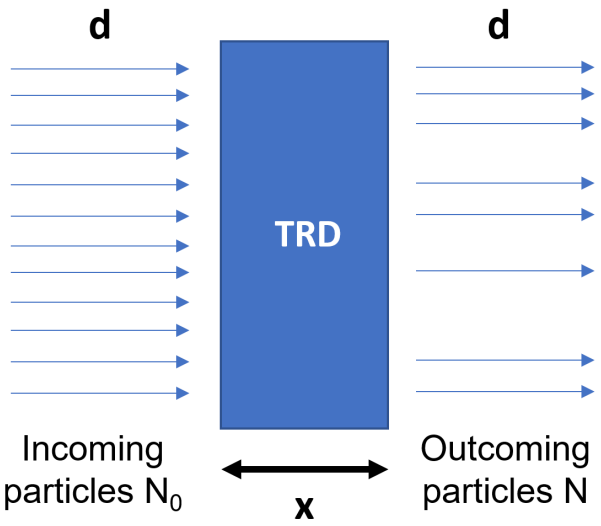

Figure 5.35: Sketch of deuteron nuclei passing through a width x of TRD.

deuterons (antideuterons), as summarized in Fig. 5.37.

Signal loss efficiency

Finally, to take into account the uncertainty in the estimate of the trigger efficiency correction, an additional 1 % contribution is added to the total systematic uncertainty of (anti)deuterons, considering the maximum spread between the corrections applied in each multiplicity class and the unity.

5.4.1 Multiplicity–differential study

In the previous Section, some of the multiplicity–differential calculations of (anti)d systematic uncertainties has been discussed and shown. In particular, those related to the signal extraction and the tracking cuts have been recalculated following the same procedure explained for the multiplicity integrated spectra for each of the four investigated multiplicity classes. From this differential study, a weak dependence on centrality has been found. Indeed, the systematic uncertainties calculated in each multiplicity class are summarized in Fig. 5.38 and 5.39. The results show that

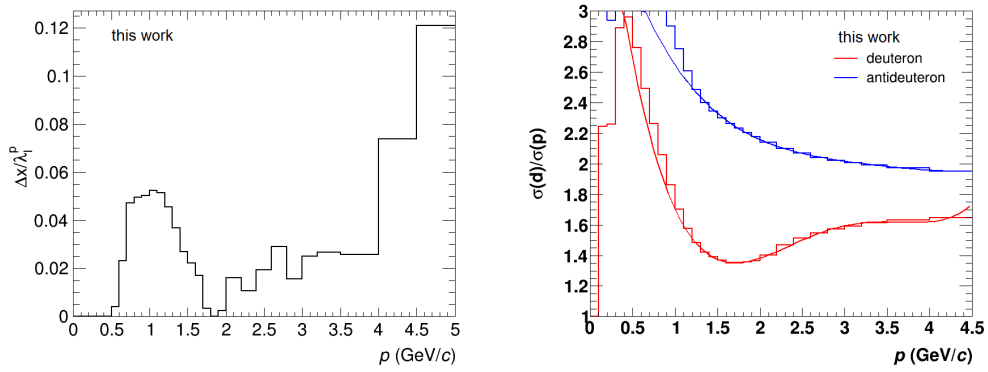

Figure 5.36: On the left the measured ratio between TRD Δx and the interaction length for protons is shown as a function of momentum. On the right the ratio of inelastic cross sections of deuterons and protons is shown, as well as the fit performed using a pol4 fuction.

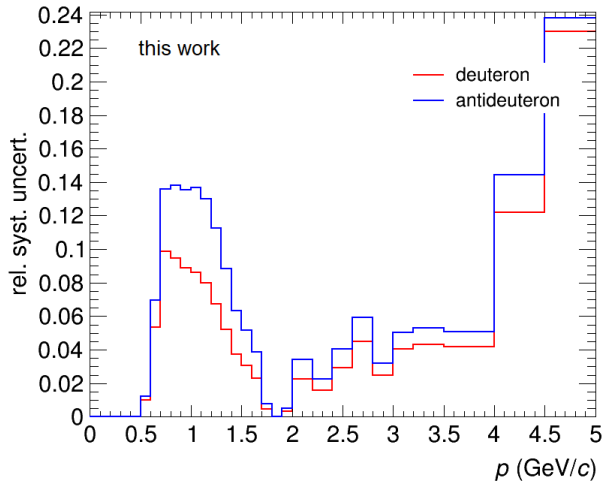

Figure 5.37: Contribution to systematic uncertainty due to the TRD material budget for (anti)d.

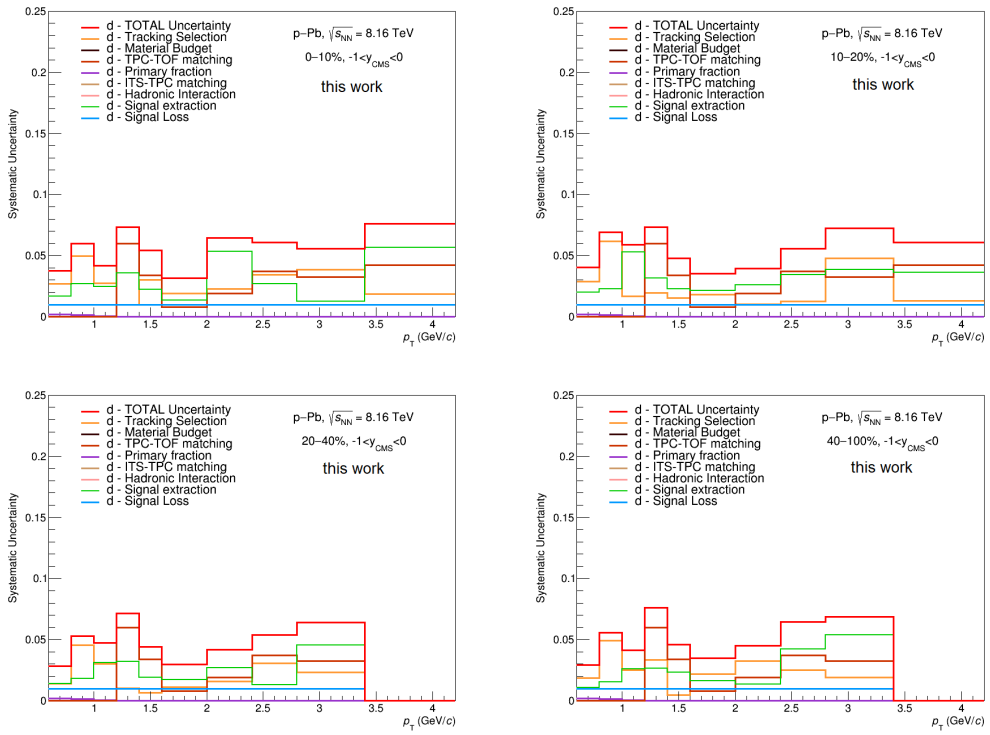

Figure 5.38: Systematic uncertainties for deuterons in each multiplicity class.

the systematic uncertainties are quite comparable with the multiplicity integrated results, hence the latter are used for all multiplicity classes, in order to avoid variations due to the limited amount of available data.

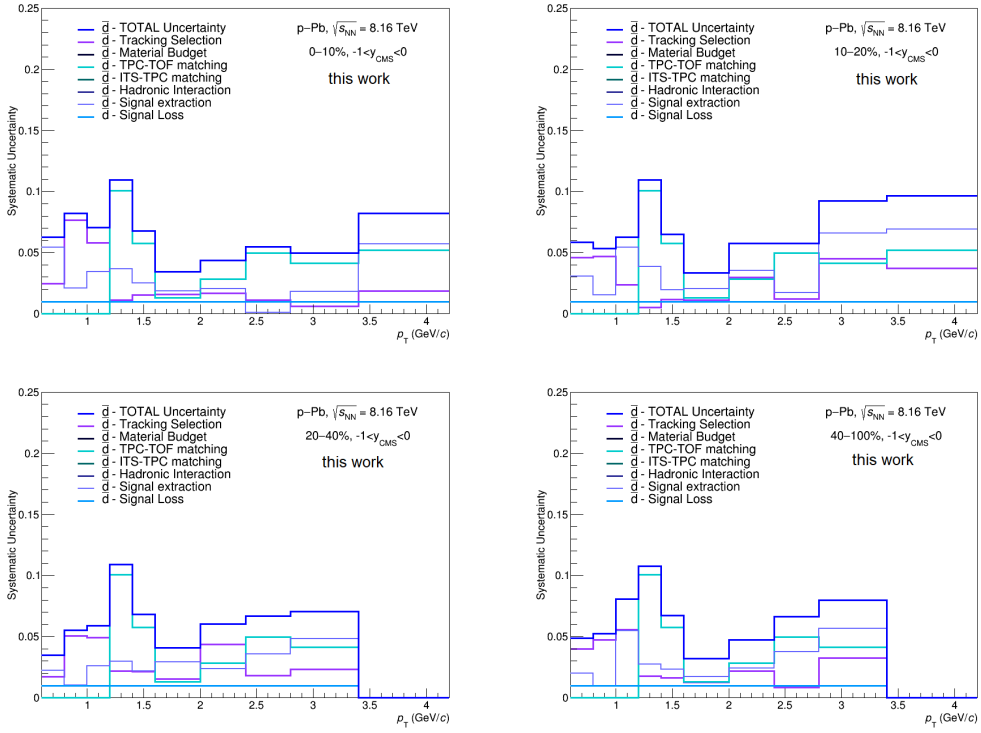

Figure 5.39: Systematic uncertainties for antideuterons in each multiplicity class.

Chapter 6

Results and discussion

6.1 Final results

In this Section the final results of the light (anti)nuclei analysis in p–Pb collisions at $\sqrt{s_{\rm NN}}$ = 8.16 TeV are illustrated and discussed. In the previous Chapter, the analysis techniques to obtain the raw spectra and all the applicable corrections to obtain the integrated yields have been discussed.
The transverse momentum spectra of (anti)nuclei are obtained applying the corresponding corrections to the raw spectra, as described in the following equations respectively for (anti)^{3}He and (anti)d:

$$(\text{anti})^3\text{He} : \frac{d^2N}{dydp_{\rm T}} = \frac{1}{N_{\rm events}} \frac{f_{\rm primary}(p_{\rm T}) N_{\rm obs}(p_{\rm T})}{\Delta y \Delta p_{\rm T} \epsilon(p_{\rm T})} (1 - f_{\rm feed-down}) \quad (6.1)$$

$$(\text{anti})\text{d} : \quad \frac{d^2N}{dp_{\rm T}dy} = \frac{1}{N_{\rm events}} \frac{f_{\rm primary}(p_{\rm T}) N_{\rm obs}(p_{\rm T})}{\Delta y \Delta p_{\rm T} \epsilon(p_{\rm T})} \frac{\epsilon_{\rm event}}{\epsilon_{\rm signal}} \epsilon_{\rm mult} \quad (6.2)$$

being $N_{\rm obs}$ the raw counts of each $p_{\rm T}$ spectrum, $N_{\rm events}$ the number of events of the analyzed dataset (i.e. 37.85 million events), $f_{\rm primary}$ and $f_{\rm feed-down}$ the primary fractions with respect to secondary nuclei contamination from material and from hypertriton weak-decay, respectively,

$\epsilon_{\rm event}$, $\epsilon_{\rm signal}$, $\epsilon_{\rm mult}$ the efficiencies discussed in the previous Section, and finally $\Delta y \Delta p_{\rm T}$ the width of the rapidity and transverse momentum intervals.

The transverse momentum spectra and the resulting $\langle\ p_{\rm T}\ \rangle$ for both deuteron and ^{3}He analyses are calculated using the average spectra ($\frac{\rm A+\overline{A}}{2}$), being A and $\overline{\rm A}$ the nucleus and the antinucleus, respectively, as illustrated in the following. In addition, the antiparticle-to-particle ratios are shown and compared to the expectations at the LHC. Finally, the comparison to hadronization models expectations are illustrated by means of the coalescence parameters and the nucleus-to-proton yield ratios as a function of the charged-particle multiplicity density.

6.1.1 Transverse momentum spectra

The transverse momentum spectra of deuterons and antideuterons are presented separately in Fig. 6.1 for several multiplicity classes. At low $p_{\rm T}$ (below 0.8 GeV/c), only antideuterons are shown and used to obtain the integrated yield, because of a residual contamination of secondary nuclei from spallation processes. The $p_{\rm T}$ spectra are fitted using a Lévy-Tsallis functional form [186], given by:

$$\frac{d^2N}{dp_{\rm T}dy} = \frac{dN}{dy}\frac{p_{\rm T}}{nC}\frac{(n-1)(n-2)}{(nC+m(n-2))}\left(1+\frac{m_T-m}{nC}\right)^{-n} \tag{6.3}$$

where $m_{\rm T}$ is the transverse mass (defined as $\sqrt{m^2+p_{\rm T}^2}$), m is the mass of the nucleus fixed at 1.87 GeV/c^2, n and C are fit parameters.
Because of the rare production of nuclei with mass number $A > 2$, the transverse momentum spectra of (anti)^{3}He are measured only in the integrated multiplicity interval and shown in the top panel of Fig. 6.2.
In order to obtain the integrated yield of nuclei, the average spectra ((d+$\overline{\rm d}$)/2) are used, to minimize statistical effects in the resulting yields. The transverse momentum spectra of the average deuterons are presented in Fig. 6.3 for several multiplicity classes, and the average (anti)^{3}He spectrum is shown in Fig. 6.4. The average (anti)^{3}He spectrum is fitted using a Lévy-Tsallis function (Eq. 6.3), fixing the mass of the nucleus to the value m = 2.81 GeV/c. The deuteron $p_{\rm T}$–distributions become harder

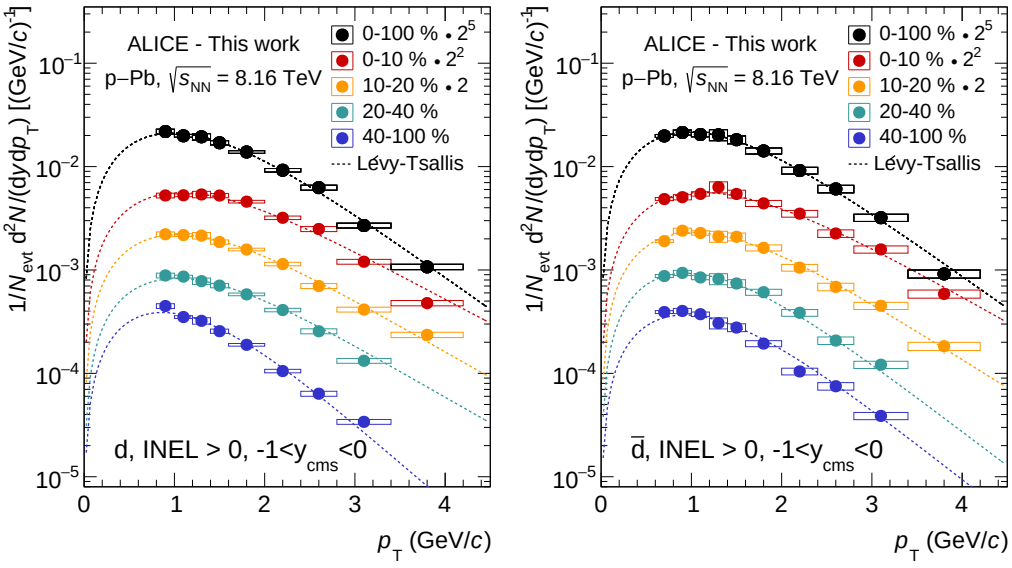

Figure 6.1: Transverse momentum spectra of deuterons (left) and antideuterons (right), in several multiplicity classes. The p_{T} distributions are fitted by means of a Lévy-Tsallis function [186] in order to extrapolate to the unmeasured regions. Boxes represent the systematic uncertainties.

as the multiplicity increases and the mean transverse momentum moves towards higher values. Such behaviour was already observed in p–Pb collisions at lower energies [169] and in Pb–Pb collisions [187].
In order to extract the integrated yields ($\mathrm{d}N/\mathrm{d}y$) for both particle species, extrapolation to the unmeasured regions has been performed by fitting the transverse momentum spectra with the Lévy-Tsallis functional form, and adding the integral over such region to the measured p_{T}–differential yield; the resulting values of $\mathrm{d}N/\mathrm{d}y$ are reported in Table 6.1. In the case of deuterons, the resulting yield in each multiplicity class is reported as well. Each p_{T}–integrated yield is normalized to the number of events, which is different in each multiplicity class. The minimum bias spectra are normalized to the overall number of anayzed events in our dataset, which is 37.85 millions. The most central multiplicity classes 0–10% and 10–20% represent the 10% each of the total number of events, the semiperipheral multiplicity class 20–40% the 21% of the total, and finally the

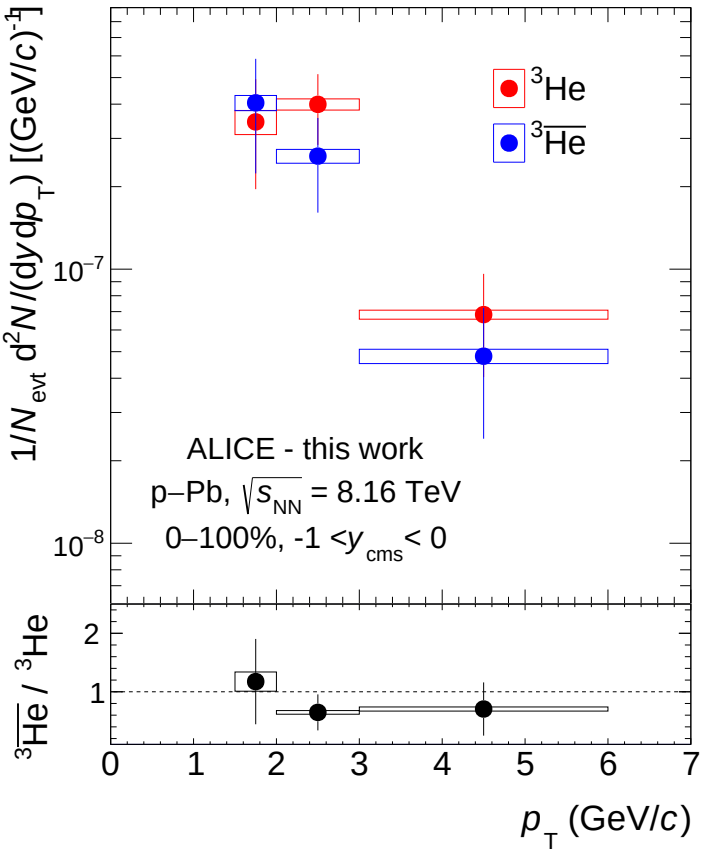

Figure 6.2: Transverse momentum spectra of (anti)^{3}He. In the bottom panel the antinuclei-to-nuclei ratio is shown. The statistical uncertainties are represented by vertical bars whereas boxes represent the systematic ones.

most peripheral class 40–100% covers the remaining 59% of the overall number of analyzed events.

In addition, the average spectra are fitted using different functional forms, obtaining similar results in the computation of the integrated yield and the mean transverse momentum, as discussed in the following. The fit of the average spectra are shown in Figs. 6.5 and 6.6, for average ^{3}He and average deuteron respectively. The used fit functions, in addition to the already mentioned Lévy-Tsallis one, are:

- Boltzmann:

$$\frac{d^2N}{dp_{\mathrm{T}}dy} = p_{\mathrm{T}} \cdot A_B \cdot m_T \cdot exp\left(\frac{-m_T}{T_B}\right) \tag{6.4}$$

- Boltzmann-Gibbs Blast Wave:

$$\frac{d^2N}{dp_{\mathrm{T}}dy} = A_{BW} \cdot m_T \cdot I_0\left(p_{\mathrm{T}}\frac{sinh\rho_0}{T_{BW}}\right) K_1\left(m_T\frac{cosh\rho_0}{T_{BW}}\right) \tag{6.5}$$

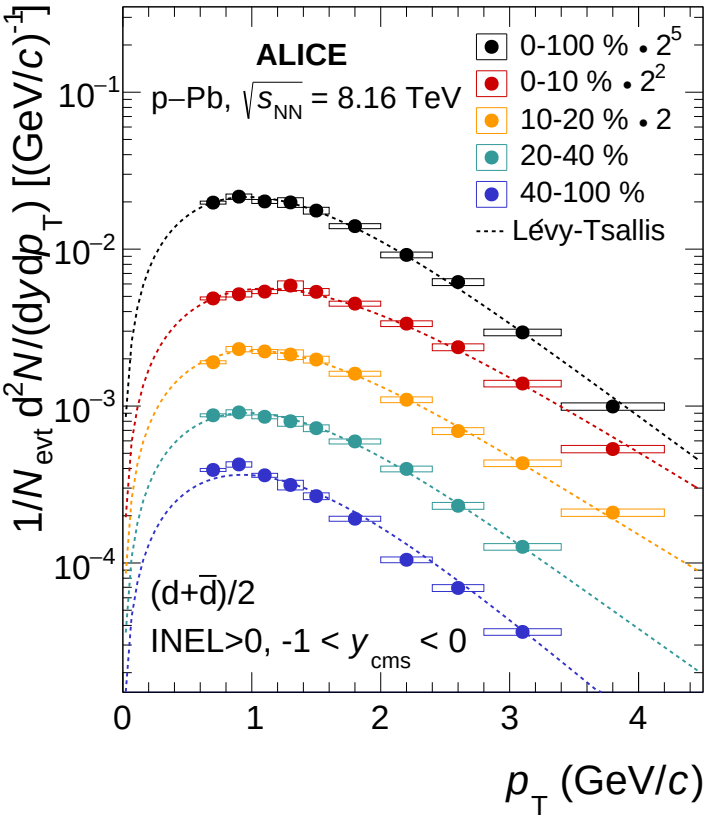

Figure 6.3: Transverse momentum spectra of the average deuterons and antideuterons, in different multiplicity classes. The p_{T} distributions are fitted by means of a Lévy-Tsallis function [186] in order to extrapolate to the unmeasured regions. Boxes represent the systematic uncertainties.

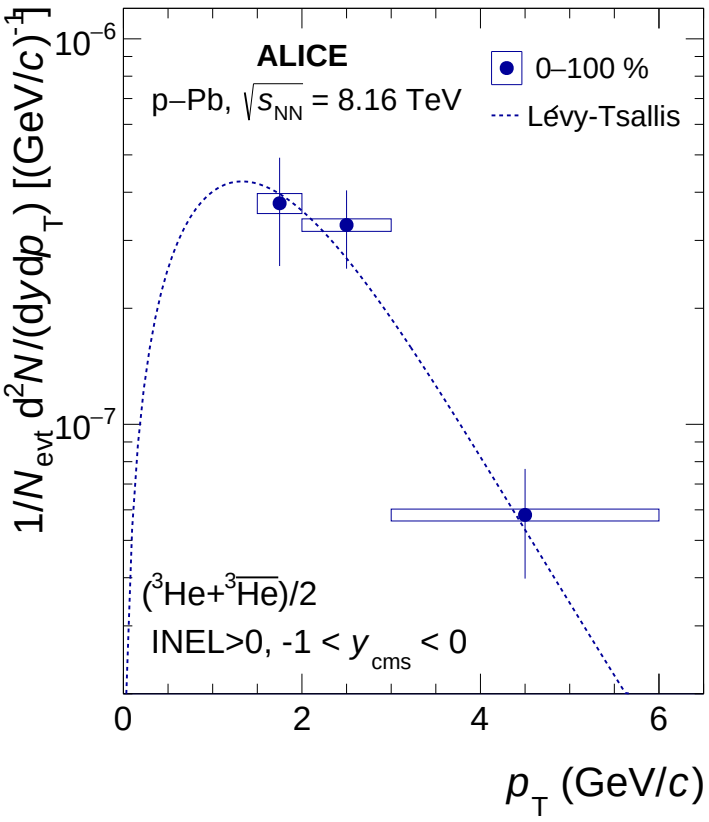

Figure 6.4: Transverse momentum spectrum of the average ^{3}He and $^3\overline{\text{He}}$, in the integrated–multiplicity class. The p_T distribution is fitted by means of a Lévy-Tsallis function [186] in order to extrapolate to the unmeasured regions. Lines represent statistical uncertainties while boxes represent the systematic ones.

- Bose-Einstein:

$$\frac{d^2N}{dp_T dy} = A_{BE} \cdot \frac{p_T}{exp\left(\frac{-m_T}{T_{BE}}\right) - 1} \tag{6.6}$$

Multiplicity class	$\langle \mathrm{d}N_{\mathrm{ch}}/\mathrm{d}\eta_{\mathrm{lab}} \rangle\big\vert_{\vert\eta_{\mathrm{lab}}\vert<0.5}$	$\mathrm{d}N/\mathrm{d}y$ [(d+$\overline{\mathrm{d}}$)/2]
min. bias	20.3 ± 0.6	$(1.27 \pm 0.01 \pm 0.04) \cdot 10^{-3}$
0-10%	47.8 ± 1.2	$(3.11 \pm 0.03 \pm 0.10) \cdot 10^{-3}$
10-20%	35.5 ± 0.9	$(2.31 \pm 0.02 \pm 0.07) \cdot 10^{-3}$
20-40%	26.9 ± 0.7	$(1.72 \pm 0.02 \pm 0.05) \cdot 10^{-3}$
40-100%	13.0 ± 0.4	$(6.43 \pm 0.07 \pm 0.20) \cdot 10^{-4}$
Multiplicity class	$\langle \mathrm{d}N_{\mathrm{ch}}/\mathrm{d}\eta_{\mathrm{lab}} \rangle\big\vert_{\vert\eta_{\mathrm{lab}}\vert<0.5}$	$\mathrm{d}N/\mathrm{d}y$ [(^{3}He+$^3\overline{\mathrm{He}}$)/2]
min. bias	20.3 ± 0.6	$(1.15 \pm 0.16 \pm 0.13) \cdot 10^{-6}$

Table 6.1: Integrated yields ($\mathrm{d}N/\mathrm{d}y$) of the average deuterons for each multiplicity class and the integrated–multiplicity class, and of the average ^{3}He in the integrated–multiplicity class calculated summing up the measured p_{T}–differential yield and the integral of the Lévy-Tsallis fit function in the unmeasured region. The statistical and the systematic uncertainties are reported as well. The mean charged-particle multiplicity density corresponding to each multiplicity class is also reported.

- Fermi-Dirac:

$$\frac{d^2N}{dp_{\mathrm{T}}dy} = p_{\mathrm{T}} \cdot A_{FD} \cdot \frac{1}{exp\left(\frac{m_T}{T_{FD}}\right) + 1} \tag{6.7}$$

- m_{T} exponential:

$$\frac{d^2N}{dp_{\mathrm{T}}dy} = p_{\mathrm{T}} \cdot A_{m_T} \cdot exp\left(-\frac{-m_T}{T_{m_T}}\right) \tag{6.8}$$

- Power law

$$\frac{d^2N}{dp_{\mathrm{T}}dy} = A_{PL}\left(1 + \frac{p_T}{p_{T0}}\right)^{-n} \tag{6.9}$$

where A_B, A_{BW}, A_{BE}, A_{FD}, A_{m_T} and A_{PL} are normalization factors, m_{T} is the transverse mass, m is the mass of the nucleus, T_B, T_{BW}, T_{BE}, T_{FD} and T_{m_T} are temperatures, I_0 and K_1 are the modified Bessel functions of

the first and second kinds respectively, and finally ρ_0 is the boost angle defined as $\rho_0 = tanh^{-1}(\beta(r))$, being $\beta(r)$ given by the surface velocity times the radius of the nucleus raised to the power of the velocity profile. More details on the modified Blast-Wave function can be found in [188]. For all the fits the mass was fixed at 2.81 GeV/c^2 in the case of ^{3}He and at 1.87 GeV/c in the case of deuterons. For the Blast-Wave fit also the temperature was fixed at 160 MeV and the velocity profile at 1.3, so that the free parameters were just two.

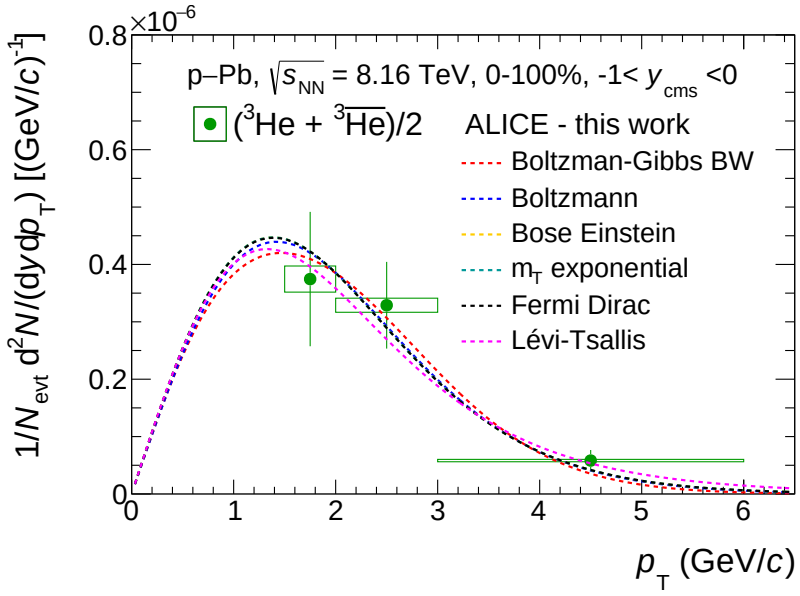

Figure 6.5: Transverse momentum spectra of the average ^{3}He and $^3\overline{\text{He}}$, in the integrated multiplicity class. The p_{T} distribution is fitted by means of several functions, as described in the text, in order to extrapolate to the unmeasured regions. Boxes represent the systematic uncertainties, while lines represent the statistical ones.

To estimate the statistical uncertainty in the yield, for both particle species, the Gaussian sampling method is used, consisting in the shift of the average (anti)nuclei data points using a random Gaussian distribution centered at the measured value of each p_{T} interval, with a standard deviation given by the statistical uncertainty of each point. Also the value of the extrapolated yield calculated as the integral of the fit function is

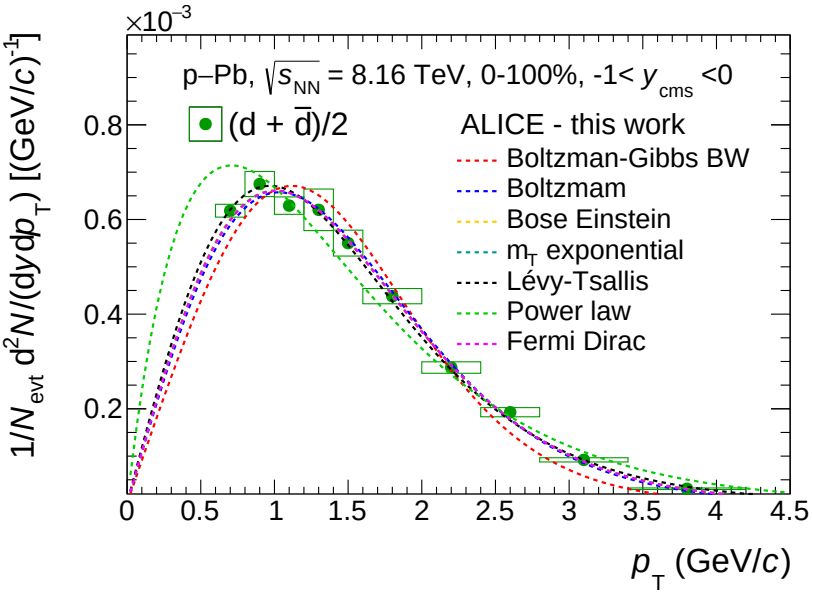

Figure 6.6: Transverse momentum spectra of the average d and $\overline{\mathrm{d}}$, in the integrated multiplicity class. The p_{T} distribution is fitted by means of several functions, as described in the text, in order to estimate the statistical and systematic uncertainties related to the extrapolation to the unmeasured regions. Boxes represent the systematic uncertainties, while lines represent the statistical ones.

Fit function	**Mean**	**RMS**	**Statistical uncertainty**
Blast-Wave	$1.13 \cdot 10^{-6}$	$1.51 \cdot 10^{-7}$	13 %
Boltzmann	$1.15 \cdot 10^{-6}$	$1.69 \cdot 10^{-7}$	15 %
Bose-Einstein	$1.17 \cdot 10^{-6}$	$1.71 \cdot 10^{-7}$	15 %
m_{T}–exponential	$1.16 \cdot 10^{-6}$	$1.71 \cdot 10^{-7}$	15 %
Fermi-Dirac	$1.16 \cdot 10^{-6}$	$1.71 \cdot 10^{-7}$	15 %
Lévy-Tsallis	$1.17 \cdot 10^{-6}$	$1.30 \cdot 10^{-7}$	11 %

Table 6.2: Results of the statistical uncertainties in the ^{3}He yield calculated using several functional forms.

varied, refitting the varied p_{T} spectra using all the functions mentioned above (using the power law in the case of deuterons only). This procedure

Fit function	Mean	RMS	Statistical uncertainty
Blast-Wave	$1.25 \cdot 10^{-3}$	$7.45 \cdot 10^{-6}$	1 %
Boltzmann	$1.25 \cdot 10^{-3}$	$7.50 \cdot 10^{-6}$	1 %
Bose-Einstein	$1.26 \cdot 10^{-3}$	$7.51 \cdot 10^{-6}$	1 %
m_{T}–exponential	$1.26 \cdot 10^{-3}$	$7.51 \cdot 10^{-6}$	1 %
Lévy-Tsallis	$1.28 \cdot 10^{-3}$	$7.60 \cdot 10^{-6}$	1 %
Power law	$1.38 \cdot 10^{-3}$	$8.00 \cdot 10^{-6}$	1 %
Fermi-Dirac	$1.26 \cdot 10^{-3}$	$7.51 \cdot 10^{-6}$	1 %

Table 6.3: Results of the statistical uncertainties in the d yield calculated using several functional forms.

has been repeated 1000 times for each functional form and the statistical uncertainty is estimated as the mean value of the ratio between the RMS and the mean value of each varied yield distribution (as shown in Fig. 6.7 for the Bose Einstein and the Lévy-Tsallis examples for both particle species). The results are summarized in Table 6.2 for ^{3}He and in Table 6.3 for d.

For the systematic uncertainty in the yields of both particle species, p_{T}–correlated and uncorrelated uncertainties have been treated differently in the error propagation. This approach, based on a better knowledge of detector effects, allowed us to reduce by a factor ~ 3 the uncertainties with respect to previous similar results [169]. The uncertainties due to secondary nuclei estimate, material budget, signal extraction, hadronic interaction - and TPC-TOF matching efficiency for (anti)d - are considered p_{T}–correlated, whereas the uncertainties due to track selection, signal loss efficiency and ITS-TPC matching efficiency - and to triton contamination subtraction for (anti)^{3}He - are considered uncorrelated in transverse momentum. Data points in the spectra are shifted upwards and downwards by the correlated part of the systematic uncertainties and refitted to provide extrapolated values. The semidifference between the two shifted values represents the p_{T}–correlated part of the systematic uncertainty. To evaluate the p_{T}–uncorrelated contribution to the total systematic uncertainty of the yield, the data points are shifted using the Gaussian sampling method. This contribution to the total systematic uncertainty in the

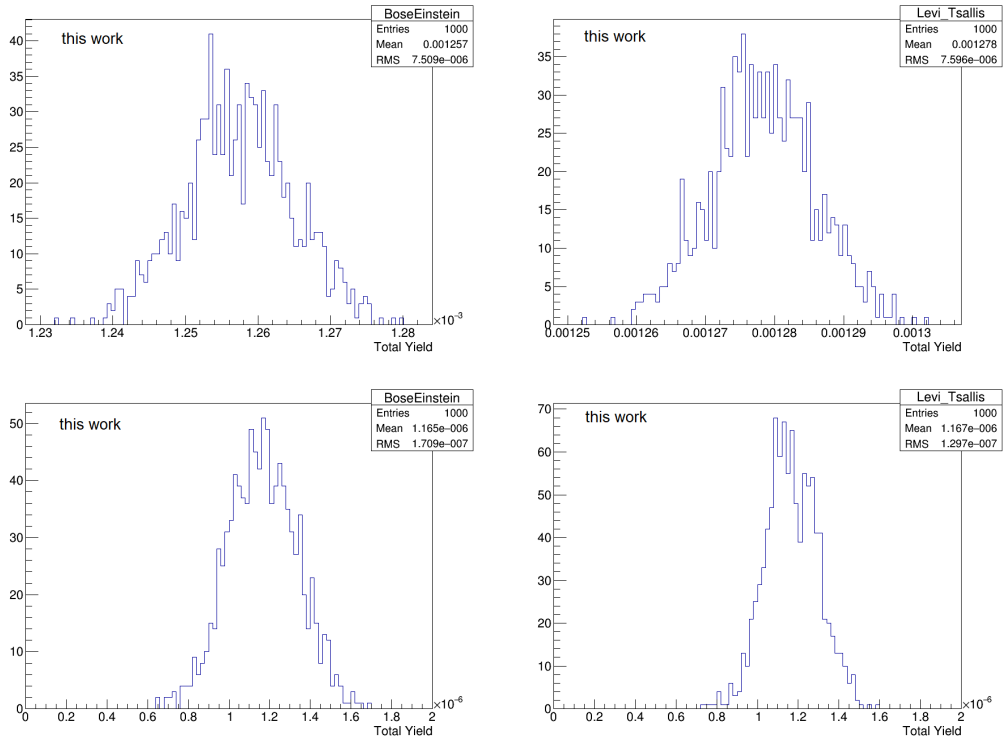

Figure 6.7: The upper plots show the varied yield to calculate the statistical uncertainty on the deuteron total yield, using the Bose Einstein (left) and the Lévy-Tsallis (right) functional forms; similar distributions for ^{3}He are shown in the bottom panels.

yield amounts to 3.0 % for d and to 11.0 % for ^{3}He. Additionally, the contribution given by the spread between the values obtained by different fit functions is also considered to estimate the systematic uncertainty in the yield. The spectra are refitted using the functions already used to estimate the statistical uncertainty. In this case, half the difference between the maximum and the minimum yield is taken as systematic uncertainty, resulting to be less than 1.0 % for d and 3.0 % for ^{3}He. All the discussed contributions have been finally summed in quadrature. The statistical and systematic uncertainties calculated for the multiplicity–integrated yields are applied for all multiplicity class results as well.

Finally, in Fig. 6.8 the yield divided by the spin degeneracy factor

Fit function	Systematic uncertainty	
	(^{3}He+$^3\overline{\text{He}}$)/2	(d+$\overline{\text{d}}$)/2
Blast-Wave	10 %	3.1 %
Boltzmann	12 %	3.0 %
Bose-Einstein	12 %	3.2 %
m_{T}–exponential	12 %	3.1 %
Fermi-Dirac	12 %	2.9 %
Lévy-Tsallis	8 %	2.9 %

Table 6.4: Results of the systematic uncertainty in the yield, for the average (anti)^{3}He and (anti)d spectra.

(2J+1) as a function of the mass number is reported. While protons and ^{3}He nuclei are fermions, having half–integer spin 1/2, deuterons are bosons and have integer spin, J = 1. The results of protons (taken from [189]), together with those of deuterons and ^{3}He presented in this thesis are compared to protons, deuterons and ^{3}He results from p–Pb collisions at 5.02 TeV [64]. From the exponential fit of such results, for each collision system, the freeze-out temperature can be estimated, testing the thermal-statistical hadronization model. The temperatures estimated with the fit function described in the following, are reported in Table 6.5:

$$\frac{dN/dy}{(2J+1)} = C \cdot exp(-m/T) \tag{6.10}$$

being C a normalization factor, m the mass of particles and T the freeze-out temperature. The results are in agreement with the expectations of the model [90].

Collision system	T (MeV)
p–Pb 5.02 TeV	154.19 $\pm$ 0.13
p–Pb 8.16 TeV	154.91 $\pm$ 0.19

Table 6.5: Results of the exponential fit to the yields of protons, deuterons and ^{3}He measured in p–Pb collisions at $\sqrt{s_{\text{NN}}}$ = 5.02 and $\sqrt{s_{\text{NN}}}$ = 8.16 TeV.

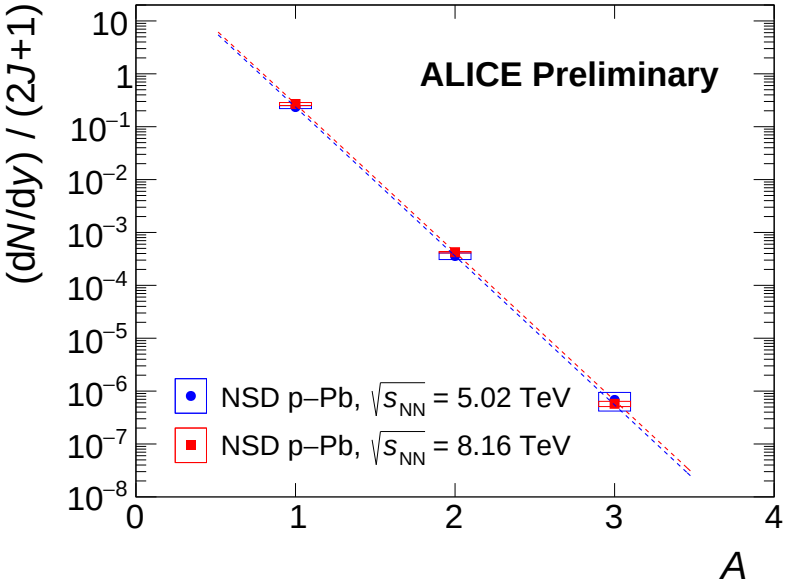

Figure 6.8: Yields of protons, deuterons and ^{3}He obtained in p–Pb collisions at 5.02 and 8.16 TeV, as a function of the mass number A.

6.1.2 Average transverse momentum

Based on the extrapolation with the fit functions, also the mean transverse momentum $\langle p_{\mathrm{T}} \rangle$ of average (anti)^{3}He and average (anti)d are calculated, in the latter case for several multiplicity classes. The $\langle p_{\mathrm{T}} \rangle$ is calculated as the mean value of the Lévy-Tsallis fit for each spectrum. The statistical uncertainty of $\langle p_{\mathrm{T}} \rangle$ is estimated through the Gaussian sampling method, as already illustrated for the statistical uncertainty of the yield. The spectra are fitted with all the functions used in the previous Section, and the statistical uncertainty is taken as the mean value of each uncertainty, resulting to be about 1% for deuterons and about 10 % for ^{3}He. For the systematic uncertainty of $\langle p_{\mathrm{T}} \rangle$, the Gaussian sampling method is used as well, since the systematic uncertainties are considered fully uncorrelated. This uncertainty results to be about 1.5 % for deuterons and about 3 % for ^{3}He. The results are reported in Table 6.6.
Finally, in Fig. 6.9 the deuteron $\langle p_{\mathrm{T}} \rangle$ as a function of the mean charged-particle multiplicity is shown and compared to similar results from the

(d+$\overline{\text{d}}$)/2 centrality class	$\langle\, p_{\mathrm{T}} \,\rangle$ (GeV/c)
min. bias	1.45 $\pm$ 0.02 $\pm$ 0.02
0-10 %	1.70 $\pm$ 0.02 $\pm$ 0.03
10-20 %	1.59 $\pm$ 0.02 $\pm$ 0.03
20-40 %	1.46 $\pm$ 0.02 $\pm$ 0.02
40-100 %	1.36 $\pm$ 0.02 $\pm$ 0.02
(^{3}He+$^3\overline{\text{He}}$)/2	2.08 $\pm$ 0.20 $\pm$ 0.06

Table 6.6: Mean transverse momentum of the average (anti)d for each multiplicity class and of the average (anti)^{3}He spectrum. The statistical and the systematic uncertainties are reported as well. The average p_{T} is obtained from the Lévy-Tsallis fit for the average (anti)deuteron spectrum, whereas for the (anti)^{3}He the average of all used functional forms is taken.

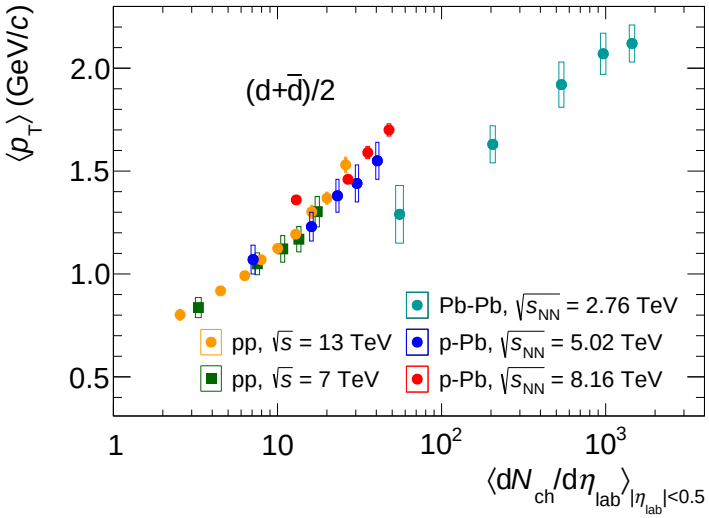

Figure 6.9: Mean p_{T} of the average deuterons as a function of $\langle \mathrm{d}N_{\mathrm{ch}}/\mathrm{d}\eta_{\mathrm{lab}} \rangle$, in comparison with other results obtained in different collision systems and energies.

ALICE Collaboration in different collision systems and at different energies [59, 62, 65, 111]. Such a comparison is very interesting because the average transverse momentum seems to have a common behaviour as

a function of multiplicity, for pp and p–Pb collisions, independent of the collision energy. The mean p_{T} seems to increase smoothly, in the low and intermediate multiplicity interval covered by pp and p–Pb collisions. The high multiplicity region covered by Pb–Pb collisions, instead, seems to have a different increasing trend, although maintaining a similar slope for increasing multiplicity. A smooth increasing trend of the average transverse momentum as a function of multiplicity is also observed for ^{3}He nuclei, as shown in Fig. 6.10, together with previous results from ALICE [64, 105, 111]. In this case, the same trend is observed for all collision systems and energies, spanning the whole multiplicity interval, although the available data for such a comparison are fewer than for deuterons.

These results can be compared to the experimental results on the average transverse momentum of non-identified charged particles, extensively described in [190]. According to such results, we expected a weak dependence on the collision energy for each collision system, and a different

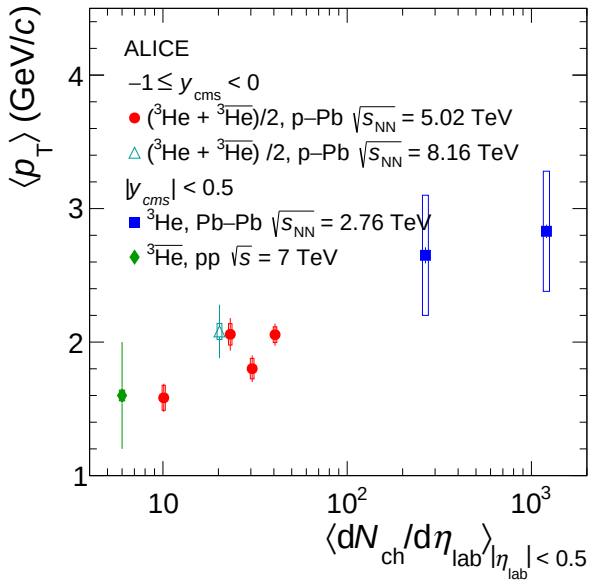

Figure 6.10: Mean p_{T} of the average ^{3}He as a function of the mean charged-particle multiplicity density $\langle \mathrm{d}N_{\mathrm{ch}}/\mathrm{d}\eta_{\mathrm{lab}} \rangle$, together with similar results obtained in different collision systems and energies.

behaviour depending on the collision system.

In the left panel of Fig. 6.11, the results from pp collisions at several energies are shown. The trend is increasing as a function of multiplicity for all energies, although the slope is slightly different. Nevertheless, the energy dependence on $\langle p_{\mathrm{T}} \rangle$ is rather weak, as observed in our comparison plots both for pp and p–Pb collisions at different energies (Figs. 6.9-6.10).

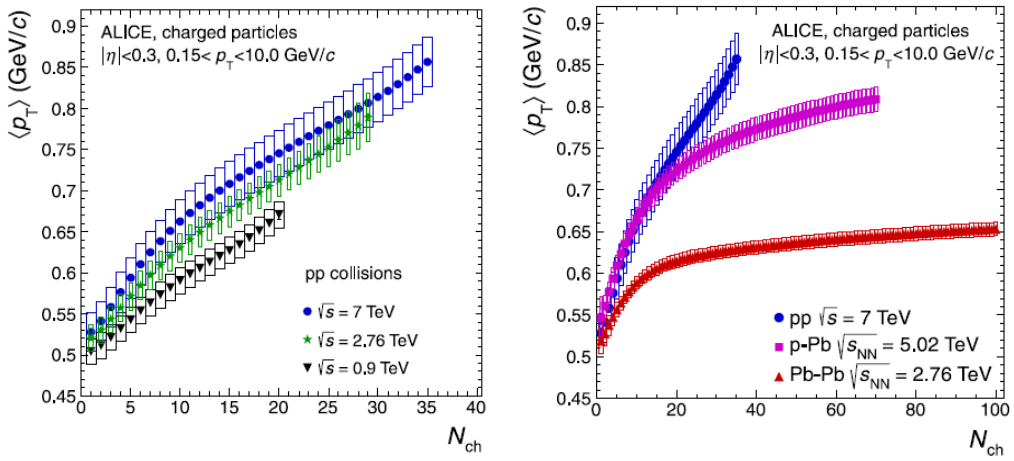

Figure 6.11: *Left.* Average transverse momentum of charged particles in the range $0.15 < p_{\mathrm{T}} < 10.0$ GeV/c as a function of charged-particle multiplicity in pp collisions at different energies ($\sqrt{s}$ = 0.9, 2.76, and 7 TeV), for $|\eta| < 0.3$. The boxes represent the systematic uncertainties on $\langle p_{\mathrm{T}} \rangle$. The statistical errors are negligible. *Right.* Average transverse momentum of charged particles versus charged-particle multiplicity in different collision systems (pp, p–Pb, Pb–Pb), for $|\eta| < 0.3$. The boxes represent the systematic uncertainties on $\langle p_{\mathrm{T}} \rangle$, whereas the statistical errors are negligible. Both figures are taken from [190].

On the other hand, looking at the right panel of Fig. 6.11, the $\langle p_{\mathrm{T}} \rangle$ shows a different behaviour depending on the collision system. In p–Pb collisions, an increase of $\langle p_{\mathrm{T}} \rangle$ with charged-particle multiplicity N_{ch} is observed, with $\langle p_{\mathrm{T}} \rangle$ values similar to the values in pp collisions up to $N_{ch} \sim 14$. At multiplicities above $N_{ch} \sim 14$, the measured $\langle p_{\mathrm{T}} \rangle$ is lower in p–Pb collisions than in pp collisions; the difference is more pronounced with increasing N_{ch}. This difference cannot be attributed to the differ-

ence in collision energy, as discussed above, and this behaviour is not reproduced in our comparison plots of light nuclei. In contrast, in Pb–Pb collisions, with increasing N_{ch}, there is only a moderate increase in $\langle p_{\mathrm{T}} \rangle$ up to high charged-particle multiplicity with a maximum value of $\langle p_{\mathrm{T}} \rangle$ = 0.685 $\pm$ 0.016 (syst) GeV/c, which is substantially lower than the maximum value in pp. Such plateau-like trend is not reproduced in our results either.
The p–Pb data exhibit features of both pp and Pb–Pb collisions, at low and high multiplicities, respectively. However, the saturation trend of $\langle p_{\mathrm{T}} \rangle$ versus N_{ch} is less pronounced in p–Pb than in Pb–Pb collisions and leads to a much higher value of $\langle p_{\mathrm{T}} \rangle$ at high multiplicities than in Pb–Pb. In conclusion, the behaviour of non-identified charged-particle $\langle p_{\mathrm{T}} \rangle$ is quite similar to that of d and ^{3}He, in the low and intermediate multiplicity intervals. The high multiplicity region, instead, shows an increasing trend for the light nuclei $\langle p_{\mathrm{T}} \rangle$, whereas the charged-particle average transverse momentum reaches a plateau at lower values.

6.1.3 Antiparticle-to-particle ratios

The antinucleus-to-nucleus ratio is measured in several multiplicity classes for deuterons and in the integrated–multiplicity class for ^{3}He, as presented in Fig. 6.12.

A weigthed mean is calculated in order to obtain the antinucleus-to-nucleus ratio and the uncertainty of the weigthed mean is taken as statistical uncertainty on such ratio. For the systematic uncertainty, the correlated and uncorrelated between particles and antiparticles parts of the systematic uncertainties are treated differently in the error propagation. The uncertainties due to track selection, material budget and feed-down fraction are considered correlated between particles and antiparticles, whereas the uncertainties due to hadronic cross section, primary fraction and the triton contamination are considered uncorrelated between (anti)nuclei. Therefore, the uncertainty of the antiparticle-to-particle ratio

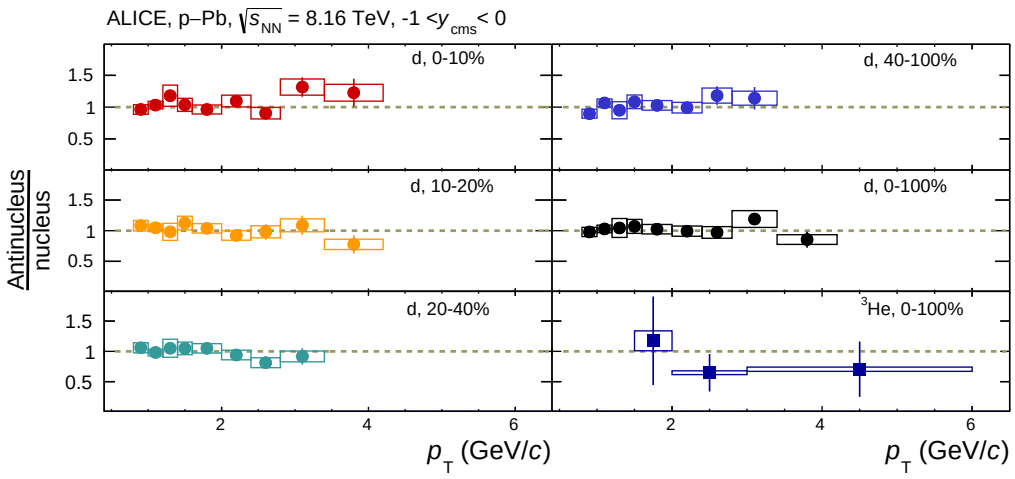

Figure 6.12: Antinuclei-to-nuclei ratios in different multiplicity classes. The statistical uncertainties are represented by vertical bars whereas boxes represent the systematic uncertainties. The dotted grey line is fixed at 1, in order to guide the eye towards the expected value of the ratio.

is calculated using the following equation:

$$\frac{\Delta R}{R} = \sqrt{\left(\frac{\Delta \overline{A}}{\overline{A}}\right)^2_{uncorr} + \left(\frac{\Delta A}{A}\right)^2_{uncorr} + \left(\frac{\Delta \overline{A}}{\overline{A}} - \frac{\Delta A}{A}\right)^2_{corr}} \tag{6.11}$$

being $\Delta A/A$ the systematic uncertainty of the nucleus in each p_T interval and $\Delta\overline{A}/\overline{A}$ that of the antinucleus.
In order to calculate such ratio with the proper uncertainty, the points of the antinucleus-over-nucleus have been shifted upwards and downwards by their systematic uncertainty, as shown in Fig. 6.13. Therefore, a weighted mean of such values is calculated, using as weight the statistical uncertainty of the ratio. The final uncertainty is given by the semidifference of the shifted weighted mean values. The results of the weighted mean for the three configurations are summarized in Table 6.7.
The resulting ratios of both $\overline{\mathrm{d}}/\mathrm{d}$ and $^3\overline{\mathrm{He}}/^3\mathrm{He}$ for all multiplicity classes in p–Pb collisions at 8.16 TeV are consistent with unity within uncertainties, as already observed in other collision systems and center-of-mass

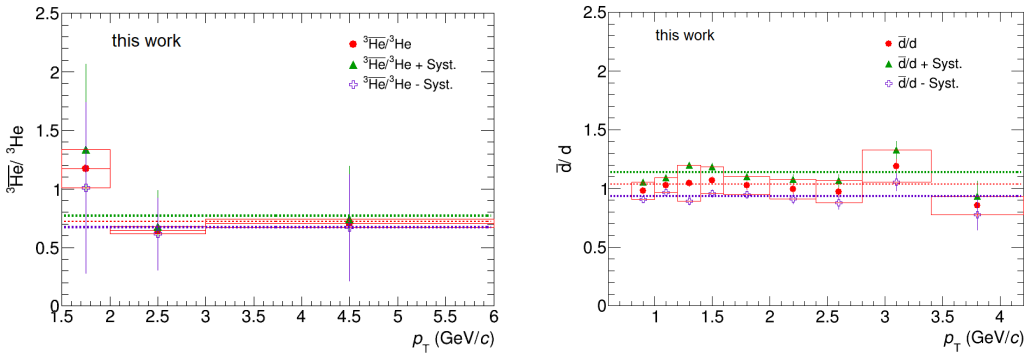

Figure 6.13: In red the weighted mean of the antinucleus-over-nucleus ratio is represented. The weight is given by the statistical uncertainty. The data are shifted upwards and downwards by their systematic uncertainties (green and violet symbols respectively).

energies by ALICE [60, 62, 64, 65, 105] and expected in case of vanishing baryochemical potential at the LHC [103].

	$^3\overline{\mathrm{He}}$-to-^{3}He ratio
Central values	0.72 $\pm$ 0.24 (stat.)
Central values + systematic	0.77 $\pm$ 0.24 (stat.)
Central values - systematic	0.67 $\pm$ 0.24 (stat.)
	$\overline{\mathrm{d}}$-to-d ratio
Central values	1.03 $\pm$ 0.01 (stat.)
Central values + systematic	1.14 $\pm$ 0.01 (stat.)
Central values - systematic	0.94 $\pm$ 0.01 (stat.)

Table 6.7: Results of the weighted mean of antinucleus-over-nucleus ratio in the three configurations described in the text.

6.2 Comparison to models

6.2.1 Coalescence parameters

The production of light (anti)nuclei can be explained via the coalescence of protons and neutrons which are close in phase space at the freeze-out and match the spin, thus forming a nucleus [109]. As already discussed in Chapt. 2, the key parameter of the coalescence models is the coalescence parameter, which is given by the ratio between the invariant yield of the nucleus with mass number A and that of protons to the power of A, being $p_{\mathrm{T}}^{\mathrm{p}} = p_{\mathrm{T}}^{A}/A$, calculated as follows:

$$B_A = \left(\frac{1}{2\pi p_{\mathrm{T}}^{A}}\left(\frac{d^2N}{dydp_{\mathrm{T}}}\right)_A\right) \Big/ \left(\frac{1}{2\pi p_{\mathrm{T}}^{p}}\left(\frac{d^2N}{dydp_{\mathrm{T}}}\right)_p\right)^A \tag{6.12}$$

The coalescence parameter is related to the production probability of the nucleus via this process and can be calculated from the overlap of the nucleus wave function and the phase space distribution of the constituents via the Wigner formalism [118].

The coalescence model can be tested through the calculation of the B_A coalescence parameter, which relates the production of light nuclei to that of its constituents. For this purpose, B_2 and B_3 parameters have been calculated using deuterons and ^{3}He, respectively. For this calculation, neutrons and protons are assumed to have the same transverse momentum spectra, since the former cannot be measured. For the proton yield, results taken from [189] have been used. Since the ^{3}He analysis is carried out only for minimum bias events, proton spectra from several multiplicity classes have been averaged in order to obtain the multiplicity-integrated spectrum. Similarly, the multiplicity intervals of protons have been averaged in order to match those of deuterons as well, as shown in Fig. 6.14. Moreover, to match the ^{3}He and deuterons transverse momentum intervals, proton spectra have been interpolated using the Blast-Wave function (as shown in Fig. 6.15 for the minimum bias ^{3}He spectrum), which is the functional form used in [189] to fit the proton spectra.

In order to take into account the non-flat shape of the transverse momentum distribution of protons inside each p_{T} interval of ^{3}He and deuteron, the integral of the Blast-Wave function divided by the bin width

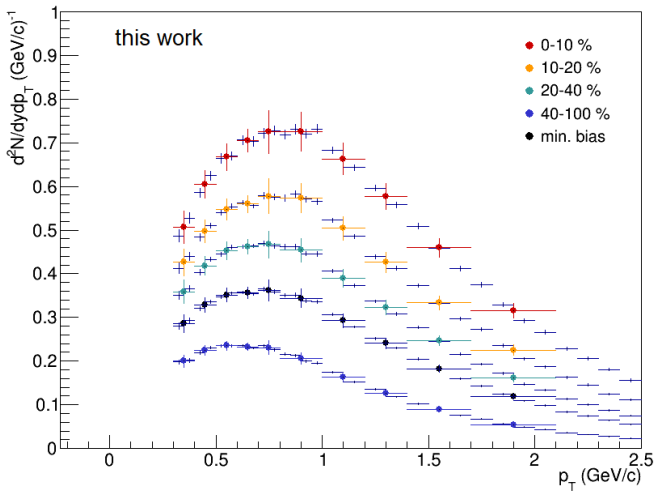

Figure 6.14: Blue dots show the original spectra of protons as shown in [189], averaged in the multiplicity classes of deuterons, whereas the coloured points show the average spectra of protons in the corresponding transverse momentum intervals of deuterons. Lines indicate the systematic uncertainties, whereas statistical uncertainties are negligible.

is taken as interpolation value. Statistical errors have been calculated using the Gaussian sampling method inside each p_{T} interval. Finally, systematic uncertainties have been calculated assuming them to be fully correlated in transverse momentum and therefore shifting upwards and downwards the values of the proton yield by their uncertainties, re-fitting the spectra and finally calculating the uncertainty as half the difference between the yields.

In Fig. 6.16 the coalescence parameters B_2 and B_3 as a function of the transverse momentum per nucleon (p_{T}/A) are shown, measured for (anti)d and (anti)^{3}He, respectively. Statistical and systematic uncertainties of the coalescence parameter related to nucleus A have been calculated with error propagation:

$$(\Delta B_A)^2 = \left(\frac{x\Delta Y^A}{(yY^p)^3}\right)^2 + \left(3y\frac{xY^A\Delta Y^p}{(yY^p)^4}\right)^2 \tag{6.13}$$

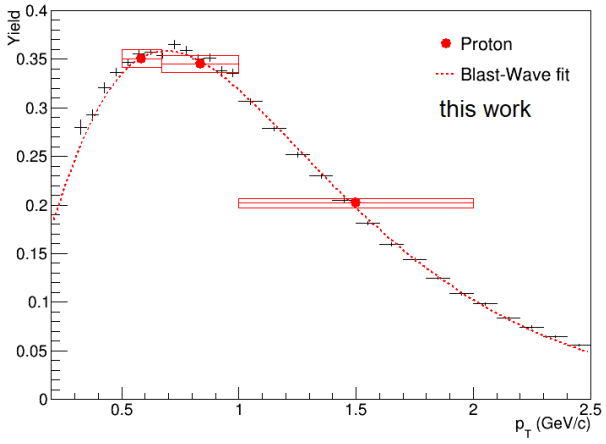

Figure 6.15: Black points and lines refer to the proton yield taken from [189], averaged to obtain the minimum bias spectrum, in the original transverse momentum intervals. The dotted red line represents the Blast-Wave fit and the red dots show the interpolated values of proton yields to match the ^{3}He transverse momentum spectrum.

being Y the yield, ΔY the uncertainty of the yield (stat. or syst.), and:

$$x = \frac{1}{2\pi p_{\mathrm{T}}^{A}}, \quad y = \frac{1}{2\pi p_{\mathrm{T}}^{p}} \tag{6.14}$$

Significant deviations from a flat trend are observed for both B_2 in all multiplicity classes and B_3. A similar trend of coalescence parameters with increasing p_{T} is also observed in recent results from the ALICE Collaboration [64, 65]. As discussed in Chapt. 2, the simple coalescence model, where only momentum correlations are considered, predicts a flat trend of the coalescence parameters with p_{T}/A for a fixed multiplicity. It was already demonstrated that, under the hypothesis of the simple coalescence model, the coalescence parameter develops an increasing trend within a wide multiplicity interval because of the different hardening of the proton and nucleus spectra with multiplicity [61]. This could explain the increasing trend of B_2 in the multiplicity intervals used for this measurement. However, a re-calculation of the coalescence parameter B_3 measured in p–Pb collisions at $\sqrt{s_{\mathrm{NN}}}$ = 5.02 TeV under the hypothesis of the

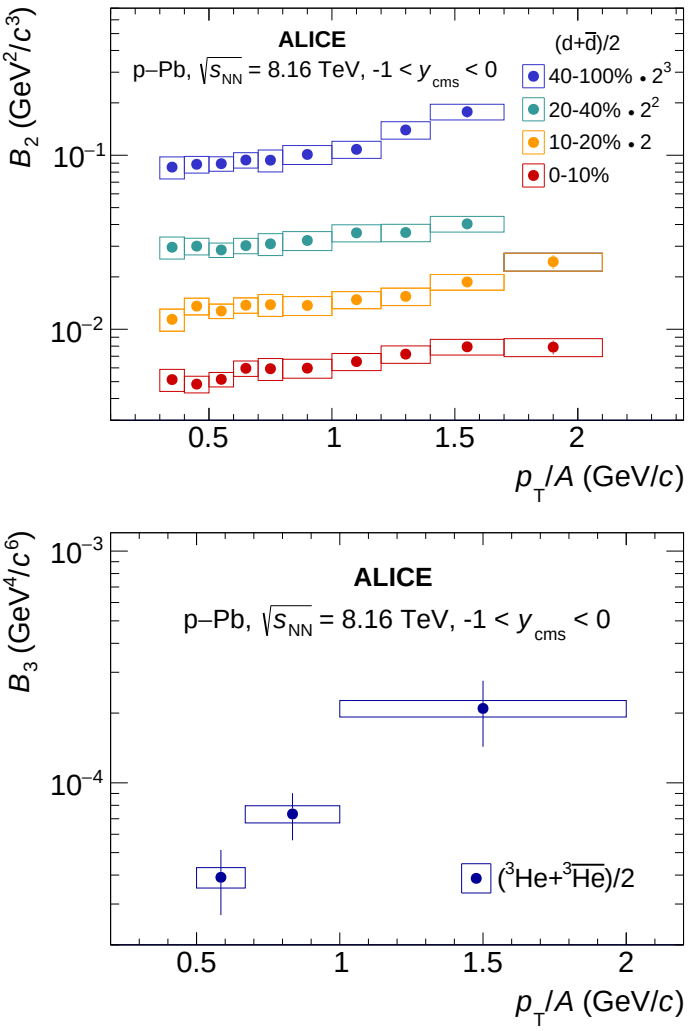

Figure 6.16: Coalescence parameters B_2 (top panel) and B_3 (bottom panel) as a function of p_T/A, measured for deuterons and ^{3}He respectively. In the case of ^{3}He, the B_3 is calculated in the integrated-multiplicity class, while for deuterons the B_2 are calculated for each multiplicity class. Statistical uncertainties are represented as vertical lines whereas boxes represent the systematic ones.

simple coalescence model did not reproduce the experimental data [64]. This implies that the increase of B_3 with p_T/A cannot be fully explained

by this kinematic effect and it is therefore a genuine physical effect.

In order to investigate the dependence of the coalescence probability on the size of the particle emitting source, as suggested by state-of-the-art coalescence models [45, 50, 130], the B_2 parameters extracted in several collision systems and LHC energies are compared as a function of the charged-particle multiplicity for a fixed value of p_{T}/A in Fig. 6.17.

The measurements show a smooth transition from low to high charged-particle multiplicity densities, which correspond to an increasing system size. The decreasing trend of B_A with increasing multiplicity suggests that the dominant production mechanism evolves smoothly as a function of the system size and is independent of the collision system and center-of-mass energy. The experimental results are compared to the theoretical calculations from coalescence [45], using two different parameterizations of the size of the source as a function of multiplicity. Parameterization A is based on a fit of the source radii measured by ALICE as a function of multiplicity using femtoscopic techniques [44]. Parameterization B, instead, uses parameters constrained to reproduce the B_2 of deuterons as extracted by ALICE in central (0–10%) Pb–Pb collisions at $\sqrt{s_{\mathrm{NN}}}$ = 2.76 TeV. Parameterization B is less favoured by the p–Pb at $\sqrt{s_{\mathrm{NN}}}$ = 8.16 TeV results with respect to the parameterization A.

Future dedicated studies of the relation between source size and multiplicity (and as a function of p_{T}) will be crucial to further constrain or test the coalescence models.

6.2.2 Ratio to protons and pions

The ratio between the measured yields of nuclei and that of protons is also sensitive to the light nuclei production mechanism. In Fig. 6.18 the yield ratios to protons for deuterons (top panel), ^{3}H and ^{3}He (bottom panel) as a function of $\langle \mathrm{d}N_{\mathrm{ch}}/\mathrm{d}\eta_{\mathrm{lab}} \rangle$ measured in pp, p–Pb and Pb–Pb collisions [58, 60, 169] are shown and compared to the expectations of the models. The canonical statistical model (CSM) calculations used correspond to a chemical freezeout temperature of 155 MeV and correlation volumes extending from one to three units of rapidity [101]. For the coalescence calculations in the case of $A = 3$ nuclei, predictions from both two-body and three-body coalescence are considered [49]. In the

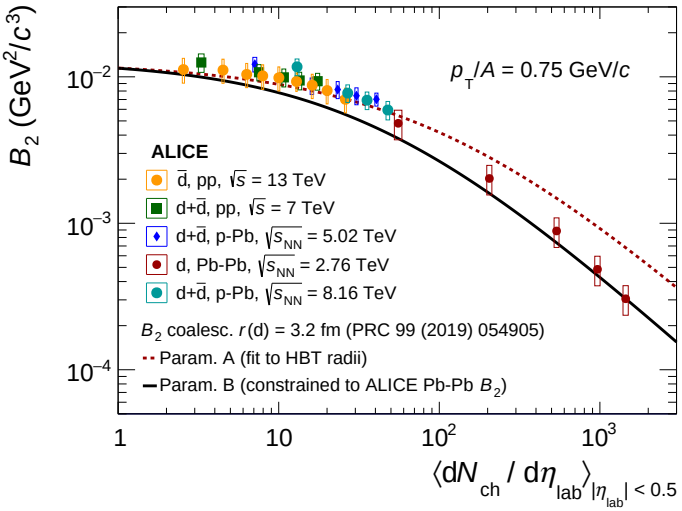

Figure 6.17: B_2 as a function of the mean charged-particle multiplicity density for a fixed value of $p_T/A = 0.75$ GeV/c. The experimental results are compared to the coalescence calculations from [45] using two different parametrizations for the system size as a function of the mean charged-particle multiplicity density.

two-body coalescence of ^{3}He (^{3}H), a two-step process is assumed: the deuteron is first formed by the coalescence of a proton and a neutron and then the ^{3}He (^{3}H) is formed by the coalescence of the deuteron and a proton (neutron). In the three-body coalescence, three nucleons directly form ^{3}He (^{3}H) at the same time.

A smooth increase of d/p and ^{3}He/p ratios with the system size is observed, reaching constant values in Pb–Pb collisions, in agreement with the grand-canonical statistical model [191]. The two ratios show a similar trend with $\langle dN_{ch}/d\eta_{lab} \rangle$, however the increase from pp to Pb–Pb results is about a factor of 3 larger for ^{3}He/p than for d/p.

The observed evolution of the d/p ratio is well described by the coalescence approach over the full multiplicity interval covered by the existing measurements. The CSM calculations asymptotically converge towards the grand-canonical limit at high multiplicity and they are both consistent with the Pb–Pb measurements at $\sqrt{s_{NN}} = 2.76$ TeV within the current uncertainties. At low and intermediate multiplicities, these calculations

provide only a qualitative description of this ratio, with the version using $V_c = dV/dy$ being consistent with the data at intermediate multiplicity and the version using $V_c = 3dV/dy$ at low multiplicity only.

The ^{3}He/p and ^{3}H/p ratios, shown in Fig. 6.18, are fairly well described by the coalescence approach at low and high charged-particle multiplicity densities, although significant discrepancies are observed at intermediate multiplicities, where the predictions overestimate the data. Similarly to the d/p ratio, the CSM calculations provide a qualitative description of the data at low and intermediate multiplicities and are closer to the data only in the grand-canonical limit. The high multiplicity behaviour of the nuclei-to-proton yield ratios will be better constrained with the upcoming results from Pb–Pb collisions at $\sqrt{s_{\rm NN}}$ = 5.02 TeV [192].

The consistency of models describing the hadron chemistry in high-energy hadronic collisions can be tested by comparing the model predictions with the measured yields for different hadron species, or alternatively, with yield ratios of different hadrons. This comparison is particularly important for the CSM considering that the description of the proton-to-pion yield ratio by state-of-the-art implementation of this model is not satisfactory. The predictions from the CSM model are shown in comparison with the measured nuclei-to-pion yield ratios in Fig. 6.19. For deuterons, the measured ratios are described only qualitatively at low and intermediate multiplicities, while the model predictions are consistent with the Pb–Pb data within uncertainties. For nuclei with A = 3, instead, the ratio to pion yields is in agreement with the expectations of the CSM across all multiplicities.

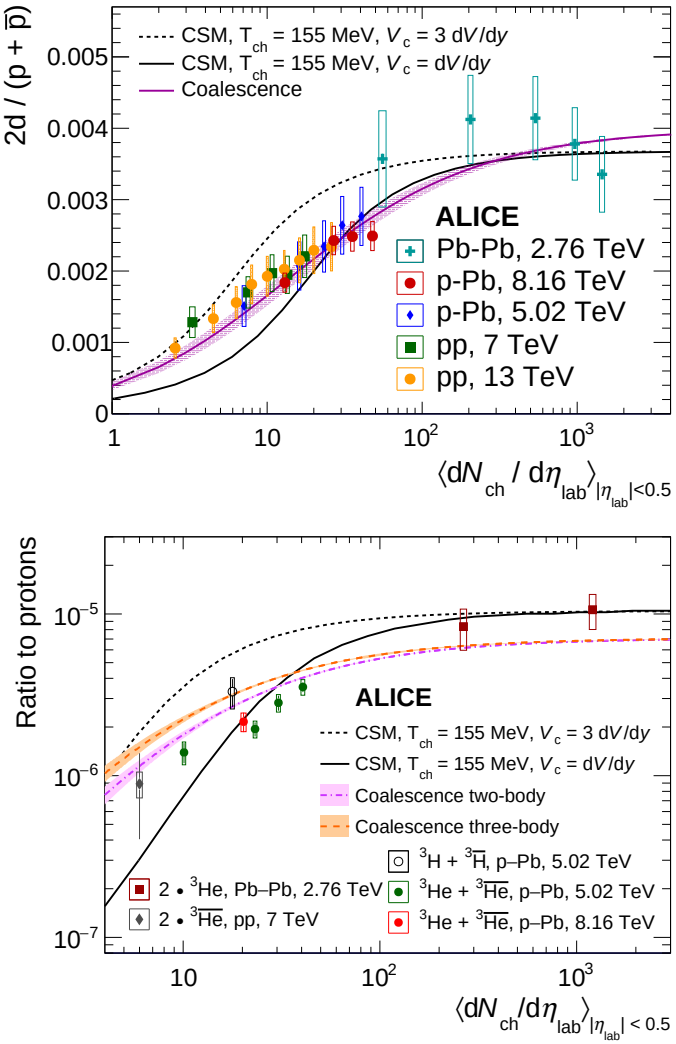

Figure 6.18: Deuteron (top panel), (anti)^{3}He and (anti)^{3}H (bottom panel) over proton ratios as a function of the charged-particle multiplicity in different collision systems and energies. Statistical uncertainties are represented as vertical lines whereas boxes represent the systematic ones. The results are compared to the expectations of SHM and Coalescence models.

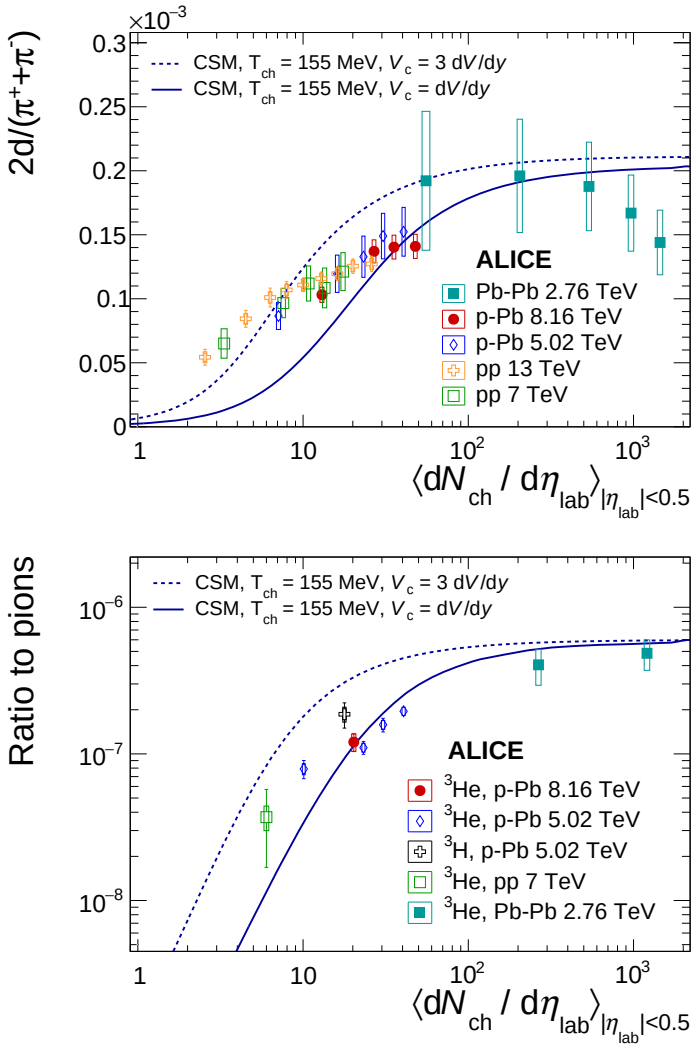

Figure 6.19: Deuteron (top panel), (anti)^{3}He and (anti)^{3}H (bottom panel) over pion ratios as a function of the charged-particle multiplicity in different collision systems and energies. Statistical uncertainties are represented as vertical lines whereas boxes represent the systematic ones. The results are compared to the expectations of vanilla CSM.

6.3 Conclusions

The first measurements of (anti)deuteron and (anti)^{3}He production in p–Pb collisions at $\sqrt{s_{\rm NN}}$ = 8.16 TeV have been presented and discussed. These results contribute to the understanding of the light (anti)nuclei production mechanism complementing the existing picture, which includes measurements done in different collision systems and center-of-mass energies.

A hardening of the (anti)deuteron $p_{\rm T}$ spectra with increasing multiplicity is observed, as already seen in previous results. The antiparticle-to-particle ratios, measured as a function of $p_{\rm T}$ and — in case of (anti)d — in several multiplicity classes, are consistent with unity within uncertainties, as expected at mid-rapidity at LHC energies. The average transverse momentum, in the low and intermediate multiplicity regions, shows features already observed in non-identified charged-particle $\langle p_{\rm T} \rangle$. In the high-multiplicity region, instead, an increasing trend of light nuclei average transverse momentum is observed, whereas the charged-particle $\langle p_{\rm T} \rangle$ reaches a plateau at a lower value of mean $p_{\rm T}$.

The production mechanisms of (anti)deuterons and (anti)^{3}He are investigated by comparing the multiplicity dependence of the coalescence parameters B_A and of their yields relative to protons and pions, to the predictions of the canonical statistical model and the coalescence model. A smooth evolution of these observables with multiplicity across different collision systems and energies is seen. The intermediate multiplicity range, which is covered in this measurement, is particularly interesting as it links existing results in pp and Pb–Pb collisions, corresponding to small and large system sizes, respectively. The results of B_2 as a function of the mean charged-particle multiplicity density show a good agreement with the coalescence model that uses the parameterization of the source radii based on femtoscopic techniques.

The results presented in this work, together with existing measurements in other multiplicity intervals, corroborate a better description of the deuteron production measurements by the coalescence model than by the canonical statistical hadronization model. However, in the case of the ^{3}He/p ratio, significant deviations are seen at intermediate multiplicities between the data and the predictions of both the two-body and the

three-body coalescence calculations.

Implementations of the CSM with a fixed correlation volume cannot describe quantitatively the nucleus-to-proton and the nucleus-to-pion ratios in the full multiplicity range spanned by the ALICE measurements, but capture the increasing trend qualitatively. At high multiplicity, CSM calculations are consistent with the data in the grand canonical limit.

The upcoming Run3 data will allow further and more precise measurements of light (anti)nuclei production, enhancing of a factor 10^3–10^4 the collected data. With such a large amount of available data it will be possible to span wider transverse momentum intervals and explore a finer multiplicity-differential study of such probes. Hence, more precise constraints of the hadronization models will be possible, to further discriminate among the production mechanisms so far hypotesized.

Bibliography

[1] E. V. Shuryak, "Quark-Gluon Plasma and Hadronic Production of Leptons, Photons and Psions," *Phys. Lett. B* **78** (1978) 150.

[2] Y. Ne'eman, "Derivation of strong interactions from a gauge invariance," *Nucl. Phys.* **26** (1961) 222–229.

[3] M. Gell-Mann, "A Schematic Model of Baryons and Mesons," *Phys. Lett.* **8** (1964) 214–215.

[4] G. Zweig, *An SU(3) model for strong interaction symmetry and its breaking. Version 2*. Lichtenberg, D. B. and Rosen, Simon Peter, 2, 1964.

[5] O. W. Greenberg, "QUARKS: RESOURCE LETTER Q-1," *Am. J. Phys.* **50** (1982) 1074–1089.

[6] E. Eichten, K. Gottfried, T. Kinoshita, J. B. Kogut, K. D. Lane, and T.-M. Yan, "The Spectrum of Charmonium," *Phys. Rev. Lett.* **34** (1975) 369–372. [Erratum: Phys.Rev.Lett. 36, 1276 (1976)].

[7] **MILC** Collaboration, A. Bazavov *et al.*, "Nonperturbative QCD Simulations with 2+1 Flavors of Improved Staggered Quarks," *Rev. Mod. Phys.* **82** (2010) 1349–1417, `arXiv:0903.3598 [hep-lat]`.

[8] G. Parisi, R. Petronzio, and F. Rapuano, "A Measurement of the String Tension Near the Continuum Limit," *Phys. Lett. B* **128** (1983) 418–420.

[9] K. A. Olive *et al.*, "Review of Particle Physics," *Chin. Phys. C* **38** (2014) 090001.

[10] M. Tanabashi *et al.*, "Review of Particle Physics," *Phys. Rev. D* **98** no. 3, (2018) 030001.

[11] M. E. Peskin and D. V. Schroeder, *An Introduction to quantum field theory*. USA: Addison-Wesley, 1995. https://physics.weber.edu/schroeder/qftbook.html.

[12] H. Suganuma, H. Ichie, F. Okiharu, and T. Takahashi, "Lattice qcd study for confinement and hadrons,".

[13] A. Yamamoto and H. Suganuma, "Relevant energy scale of color confinement from lattice QCD," *Phys. Rev. D* **79** (2009) 054504, arXiv:0811.3845 [hep-lat].

[14] P. Braun-Munzinger, V. Koch, T. Schäfer, and J. Stachel, "Properties of hot and dense matter from relativistic heavy ion collisions," *Phys. Rept.* **621** (2016) 76–126, arXiv:1510.00442 [nucl-th].

[15] M. G. Alford, A. Schmitt, K. Rajagopal, and T. Schäfer, "Color superconductivity in dense quark matter," *Rev. Mod. Phys.* **80** (2008) 1455–1515, arXiv:0709.4635 [hep-ph].

[16] A. Chodos, R. L. Jaffe, K. Johnson, C. B. Thorn, and V. F. Weisskopf, "A New Extended Model of Hadrons," *Phys. Rev. D* **9** (1974) 3471–3495.

[17] O. Philipsen, "Lattice QCD at finite temperature and density," *Eur. Phys. J. ST* **152** (2007) 29–60, arXiv:0708.1293 [hep-lat].

[18] Z. Fodor and C. Hoelbling, "Light hadron masses from lattice qcd," *Rev. Mod. Phys.* **84** (Apr, 2012) 449–495. https://link.aps.org/doi/10.1103/RevModPhys.84.449.

[19] K. Johnson, "The M.I.T. Bag Model," *Acta Phys. Polon. B* **6** (1975) 865.

[20] G. Martinez, "Advances in Quark Gluon Plasma," 4, 2013. arXiv:1304.1452 [nucl-ex].

[21] **ALICE** Collaboration, J. Adam, D. Adamová, M. M. Aggarwal, and M. Zyzak, "Centrality Dependence of the Charged-Particle Multiplicity Density at Midrapidity in Pb-Pb Collisions at $\sqrt{s_{NN}} = 5.02$ TeV," *Phys. Rev. Lett.* **116** (Jun, 2016) 222302. https://link.aps.org/doi/10.1103/PhysRevLett.116.222302.

[22] J. Adam, D. Adamová, M. Aggarwal, X. Zhu, A. Zichichi, A. Zimmermann, M. Zimmermann, S. Zimmermann, G. Zinovjev, and J. Zmeskal, "Centrality dependence of the pseudorapidity density distribution for charged particles in pb–pb collisions at snn=5.02 tev," *Physics Letters B* **772** (2017) 567–577. https://www.sciencedirect.com/science/article/pii/S0370269317305646.

[23] P. Foka and M. A. Janik, "An overview of experimental results from ultra-relativistic heavy-ion collisions at the cern lhc: Bulk properties and dynamical evolution," *Reviews in Physics* **1** (2016) 154–171. https://www.sciencedirect.com/science/article/pii/S2405428316300156.

[24] **ALICE** Collaboration, J. Adam *et al.*, "Measurement of transverse energy at midrapidity in Pb-Pb collisions at $\sqrt{s_{NN}} = 2.76$ TeV," *Phys. Rev. C* **94** (Sep, 2016) 034903. https://link.aps.org/doi/10.1103/PhysRevC.94.034903.

[25] M. L. Miller, K. Reygers, S. J. Sanders, and P. Steinberg, "Glauber modeling in high energy nuclear collisions," *Ann. Rev. Nucl. Part. Sci.* **57** (2007) 205–243, arXiv:nucl-ex/0701025.

[26] M. Strickland, "Anisotropic Hydrodynamics: Three lectures," *Acta Phys. Polon. B* **45** no. 12, (2014) 2355–2394, arXiv:1410.5786 [nucl-th].

[27] U. W. Heinz, "Concepts of heavy ion physics," in *2nd CERN-CLAF School of High Energy Physics*. 7, 2004. arXiv:hep-ph/0407360.

[28] C. Gale, S. Jeon, and B. Schenke, "Hydrodynamic Modeling of Heavy-Ion Collisions," *Int. J. Mod. Phys. A* **28** (2013) 1340011, arXiv:1301.5893 [nucl-th].

[29] P. Rosnet, "Quark-Gluon Plasma: from accelerator experiments to early Universe," in *11th Rencontres du Vietnam: Cosmology: 50 years after CMB discovery*. 10, 2015. arXiv:1510.04200 [hep-ph].

[30] J. W. Cronin, H. J. Frisch, M. J. Shochet, J. P. Boymond, R. Mermod, P. A. Piroue, and R. L. Sumner, "Production of hadrons with large transverse momentum at 200, 300, and 400 GeV," *Phys. Rev. D* **11** (1975) 3105–3123.

[31] **CMS** Collaboration, V. Khachatryan *et al.*, "Charged-particle nuclear modification factors in PbPb and pPb collisions at $\sqrt{s_{\mathrm{N\,N}}} = 5.02$ TeV," *JHEP* **04** (2017) 039, arXiv:1611.01664 [nucl-ex].

[32] **ALICE** Collaboration, B. Abelev *et al.*, "Transverse Momentum Distribution and Nuclear Modification Factor of Charged Particles in p+Pb Collisions at $\sqrt{s_{NN}}$=5.02 TeV," *Phys. Rev. Lett.* **110** (Feb, 2013) 082302. https://link.aps.org/doi/10.1103/PhysRevLett.110.082302.

[33] **CMS** Collaboration, S. Chatrchyan *et al.*, "Observation and studies of jet quenching in PbPb collisions at nucleon-nucleon center-of-mass energy = 2.76 TeV," *Phys. Rev. C* **84** (2011) 024906, arXiv:1102.1957 [nucl-ex].

[34] **ALICE** Collaboration, B. Abelev *et al.*, "Pion, Kaon, and Proton Production in Central Pb–Pb Collisions at $\sqrt{s_{NN}} = 2.76$ TeV," *Phys. Rev. Lett.* **109** (2012) 252301, arXiv:1208.1974 [hep-ex].

[35] **STAR** Collaboration, B. I. Abelev *et al.*, "Systematic Measurements of Identified Particle Spectra in pp, d^+ Au and Au+Au Collisions from STAR," *Phys. Rev. C* **79** (2009) 034909, arXiv:0808.2041 [nucl-ex].

[36] **PHENIX** Collaboration, S. S. Adler *et al.*, "Identified charged particle spectra and yields in Au+Au collisions at S(NN)**1/2 = 200-GeV," *Phys. Rev. C* **69** (2004) 034909, arXiv:nucl-ex/0307022.

[37] I. A. Karpenko and Y. M. Sinyukov, "Kaon and pion femtoscopy at top RHIC energy in hydrokinetic model," *Phys. Part. Nucl. Lett.* **8** no. 9, (2011) 981–984, arXiv:1103.5125 [nucl-th].

[38] Y. A. Karpenko and Y. M. Sinyukov, "Femtoscopic scales in central A+A collisions at RHIC and LHC energies in hydrokinetic model," *J. Phys. G* **38** (2011) 124059, arXiv:1107.3745 [nucl-th].

[39] P. Bozek, "Flow and interferometry in 3+1 dimensional viscous hydrodynamics," *Phys. Rev. C* **85** (2012) 034901, arXiv:1110.6742 [nucl-th].

[40] **ALICE** Collaboration, J. Adam *et al.*, "Anisotropic flow of charged particles in Pb-Pb collisions at $\sqrt{s_{\rm NN}} = 5.02$ TeV," *Phys. Rev. Lett.* **116** no. 13, (2016) 132302, arXiv:1602.01119 [nucl-ex].

[41] A. Andronic, P. Braun-Munzinger, and J. Stachel, "Hadron production in central nucleus-nucleus collisions at chemical freeze-out," *Nucl. Phys. A* **772** (2006) 167–199, arXiv:nucl-th/0511071.

[42] A. Andronic, "An overview of the experimental study of quark-gluon matter in high-energy nucleus-nucleus collisions," *Int. J. Mod. Phys. A* **29** (2014) 1430047, arXiv:1407.5003 [nucl-ex].

[43] R. Hanbury Brown and R. Q. Twiss, "A Test of a new type of stellar interferometer on Sirius," *Nature* **178** (1956) 1046–1048.

[44] **ALICE** Collaboration, B. B. Abelev *et al.*, "Freeze-out radii extracted from three-pion cumulants in pp, p–Pb and Pb–Pb collisions at the LHC," *Phys. Lett. B* **739** (2014) 139–151, arXiv:1404.1194 [nucl-ex].

[45] F. Bellini and A. P. Kalweit, "Testing production scenarios for (anti-)(hyper-)nuclei and exotica at energies available at the CERN

Large Hadron Collider," *Phys. Rev. C* **99** (May, 2019) 054905. https://link.aps.org/doi/10.1103/PhysRevC.99.054905.

[46] **ALICE** Collaboration, J. Adam *et al.*, "Centrality dependence of pion freeze-out radii in Pb-Pb collisions at $\sqrt{s_{NN}} = 2.76$ TeV," *Phys. Rev. C* **93** no. 2, (2016) 024905, arXiv:1507.06842 [nucl-ex].

[47] **ALICE** Collaboration, J. Adam *et al.*, "Two-pion femtoscopy in p-Pb collisions at $\sqrt{s_{\rm NN}} = 5.02$ TeV," *Phys. Rev. C* **91** (2015) 034906, arXiv:1502.00559 [nucl-ex].

[48] **ALICE** Collaboration, B. Abelev *et al.*, "Charged kaon femtoscopic correlations in pp collisions at $\sqrt{s} = 7$ TeV," *Phys. Rev. D* **87** no. 5, (2013) 052016, arXiv:1212.5958 [hep-ex].

[49] K.-J. Sun, C. M. Ko, and B. Dönigus, "Suppression of light nuclei production in collisions of small systems at the Large Hadron Collider," *Phys. Lett.* **B792** (2019) 132–137, arXiv:1812.05175 [nucl-th].

[50] P. Braun-Munzinger and B. Dönigus, "Loosely-bound objects produced in nuclear collisions at the lhc," *Nuclear Physics A* **987** (2019) 144 – 201. http://www.sciencedirect.com/science/article/pii/S0375947419300405.

[51] U. W. Heinz, "The Little bang: Searching for quark gluon matter in relativistic heavy ion collisions," *Nucl. Phys. A* **685** (2001) 414–431, arXiv:hep-ph/0009170.

[52] U. W. Heinz, "Towards the Little Bang Standard Model," *J. Phys. Conf. Ser.* **455** (2013) 012044, arXiv:1304.3634 [nucl-th].

[53] **ALICE** Collaboration, S. Acharya *et al.*, "Production of ^{4}He and $^4\overline{\rm He}$ in Pb-Pb collisions at $\sqrt{s_{\rm NN}}$ = 2.76 TeV at the LHC," *Nucl. Phys.* **A971** (2018) 1–20, arXiv:1710.07531 [nucl-ex].

[54] **STAR** Collaboration, J. W. Harris, "The STAR experiment at the relativistic heavy ion collider," *Nucl. Phys. A* **566** (1994) 277C–285C.

[55] **PHENIX** Collaboration, J. C. Gregory *et al.*, "PHENIX experiment at RHIC," *Nucl. Phys. A* **566** (1994) 287C–298C.

[56] **ALICE** Collaboration, K. Aamodt *et al.*, "The ALICE experiment at the CERN LHC," *JINST* **3** (2008) S08002.

[57] **ALICE** Collaboration, J. Adam *et al.*, "Precision measurement of the mass difference between light nuclei and anti-nuclei," *Nature Phys.* **11** no. 10, (2015) 811–814, arXiv:1508.03986 [nucl-ex].

[58] **ALICE** Collaboration, J. Adam *et al.*, "Production of light nuclei and anti-nuclei in pp and Pb–Pb collisions at energies available at the CERN Large Hadron Collider," *Phys. Rev.* **C93** no. 2, (2016) 024917, arXiv:1506.08951 [nucl-ex].

[59] **ALICE** Collaboration, S. Acharya *et al.*, "Measurement of deuteron spectra and elliptic flow in Pb-Pb collisions at $\sqrt{s_{\rm NN}}$ = 2.76 TeV at the LHC," *Eur. Phys. J.* **C77** no. 10, (2017) 658, arXiv:1707.07304 [nucl-ex].

[60] **ALICE** Collaboration, S. Acharya *et al.*, "Production of deuterons, tritons, ^{3}He nuclei and their antinuclei in pp collisions at $\sqrt{s}$ = 0.9, 2.76 and 7 TeV," *Phys. Rev.* **C97** no. 2, (2018) 024615, arXiv:1709.08522 [nucl-ex].

[61] **ALICE** Collaboration, S. Acharya *et al.*, "Multiplicity dependence of (anti-)deuteron production in pp collisions at $\sqrt{s}$ = 7 TeV," *Phys. Lett. B* **794** (2019) 50–63, arXiv:1902.09290 [nucl-ex].

[62] **ALICE** Collaboration, S. Acharya *et al.*, "Multiplicity dependence of light (anti-)nuclei production in p–Pb collisions at $\sqrt{s_{\rm NN}}$ = 5.02 TeV," *Phys. Lett. B* **800** (2020) 135043, arXiv:1906.03136 [nucl-ex].

[63] **ALICE** Collaboration, S. Acharya *et al.*, "Measurement of the (anti-)^{3}He elliptic flow in Pb-Pb collisions at $\sqrt{s_{\rm NN}}$ = 5.02 TeV," *Phys. Lett.* **B805** (2020) 135414, arXiv:1910.09718 [nucl-ex].

[64] **ALICE** Collaboration, S. Acharya *et al.*, "Production of (anti-)^{3}He and (anti-)^{3}H in p–Pb collisions at $\sqrt{s_{\rm NN}}$ = 5.02 TeV," *Phys. Rev.* **C101** no. 4, (2020) 044906, arXiv:1910.14401 [nucl-ex].

[65] **ALICE** Collaboration, S. Acharya *et al.*, "(Anti-)deuteron production in pp collisions at $\sqrt{s} = 13$ TeV," *Eur. Phys. J.* **C80** no. 9, (2020) 889, arXiv:2003.03184 [nucl-ex].

[66] **ALICE** Collaboration, S. Acharya *et al.*, "Elliptic and triangular flow of (anti)deuterons in Pb-Pb collisions at $\sqrt{s_{\rm NN}}$ = 5.02 TeV," arXiv:2005.14639 [nucl-ex].

[67] **E878** Collaboration, M. J. Bennett *et al.*, "Light nuclei production in relativistic Au + nucleus collisions," *Phys. Rev. C* **58** (1998) 1155–1164.

[68] **E802** Collaboration, L. Ahle *et al.*, "Proton and deuteron production in Au + Au reactions at 11.6 A-GeV/c," *Phys. Rev. C* **60** (1999) 064901.

[69] **E864** Collaboration, T. A. Armstrong *et al.*, "Measurements of light nuclei production in 11.5 A-GeV/c Au + Pb heavy ion collisions," *Phys. Rev. C* **61** (2000) 064908, arXiv:nucl-ex/0003009.

[70] **E864** Collaboration, T. A. Armstrong *et al.*, "Anti-deuteron yield at the AGS and coalescence implications," *Phys. Rev. Lett.* **85** (2000) 2685–2688, arXiv:nucl-ex/0005001.

[71] **NA52 (NEWMASS)** Collaboration, G. Ambrosini *et al.*, "Baryon and anti-baryon production in lead-lead collisions at 158 A-GeV/c," *Phys. Lett. B* **417** (1998) 202–210.

[72] **STAR** Collaboration, C. Adler *et al.*, "$\overline{\rm d}$ and $^3\overline{\rm He}$ production in $\sqrt{s_{\rm NN}}$ = 130 GeV Au + Au collisions," *Phys. Rev. Lett.* **87** (2001) 2623011–2623016.

[73] **PHENIX** Collaboration, S. S. Adler *et al.*, "Deuteron and antideuteron production in Au + Au collisions at 200 GeV," *Phys. Rev. Lett.* **94** (2005) 122302, arXiv:nucl-ex/0406004.

[74] **BRAHMS** Collaboration, I. Arsene *et al.*, "Rapidity dependence of deuteron production in Au+Au collisions at $\sqrt{s_{\rm NN}}$ = 200 GeV," *Phys. Rev. C* **83** (2011) 044906, arXiv:1005.5427 [nucl-ex].

[75] **STAR** Collaboration, H. Agakishiev *et al.*, "Observation of the antimatter helium-4 nucleus," *Nature* **473** (2011) 353, arXiv:1103.3312 [nucl-ex]. [Erratum: Nature 475 (2011) 412].

[76] **STAR** Collaboration, L. Adamczyk *et al.*, "Measurement of elliptic flow of light nuclei at $\sqrt{s_{\rm NN}} = 200$, 62.4, 39, 27, 19.6, 11.5, and 7.7 GeV at the BNL Relativistic Heavy Ion Collider," *Phys. Rev. C* **94** no. 3, (2016) 034908, arXiv:1601.07052 [nucl-ex].

[77] **STAR** Collaboration, J. Adam *et al.*, "Beam energy dependence of (anti-)deuteron production in Au + Au collisions at the BNL Relativistic Heavy Ion Collider," *Phys. Rev. C* **99** no. 6, (2019) 064905, arXiv:1903.11778 [nucl-ex].

[78] B. Alper *et al.*, "Large angle production of stable particles heavier than the proton and a search for quarks at the cern intersecting storage rings," *Phys. Lett. B* **46** (1973) 265–268.

[79] **Fermilab E735** Collaboration, T. Alexopoulos, E. W. Anderson, N. N. Biswas, A. Bujak, *et al.*, "Cross sections for deuterium, tritium, and helium production in $\overline{p}p$ collisions at $\sqrt{s} = 1.8$ tev," *Phys. Rev. D* **62** (Sep, 2000) 072004. https://link.aps.org/doi/10.1103/PhysRevD.62.072004.

[80] **ALEPH** Collaboration, S. Schael *et al.*, "Deuteron and anti-deuteron production in e+ e- collisions at the Z resonance," *Phys. Lett. B* **639** (2006) 192–201, arXiv:hep-ex/0604023.

[81] J. Simon-Gillo, H. Boggild, J. Boissevain, M. Cherney, *et al.*, "Deuteron and anti-deuteron production in cern experiment na44," *Nuclear Physics A* **590** no. 1, (1995) 483–486. https://www.sciencedirect.com/science/article/pii/0375947495002594.

[82] **NA49** Collaboration, T. Anticic *et al.*, "Energy and centrality dependence of deuteron and proton production in Pb + Pb collisions at relativistic energies," *Phys. Rev. C* **69** (2004) 024902.

[83] **British-Scandinavian-MIT** Collaboration, S. Henning *et al.*, "Production of Deuterons and anti-Deuterons in Proton Proton Collisions at the CERN ISR," *Lett. Nuovo Cim.* **21** (1978) 189.

[84] **H1** Collaboration, A. Aktas *et al.*, "Measurement of anti-deuteron photoproduction and a search for heavy stable charged particles at HERA," *Eur. Phys. J. C* **36** (2004) 413–423, arXiv:hep-ex/0403056.

[85] **ZEUS** Collaboration, S. Chekanov *et al.*, "Measurement of (anti)deuteron and (anti)proton production in DIS at HERA," *Nucl. Phys. B* **786** (2007) 181–205, arXiv:0705.3770 [hep-ex].

[86] E. G. Kessler, Jr., "The Deuteron Binding Energy and the Neutron Mass," *Phys. Lett. A* **255** (1999) 221.

[87] P. Braun-Munzinger, K. Redlich, and J. Stachel, "Particle production in heavy ion collisions," arXiv:nucl-th/0304013.

[88] A. Andronic, P. Braun-Munzinger, J. Stachel, and H. Stocker, "Production of light nuclei, hypernuclei and their antiparticles in relativistic nuclear collisions," *Phys. Lett. B* **697** (2011) 203–207, arXiv:1010.2995 [nucl-th].

[89] S. Wheaton and J. Cleymans, "THERMUS: A Thermal model package for ROOT," *Comput. Phys. Commun.* **180** (2009) 84–106, arXiv:hep-ph/0407174.

[90] A. Andronic, P. Braun-Munzinger, K. Redlich, and J. Stachel, "Decoding the phase structure of qcd via particle production at high energy," *Nature* **561** (10, 2017) 321–330.

[91] G. Torrieri, S. Jeon, J. Letessier, and J. Rafelski, "SHAREv2: Fluctuations and a comprehensive treatment of decay feed-down," *Comput. Phys. Commun.* **175** (2006) 635–649, arXiv:nucl-th/0603026.

[92] **STAR** Collaboration, B. I. Abelev *et al.*, "Identified particle production, azimuthal anisotropy, and interferometry measurements in Au+Au collisions at s(NN)**(1/2) = 9.2- GeV," *Phys. Rev. C* **81** (2010) 024911, arXiv:0909.4131 [nucl-ex].

[93] J. Cleymans, H. Oeschler, and K. Redlich, "Influence of impact parameter on thermal description of relativistic heavy ion collisions at (1-2) A-GeV," *Phys. Rev. C* **59** (1999) 1663, arXiv:nucl-th/9809027.

[94] A. Andronic, P. Braun-Munzinger, and J. Stachel, "Thermal hadron production in relativistic nuclear collisions: The Hadron mass spectrum, the horn, and the QCD phase transition," *Phys. Lett. B* **673** (2009) 142–145, arXiv:0812.1186 [nucl-th]. [Erratum: Phys.Lett.B 678, 516 (2009)].

[95] J. Manninen and F. Becattini, "Chemical freeze-out in ultra-relativistic heavy ion collisions at s(NN)**(1/2) = 130 and 200-GeV," *Phys. Rev. C* **78** (2008) 054901, arXiv:0806.4100 [nucl-th].

[96] **STAR** Collaboration, M. M. Aggarwal *et al.*, "Scaling properties at freeze-out in relativistic heavy ion collisions," *Phys. Rev. C* **83** (2011) 034910, arXiv:1008.3133 [nucl-ex].

[97] M. Kaneta and N. Xu, "Centrality dependence of chemical freeze-out in Au+Au collisions at RHIC," in *17th International Conference on Ultra Relativistic Nucleus-Nucleus Collisions (Quark Matter 2004)*. 5, 2004. arXiv:nucl-th/0405068.

[98] F. Becattini, M. Gazdzicki, A. Keranen, J. Manninen, and R. Stock, "Chemical equilibrium in nucleus nucleus collisions at relativistic energies," *Phys. Rev. C* **69** (2004) 024905, arXiv:hep-ph/0310049.

[99] J. Letessier and J. Rafelski, "Hadron production and phase changes in relativistic heavy ion collisions," *Eur. Phys. J. A* **35** (2008) 221–242, arXiv:nucl-th/0504028.

[100] A. Dumitru, L. Portugal, and D. Zschiesche, "Inhomogeneous freeze-out in relativistic heavy-ion collisions," *Phys. Rev. C* **73** (2006) 024902, arXiv:nucl-th/0511084.

[101] V. Vovchenko, B. Dönigus, and H. Stoecker, "Multiplicity dependence of light nuclei production at LHC energies in the

canonical statistical model," *Phys. Lett. B* **785** (2018) 171–174, arXiv:1808.05245 [hep-ph].

[102] V. Vovchenko, "The Thermal-FIST package." https://github.com/vlvovch/Thermal-FIST.

[103] **ALICE** Collaboration, E. Abbas *et al.*, "Mid-rapidity anti-baryon to baryon ratios in pp collisions at $\sqrt{s}$ = 0.9, 2.76 and 7 TeV measured by ALICE," *Eur. Phys. J. C* **73** (2013) 2496, arXiv:1305.1562 [nucl-ex].

[104] **ALICE** Collaboration, S. Acharya *et al.*, "Production of ^{4}He and $^4\overline{\mathrm{He}}$ in Pb–Pb collisions at $\sqrt{s_{\mathrm{NN}}}$ = 2.76 TeV at the LHC," *Nucl. Phys.* **A971** (2018) 1–20, arXiv:1710.07531 [nucl-ex].

[105] **ALICE** Collaboration, J. Adam *et al.*, "Production of light nuclei and anti-nuclei in pp and Pb–Pb collisions at energies available at the CERN Large Hadron Collider," *Phys. Rev. C* **93** (Feb, 2016) 024917. https://link.aps.org/doi/10.1103/PhysRevC.93.024917.

[106] **ALICE** Collaboration, J. Adam *et al.*, "$^3_\Lambda$H and $^3_{\overline{\Lambda}}\overline{\mathrm{H}}$ production in Pb–Pb collisions at $\sqrt{s_{\mathrm{NN}}} = 2.76$ TeV," *Phys. Lett.* **B754** (2016) 360–372, arXiv:1506.08453 [nucl-ex].

[107] V. Vovchenko, B. Dönigus, and H. Stoecker, "Canonical statistical model analysis of p-p , p -Pb, and Pb-Pb collisions at energies available at the CERN Large Hadron Collider," *Phys. Rev. C* **100** no. 5, (2019) 054906, arXiv:1906.03145 [hep-ph].

[108] V. Vovchenko, M. I. Gorenstein, and H. Stoecker, "Finite resonance widths influence the thermal-model description of hadron yields," *Phys. Rev. C* **98** no. 3, (2018) 034906, arXiv:1807.02079 [nucl-th].

[109] S. T. Butler and C. A. Pearson, "Deuterons from High-Energy Proton Bombardment of Matter," *Phys. Rev.* **129** (1963) 836–842.

[110] J. I. Kapusta, "Mechanisms for deuteron production in relativistic nuclear collisions," *Phys. Rev.* **C21** (1980) 1301–1310. https://link.aps.org/doi/10.1103/PhysRevC.21.1301.

[111] **ALICE** Collaboration, S. Acharya *et al.*, "Production of deuterons, tritons, ^{3}He nuclei and their antinuclei in pp collisions at $\sqrt{s}$ = 0.9, 2.76 and 7 TeV," *Phys. Rev. C* **97** no. 2, (2018) 024615, arXiv:1709.08522 [nucl-ex].

[112] T. Sjostrand, S. Mrenna, and P. Z. Skands, "A Brief Introduction to PYTHIA 8.1," *Comput. Phys. Commun.* **178** (2008) 852–867, arXiv:0710.3820 [hep-ph].

[113] **ALICE** Collaboration, "Supplemental material: afterburner for generating light (anti-)nuclei with QCD-inspired event generators in pp collisions,". https://cds.cern.ch/record/2285500.

[114] S. Albergo *et al.*, "Light nuclei production in heavy ion collisions at relativistic energies," *Phys. Rev. C* **65** (2002) 034907.

[115] **NA49** Collaboration, T. Anticic *et al.*, "Energy and centrality dependence of deuteron and proton production in Pb + Pb collisions at relativistic energies," *Phys. Rev. C* **69** (2004) 024902.

[116] **PHENIX** Collaboration, S. S. Adler *et al.*, "Deuteron and antideuteron production in Au + Au collisions at s(NN)**(1/2) = 200-GeV," *Phys. Rev. Lett.* **94** (2005) 122302, arXiv:nucl-ex/0406004.

[117] A. Mekjian, "Thermodynamic Model for Composite Particle Emission in Relativistic Heavy Ion Collisions," *Phys. Rev. Lett.* **38** (1977) 640–643.

[118] R. Scheibl and U. W. Heinz, "Coalescence and flow in ultrarelativistic heavy ion collisions," *Phys. Rev.* **C59** (1999) 1585–1602, arXiv:nucl-th/9809092 [nucl-th].

[119] H. Sato and K. Yazaki, "On the coalescence model for high energy nuclear reactions," *Phys. Lett. B* **98** no. 3, (1981) 153 – 157.

[120] M. Gyulassy, K. Frankel, and E. a. Remler, "DEUTERON FORMATION IN NUCLEAR COLLISIONS," *Nucl. Phys. A* **402** (1983) 596–611.

[121] S. Mrowczynski, "Anti-nucleon sources in heavy ion collisions," *Phys. Lett. B* **308** (1993) 216–219.

[122] P. Danielewicz and G. F. Bertsch, "Production of deuterons and pions in a transport model of energetic heavy ion reactions," *Nucl. Phys. A* **533** (1991) 712–748.

[123] P. Danielewicz and P. Schuck, "Formulation of particle correlation and cluster production in heavy-ion-induced reactions," *Phys. Lett. B* **274** (1992) 268–274.

[124] C. B. Dover, U. W. Heinz, E. Schnedermann, and J. Zimanyi, "Relativistic coalescence model for high-energy nuclear collisions," *Phys. Rev. C* **44** (1991) 1636–1654.

[125] S. Leupold and U. W. Heinz, "Coalescence model for deuterons and anti-deuterons in relativistic heavy ion collisions," *Phys. Rev. C* **50** (1994) 1110–1128.

[126] P. J. Mohr, D. B. Newell, and B. N. Taylor, "CODATA Recommended Values of the Fundamental Physical Constants: 2014," *Rev. Mod. Phys.* **88** no. 3, (2016) 035009, arXiv:1507.07956 [physics.atom-ph].

[127] G. Ropke, "Light nuclei quasiparticle energy shift in hot and dense nuclear matter," *Phys. Rev. C* **79** (2009) 014002, arXiv:0810.4645 [nucl-th].

[128] **ALICE** Collaboration, B. Abelev *et al.*, "Centrality dependence of π, K, p production in Pb-Pb collisions at $\sqrt{s_{NN}}$ = 2.76 TeV," *Phys. Rev. C* **88** (2013) 044910, arXiv:1303.0737 [hep-ex].

[129] **ALICE** Collaboration, J. Adam *et al.*, "Measurement of pion, kaon and proton production in proton–proton collisions at $\sqrt{s} = 7$ TeV," *Eur. Phys. J. C* **75** no. 5, (2015) 226, arXiv:1504.00024 [nucl-ex].

[130] S. Mrowczynski, "Production of light nuclei at colliders – coalescence vs. thermal model," *Eur. Phys. J. ST* **229** no. 22-23, (2020) 3559–3583, arXiv:2004.07029 [nucl-th].

[131] M. Cirelli, N. Fornengo, M. Taoso, and A. Vittino, "Anti-helium from Dark Matter annihilations," *JHEP* **08** (2014) 009, arXiv:1401.4017 [hep-ph].

[132] K. Blum, K. C. Y. Ng, R. Sato, and M. Takimoto, "Cosmic rays, antihelium, and an old navy spotlight," *Phys. Rev. D* **96** no. 10, (2017) 103021, arXiv:1704.05431 [astro-ph.HE].

[133] M. Korsmeier, F. Donato, and N. Fornengo, "Prospects to verify a possible dark matter hint in cosmic antiprotons with antideuterons and antihelium," *Phys. Rev. D* **97** no. 10, (2018) 103011, arXiv:1711.08465 [astro-ph.HE].

[134] S. Ahlen *et al.*, "An Antimatter spectrometer in space," *Nucl. Instrum. Meth. A* **350** (1994) 351–367.

[135] F. Donato, D. Maurin, P. Salati, A. Barrau, G. Boudoul, and R. Taillet, "Anti-protons from spallations of cosmic rays on interstellar matter," *Astrophys. J.* **563** (2001) 172–184, arXiv:astro-ph/0103150.

[136] **AMS** Collaboration, M. Aguilar, L. Ali Cavasonza, *et al.*, "Antiproton flux, antiproton-to-proton flux ratio, and properties of elementary particle fluxes in primary cosmic rays measured with the alpha magnetic spectrometer on the international space station," *Phys. Rev. Lett.* **117** (Aug, 2016) 091103. https://link.aps.org/doi/10.1103/PhysRevLett.117.091103.

[137] **ALICE** Collaboration, N. Sharma, "Production of nuclei and antinuclei in pp and Pb-Pb collisions with ALICE at the LHC," *J. Phys. G* **38** (2011) 124189, arXiv:1109.4836 [nucl-ex].

[138] A. Ibarra and S. Wild, "Prospects of antideuteron detection from dark matter annihilations or decays at AMS-02 and GAPS," *JCAP* **02** (2013) 021, arXiv:1209.5539 [hep-ph].

[139] J. Silk *et al.*, *Particle Dark Matter: Observations, Models and Searches*. Cambridge Univ. Press, Cambridge, 2010.

[140] T. Aramaki *et al.*, "Review of the theoretical and experimental status of dark matter identification with cosmic-ray antideuterons," *Phys. Rept.* **618** (2016) 1–37, arXiv:1505.07785 [hep-ph].

[141] N. Fornengo, L. Maccione, and A. Vittino, "Dark matter searches with cosmic antideuterons: status and perspectives," *JCAP* **09** (2013) 031, arXiv:1306.4171 [hep-ph].

[142] C. J. Hailey, "An indirect search for dark matter using antideuterons: the GAPS experiment," *New J. Phys.* **11** no. 10, (2009) 105022.

[143] H. Fuke *et al.*, "Search for cosmic-ray antideuterons," *Phys. Rev. Lett.* **95** (2005) 081101, arXiv:astro-ph/0504361.

[144] K. Abe *et al.*, "Search for Antihelium with the BESS-Polar Spectrometer," *Phys. Rev. Lett.* **108** (2012) 131301, arXiv:1201.2967 [astro-ph.CO].

[145] S. Ting. https://home.cern/news/news/experiments/latest-results-ams-experiment.

[146] V. Poulin, P. Salati, I. Cholis, M. Kamionkowski, and J. Silk, "Where do the AMS-02 antihelium events come from?," *Phys. Rev. D* **99** no. 2, (2019) 023016, arXiv:1808.08961 [astro-ph.HE].

[147] F. Donato, N. Fornengo, and D. Maurin, "Antideuteron fluxes from dark matter annihilation in diffusion models," *Phys. Rev. D* **78** (2008) 043506, arXiv:0803.2640 [hep-ph].

[148] W. Herr and B. Muratori, "Concept of luminosity,". https://cds.cern.ch/record/941318.

[149] "The CERN accelerator complex," 2012. https://home.cern/science/accelerators/accelerator-complex.

[150] S. van der Meer, "Calibration of the effective beam height in the ISR," Tech. Rep. CERN-ISR-PO-68-31. ISR-PO-68-31, CERN, Geneva, 1968. https://cds.cern.ch/record/296752.

[151] "The ATLAS experiment." https://atlas.cern/.

[152] "The CMS experiment." https://cms.cern/.

[153] "The ALICE experiment." https://alice.cern/.

[154] "The LHCb experiment." https://lhcb-public.web.cern.ch/.

[155] **ALICE** Collaboration, B. Abelev *et al.*, "Performance of the ALICE Experiment at the CERN LHC," *Int. J. Mod. Phys.* **A29** (2014) 1430044, arXiv:1402.4476 [nucl-ex].

[156] **ALICE** Collaboration, K. Aamodt *et al.*, "The ALICE experiment at the CERN LHC," *JINST* **3** (2008) S08002.

[157] **ALICE** Collaboration, K. Aamodt *et al.*, "Alignment of the ALICE Inner Tracking System with cosmic-ray tracks," *JINST* **5** (2010) P03003, arXiv:1001.0502 [physics.ins-det].

[158] J. Alme, Y. Andres, H. Appelshäuser, S. Bablok, N. Bialas, *et al.*, "The ALICE TPC, a large 3-dimensional tracking device with fast readout for ultra-high multiplicity events," *Nucl. Instrum. Meth.* **A622** (2010) 316–367, arXiv:1001.1950 [physics.ins-det].

[159] A. Akindinov *et al.*, "Performance of the ALICE Time-Of-Flight detector at the LHC," *Eur. Phys. J. Plus* **128** (2013) 44.

[160] **ALICE** Collaboration, P. Cortese *et al.*, "ALICE technical design report on forward detectors: FMD, T0 and V0,".

[161] **ALICE** Collaboration, J. Adam *et al.*, "Determination of the event collision time with the ALICE detector at the LHC," *Eur. Phys. J. Plus* **132** no. 2, (2017) 99, arXiv:1610.03055 [physics.ins-det].

[162] **ALICE** Collaboration, M. Gallio, W. Klempt, L. Leistam, J. De Groot, and J. Schükraft, *ALICE Zero-Degree Calorimeter (ZDC): Technical Design Report*. Technical design report. ALICE. CERN, Geneva, 1999. https://cds.cern.ch/record/381433.

[163] **ALICE** Collaboration, B. Abelev *et al.*, "Upgrade of the ALICE Experiment: Letter of Intent," Tech. Rep. CERN-LHCC-2012-012. LHCC-I-022. ALICE-UG-002, CERN, Geneva, Aug, 2012. https://cds.cern.ch/record/1475243.

[164] M. Mager, "Alpide, the monolithic active pixel sensor for the alice its upgrade," *Nuclear Instruments and Methods in Physics Research Section A: Accelerators, Spectrometers, Detectors and Associated Equipment* **824** (2016) 434–438. https://www.sciencedirect.com/science/article/pii/S0168900215011122. Frontier Detectors for Frontier Physics: Proceedings of the 13th Pisa Meeting on Advanced Detectors.

[165] **ALICE** Collaboration, C. Lippmann, "Upgrade of the ALICE Time Projection Chamber,".

[166] **ALICE** Collaboration, A. J *et al.*, "Addendum to the Technical Design Report for the Upgrade of the ALICE Time Projection Chamber,". https://cds.cern.ch/record/1984329.

[167] F. Sauli, "GEM: A new concept for electron amplification in gas detectors," *Nucl. Instrum. Meth. A* **386** (1997) 531–534.

[168] **ALICE** Collaboration, J. Adam *et al.*, "Particle identification in ALICE: a Bayesian approach," *Eur. Phys. J. Plus* **131** no. CERN-EP-2016-023. CERN-EP-2016-023, (Feb, 2016) 168. 31 p. https://cds.cern.ch/record/2127042.

[169] **ALICE** Collaboration, S. Acharya *et al.*, "Multiplicity dependence of light (anti-)nuclei production in p–Pb collisions at $\sqrt{s_{\mathrm{NN}}}$ = 5.02 TeV," *Physics Letters B* **800** (10, 2019) 135043.

[170] Tilsner, H., Alt, T., Aurbakken, K., Grastveit, G., Helstrup, H., Lindenstruth, V., Loizides, C., Nystrand, J., Roehrich, D., Skaali, B., Steinbeck, T., Ullaland, K., Vestbo, A., and Vik, T., "The high-level trigger of ALICE," *Eur Phys J C* **33** (2004) s1041–s1043. https://doi.org/10.1140/epjcd/s2004-03-1806-1.

[171] D. Huffman, "A method for the construction of minimum-redundancy codes," *Resonance* **11** (02, 2006) 91–99.

[172] I. Belikov, "Event reconstruction and particle identification in the ALICE experiment at the LHC," *EPJ Web of Conferences* **70** (03, 2014) 00029.

[173] "The AliRoot Framework." `http://alice-offline.web.cern.ch/AliRoot/Manual.html`.

[174] X.-N. Wang and M. Gyulassy, "Hijing: A monte carlo model for multiple jet production in pp, pA, and AA collisions," *Phys. Rev.* **D44** (1991) 3501–3516. `https://link.aps.org/doi/10.1103/PhysRevD.44.3501`.

[175] R. Brun, F. Bruyant, F. Carminati, S. Giani, M. Maire, A. McPherson, G. Patrick, and L. Urban, "GEANT Detector Description and Simulation Tool, Program Library Long Write-up,". `https://doi.org/10.17181/CERN.MUHF.DMJ1`.

[176] **ALICE** Collaboration, J. Abelev *et al.*, "ALICE: Technical proposal for A Large Ion Collider Experiment at the CERN LHC,".

[177] M. Ivanov, K. Safarik, Y. Belikov, and J. Bracinik, "Tpc tracking and particle identification in high-density environment,".

[178] **UA5** Collaboration, G. J. Alner *et al.*, "An Investigation of Multiplicity Distributions in Different Pseudorapidity Intervals in anti-p p Reactions at a CMS Energy of 540-GeV," *Phys. Lett. B* **160** (1985) 193–198.

[179] **ALICE** Collaboration, K. Aamodt *et al.*, "Charged-particle multiplicity measurement in proton-proton collisions at $\sqrt{s} = 0.9$ and 2.36 TeV with ALICE at LHC," *Eur. Phys. J. C* **68** (2010) 89–108, `arXiv:1004.3034 [hep-ex]`.

[180] **ALICE** Collaboration, B. Abelev *et al.*, "Centrality determination of Pb-Pb collisions at $\sqrt{s_{NN}}$ = 2.76 TeV with ALICE," *Phys. Rev. C* **88** no. 4, (2013) 044909, `arXiv:1301.4361 [nucl-ex]`.

[181] H. Kamada, J. Golak, K. Miyagawa, H. Witała, and W. Glöckle, "π-mesonic decay of the hypertriton," *Phys. Rev. C* **57** (Apr, 1998) 1595–1603. https://link.aps.org/doi/10.1103/PhysRevC.57.1595.

[182] R. Barlow, "Systematic errors: Facts and fictions," in *Conference on Advanced Statistical Techniques in Particle Physics*, pp. 134–144. 7, 2002. arXiv:hep-ex/0207026.

[183] https://twiki.cern.ch/twiki/bin/view/ALICE/AliDPGtoolsTrackSystematicUncertainty.

[184] A. Ingemarsson, G. Arendse, A. Auce, R. Carlson, A. Cowley, A. Cox, S. Förtsch, R. Johansson, B. Karlson, M. Lantz, J. Peavy, J. Stander, G. Steyn, and G. Tibell, "Reaction cross sections of intermediate energy ^{3}He-particles on targets from ^{9}Be to ^{208}Pb," *Nuclear Physics A* **696** no. 1, (2001) 3 – 30. http://www.sciencedirect.com/science/article/pii/S0375947401011162.

[185] A. Auce, R. F. Carlson, A. J. Cox, A. Ingemarsson, R. Johansson, P. U. Renberg, O. Sundberg, and G. Tibell, "Reaction cross sections for 38, 65, and 97 MeV deuterons on targets from ^{9}Be to ^{208}Pb," *Phys. Rev. C* **53** (Jun, 1996) 2919–2925. https://link.aps.org/doi/10.1103/PhysRevC.53.2919.

[186] C. Tsallis, "Possible Generalization of Boltzmann-Gibbs Statistics," *J. Statist. Phys.* **52** (1988) 479–487.

[187] **ALICE** Collaboration, S. Acharya *et al.*, "Measurement of deuteron spectra and elliptic flow in Pb–Pb collisions at $\sqrt{s_{\rm NN}}$ = 2.76 TeV at the LHC," *Eur. Phys. J.* **C77** (2017) 658, arXiv:1707.07304 [nucl-ex].

[188] L. Li and F.-H. Liu, "Excitation functions of kinetic freeze-out temperature and transverse flow velocity in proton-proton collisions," arXiv:1805.03342 [hep-ph].

[189] **ALICE** Collaboration, "Production of pions, kaons and protons in p–Pb collisions at 8.16 TeV,". https://alice-notes.web.cern.ch/node/769. internal note.

[190] **ALICE** Collaboration, B. Abelev *et al.*, "Multiplicity dependence of the average transverse momentum in pp, p–Pb, and Pb–Pb collisions at the LHC," *Physics Letters B* **727** no. 4, (2013) 371 – 380. http://www.sciencedirect.com/science/article/pii/S0370269313008617.

[191] A. Andronic, P. Braun-Munzinger, K. Redlich, and J. Stachel, "Decoding the phase structure of QCD via particle production at high energy," *Nature* **561** (2018) 321–330, arXiv:1710.09425 [nucl-th].

[192] **ALICE** Collaboration, S. Acharya *et al.*, "Preliminary Physics Summary: Deuteron and anti-deuteron production in pp collisions at $\sqrt{s}$ = 13 TeV and in Pb–Pb collisions at $\sqrt{s_{\mathrm{NN}}}$ = 5.02 TeV ,". https://cds.cern.ch/record/2272148.

Acknowledgments

The last three years have been the most challenging years of my life. I worked on this thesis with the excitement and the curiosity that every new challenge deserves. I dedicated my time and energies to my Ph.D., learning as much as possible from every person I encountered in this path and from every mistake I made in the process. At the same time, my Ph.D. project saved me during the rough times of my life after 2018, giving me something to focus on when my mind was too heavy.

Most of the people I love in my life does not really understand what I do for a living. Nevertheless, they have always been there for me when I needed to talk or to let off steam, showing a deep interest for me and my work, and I would like to thank them for their support and encouragement.

I would like to thank my family members — my dad, Federica, Andrea and Francesca — that have been there the whole time. Their constant and loving support, even through some crazy times, made this all possible. Being aware that I had their unconditional support and encouragement made all my difficulties easier to overcome.

My professors Franco Riggi and Paola La Rocca have guided me with patience and care during these years. They enriched me greatly, both professionally and personally. I am well aware of how lucky I have been to have them as supervisors. They have a wide and deep knowledge of physics and a kind and generous attitude with students. I have largely benefited from their advice, suggestions, comments and critical observations about my work. They have been constantly present throughout my

time as their Ph.D. student, being available for discussions and promptly replying to all my questions and doubts. I learned everything I know from them, and I will always be grateful to them for the opportunities and the trust they gave me during these years. They are much more than just my professors, by now. We shared many laughs and experiences during the past years and hopefully we will share many more in the future.

This work would not have been possible without the constant support of Alberto. I would like to thank him for his kind support and crucial help during my Ph.D. He bore my ups and downs through my Ph.D., standing my outbursts in the frustrating moments and celebrating my achievements. He is not only my favourite colleague, but also a dear friend of mine.

I also had some *cheerleaders* during these years that I would like to thank: my oldest and dearest friend Maria, she is a certainty in my life since decades and my best partner in crime; Giulia V., my dear deskmate and kind friend since childhood; my close friend Serena, she has always a nice thought for me at critical moments. My balcony-mates Emilio, Federica, Giulia P., they are very close to me despite the physical distance among us. Their warm and kind presence has been a guarantee during these years. My colleagues Selene, Cinzia, Claudio, Melanie, who cheered me up with their presence and laughs during our years at university.

I am very proud of having accomplished this thesis at the University of Catania, that trained me as a scientist and as a person for eight beautiful years. I will always be grateful for all the opportunities I had there.

I would have liked to dedicate this thesis to my mum, but she cannot see nor hear me anymore. However, I am pretty sure she would have been very proud of me and she would have told everyone about my doctoral graduation. I will take care of this latter aspect.